

Ph.D. Thesis

---

# Electrically heated steam methane reforming

---

**Sebastian Thor Wismann**

Supervisor: Professor Ib Chorkendorff

Co-supervisors: Professor Cathrine Frandsen

Research Engineer Peter M. Mortensen

Technical University of Denmark

Department of Physics

Surface Science and Catalysis (SurfCat)

August 2019



## Preface

This thesis is submitted as part of the requirement for obtaining a PhD degree at the Technical University of Denmark. The presented research is supported by Innovation Fund Denmark (File No. 5160-00004B) and the Villum Foundation (Grant 9455). The work presented herein was performed from September 1<sup>st</sup> 2016 to August 31<sup>st</sup> 2019, in the Surface Science and Catalysis group (Surfcat) under supervision of Professor Ib Chorkendorff, Professor Cathrine Frandsen, and Research Engineer at Haldor Topsoe, Peter M. Mortensen. Most of the experimental work detailed within was performed in collaboration with Haldor Topsoe A/S (Preparation/Characterization) and Danish Technological Institute (Reactor tests).

I would sincerely like to thank my supervisors for setting the framework of the project, being supportive of alternative approaches, and their insight and comments from individual areas of expertise when my “*compact illustration*” of results got a little too carried away. I would also like to thank Jakob S. Engbæk and Søren B. Vendelbo for their extensive insight, ranging from applied practical experience to detailed theoretical physics. I would like to thank my colleagues Mads R. Almind, Nikolaj Langemark, and Miriam Varón for their assistance and insight regarding synthesis, characterization, and discussion of - at the time - inexplicable phenomena. I would like to express my gratitude to all my wonderful colleagues at SurfCat, who creates the environment of engaged and helpful researchers, always ready to discuss vexing results or troubleshoot an experiment.

Finally I would like to thank my family and friends, for enduring being subjected to my extremely interesting explanation of obscure details, that at the time seemed very important (at least to me). I dedicate this work to Sofie, who not only endured, but at times showed actual interest, and who always supported me.

## **Abstract**

Increasing focus on sustainability has driven a growing implementation of renewable energy in recent years, resulting in economically competitive costs of renewable electricity compared to electricity generated from fossil fuels. However, the lack of solutions for efficient storage of excess renewable energy creates a demand for technologies compatible with the intermittent nature of renewable energy production. Production of synthesis gas by steam methane reforming (SMR) is a strongly endothermic reaction, today heated by combustion of fossil fuel. Global production of syngas accounts for ca. 3% of all CO<sub>2</sub> emissions. Electrification of the SMR process can supplant the combustion as heat source, reducing emissions by a third.

This thesis describes the research into two types of electrical heating: induction and resistance heating. The work is based on experimental results at laboratory scale, elucidated by computational fluid dynamics modelling, which is further used to extrapolate to industrial relevant conditions, to gauge the potential of the respective technologies.

Electrification of the SMR process provides several substantial benefits compared to current industry. In this thesis, we show that thermal gradients are practically eliminated, providing a substantial increase in catalyst effectiveness. Additionally, it is found that integrated heating enables reactors at industrial capacity two orders of magnitude smaller than current fired reformers. The lower thermal mass enables start-up within minutes, potentially compatible with the intermittent nature of renewable energy. Moreover, electrically heated SMR significantly reduce flue gas from combustion, enabling changes to current plant designs. With compact reactors and less heat recovery, electrically heated SMR is less susceptible to economy of scale, and offers a flexible and scalable platform.

Induction-heated reforming by magnetic hysteresis of a ferromagnetic catalyst or susceptor for high temperature endothermic reactions presents a paradigm shift for direct heating of endothermic processes, supplying heat directly to the catalytic sites. Here, it is demonstrated how the traditional temperature profile is inverted by hysteresis heating, effectively removing all limitations of thermal conductivity within the catalytic bed. It is shown how

the Curie temperature can serve as a safety limit, but at the same time limits application at industrial conditions. Adding layers of increasing Co/Ni ratio to increase the effective Curie temperature can extend the operational temperature range.

It is shown how resistance-heated reforming enables improved reaction control, and supports operation at harsher conditions and higher methane conversion than conventional fired reformers. Moreover, paths for significant improvement in reactor capacity per volume is predicted by optimizing reactor dimensions and geometry, tailoring the effectiveness factor up to 75%, potentially reducing the required amount of catalyst by 2 orders of magnitude.

In summary, electrically heated SMR provides a new, flexible, and competitive, platform for greener production of syngas. Electrification of SMR could reduce CO<sub>2</sub> emissions by nearly 1% if implemented on a global scale. Flexible operation capacity, and fast transient behavior, shows promise considering compatibility with the intermittent nature of renewable energy production. Significant reduction in reactor volume and improvements in catalyst efficiency enables simplification in current industrial plants, and enables efficient operation at smaller scales. Electrification of endothermic processes is an important step towards a sustainable society.

## Resumé

Et stigende fokus på bæredygtighed har i løbet af de seneste år medført en hurtigt voksende implementering af vedvarende energi, hvilket har resulteret i faldende priser på grøn elektricitet, nu sammenlignelige med elproduktion fra fossile brændsler. Den primære udfordring for vedvarende energikilder er den varierende produktion, kombineret med en udpræget mangel på effektive løsninger til opbevaring af overproduktion i stor skala. Der er derfor stor interesse for teknologier som er kompatible med den varierende produktion af grøn strøm. Produktion via dampreformerer af naturgas (*Steam methane reforming*) er en stærkt endotherm proces, der i dag opvarmes ved afbrænding af yderligere fossile brændstoffer. Den samlede produktion af syntesegas svarer til næsten 3% af globale CO<sub>2</sub> udledninger. Ved i stedet at anvende vedvarende elektricitet til opvarmning er det muligt at reducere udledningen af CO<sub>2</sub> med omkring en tredjedel.

Denne afhandling beskriver undersøgelser af to typer elektrisk opvarmning; induktion og modstands opvarmning. Projektet er baseret på eksperimentelt arbejde i laboratorie skala, med henblik på at belyse relevante fænomener igennem CFD modellering (*Computational Fluid Dynamics*). Med udgangspunkt i de implementerede CFD modeller er det muligt at kvantificere problemstillinger, samt potentialet for skalering til industrielle betingelser.

Anvendelse af elektrisk opvarmning tilbyder nye fordele i forhold til nuværende industrielle processer. Igennem denne afhandling illustreres det hvordan begrænsende temperatur gradienter kan omgås, hvilket resulterer i betydeligt mere effektiv anvendelse af katalysatoren. Ved at integrere varmekilden er det muligt reducere størrelsen af en reaktor med op til to størrelsesordner i forhold til opvarmning med fossile brændsler. Den resulterende lavere termiske masse giver muligheden for at starte en reaktor indenfor få minutter, hvilket skaber et grundlag for implementering kompatibel med den fluktuerende produktion af vedvarende energi. Derudover begrænses mængden af røggas drastisk, hvilket begrænser mængden af nødvendige varmevekslere. Elektrisk opvarmede reaktorer er mindre afhængige af total kapacitet end nuværende industrielle anlæg, og giver en mulighed for implementering i mindre skala.

Med induktionsopvarmning via magnetisk hysteresis er det muligt at opvarme en ferromagnetisk katalysator direkte, hvilket løser de primære begrænsninger for den industrielle proces i dag. Ved direkte at varme de katalytiske partikler fjernes begrænsende varmetransport, og den klassiske temperatur profil for en endotherm reaktion inverteres. Det er vist hvordan opvarmningen er reguleret af Curie temperaturen, hvilket samtidig repræsenterer en udfordring for at operere ved industrielle betingelser. Variation af Co/Ni sammensætning giver muligheden for at øge Curie temperaturen, og dermed optimere effektivitet og maksimal temperatur.

Opvarmning via et integreret varmeelement holder reaktionen tæt på ligevægt, og giver mulighed for at opnå en højere omsætning af metan end muligt i konventionelle anlæg. Optimering af geometri og reaktionsbetingelser kan øge udnyttelsen af katalysatoren op til 75%, og dermed drastisk reducere den nødvendige mængde.

Elektrisk opvarmet dampreformering tilbyder en ny, fleksibel, og konkurrencedygtig platform til produktion af grønnere syntese gas. Elektrisk opvarmning af al eksisterende syntesegasproduktion kan reducere den samlede globale CO<sub>2</sub> udledning med op mod 1%. Flexibel reaktor kapacitet og hurtig opstart tyder lovende for reaktor design kompatibel med anvendelse af overproduktion af vedvarende energi. Elektrisk opvarmning af endotherme processer er et vigtigt skridt imod et bæredygtigt samfund.

## List of publications

- ***Electrified Methane Reforming: A compact approach to greener industrial hydrogen production***  
Wismann, S.T, Engbæk, J.S, Vendelbo, S.B., Eriksen, W.L., Bendixen, F.B., Aasberg-Petersen, K., Frandsen, C., Chorkendorff, I., Mortensen, P.M.  
Science, **364**, 756-759, 2019.  
*Appended*
- ***Electrified Methane Reforming: Understanding the dynamic interplay***  
Wismann, S.T, Engbæk, J.S, Vendelbo, S.B., Eriksen, W.L., Frandsen, C., Mortensen, P.M., Chorkendorff, I.  
Submitted to Industrial Engineering and Chemistry Research.  
August 2019  
*Manuscript appended*
- ***Electrified Methane Reforming: Transient thermal response and assessment of carbon activity***  
Wismann, et al., *in preparation*  
*Abstract appended*
- ***Advantages of high temperature hysteresis heating for methane reforming,***  
Wismann et al., *in preparation*
- ***The magnetic and catalytic properties of  $\text{Co}_x\text{Ni}_{1-x}$  for steam methane reforming by hysteresis heating***  
Almind et al., *in preparation*
- Patent: PA 2019 00932 ***Ferromagnetic catalyst support for induction heated catalysis***

# Nomenclature

## Abbreviations

AMU	Atomic mass unit
CFD	Computational fluid dynamics
DFT	Density functional theory
DME	Dimethylether
DTI	Danish Technological Institute
DTU	Technical University of Denmark
FCC	Face centered cubic
FID	Flame ionization detector
FT	Fischer-Tropsch
GC	Gaschromatography
HCP	Hexagonal close packed
ID	Inner diameter
KU	University of Copenhagen
LCOE	Levelized cost of electricity
LPG	Liquid petroleum gas
MeOH	Methanol
MS	Mass spectrometry
OD	Outer diameter
PSA	Pressure swing adsorper
Re	Reynolds Number
RPM	Revolutions per minute
S/C	Steam-to-Carbon ratio
SAR	Specific absorption rate
SE	Sorption-enhanced
SEM	Scanning electron microscopy
SMR	Steam methane reforming
TC	Thermocouple
TCD	Thermal conductivity detector
TEM	Transmission electron microscopy
VSM	Vibrating sample magnetrometry
WGS	Water-gas-shift
XRD	X-ray diffraction

## Selected Variables

$B$	Magnetic field [T]
$D_{eff}$	Effective diffusion [ $m^2/s$ ]
$D_i$	Internal diameter [m]
$D_K$	Knudsen diffusion [ $m^2/s$ ]
$D_m$	Molecular diffusion [ $m^2/s$ ]
$d_p$	Particle diameter [m]
$k_{eff}$	Effective heat conductivity [W/m/K]
$L$	Reactor length [m]
$M_S$	Saturation magnetization [T]
$M_w$	Molecular weight [kg/mol]
$p_i$	Partial pressure [bar]
$Q_i$	Heat source/sink [ $W/m^3$ ]
$R$	Gas constant [J/mol/K]
$r$	radial coordinate [m]
$R_i$	Reaction rate [ $kg/m^3/s$ ]
$T$	Temperature [ $^{\circ}C$ ]
$T_C$	Curie Temperature [ $^{\circ}C$ ]
$X_{CH_4}$	Methane conversion [%]
$z$	axial coordinate [m]
$\beta$	Approach to equilibrium [K]
$\varepsilon_r$	Emissivity
$\eta_{cat}$	Effectiveness factor
$\mu_0$	Vacuum permeability [T·m/A]
$\mu_r$	Relative permeability
$\kappa$	Permeability [ $m^2$ ]
$\rho_r$	Resistivity [ $\Omega \cdot m$ ]
$\theta_b$	Bulk porosity
$\theta_p$	Particle porosity



# Contents

Preface.....	i
Abstract.....	ii
Resumé.....	iv
List of publications.....	vi
Nomenclature .....	vii
<b>1. Introduction.....</b>	<b>1</b>
<b>1.1. Climate concerns.....</b>	<b>1</b>
<b>1.2. Synthesis gas.....</b>	<b>3</b>
<b>1.3. Electrical heating.....</b>	<b>8</b>
<b>1.4. Thesis outline.....</b>	<b>15</b>
<b>2. Experimental setups.....</b>	<b>16</b>
<b>2.1. Resistance heated washcoat.....</b>	<b>17</b>
<b>2.2. Requirements for induction heated catalysts .....</b>	<b>18</b>
<b>2.3. Induction heating setup.....</b>	<b>20</b>
<b>3. Development of universal susceptor .....</b>	<b>23</b>
<b>4. Computational fluid dynamics: Implementation .....</b>	<b>29</b>
<b>4.1 Resistance-heated model.....</b>	<b>31</b>
<b>4.2. Induction-heated model.....</b>	<b>37</b>
<b>4.3. Model verification .....</b>	<b>44</b>
<b>4.4. Characteristic timescales.....</b>	<b>46</b>
<b>5. Induction heating .....</b>	<b>49</b>
<b>5.1. Induction-heated reforming: Experimental .....</b>	<b>49</b>
<b>5.2. Induction-heated reforming: Model predictions.....</b>	<b>51</b>
<b>5.3. Hysteresis heating reaction control .....</b>	<b>56</b>
<b>5.4. Application of hysteresis heating.....</b>	<b>62</b>

<b>6.</b>	<b>Resistance heating</b> .....	66
6.1.	Experimental results.....	66
6.2.	Thermal gradients.....	69
6.3.	Catalytic effectiveness factor.....	72
6.4.	Transient response.....	76
6.5.	Scaling to industrial conditions.....	78
6.6.	Process intensification.....	84
6.7.	Industrial applications.....	89
<b>7.</b>	<b>Summary</b> .....	93
<b>8.</b>	<b>Bibliography</b> .....	96
<b>9.</b>	<b>Appendix</b> .....	110
9.1	<b>Appendix A: Appended papers</b> .....	110
9.1.1	Paper 1.....	110
9.1.2	Paper 2.....	115
9.1.3	Paper 3.....	152
9.2	<b>Appendix B: Estimation of simulation data</b> .....	153
9.3	<b>Appendix C: Supplementary figures</b> .....	159
9.4	<b>Appendix D: Thermocouple model system</b> .....	164
9.5	<b>Appendix E: Conventional SMR lab scale reactor model</b> ....	166



# 1. Introduction

This chapter serves as an introduction to the motivation, science, and industrial relevance of the research behind this thesis, elucidating the growing environmental challenges, and introducing the technology and applications of modern synthesis gas production. At the end of this chapter, an outline of the thesis briefly introduces the content of the ensuing chapters.

## 1.1. Climate concerns

It has become abundantly clear that implementation of sustainable solutions on a large scale is required to avoid potentially disastrous changes to our climate. The rise in global temperature, a direct cause for the more visual effects of climate change, is often correlated to the steadily increasing carbon emissions from the combustion of fossil fuels.<sup>1-4</sup> A substantial reduction of anthropogenic carbon emissions is required to prevent potential irreversible changes to the climate.<sup>5,6</sup>

Generation of heat and electricity accounts for nearly half of all CO<sub>2</sub> emissions through the combustion of fossil fuels.<sup>1</sup> Technologies for production of renewable electricity are readily available, and at today's market, competitive compared to generation of electricity based on fossil fuels, as seen in Figure 1.1.<sup>7,8</sup>

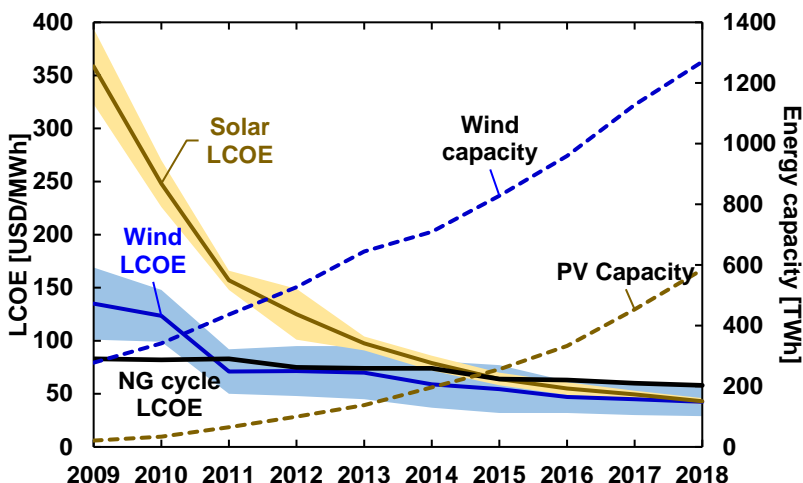


Figure 1.1: Electricity cost and implementation Development of levelized cost of unsubsidized electricity, and global production capacity.<sup>1,7,9</sup>

## 1. Introduction

---

Especially photovoltaics has seen a momentous decrease in production costs, and large-scale facilities are now competitive sources of electricity.<sup>7,10</sup> Further reduction is anticipated for the cost of renewable electricity, due to development of more efficient processes, as the global capacity increases.<sup>7,11</sup> This is in contrast to fossil-fueled based processes, where carbon sources are becoming increasingly scarce and inaccessible.<sup>12</sup>

Even though renewable electricity is economically competitive, and mandatory in the transformation to a sustainable society, the intermittent nature of renewable energy sources is a challenge.<sup>13</sup> Modern electronics demand a very stable supply of energy, which in a society based on renewable energy is ensured by a substantial surplus of capacity for production of renewable energy.<sup>14</sup> Today, there is a distinct lack of implemented solutions for efficient large-scale energy storage, resulting in periods with a large excess of renewable energy.<sup>13</sup> Hydropower can achieve high efficiency and on-demand capacity, but requires favorable geography, making it difficult to scale. In addition, artificial dams can have a large impact on local environment, and are not effective per area relative to other sources of renewable energy.<sup>15,16</sup>

Considering climate concerns and continuously cheaper electricity, why not just make hydrogen through electrolysis, a process with no CO<sub>2</sub> emissions? While many arguments can be made, two will be considered here. One is energy density. While hydrogen has an outstanding gravimetric energy density (120 MJ/kg), the volumetric density, even at 690 bars (and 25°C), is half that of methanol. To put the energy density of liquid chemical fuels into perspective consider a park of 20 wind turbines, each generating ca. 2 MW on a windy day, in total supplying 40.000 households with electric energy.<sup>17,18</sup> In comparison, when fueling a car, ca. 1L of fuel is pumped a second, equivalent to an energy transfer of 42 MW if the fuel is diesel. As practically all combustible fuels are based on carbon, syngas from the SMR process is a relevant starting point.

The second argument is current economy. In short, a single molecule of hydrogen produced by electrolysis thermodynamically requires four times more energy input, compared to hydrogen produced from natural gas. While it is likely, electricity or climate constraints eventually will favor electrolysis and processes based on captured CO<sub>2</sub>, it is ill suited for our current

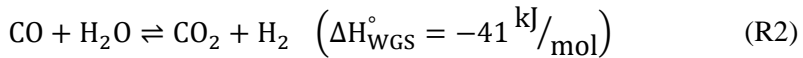
infrastructure.

Production of syngas today relies combustion of fossil fuels, and in total accounts for nearly 3% of global CO<sub>2</sub> emissions, making it highly susceptible to carbon taxes.<sup>4,19,20,27,28</sup>

This work investigates the technical potential in utilizing renewable energy for the production of synthesis gas by steam methane reforming (SMR) in an electrified reformer. To illustrate why electrification is interesting beyond the immediate environmental benefit we need to look at the applications and limitations of current industry.

## 1.2. Synthesis gas

Synthesis gas, or syngas, is a mixture of hydrogen and carbon oxides, with the composition tuned depending on the intended use. Syngas is used in a plethora of chemical products, notably the production of ammonia fertilizer. Other products include synthesis of methanol, fuels, and a several chemical intermediates.<sup>19</sup> Nearly 80% of the global hydrogen supply is based reforming of natural gas and oil, where steam reacts with hydrocarbons.<sup>21</sup> For methane the reaction proceeds according to reaction 1 and 2.



The overall SMR reaction is strongly endothermic, and is typically operated at 30 bars and 850-950°C.<sup>22-24</sup> While the SMR process itself produces stoichiometric quantities of CO<sub>2</sub>, a significant fraction is typically integrated in the product chemical, for instance by production of urea (from ammonia) or methanol.<sup>19</sup> About a third of the CO<sub>2</sub> emissions from the SMR process is from combustion of fuel supplying the reaction with heat.<sup>22,23,25,26</sup>

A typical large-scale SMR plant for production of hydrogen (>50.000 Nm<sup>3</sup> H<sub>2</sub>/h) consists of a number of unit operations.<sup>22,29</sup> A typical layout for the process is illustrated in Figure 1.2.

## 1. Introduction

---

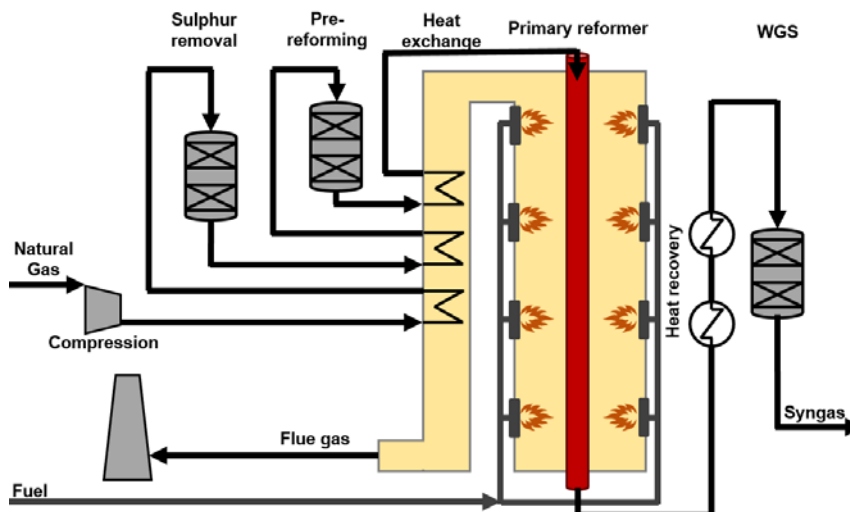


*Figure 1.2: Conventional fired SMR plant Schematic of a typical fired SMR plant, consisting of a desulphurization unit, a pre-reformer, the primary reformer, and water-gas-shift reactors. The flows and heat exchanges are indicated. For hydrogen production, additional heat recovery and a pressure-swing-adsorber (PSA) would separate hydrogen from the syngas, and recycle the offgas to the furnace to reduce fuel consumption.<sup>22</sup>*

A feed of natural gas can contain trace amounts of sulfur, detrimental to catalyst activity,<sup>30</sup> which is removed in the desulphurization unit.<sup>22,31</sup> The pre-reformer operates at ca. 450°C, converting all higher hydrocarbons with steam to a process gas consisting of methane, hydrogen, steam, and carbon oxides.<sup>22</sup> The process gas is then pre-heated, utilizing heat-recovery from the flue gas, to ca. 650°C, before entering the primary reformer,<sup>22</sup> the largest, most complex, and most expensive unit operation of an SMR plant.<sup>32</sup>

The bulk of the reaction takes place in the primary reformer, consisting of hundreds of narrow (8-15 cm diameter) and long (10-14 m) tubes filled with catalyst pellets, placed in a large furnace chamber. The catalyst is typically based on nickel for economic reasons, though other materials (Ru, Rh) display higher intrinsic activity.<sup>22,31</sup> The catalyst pellets are shaped to minimize pressure drop and maximize surface area. Multiple burners are arranged in highly optimized positions for optimal distribution of heat.<sup>22-24,33</sup>

The product composition is determined by the thermodynamic equilibrium depending on feed composition, pressure, and temperature. The equilibrium composition of a typical feed gas with a steam-to-carbon ratio (S/C) of 1.8 is shown in Figure 1.3.

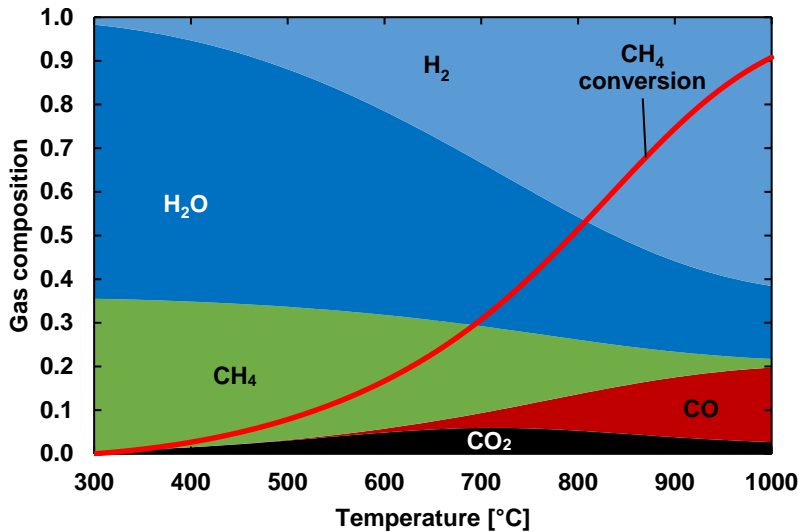


Figure 1.3: Equilibrium composition Equilibrium composition of a typical process gas as a function of temperature at 30 bar and S/C 1.8.

The high CO content at high temperatures (Fig. 1.3), can be shifted towards a higher hydrogen content according to the water-gas-shift reaction (WGS, Reaction 2), at temperatures from 200-450°C in a downstream shift reactor (Fig. 1.2).<sup>22</sup> Low residence time and a selective catalyst inhibits the Sabatier reaction (Reverse reaction 1). Residual steam in the process gas is removed by condensation and recycled (Not included in Figure 1.2).

For production of hydrogen (e.g. for ammonia) the dry gas is separated by parallel pressure-swing-adsorbers (PSA) into a stream of 99.9% pure hydrogen, and an offgas consisting of residual methane, carbon oxides, and ca. 20% hydrogen.<sup>23</sup> The offgas is recycled, and supplements the fuel for combustion in the primary reformer.

### Limitations of fired reformers

The performance of endothermic processes depend strongly on the distribution of heat. The thermodynamics of steam methane reforming (Reaction 1) are inversely impacted by pressure according to Le Chatelier's principle.<sup>34</sup> However, as the primary consumers of syngas such as ammonia, methanol, and Fischer-Tropsch synthesis, are facilitated at high pressure, process economy favors operating the SMR at high pressure (20-40 bar) to

## 1. Introduction

---

decrease overall compression cost in the plant design.<sup>35</sup> Consequently, 850-950°C is required to reach reasonable methane conversion (Fig. 1.3).

Decades of commercial optimization has resulted in modern large-scale industrial reformers utilizing long and narrow tubular reactors, with heat supplied from combustion and transferred via radiation.<sup>23,36</sup> Despite tubular reactors less than 12 cm in diameter, heat transport is limiting reactor performance, rather than reaction kinetics. The harsh conditions of the reactions (>850°C, high partial pressure of steam, 30 bars), demands materials with ceramic traits for safe operation (ie. strong corrosion resistances and small expansion coefficients). For the tubular reactors, expensive “super alloys” such as Incoloy (FeNiCrAlTiC) are used, while the catalyst pellets are based on a highly porous alumina based support. The low thermal conductivity of such materials creates steep thermal gradients across the reactor wall and catalyst bed, limiting catalyst utilization.<sup>22,35,37</sup> A typical industrial reformer has a catalytic effectiveness factor between 2-10%, ie. less than 10% of the available catalytic activity is utilized.<sup>22,29,38</sup>

The steep thermal gradients across the reactor wall induce thermal stress, decreasing reactor lifetime,<sup>35</sup> and mandates several days for safe start-up of fired industrial reformers.<sup>22</sup> Additionally, the thermal gradients at high temperature increase the risk of carbon deposition, a detrimental phenomenon to plant operation.<sup>39</sup> The risk of carbon deposition is controlled by thermodynamics, using the steam-to-carbon ratio (S/C), where additional steam shifts thermodynamic equilibrium favorably for methane conversion, and decreases the risk of carbon deposition. However, a high S/C increase the energy required to heat the excess steam.

To avoid hotspots, and concomitantly increased risk of carbon deposition and thermal stresses, precise heating of the reactors is critical. As mentioned, the tubular reactors are heated in large furnace chambers, with burners positioned for optimal distribution of heat. The combustion must occur at several hundred degrees higher than the reaction to generate sufficient inward flux, typically 60-150 kW/m<sup>2</sup>.<sup>22-24</sup> The flame jets are typically pointed away or along the tubular reactors, transferring heat by radiation and convection. Depending on the setup, a nearly uniform flux can be achieved, but at the expense of very large furnace chambers, where typically less than 2% of the total volume is catalyst.<sup>23,40</sup> Modern SMR plants operate at efficiencies near 95%,<sup>22,33,41</sup> but only due to substantial heat recovery and steam economy, as

the primary reformer only transfer around 50% of the fuel energy to the process gas, the rest leaving as latent heat in the flue gas above 1000°C.<sup>23,24</sup> Large furnace chambers, compression of gas, and extensive heat recovery favors operation at large scale, typically referred to as *economy of scale*, restricting economic operation to large centralized plants.

From an environmental perspective, the combustion of fossil fuels to heat the strongly endothermic reaction generates excess CO<sub>2</sub>. A fired SMR reformer produce 7.7-10.4 kg CO<sub>2</sub>/kg H<sub>2</sub> depending on efficiency, fuel and feed, where 5.5 kg CO<sub>2</sub>/kg H<sub>2</sub> is from the stoichiometric reaction at full conversion.<sup>23,25,26</sup> Heating all syngas production without contribution from combustion can reduce global CO<sub>2</sub> emissions up to 1% if implemented on a global scale.<sup>28</sup>

Despite decades on commercial optimization of the industrial SMR technology, facing the same challenges, the technology has overall changed very little.

### **Increasing SMR performance**

Thermal conductivity is the primary limitation for the performance of the industrial SMR process today. Optimization can be roughly divided in four categories; improvement of materials, integration of unit operations, shifting equilibrium conditions, or decreasing the length scale for heat transfer.

Monolithic structures of materials with high conductivity can replace traditional catalyst pellets to decrease temperature gradients within the tubular reactor.<sup>42</sup> However, improved performance is moderate and thermal expansion is a challenge.<sup>43</sup>

Integration of unit operations can lead to substantial process intensification. An example is the autothermal reformer (ATR), integrating heat supply into the reactor.<sup>22,31</sup> Pure oxygen is mixed into the feed, which is partially combusted in a reaction chamber, supplying latent heat to the gas, followed by an adiabatic reaction step. The ATR is significantly more compact than the SMR, and typically considered an alternate technology to SMR. However, the requirement of pure oxygen restrict operation to at large scale, and the product gas has a lower hydrogen to carbon monoxide content.<sup>22</sup>

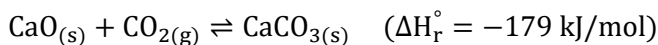
Integration of selective membranes into the reactor, removes the need for a subsequent purification step, and enables production of very pure hydrogen

## 1. Introduction

---

at lower reaction temperatures, as selective removal of species shift of the overall thermodynamic equilibrium.<sup>44</sup> Membrane reactors has successfully been implemented at small scale,<sup>45</sup> but do not scale well to industrial conditions due to the significant pressure drop necessary for reasonable flux through current available membranes.<sup>46</sup>

Another approach for shifting the equilibrium, and partly integrate a source of heat, is by sorption enhancement (SE). SE-SMR typically focus on the removal of carbon dioxide, for instance by reaction with calcium oxide to calcium carbonate:



Formation of calcium carbonate is exothermic, and can supply heat to the SMR reaction while removing carbon dioxide, shifting the thermodynamics towards production of additional hydrogen according to Le Chateliers principle.<sup>47,48</sup> A secondary step is necessary to regenerate the sorbent material (CaO), and while cyclical reactors are a possibility, sintering of materials decrease lifetime severely, and SE-SMR is not currently implemented at industrial scale.<sup>48</sup>

The most effective way to remove large thermal difference is by decreasing the characteristic length scale for heat transfer. For a fired, packed bed reformer, the characteristic length scale is across reactor wall and the catalyst pellets. In micro-reactors, adjacent narrow channels (<1 mm) minimize the distance heat has to be transferred, enabling up to 90% reduction of reactor volume.<sup>49</sup> SMR has successfully been scaled to industrial quantities in micro reactors (36.000 Nm<sup>3</sup> H<sub>2</sub>/h), but the very short contact times limit reaction control, and complex manifolds are required.<sup>49,50</sup> High-pressure combustion is thermodynamically unfavorable, limiting operation pressure due to thin channel walls.

In common for the alternatives covered above, is a heat supply relying on combustion of fossil fuels contributing to the CO<sub>2</sub> emissions.

### 1.3. Electrical heating

It is desirable to utilize excess renewable energy for chemical synthesis (Power-to-X), and at the same time, decrease CO<sub>2</sub> emissions. Electric heating enables accurate thermal control and improved energy efficiency, delivering

heat directly to the desired task. Resistance heating is common in lab scale furnaces, and heat similarly to a fired furnace, though with better control of individual heating zones. Electricity can also heat through generation of an electromagnetic interaction supplying heat. Electromagnetic heating can supply the heat directly, for instance by utilizing microwaves or magnetic hysteresis, enabling the metallic catalyst particle to be the heat source.<sup>51</sup> However, electromagnetic heating can add additional constraints on reactor design. For example will the high steam partial pressures of SMR absorb microwaves within 2 cm, demanding a radically different reactor design for large-scale production, which is yet unavailable.<sup>52,53</sup>

This work investigates the performance of two types of electrical heating; integrated resistive heating, and hysteresis heating by induction.

### **Resistance heating**

Direct resistance heating, or Joule heating, is the heat loss incurred by a current passing through a material. The heat loss is proportional to the resistance, which depends on geometry and material.

Resistance heating has previously been proposed for high temperature endothermic processes. Alagy et al., proposed inserting electrically heated rods in a packed bed to provide an efficient energy source, and a simpler and scalable reactor design for the pyrolysis of hydrocarbons.<sup>54</sup> Rieks et al., used a catalytically coated conductor to demonstrate dry methane reforming at temperatures exceeding what is feasible in conventional reformers, using a wash-coated heating element.<sup>55</sup> A different design was proposed by Mleczko et al., based on alternating layers of a coiled heating elements and catalyst, enabling high heating rates between adiabatic reaction steps.<sup>56</sup> Kameyama et al., demonstrated how anodization of an FeCrNi alloy could provide a high surface area alumina wash-coat, enabling electrically heated SMR reactors for domestic applications, with start-up times in seconds and good long-term stability.<sup>57</sup> They further predicted the absence of thermal gradients across the reactor, when utilizing integrated electrical heating.<sup>58</sup>

With the absence of thermal gradients, electrically heated reforming can resolve the primary limitation of fired reformers, but how effectively? How does the absence of thermal gradients influence catalytic performance? Is electrical heating applicable at industrial conditions? In short, what are the advantage and disadvantages of electrically heated reforming? This is

## 1. Introduction

addressed in Chapter 6 of this thesis, which describes the results obtained from detailed measurements of fully electrically heated laboratory scale reformer (See chapter 2), and the insights and predictions gained from the corresponding computational fluid dynamics (CFD) model (See Chapter 4).

### Induction heating

Induction heating is generated by an alternating magnetic field, and provides a non-contact heat source, which supplies heat through three different mechanisms: Eddy currents, magnetic hysteresis, and magnetic resonance. The dominating mechanism depends on material properties, size, and frequency. The different mechanisms are illustrated in Figure 1.4.

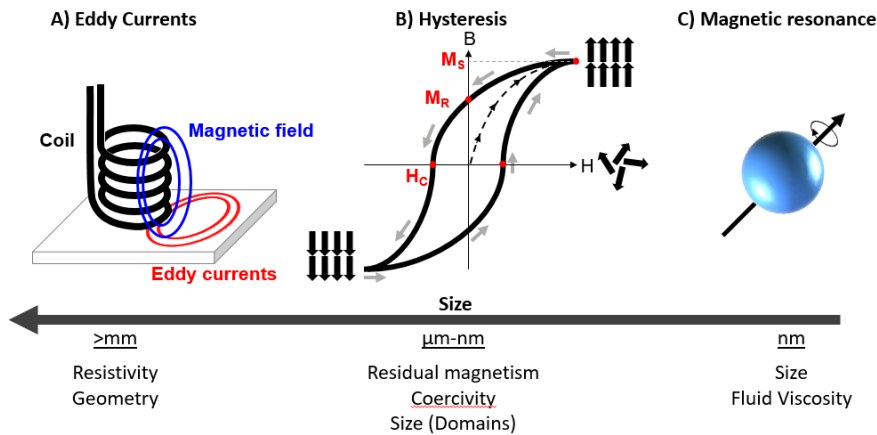


*Figure 1.4: Induction heating mechanisms and their dominant regimes A) Eddy current heating by induced currents. B) Magnetic hysteresis loop. The area is equivalent to the hysteresis heating. C) Heating by magnetic resonance for superparamagnetic particles.*

Eddy currents are currents induced in a conducting element by the oscillating field, heating via Joule effect (Fig. 1.4A). Heating by eddy currents is common in industry, for instance for induction furnaces or surface temperature treatments.<sup>59</sup> It is also the dominant mechanism for induction cooktops in household use. Heating by eddy currents in thin wires can be estimated by equation 1.1:

$$P_{EC} = \frac{\pi^2 B^2 d^2 f^2}{12\rho_r} \left[ \frac{W}{m^3} \right] \quad (1.1)$$

Here  $B$  is the magnetic field [T],  $d$  is the wire diameter [m],  $f$  the frequency [Hz], and  $\rho_r$  the material resistivity [ $\Omega \cdot m$ ]. This only applies to thin wires due to the induced current inducing a magnetic field with opposing polarity, creating a skin depth effect:

$$\delta = \sqrt{\frac{2\rho_r}{f\mu_0\mu_r}} [m] \quad (1.2)$$

Here  $\mu_0$  is the permeability of vacuum ( $\mu_0 = 4\pi 10^{-7} \left[\frac{Tm}{A}\right]$ ), and  $\mu_r$  the relative permeability, which for ferromagnetic materials exceed unity.  $\delta$  is the skin depth, an approximation of the magnetic field penetration into the material, and consequently the volume heated by eddy currents. For larger elements, eddy currents will only supply heat to the surface.

### **Hysteresis heating**

When the skin depth is equal to, or smaller than, the heated object, a significant part of the heat can be supplied from magnetic hysteresis (Fig. 1.4B). Hysteresis heating of particles is equivalent to the area of the hysteresis loop, and as such proportional to the coercivity ( $H_C$ ) and saturation magnetization ( $M_S$ ):<sup>60</sup>

$$P_{Hyst} \propto 2\mu_0 H_C M_S \quad (1.3)$$

Coercivity is the material's "resistance" to reverse the direction of the magnetic field, and is only present in ferromagnetic materials. The saturation magnetization is how magnetic a material in a strong magnetic field. The remnant magnetization is the residual magnetism without an applied magnetic field. The saturation magnetization declines steeply near the Curie temperature (Fig. 1.5).

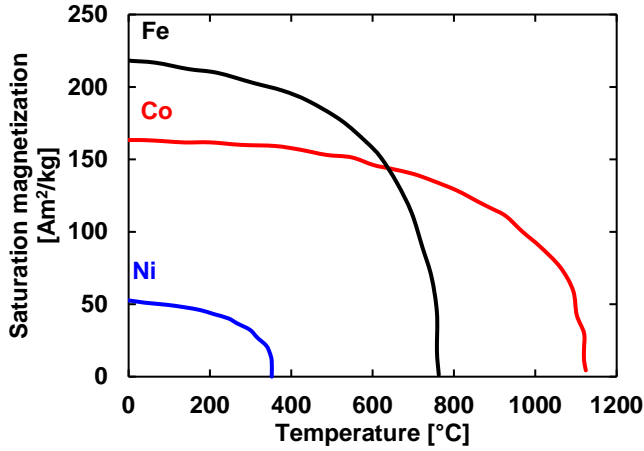


Figure 1.5: Temperature dependent magnetization Saturation magnetization,  $M_s$ , of the ferromagnetic elements.  $M_s$  decays weakly as a function of temperature, and sharply at the Curie temperature.<sup>60,61</sup>

For materials with high coercivity, strong magnetic fields are required to reverse the magnetic field or to reach saturation magnetization. The magnetic coercivity depends on the size and type of domain. The highest coercivity for a material is achieved for single domains (Fig. 1.6), as multiple domains enable internal containment of the magnetic flux as demanded by Ampere’s Law.

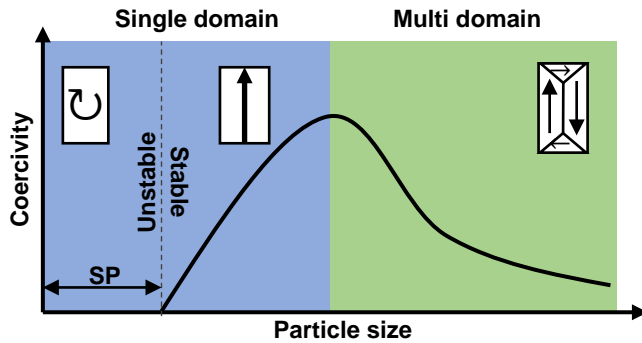


Figure 1.6: Magnetic coercivity as a function of particle size Magnetic particles can be distinguished as single and multidomain. The highest coercivity is achieved in transition between single and multi domain. Very small particles are superparamagnetic, and have a net coercivity of zero. As the particles increase in size, the coercivity decreases.<sup>62</sup>

The transition between single and multi domains depend on material, shape, and temperature.<sup>60</sup> For cobalt at elevated temperatures, the transition to multi domains is approximately at 30 nm.<sup>63-65</sup> It should be noted this is a very rough estimate, not accounting for the HCP to FCC transition.

The magnetic orientation of a domain can spontaneously change direction through Néel relaxation. The frequency at which this occurs is strongly dependent on size, and for very small particles the change of magnetic orientation may occur faster than the oscillations of the applied magnetic field, yielding an apparent coercivity of zero.<sup>66</sup> The Néel relaxation time is defined as:<sup>67</sup>

$$\tau_{\text{Néel}} = \tau_0 \cdot \exp\left(\frac{k_B T}{K_A V}\right) \quad (1.4)$$

Where  $\tau_0$  is a reference time,  $k_B$  the Boltzmann constant,  $K_A$  the anisotropy constant, and  $V$  the particle volume. When  $\tau_{\text{Néel}} < \tau_{\text{Frequency}}$  the particle is superparamagnetic.<sup>60,65</sup> Superparamagnetic particles have no hysteresis, and consequently does not contribute to hysteresis heating.<sup>68</sup> Superparamagnetic particles can heat when oscillated at their resonance frequency, which is typically in the MHz-GHz range, but contribute negligible at frequencies below.<sup>69,70</sup>

Magnetic (nano)particles suspended in a fluid can heat by Brownian relaxation, where the particle physically flips with the oscillating field (instead of the magnetic field), with heating proportional to the viscosity of the fluid.<sup>60,71</sup>

### **Applied induction heating for endothermic reactions**

Due to skin depth effects, heating by eddy currents is concentrated near the surface of a conducting object. It is frequently used in metallurgy to anneal the surface of wires and pipes, where an induction coil can supply heat locally and fast.<sup>51</sup> Induction heating enables energy transfer exceeding what is practical for combustion processes, and heating by eddy currents has been demonstrated for the SMR process.<sup>72</sup>

On the other end of the scale, is the application of superparamagnetic nanoparticles, for instance used for hyperthermia treatment.<sup>60,73</sup>

Induction heating has some interesting applications for catalysis, as demonstrated by Kirschning et al., who utilized copper wire, steel beads, and

## 1. Introduction

---

superparamagnetic iron oxide nanoparticles to investigate each of the induction heating mechanism, obtaining improved reaction rates and yields in organic synthesis at temperatures up to 350°C.<sup>74-76</sup> Bordet et al., demonstrated effective hydrogenation of CO<sub>2</sub> (methanation) using iron carbide composite nanoparticles at temperatures up to 350°C.<sup>77</sup> Recently, Varsano et al. performed dry methane reforming at temperature reaching 850°C using a pelletized Ni<sub>60</sub>Co<sub>40</sub> alloy, but with a significant loss in efficiency when reducing pellet dimensions indicating strong eddy current contribution.<sup>78</sup>

Hysteresis heating is the interesting mechanism when it comes to heating the catalytic sites directly and efficiently. Effective induction heating requires the susceptor to be ferromagnetic, limiting applicable elements to Ni (T<sub>C</sub> 358°C), Fe (T<sub>C</sub> 770°C), and Cobalt (T<sub>C</sub> 1121°C), or alloys thereof.<sup>79</sup> As SMR at industrial conditions requires temperatures exceeding 850°C, cobalt is mandatory to raise the Curie temperature sufficiently. Mortensen et al., demonstrated how hysteresis heating of supported CoNi nanoparticles can supply sufficient heat to reach 98% methane conversion for the SMR process at ambient pressure, while serving as both susceptor and catalytically active site, and displaying good long term stability.<sup>80,81</sup> They further propose how adjusting the alloy composition, thereby regulating the Curie temperature, serves as a thermal control. Almind et al. predicted improved efficiency as the induction heated reformer is scaled to industrial capacities, obtaining compact reactors with fast thermal response.<sup>82</sup>

Induction heating through hysteresis of a ferromagnetic catalyst enables heat supply selectively at the catalyst sites. Investigation into the phenomena of hysteresis heated catalyst and how this influence the catalytic performance and temperature profiles based on an experimental setup is covered in Chapter 5 of this thesis. The experimental setup is described in Section 2.3, and the implemented CFD model in Chapter 4.3. Furthermore, the development of a universal susceptor for high temperature hysteresis heating is discussed, in terms of favorable magnetic and chemical properties (Chapter 3).

## 1.4. Thesis outline

This thesis covers a brief summary of the published (and intended to be be) work on the potential of electrically heated SMR. Below is a short description of the content of each chapter in this thesis.

**Chapter 2: *Experimental setups.*** This chapter briefly describes the preparation, characterization, and experimental setups.

**Chapter 3: *Development of universal suscepter.*** This chapter briefly covers the preliminary results from the development of a magnetic suscepter intended for hysteretic induction heating for any high temperature environment.

**Chapter 4: *Computational fluid dynamics: Implementation.*** This chapter briefly introduce the theory behind CFD modelling, how it was implemented for the different experimental setups, and how the model was validated and used for evaluation.

**Chapter 5: *Induction heating.*** This chapter includes results of preliminary experimental work, model predictions, and a discussion of the presented results and their applications.

**Chapter 6: *Resistance heating.*** This chapter includes experimental results, model predictions, including carbon activity and effectiveness factors. Each sub section contains a brief discussion of application potential. The chapter is finished by a summary of the potential applications and limitations.

**Chapter 7: *Summary & final remarks***

## 2. Experimental setups

In this work, two different catalytic configurations were investigated for steam methane reforming, each utilizing a different type of electrical heating. A reactor heated directly by resistance heating, and a ferromagnetic catalyst heated by induction heating. Both configurations were tested at ambient pressure in a lab scale setup at Danish Technological Institute (DTI) built by Jakob S. Engbæk and Søren B. Vendelbo.

### Reactor setup

The setup is supplied with N<sub>2</sub>, H<sub>2</sub>, CH<sub>4</sub>, and Ar. Steam is supplied via vaporized demineralized water, dosed by a *Knauer smartline* HPLC pump. The gas composition is regulated by flow controllers (*SLA850 Brooks digital*) at the inlet, mixed with steam, and pre-heated to 105-125°C to prevent condensation. All experiments were performed in a mixture of CH<sub>4</sub>, H<sub>2</sub>O and H<sub>2</sub> (30/60/10), to avoid carbon deposition, and to keep the catalyst reduced at the inlet where the temperature is lowest. Both catalyst configurations were reduced *in-situ* in 200 Nml H<sub>2</sub>/min at temperatures exceeding 500°C.

Steam was removed by condensation in a drain trap (*Armstrong 11LD*), and the dry gas composition was measured with gas chromatography (GC, *Agilent 7890 GC System with TCD/FID*). For transient measurements of the resistance heated configuration, gas composition was monitored with mass spectrometry (MS, *Spectra, Microvision plus, 0-200 AMU*).

For both configurations, power was supplied from the grid, and transformed to desired frequency and current. The resistance-heated reformer was operated at 50 Hz, and the ca. 220V from the grid was transformed via a vario transformer and a set of coils. The induction coil was powered by an induction oven (*UPT-S2 Ultraflex power supply*), and for the presented measurements operated at 196 kHz.

Accurate and reliable temperature measurements are essential for controlling endothermic reactions. Outside the electrically heated configurations, standard K-type thermocouples was used. Due to the small geometry of the resistance heated reactor, and the induced error in an induction coil, spotwelded thermocouples and an infrared pyrometer was used to monitor temperature.

Preparation, characterization, mounting, and temperature measurements for the different configurations are described in the following sections.

### 2.1. Resistance heated washcoat

Preparation of the resistance-heated reactor was undertaken by Winnie L. Eriksen at Topsoe, based on a 50 cm FeCrAl tube with an outer diameter of 6mm acquired from Goodfellow. A 130  $\mu\text{m}$  porous zirconia coat was applied to the internal surface, and a section was removed in each end (Fig. 2.1A). After calcination, the washcoat was impregnated with nickel to provide the catalytic activity. Further details on the preparation can be found in the supplementary material of the published work (Appendix 9.1.2).

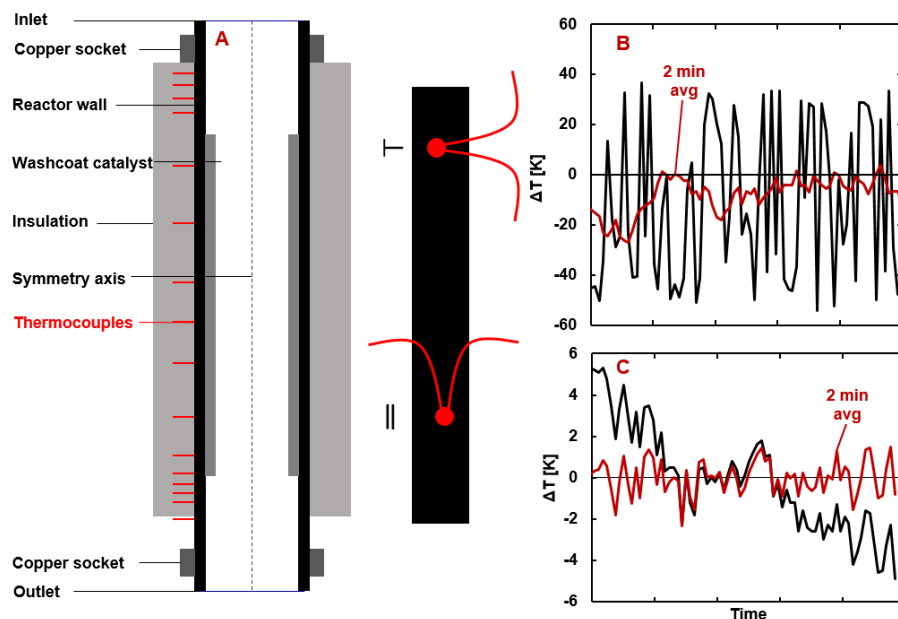


**Figure 2.1: Reactor geometry and optimal spotwelding** A) 2D cross section of the geometry for the washcoated reactor. Thermocouple positions are marked with red. The illustration is not to scale. B-C) Difference between perpendicular (B) and parallel (C) spotweld of thermocouples. The perpendicular fluctuate up to  $\pm 50^\circ\text{C}$  relative to 1 hour average at steady state. The red line indicate an average evaluated over 2 minutes, but still fluctuate up to  $20^\circ\text{C}$ . The parallel deviate less than  $6^\circ\text{C}$ , and the slope indicate it is not a measurement at steady state. When evaluated as a 2 minute average, the deviation is less than  $2^\circ\text{C}$ .

To measure the temperature profile along the reactor, multiple K-type thermocouples (0.25 mm, Goodfellow) was spotwelded to the external

## 2. Experimental setup and methods

---

surface (Fig. 2.1A), and monitored with an *SR630 Thermocouple monitor*, with an internal resistance of 10 M $\Omega$  and relays, enabling measurement of a single channel at a time, preventing short-circuit. Precise placement of the spotwelded thermocouples, parallel to the direction of the current (Fig. 2.1B), is crucial to avoid an applied bias, as the potential gradient along the reactor exceeds the range monitored in K-type thermocouples by 2 orders of magnitude. At 50 Hz, the current induced by the magnetic field is negligible. No fluctuation is observed from shielded thermocouples, however, steep gradients near the wall mandates good contact to minimize measurement error (Supplementary Figure S9.3.1).

The resistance heated reactor was mounted using copper sockets, ensuring good current distribution at the contact points. Using fine grade sandpaper, abrasions were made in the surface oxide prior to mounting to minimize contact resistance, measured by a sourcemeter (*Keithley 2400*). Current was measured continually used current clamp (*Keysight 1146B*), with potential monitored by an oscilloscope (*Agilent infiniiVision DSO-X 2014A*).

To avoid short-circuit, the copper clamps were mounted on a glassfiber composite, which limited the maximum flowrate to 1700 Nml/min (at ca. 800°C), due to convection heating of the downstream copper socket, reaching temperatures exceeding the glass transition temperature of the composite (~180°C).

### **2.2. Requirements for induction heated catalysts**

All materials exhibit one of three types of magnetic behavior: diamagnetic, paramagnetic, or ferromagnetic, depending on composition, temperature, and particle size. A catalyst susceptible to induction heating by hysteresis requires a ferromagnetic component, with a Curie temperature exceeding the reaction temperature. Only three elements, iron, cobalt, and nickel, are ferromagnetic above room temperature. A list of the ferromagnetic alloys and their curie temperature are listed in Table 2.1.

---

## 2. Experimental setups and methods

---

*Table 2.1: Curie Temperature Curie temperature for selected elements and their ferro/ferrimagnetic oxides and carbides.*<sup>79</sup>

Element(s)	Curie temperature [°C]
Fe	770
Co	1180
Ni	358
$\gamma$ -Fe <sub>2</sub> O <sub>3</sub>	600
Fe <sub>3</sub> O <sub>4</sub>	580
Fe <sub>x</sub> C <sub>y</sub>	250-450
Ni <sub>3</sub> Fe	620
CoFe	986
NiFe <sub>2</sub> O <sub>4</sub>	585

Oxidation or carbonization decrease the Curie temperature, however most oxides are not ferromagnetic, and thus not relevant for hysteresis heating.

Nickel is abundant, and frequently used in catalyst for SMR, however the Curie temperature is insufficient for hysteresis heating.<sup>22,29,83,84</sup> For practical applications, a Curie temperature exceeding 850°C is required, mandating a fraction of cobalt in the catalyst. For pure hysteresis heating, this can be implemented two ways: M<sub>x</sub>Co<sub>1-x</sub> alloys or separate cobalt particles distributed in the support matrix. Cobalt is required for the Curie temperature; however, a catalytically active alloy requires a second material displaying SMR activity. Of the active elements for SMR (Ni, Ru, Rh, Pt), only nickel has a Curie temperature above room temperature, which might not be critical, but supports higher Curie temperatures for the alloy. As a rule of thumb, the Curie temperature of an alloy can be estimated from the mass fraction and the Curie temperature of the pure elements.<sup>79</sup>

The first tests of Ni<sub>x</sub>Co<sub>1-x</sub>-based catalysts were carried out by Mortensen et al.,<sup>80</sup> demonstrating a direct correlation between Ni/Co ratio and catalytic activity, and hysteresis area scaling with cobalt content. The synthesis was

## 2. Experimental setup and methods

---

later improved by Vinum et al., obtaining a uniform distribution of particles with homogeneous Co-Ni composition, resulting in improved performance.<sup>81</sup>

### 2.3. Induction heating setup

Hysteresis heating by induction introduces additional constraints compared to the simpler approach used for direct resistive heating introduced in Section 2.1. For uniform supply of heat, it is important the sample is not magnetically shielded, preventing the use of conductive materials. A  $\text{Ni}_{0.5}\text{Co}_{0.5}$  spinel synthesized by Morten Vinum was used for the catalytic tests.<sup>81</sup> It is assumed the catalyst sample is not in itself shielding, as the metallic loading constitutes less than 5% by volume. The catalyst was comminuted to a 0.5-1 mm fraction, and loaded above a quartz wool plug, in a quartz tube (15.2 mm OD, 12 mm ID), surrounded by a coil, as illustrated in Figure 2.2.

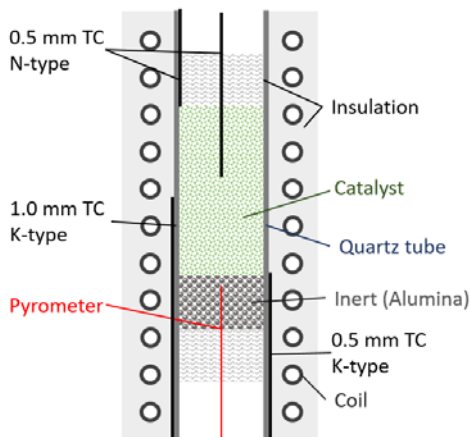


**Figure 2.2: Induction heated reactor configuration** Illustration of the typical coil configuration for experiments. A quartz wool plug is used to align the pyrometer to the reactor center, and the catalytic bed is loaded on top. The catalytic sample is centered in the watercooled coil. A granular insulation separates the quartz wall from the coil. Two 0.5 mm N-type thermocouples are inserted in the top, one ca. 2 cm into the sample in the center, and one at the edge near the top.

Dimensions of the coil has significant influence on the reactor performance in terms of the generated magnetic field, inductance losses, and thermal gradients between reactor and coil. A narrow coil with many windings will generate the strongest, and most uniform magnetic field. However, the resistance of the copper coil is strongly dependent on temperature, and the coil is continually cooled to 20°C. As SMR at ambient pressure requires 700-

---

## 2. Experimental setups and methods

750°C, an optimum coil diameter depends on insulation and magnetic dissipation. Based on a study of coil efficiency from the same setup,<sup>82</sup> a 13.5 cm long coil with 17 windings of 6mm (OD) copper tubing and internal diameter of 26 mm was used for all measurements. A 4 cm catalytic bed was placed in the middle of the coil, to ensure a uniform magnetic field. The induction oven (*UPT-S2 Ultraflex*) operated at 196 kHz could generate magnetic fields up to 35 mT in the given coil. A granular silica based high-temperature insulation (FreeFlow) was used around the coil.

Several thermocouples (TC) was used to measure the temperature, as indicated on Figure 2.2. To minimize the effect supplied to the TCs via eddy currents, 0.5 mm, non-magnetic N-type thermocouples were used. This effect can readily be seen when compared to larger K-type TC, when changing the applied magnetic field (Fig. 2.3).

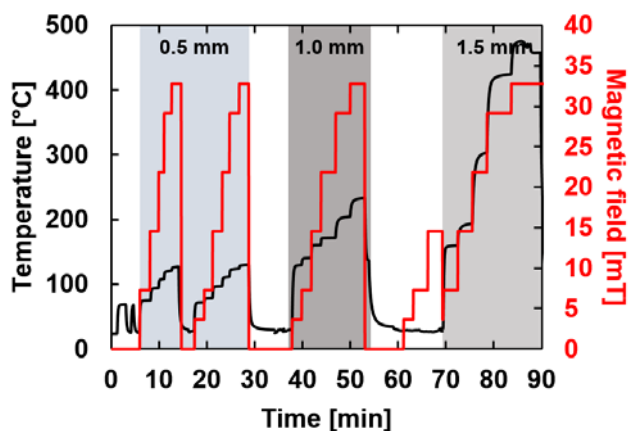


*Figure 2.3: Induced thermocouple effect* Measured temperature for K-type TCs of various diameter placed alone in the center of the coil. A significantly higher temperature is measured for increasing diameter, increasing the risk of hotspots, and induced bias on temperature measurements. Measurement by Jakob S. Engbæk (DTI).

A difference of nearly 400°C is measured at a field of 32 mT when measuring the temperature with a 0.5 mm compared to a 1.5 mm K-type TC. The deviation is related to induced eddy currents in the TC, scaling with the diameter. Induced current in the TCs create a local hotspot, adding a bias to the measured temperature, and for the larger TCs could influence methane conversion, due to the additional energy provided. The induced potential is assumed negligible. Using a non-magnetic TC (Eg. N-type) is expected to

## 2. Experimental setup and methods

---

further reduce the measurement error. It should be noted the transient response to a change in magnetic field is within 3 seconds for all TCs.

To measure temperature independent of the magnetic field, the outlet temperature was measured just below the catalytic bed with an infrared pyrometer (*Maurer IR QKTRD 1485*), using a 0.2 mm optical quartz fiber (*LaserComponents*). An infrared pyrometer measures the inherent infrared radiation exhibited by any hot material.<sup>85</sup> The radiation intensity is converted to a temperature based on blackbody radiation theory, using a temperature dependent emissivity to account for deviations. The pyrometer was calibrated against the inert alumina spheres (3 mm, Sigma Aldrich) prior to experiments in a tube furnace against a K-type TC (Supplementary Figures S9.3.2-3). The measurements are used in the results in Chapter 5 and 6.

### **3. Development of universal susceptor**

To reach the high temperatures required for SMR by hysteresis heating, cobalt is mandatory, as it is the only element with a sufficiently high Curie temperature (Table 2.1). Nickel is the most abundant catalyst used for SMR,<sup>22</sup> however it is magnetically softer than cobalt, and alloying decreases the Curie temperature. Due to their similarity, alloys of cobalt and nickel are readily formed at elevated temperatures.<sup>86</sup>

Separating the susceptor and the catalytic site, in theory, enables an evenly distributed supply of heat up to the Curie temperature of pure cobalt (1121°C). Pure cobalt is a stronger magnet than nickel and displays a higher coercivity for nanoparticles, which in theory corresponds to improved hysteresis heating.<sup>60,79</sup> In addition, the separation of susceptor and catalyst enables variable loading of the magnetic susceptor to meet reaction demands, for instance a high supply of heat towards the outlet where only minor catalytic activity is required due to the high temperatures.

#### **Thermodynamic controlled oxidation**

To keep the cobalt susceptor separate from the nickel catalyst, and improve its chemical stability, a procedure for generating a protective layer was developed based on thermodynamic controlled oxidation. Thermodynamic calculations are performed in the program HSC 6.1.

Aluminum oxide ( $\text{Al}_2\text{O}_3$ ) is one of the most stable compounds, and an abundant constituent in alloys to improve chemical stability. Aluminum is well known to form thin oxide layers, which effectively limit further oxidation.

In an atmosphere of oxygen, all non-precious metals will instantly form a layer of metal oxide. Over time, the thickness of the layer increases at a rate determined by mass transfer and the thermodynamic potential. Formation of aluminum oxide is extremely facile, but the initial layer inhibits diffusion of oxygen, effectively slowing the rate of oxidation below quantifiable levels. The diffusion rate is temperature dependent, and high temperature will facilitate continued growth of the oxide layer.

### 3. Development of universal susceptor

---

An atmosphere of hydrogen and steam enables selective oxidization of aluminum, keeping cobalt in a reduced state, by establishing an equilibrium. The controlled oxidation reaction for a metal in an atmosphere of hydrogen and steam and the equilibrium constants is given in Equations 3.1 and 3.2, respectively.



$$K_{eq} = \frac{p_{H_2}}{p_{H_2O}} \quad (3.2)$$

If the  $H_2/H_2O$  ratio exceeds the equilibrium constant for a given reaction, reduction of the metal oxide will occur. Figure 3.1 illustrates the thermodynamic oxidation potential for cobalt and nickel.

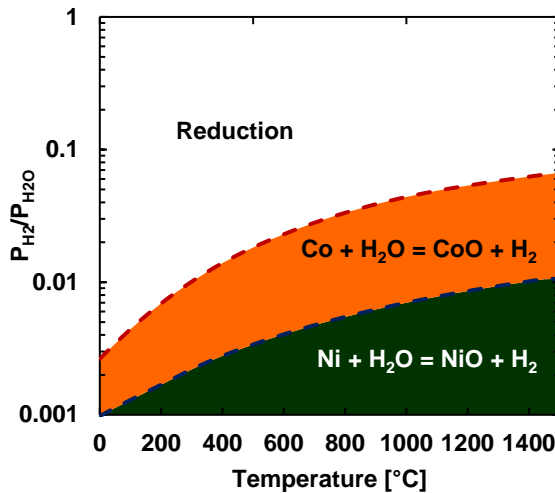


*Figure 3.1: Thermodynamic conditions for reduction Oxidation potential for cobalt and nickel as  $H_2/H_2O$  ratio as a function of temperature in a controlled atmosphere of steam and hydrogen. A  $H_2/H_2O$  exceeding 0.1 should thermodynamically prevent oxidation. Based on calculations in HSC 6.1.*

Nickel is less reactive than cobalt, and reduces more facile, as seen from the lower required hydrogen partial pressure required. For cobalt, a  $H_2/H_2O$  ratio exceeding 0.05 at 900°C should prevent oxidation. For comparison, the  $H_2/H_2O$  ratio required to thermally reduce alumina exceeds  $10^{11}$ , and the

### 3. Development of universal susceptor

reason why aluminum is typically produced by electrolysis (Supplementary Figure S.9.3.4).

In an effort to apply an aluminum oxide layer to protect a magnetic cobalt susceptor for SMR,  $\text{Co}_{0.79}\text{Al}_{0.21}$  particles (Goodfellow) was oxidized in an atmosphere of 5:1  $\text{H}_2/\text{H}_2\text{O}$  in 95% argon, thermodynamically limiting the formation of cobalt oxide (Fig. 3.1). Due to oxygen trace in the gas supply (20 ppm), a higher hydrogen content than required was used to suppress the oxidation kinetics.

As oxidation of aluminum is thermodynamically favorable, and initially very facile, the procedure aims at forming a continuous shell of alumina around a core of pure cobalt. It is critical to extract as much aluminum from the cobalt core as possible, as mixing greatly diminish the magnetic properties.  $\text{CoAl}$  is paramagnetic above 50% Al content, but any alumina content greatly lowers the Curie temperature (Fig. 3.2).<sup>87</sup>

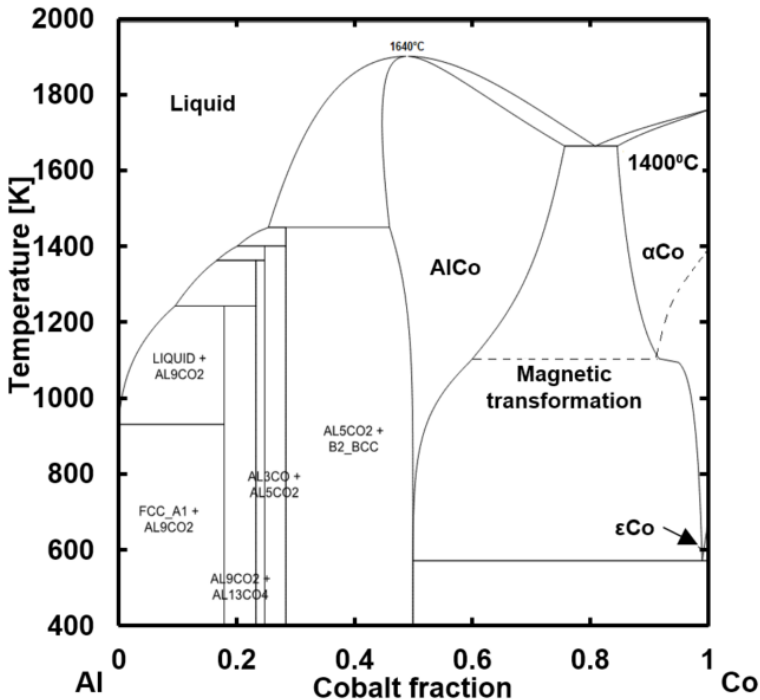


*Figure 3.2: Co-Al phase diagram* Binary Co-Al phase diagram with approximate Curie temperature. Figure adapted from <sup>86,87</sup>. Aluminum content in cobalt reduce the Curie temperature. Pure cobalt transition from HCP to FCC structure at 422°C.

### 3. Development of universal susceptor

---

As the thermodynamic controlled oxidation proceeds, the overall oxidation can proceed by two mechanisms; diffusion of aluminum to the surface, or diffusion of oxygen into the particles.<sup>88,89</sup> To form a protective layer it is imperative the oxidation occurs by the former. To achieve Curie temperatures exceeding 1000°C, the residual aluminum content must be less than 5at% (Fig. 3.2). The effect of temperature and time for the controlled oxidation is illustrated in Figure 3.3 and 3.4 respectively.

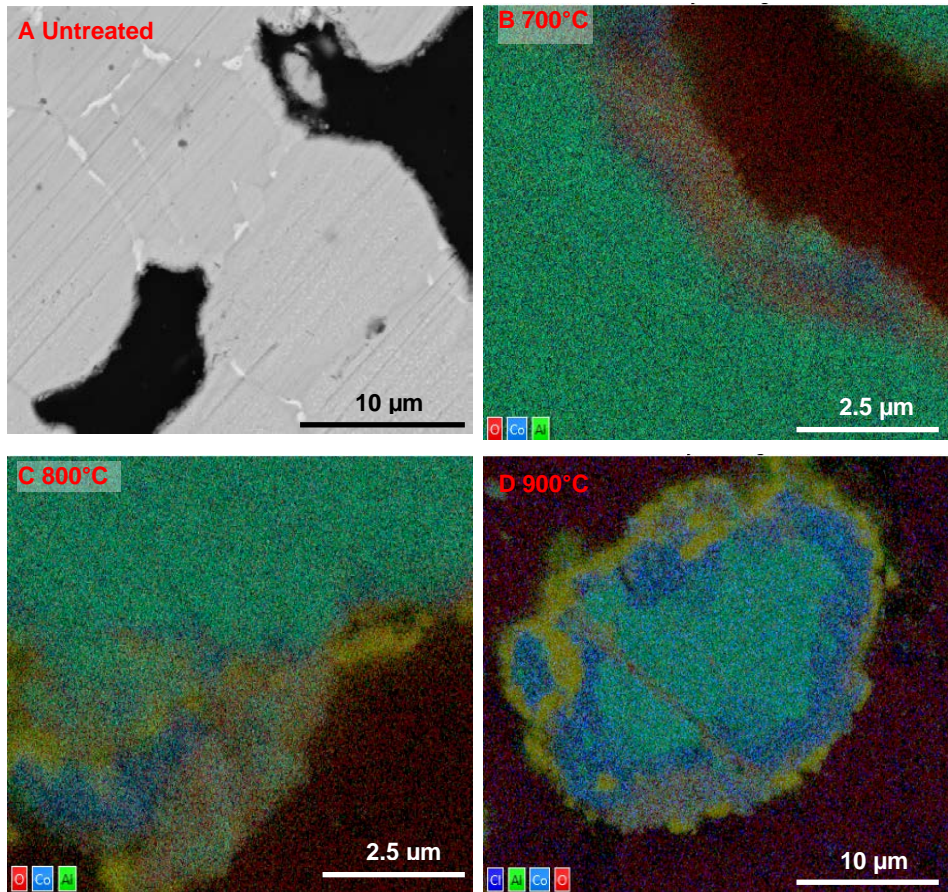


*Figure 3.3: Cross section of CoAl samples Scanning electron microscopy, using EDX of sample cross section by encasing in epoxy. Samples of  $\text{Co}_{79}\text{Al}_{21}$  was treated in 5:1  $\text{H}_2/\text{H}_2\text{O}$  in argon for 8h. Sample preparation by Winnie L. Eriksen (Topsoe), Analysis by Nikolaj Langemark (DTU). Images reproduced from unpublished literature.<sup>90</sup>*

### 3. Development of universal susceptor

As seen from the elemental map cross section in Figure 3.3, 900°C is required to form an (almost) complete shell. Figure 3.3D shows a rim partially depleted of alumina below the alumina shell. However, the particle core still contains both cobalt and alumina equivalent to the initial composition (79:21). Increased treatment time did not distinguishably alter the composition further, as shown in the XRD analysis in Figure 3.4.

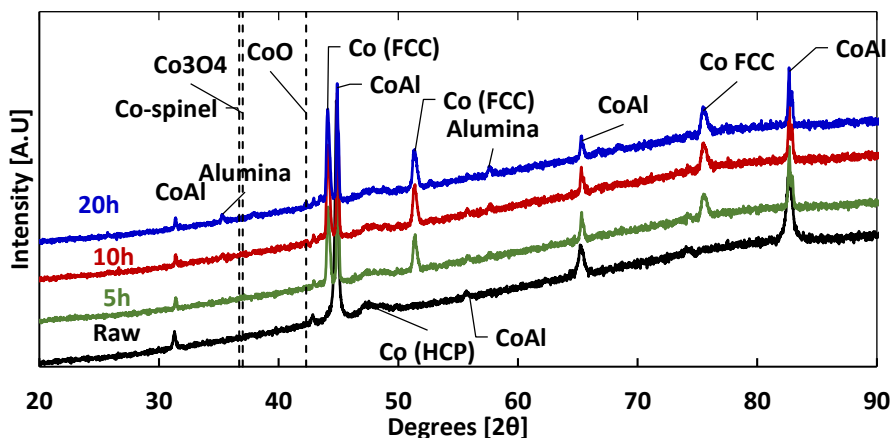


*Figure 3.4: XRD spectra of the raw and treated  $\text{Co}_{79}\text{Al}_{21}$  samples. The samples were treated in 5:1  $\text{H}_2/\text{H}_2\text{O}$  at 900°C. The dotted lines indicate expected position for oxide phases. The high background is due to fluorescence from the cobalt, as the emitted X-rays are indistinguishable from the copper source by the monochromator and filter available.*

No significant change is observed increasing treatment time from 5 to 20h (at 900°C), indicating strong diffusion limitation across the alumina layer. No formation of cobalt oxide containing phases are distinguishable. A significant fraction of the CoAl alloy remains unchanged as seen from the peaks near 45°.

To achieve further depletion of aluminum in the core, the sample was comminuted by ball milling (Fritsch, *PULVERISETTE 7*) in 4:1 heptane/oleic acid for 2 hours (500 rpm). The comminution reduced the average particle size to less than 20 μm, which after thermal treatment showed increased hysteresis area (Fig. 3.5).

### 3. Development of universal suscepter

---

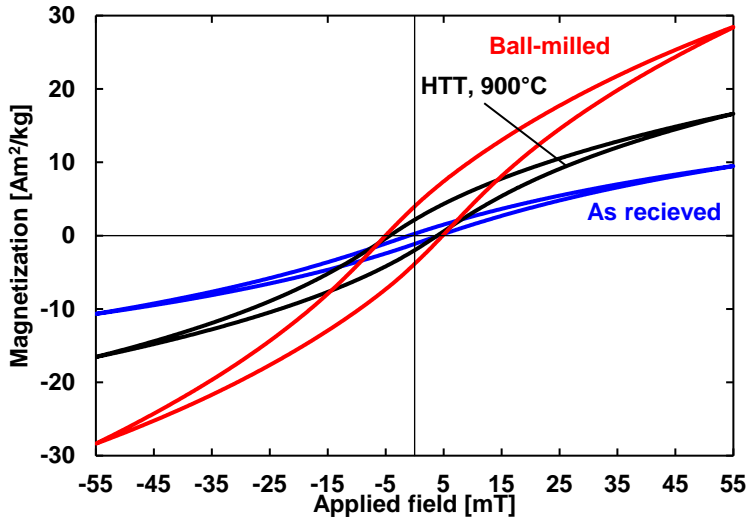


*Figure 3.5: Hysteresis of CoAl samples* Hysteresis loop measured by vibrating sample magnetometry (VSM) at 55 mT. The blue line is the sample as received, measured at 25°C. The hydrothermally treated sample (HTT) was exposed to 5:1 H<sub>2</sub>/H<sub>2</sub>O for 10h at 900°C. The raw sample was comminuted by ball-milling, and treated similarly. VSM data provided by Mads R. Almind.

The higher magnetization of the comminuted sample indicates improved alumina depletion from the core. As more aluminum is extracted, the sample becomes magnetically harder, indicated by the slightly increasing coercivity. The large discrepancy between the observed magnetization relative to that of pure cobalt (160 Am<sup>2</sup>/kg), indicates far from all the aluminum is depleted.<sup>61</sup> It should be noted 55 mT is insufficient to reach full magnetic saturation. Integration of the area of the hysteresis loop at 55 mT provides 0.073 J/kg, 0.177 J/kg, and 0.371 J/kg for the raw, treated, and comminuted sample respectively.

For comparison, Fe<sub>2.2</sub>C particles reported by Bordet et al.<sup>77</sup> had a hysteresis area of 32 J/kg (At 47 mT), though a Curie temperature around 357°C. The Co<sub>0.5</sub>Ni<sub>0.5</sub>/Al<sub>2</sub>O<sub>3</sub> sample prepared by Vinum et al.<sup>81</sup> displayed a Curie temperature of 892°C, and a hysteresis area of 0.367 J/kg at 45 mT .

The hysteresis area of the CoAl samples are calculated with respect to total sample weight, and full depletion of aluminum is expected to improve magnetization substantially.

This remains work in progress at the time of writing.

## 4. Computational fluid dynamics: Implementation

Mathematical representation of physical phenomena is the core of natural science. Fluid dynamics is the theoretical description of a fluids momentum profile as a function of viscosity, density, pressure, and geometry. The general equation for fluid motion is the Navier-Stokes equation, which for an incompressible fluid in steady state, with negligible influence from gravity, can be written as equation 4.1:<sup>85</sup>

$$\rho(\mathbf{v} \cdot \nabla)\mathbf{v} = -\nabla p + \mu \nabla^2 \mathbf{v} \quad (4.1)$$

Here  $\rho$  is the fluid density,  $\mathbf{v}$  the velocity vector (eg.  $\langle v_x, v_y, v_z \rangle$  in Cartesian coordinates),  $\nabla$  a differential operator,  $p$  the pressure, and  $\mu$  the fluids dynamic viscosity. For simple problems, such as laminar flow in a cylindrical tube, analytical solutions can be obtained with few assumptions. The complexity increases as more layers of physical phenomena are introduced into the model, such as energy and mass transport. Eventually, analytical solutions are impossible without generous assumption that might reduce the validity or applicable range of the model.

Computational fluid dynamics (CFD) seeks solutions to the same equations, but numerically, enabling increased complexity, especially in terms of geometry. With current access to high performance computing, CFD software, such as Comsol, Ansys, and OpenFoam, are readily available tools for chemical engineering. The presented work is based on COMSOL 5.2a-5.4.

A CFD model is based on a mesh, consisting of points or cells, distributed across the relevant domains. Refining the mesh resolution is crucial for CFD modelling, as a mesh too coarse can yield incorrect predictions. It can be compared to rounding too many digits during calculations, providing either an inaccurate answer, or no answers at all. An excessively fine mesh, will unnecessarily increase computation time, without yielding additional information. Additionally different types of mesh are better suited for different phenomena, often related to characteristic length scales. Figure 4.1 shows three examples of mesh types and their applications.

#### 4. CFD model implementation

---

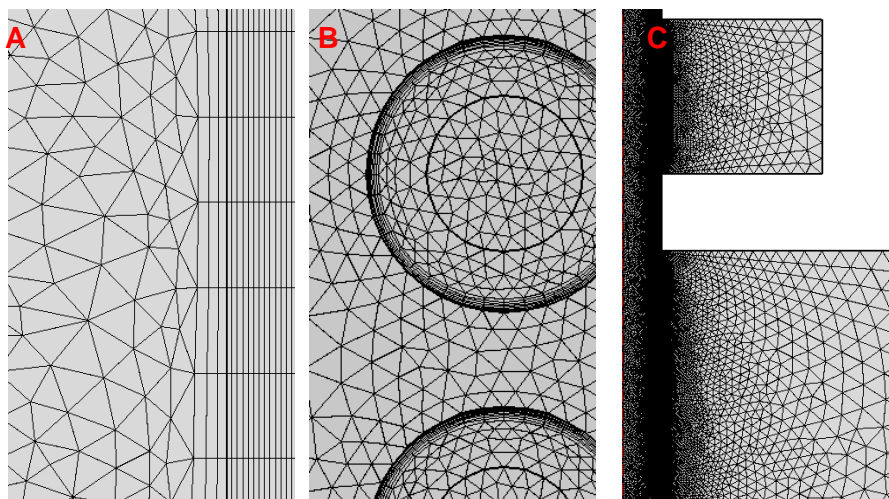


**Figure 4.1: Different mesh types and application** A) Structured quadratic mesh, with a 10:1 length to height ratio used to model radial profiles in a thin washcoat. B) Boundary layers in coil windings to more accurately obtain information on current density. For full accuracy, resolution should be atleast an order of magnitude higher than the skindepth of the given material. C) Coarse triangular mesh in insulation of resistance-heated ambient reformer with long length scales and conduction of heat as the only physics.

For processes where the gradients vary significantly in a single direction, a “mapped” mesh can provide high resolution in the relevant direction. Such a process could for instance be the reaction rates, where a high resolution of the mesh in radial direction is required to resolve diffusion phenomena of the steep radial concentration gradients (Fig. 4.1A). For surface specific phenomena, such as flow boundary layers or electric fields, additional layers can be added near the surface to locally increase resolution (Fig. 4.1B). Simpler phenomena, such as thermal conductivity in solids can typically achieve reasonable solutions with a coarse mesh (Fig. 4.1C). A mesh sensitivity analysis with increasingly refined mesh can be performed to estimate when higher resolution no longer influence the solution (Supplementary Figure S9.3.5). Meshing the transition between domains should be done with care, as different physics can require different resolution to obtain satisfactory results (Fig. 4.1C). Resolving individual particles in a packed bed would likely provide a more realistic solution, but with a significant increase in computational time, without necessarily providing more detailed information than through assumptions.<sup>37</sup>

### 4.1 Resistance-heated model

To assign appropriate mesh, physics and boundary conditions must be assigned to the domains of the model. The domains for fluid momentum, mass transport, heat transport, and electric fields, for the resistance-heated model are illustrated in Figure 4.2.

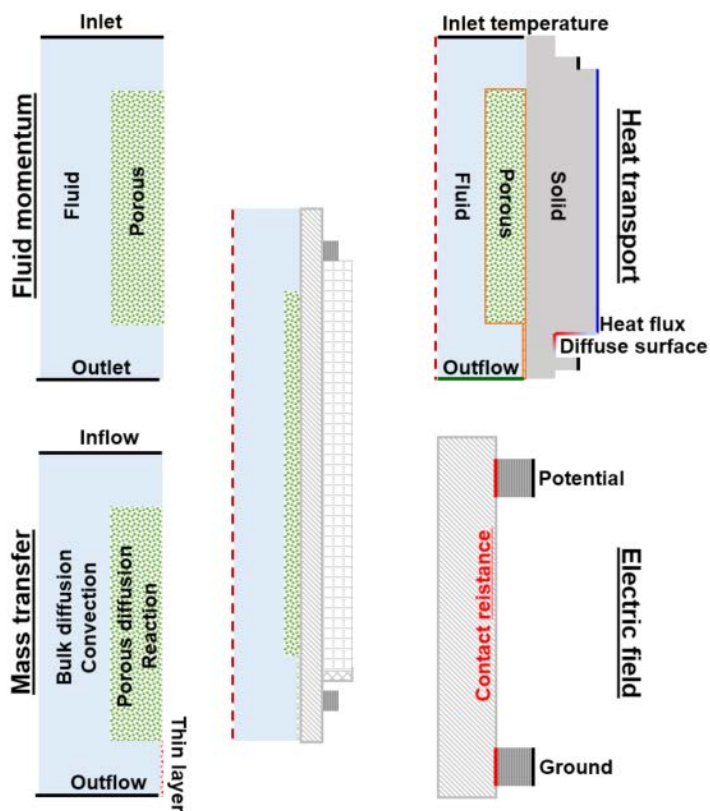


*Figure 4.2: CFD Domains* Different CFD domains for each physics node in the resistance heated model for ambient pressure experiments. For heat transport the blue line shows external heat flux boundary, where the gradient line shows radial and flux losses. Solid black lines for heat transport indicate specified temperatures. The orange line around the porous domain (and thin layer) is to indicate the heat sink from the endothermic reactions. The outflow (heat transport) includes convective losses.

The model was implemented in an axi-symmetrical geometry, a good approximation for tubular reactors, to remove a dimension from the differential equations, significantly reducing computation time. A thin layer

#### 4. CFD model implementation

---

was implemented near the outlet, due to a thin ( $<5\ \mu\text{m}$ ) residual layer of nickel containing coat towards the outlet (Fig 4.3). The residual coat was an artifact of the preparation procedure.

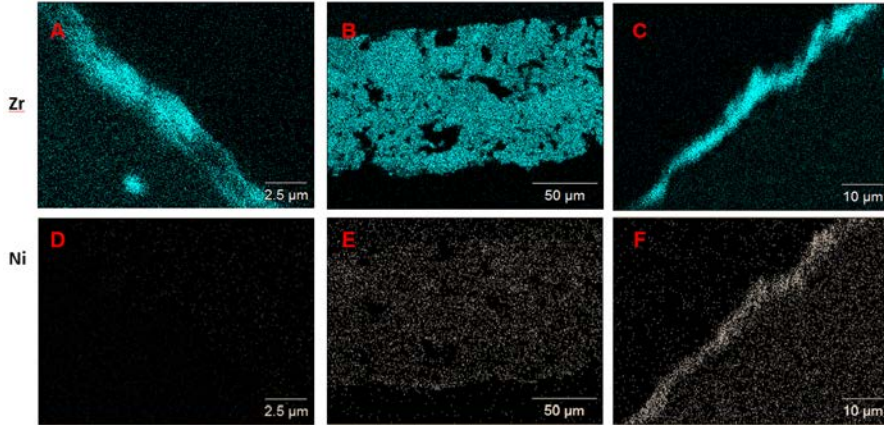


*Figure 4.3: Cross section SEM EDX elemental maps of zirconia and nickel signals sampled on a cross-section taken from inlet (A+D), coat (B+E), and outlet (C+F). As seen from A & C, there is a thin layer of residual zirconia coat present, but from D-F, that nickel is only present in the coat and residual coat towards the outlet.*

From the SEM cross section it is apparent that no nickel is present at the inlet of the reactor (4.3D), but evenly distributed in the coat. Because the residual layer at the outlet was less than  $5\ \mu\text{m}$ , it is modelled as a “thin layer”, and is not meshed. As a result, it does not account for mass transport limitations.

The equations describing the different physics (Fluid momentum, mass transfer, heat transport, electrical fields, reaction kinetics, and their interaction are briefly described in the following section. Further details can be found in the supplementary material (Appendix 9.1.2).

#### **Standard equations**

##### Fluid momentum equation

Fluid motion was implemented as the Brinkman equation, which reduces to the Navier-Stokes (Eq. 4.1) for non-porous domains.<sup>91</sup>

$$\frac{\rho}{\theta_b} (\mathbf{v} \cdot \nabla) \frac{\mathbf{v}}{\theta_b} = -\nabla p + \nabla \cdot \left[ \frac{1}{\theta_b} \left\{ \mu_{mix} \nabla \mathbf{v} - \frac{2}{3} \mu_{mix} (\nabla \cdot \mathbf{v}) \mathbf{I} \right\} \right] - \frac{\mu_{mix}}{\kappa} \mathbf{v} \quad (4.2)$$

Here  $\theta_b$  is the bulk porosity, and  $\kappa$  the permeability [ $\text{m}^2$ ] related to the pressure drop. The mixture averaged viscosity was calculated as:<sup>85</sup>

$$\mu_{mix} = \sum_{i=1}^N \frac{x_i \mu_i}{\sum_j x_j \Phi_{ij}} \quad (4.3)$$

Where  $x_i$  is the molar fraction of species  $i$ , and  $\Phi_{ij}$  is a dimensionless quantity accounting for non-linear behavior for mixtures of non-polar gasses at moderate pressure.<sup>85</sup> Further details are included in Appendix 9.2.

#### Mass transport & reaction kinetics

Mass transport was implemented as:<sup>85</sup>

$$\rho (\nabla \cdot \mathbf{u}) \omega_i = -\nabla \cdot \mathbf{j}_i + R_i \quad (4.4)$$

Here,  $\omega_i$  is the mass fraction of species  $i$ ,  $\mathbf{j}_i$  mass flux vector [ $\text{kg}/\text{m}^2$ ], and  $R_i$  a rate expression for consumption or production [ $\text{kg}/\text{m}^3/\text{s}$ ]. The mass flux is defined as:

$$\mathbf{j}_i = -\rho D_{eff} \frac{\nabla x_i}{x_i} \quad (4.5)$$

Here,  $D_{eff}$  is an effective, mixture-averaged diffusion coefficient [ $\text{m}^2/\text{s}$ ], accounting for tortuosity by the Bruggeman correlation<sup>92</sup>, which for porous domains is calculated as:<sup>91</sup>

$$D_{eff} = \frac{\theta_p}{\tau} \left( \frac{1}{\bar{D}_m} + \frac{1}{D_{i,K}} \right)^{-1}, \tau = (\theta_p)^{-1/2} \quad (4.6)$$

Here,  $\bar{D}_m$  is the averaged molecular diffusion, and  $D_{i,K}$  – the Knudsen diffusion<sup>93</sup>:

$$D_K = \frac{d_{pore}}{3} \sqrt{\frac{8RT}{\pi \bar{M}_w}} \quad (4.7)$$

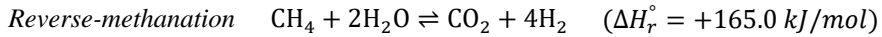
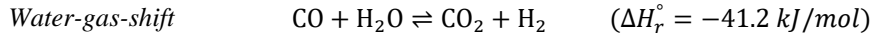
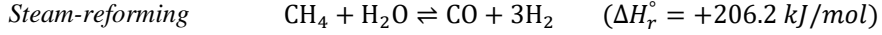

---

#### 4. CFD model implementation

---

Where  $d_{pore}$  is the average pore diameter of the porous layer.

Reaction kinetics are implemented based on the Langmuir-Hinshelwood type model developed by Xu & Froment for Reaction 1-3:<sup>83</sup>



The reaction rates are implemented in the porous domain as:

$$R_{SMR} = k_{as} \frac{k_1 p_{\text{CH}_4} p_{\text{H}_2\text{O}} \rho_{\text{coat}} (1 - \beta)}{p_{\text{H}_2}^{2.5} \text{DEN}^2}, \quad \beta = \frac{p_{\text{H}_2}^3 p_{\text{CO}}}{K_1 p_{\text{CH}_4} p_{\text{H}_2\text{O}}} \quad (4.8)$$

Where  $k_{as}$  is an activity fitting factor,  $k_1$  an Arrhenius reaction rate, and  $\beta$  the approach to equilibrium. The value of  $\beta$  determines the direction of the reaction. Equation 4.4 is implemented for each species ( $\text{CH}_4$ ,  $\text{H}_2\text{O}$ ,  $\text{CO}$ ,  $\text{H}_2$ ,  $\text{CO}_2$ ), where the source term is defined based on reaction rates. For  $\text{H}_2$  the term is:

$$R_{\text{H}_2} = (3R_{SMR} - R_{WGSS} + 4R_{RM})M_{w,\text{H}_2} \left[ \frac{\text{kg}}{\text{m}^3\text{s}} \right] \quad (4.9)$$

#### Heat transport

Heat transport is implemented based on equation 4.10:<sup>85</sup>

$$\rho C_p \mathbf{v} \cdot \nabla T = k_{eff} \nabla^2 T + Q_n \quad (4.10)$$

For non-fluid domains, the velocity term is zero.  $k_{eff}$  is the effective thermal conductivity, and  $Q_n$  is a source term.  $Q_n$  is an additive term, which in the catalytic region is the heat consumed by the endothermic reaction, and in the reactor wall, the heat supplied by the resistance heating. For the ambient model, the term also include radiation losses (Fig. 4.2). The effective conductivity for the fluid is implemented equivalent to viscosity (Eq. 4.3), while it in solid domains is the thermal conductivity of the given material. All conductivities are implemented as temperature dependent. Pressure dependence of thermal conductivity is assumed negligible.<sup>94</sup>

The effective thermal conductivity for the porous washcoat was approximated by relative volume:

$$k_{eff,porous} = \theta_p k_{fluid} + (1 - \theta_p) k_{solid} \quad (4.11)$$

Due to the short characteristic timescales for heat transport across the coat, behavior is only weakly dependent on the thermal conductivity.

### Electric fields

The electric potential and currents are implemented according to Ohm's law, with the conversion from electric current to heat defined as:

$$Q_h = \mathbf{E} \cdot \mathbf{J} \left[ \frac{W}{m^3} \right] \quad (4.12)$$

Where  $\mathbf{E}$  is the vector for electric potential [V/m], and  $\mathbf{J}$  the current density vector [A/m<sup>2</sup>]. The resistivity of FeCrAl is practically independent of temperature, and changes less than 6% from 25°C to 1000°C.<sup>95</sup> To account for this small change, the conductivity was estimated by linearization:

$$\sigma = \frac{1}{\rho_{r,ref}(1 + \alpha_r(T - T_{ref}))} \quad (4.13)$$

Where  $\rho_{r,ref}$  is the reference resistivity [ $\Omega \cdot m$ ], and  $\alpha_r$  the temperature coefficient [1/K].

### **Boundary conditions**

Definition of boundary condition type and value is critical as it represents everything not included in the model. Boundary conditions can typically be divided into three types: Constant explicit value, constant implicit value, or a dependent value. For heat transport a constant explicit value would be defined as a temperature, where the implicit value would be a constant heat flux. The dependent flux could for instance be a heat loss, defined as an outward heat flux proportional to the temperature difference. The aim of defining boundary conditions is to best represent reality, to reduce the modelled domain. This section briefly describes the implemented boundary conditions for the implemented CFD models.

For fluid momentum, the inlet boundary condition is defined as a fully developed laminar flow to limit the modelled reactor volume (Fig. 4.2).<sup>96</sup> The

#### 4. CFD model implementation

---

fluid volume is defined as a mass flow at the inlet, with pressure defined at the outlet. Mass transfer is defined similarly, with composition defined at the inlet, with convection profiles imported from fluid momentum.

The applied electrical potential was defined at the upper copper socket as the root-mean-square (RMS) potential. The lower copper socket was defined as ground ( $V = 0$ ). An electrical contact resistance was implemented equivalent to heat transfer based on the measured contact resistance:

$$\mathbf{n} \cdot \mathbf{J}_i = h_c \Delta V \quad (4.14)$$

Where  $\mathbf{n}$  is the normal vector to the contact resistance surface,  $\mathbf{J}_i$  the current density vector [ $A/m^2$ ],  $\Delta V$  the potential difference (measured), and  $h_c$  an electrical resistance coefficient [ $S/m^2$ ], equivalent to the heat transfer coefficient.

For the ambient resistance heated model, fixed temperature was defined at the copper sockets (Fig. 4.2), due to the altered geometry in the axi-symmetrical geometry. Heat loss from the external surface of the insulation was defined as a  $5 \text{ W/m}^2/\text{K}$  heat flux, relative to an ambient temperature of  $25^\circ\text{C}$ . The value is based on simulations with free convection and literature models,<sup>85</sup> but due to the thick insulation layer in the given setup ( $>5 \text{ cm}$ ), the value of the flux has very little influence on the results related to the reactor. The lower part of the reactor, between the insulation and lower copper socket had in addition to the heat flux ( $11 \text{ W/m}^2/\text{K}$ ) a diffuse surface yielding loss by radiation, assuming  $25^\circ\text{C}$  ambient temperature and an emissivity of 0.71, equivalent to oxidized steel. Radiation on the internal surfaces of the reactor did not influence the results, as the view factor is exceeding close to unity due to the small diameter.

#### **Resistance-heating at industrial conditions**

Industrial conditions used for the presented work is based on data provided by Topsoe for an industrial side-fired reformer, operating at  $50.000 \text{ Nm}^3 \text{ H}_2/\text{h}$ , at S/C 1.8, with  $920^\circ\text{C}$  outlet temperature at 27.7 bar. For the resistance-heated model at industrial conditions, the geometry was simplified, assuming full length coat, and ideal insulation and electrical contact (Fig. 4.4)

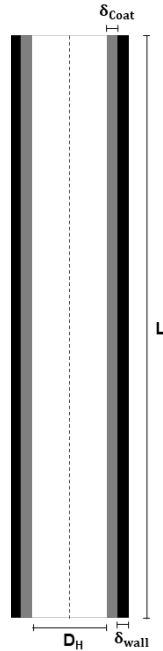


*Figure 4.4: Axisymmetrical geometry for resistance-heated model at industrial conditions. The coat is extended to the full length of the reactor, and ideal insulation and electrical contact, removing heat loss from inlet and the external surface.*

The heat loss through insulation for industrial reformers is typically less than 2%, further supported by integration of the heat source.<sup>23</sup> The inlet composition for industrial simulations in the presented work is defined as the equilibrium composition at 465°C and 30 bar, equivalent to the outlet conditions of a typical pre-reformer (Fig. 1.2).<sup>97</sup> The equilibrium composition is calculated in HSC 6.1. For S/C 1.8 the equilibrium composition is 31.8% CH<sub>4</sub>, 8.8% H<sub>2</sub>, 2.3% CO<sub>2</sub>, no CO, and water for balance. To achieve convergence of reaction kinetics, the initial CO concentration was set to 0.01% to avoid infinite gradients.

#### 4.1. Induction-heated model

The standard equations (Fluid momentum, Mass transfer, and Heat transport) are the same for the induction-heated model as the resistance heated (See Section 4.1 or Appendix 9.1.2). The induction heated model deviates from the resistance heated on three points: implementation of magnetic fields,

#### 4. CFD model implementation

hysteretic heat source, and heat transfer in the packed bed. The domains for the induction heated model is illustrated in Figure 4.5.

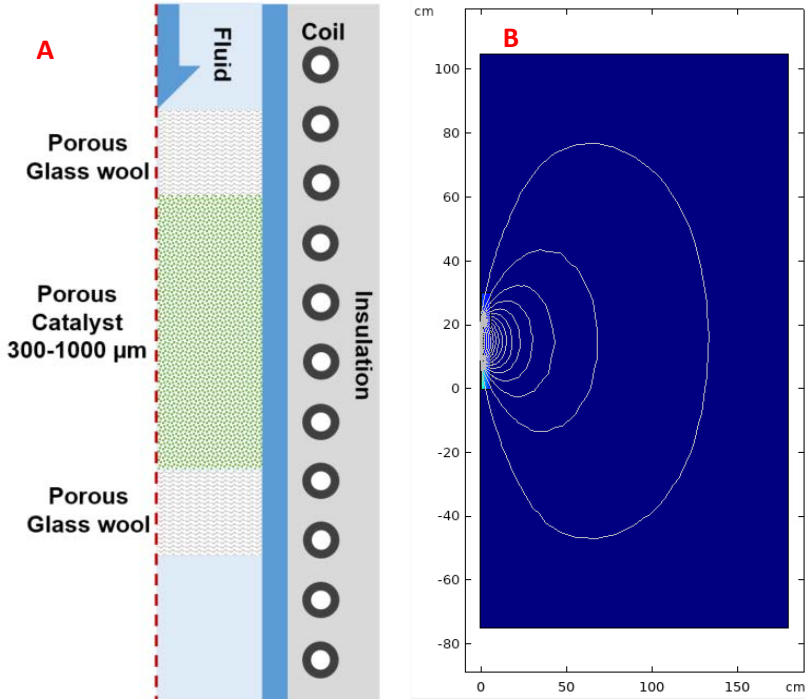


*Figure 4.5: CFD domains for induction-heated model A) Fluid, Porous, and solid domains. The catalyst serves both as heat supply and sink (Hysteresis/Endotherm reaction). Temperature is defined at the inlet, and the internal coil surface (Cooling water). B) Alternate geometry for modeling magnetic fields to account for Ampere's law.*

Good model prediction of magnetic fields requires resolving the entire field. If the magnetic field was resolved in geometry in Figure 4.5A, Ampere's law dictates full containment, yielding unrealistic gradients, and consequently incorrect magnetic fields. The magnetic field was assumed independent of temperature (a reasonable approximation considering the constant cooling of the copper coil,  $<20^{\circ}\text{C}$ ), and solved independent of the other physics.

The hysteresis heat source was prescribed the porous catalytic domain, and implemented as a heat source term into Equation 4.10. The hysteresis heat source is defined as:

$$Q_{\text{Hyst}} = A_{\text{Hyst}}(B, T) \cdot f \cdot \rho_{\text{cat}} \left[ \frac{W}{m^3} \right] \quad (4.15)$$

Where  $A_{\text{Hyst}}(B, T)$  is the hysteresis area depending on the magnetic field and temperature [J/kg],  $f$  is the frequency [196 kHz], and  $\rho_{\text{cat}}$  the sample density, calculated from sample weight and loaded dimensions (1-1.2 g/cm<sup>3</sup>). The hysteresis area was implemented as a topographic map (Fig. 4.6), as no function was found to adequately represent the relevant range of data.

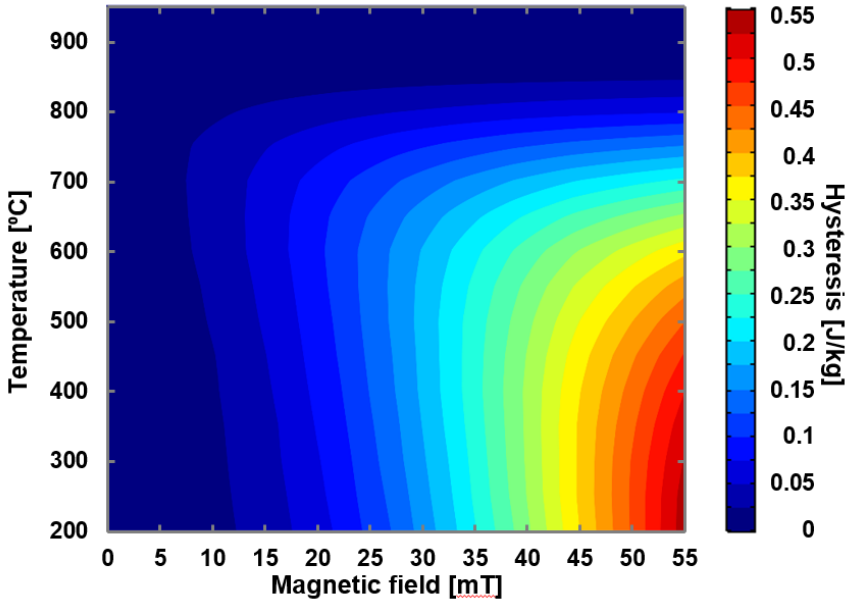


*Figure 4.6: Hysteresis area as a function of applied field and temperature* Hysteresis area calculated by integration of the hysteresis loop. Here for a  $\text{Co}_{0.5}\text{Ni}_{0.5}/\text{Al}_2\text{O}_3$  sample synthesized by Morten Vinum (Topsoe/KU). VSM measurements by Mikkel F. Hansen (DTU). VSM data treatment by Mads R. Almind (DTU).

The highest hysteresis is encountered at low temperatures and high magnetic fields. At moderate temperatures and magnetic fields (200-600°C, 20-35 mT) the hysteresis area is only weakly dependent on the temperature. A temperature dependent optimum is observed, with the optimum temperature decreasing as the magnetic field increases. This is illustrated more clearly in Figure 4.7.

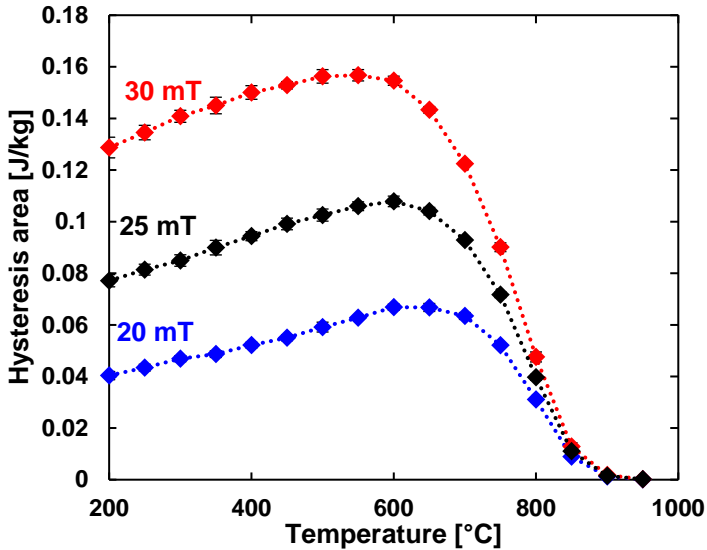


*Figure 4.7: Temperature influence of hysteresis area Hysteresis area for the relevant range of magnetic fields for induction heating. The hysteresis area increases with applied field, but decays from 600°C towards zero contribution at the Curie temperature at 892°C. Data is extracted from Figure 4.6.*

At the magnetic fields applied in the experimental setup, an optimum hysteresis is observed between 550-600°C, decreasing with applied field. It is expected the optimum is related to a coercivity decreasing faster with temperature than the magnetization, increasing the accessible hysteresis area (A taller loop at equivalent field). The rapid decline after the peak is related to decreasing magnetization as observed for the pure elements (Fig. 1.5). For pure elements, the Curie “cutoff” is typically quite steep, and the gentler slope observed for the Co-Ni spinel is likely related to a particle size distribution, where smaller particles become superparamagnetic at lower temperatures (Eq. 1.4).<sup>67,98</sup>

### Pressure drop in packed bed

As the flow within a washcoat is negligible, the pressure drop in the resistance-heated reformer is independent of the permeability,  $\kappa$ . This is not the case for a packed bed, where the pressure drop depends on fluid velocity and permeability (Eq. 4.2). The permeability was estimated by Carman-Kozeny equation, assuming spherical particles in a laminar flow<sup>91</sup>:

$$\kappa = \frac{d_p^2}{180} \frac{\theta_b^3}{(1 - \theta_b)^2} \quad (4.16)$$

Where  $D_p$  is the particle diameter, and  $\theta_b$  is the bulk porosity (different from  $\theta_p$  which is the skeletal porosity of the particles). The low range of the particle distribution fraction (500  $\mu\text{m}$ ) was used to estimate the permeability. The validity of this approximation decreases as the particle shape deviates from spherical and represents a range of sizes. However, accurate prediction of pressure drop is notoriously difficult, and it was generally found that the predicted pressure deviated less than 20% from the measured, which never exceeded 0.3 atm.

### Thermal conductivity of a packed bed

The effective thermal conductivity consists of three contributions: conduction, convection, and radiation. In the fluid phase, radiation is neglected on the assumption that the gas has an emissivity of zero at moderate temperatures.<sup>22</sup> For the porous particle, an effective thermal conductivity is required, and several are available in the literature. The simplest approach is the volume average for parallel conduction given in Equation 4.11. A similar equation for heat transport limited by materials of lower conductivity is given by:

$$k_{eff,Vol.Av.} = \frac{1}{\frac{1}{\theta_p k_{gas}} + \frac{1}{(1 - \theta_p) k_{solid}}} \quad (4.17)$$

Equation 4.17 reasonably express the lower bound for effective conductivity of a porous particle or a washcoat, where Eq. 4.11 provides the maximum relative to heat transfer by conduction. To calculate the effective thermal conductivity, the equation can be applied again using the bed porosity,  $\theta_b$ . However, convection can contribute significantly in a packed bed at elevated pressure.

There are many models for effective conductivity through a packed bed, either theoretical or empirical.<sup>85,99–101</sup> An example of the former is a model proposed by Schlünder,<sup>101</sup> also known as the Zehner-Bauer model, based on viewfactors in a unit cell of spherical particles. It divides the effective

#### 4. CFD model implementation

---

conductivity into two parts: the conductivity of a stagnant bed, and the contribution from turbulence.<sup>22,100,102</sup>

$$k_{eff} = k_{stag} + k_{turb} \quad (4.20)$$

The contribution of turbulent flow to the effective conductivity can be expressed as the Peclet number relative to the modified convective Peclet number ( $K_t$ ), in the limit of mass transfer, which can be approximated as:<sup>85,101–103</sup>

$$k_{turb} = \frac{Pe}{K_t} k_{gas} \quad (4.21)$$

$$Pe = \frac{\rho_{gas} v_0 \hat{C}_{p,gas} x_F}{k_{gas}}, \quad x_F = 1.15 D_p \quad (4.22)$$

$$K_t = 8 \left( 2 - \left( 1 - 2 \frac{d_p}{d_{tube}} \right)^2 \right) \quad (4.23)$$

Where  $x_F$  is a shapefactor from experimental fitting. A simplified version of the model proposed by Schlünder, disregarding Smoluchowski effects and oxide layers, can be expressed as:

$$k_{stag} = (1 - \sqrt{1 - \theta_b}) \left[ 1 + \theta_b \frac{k_R}{k_{gas}} \right] + \sqrt{1 - \theta_b} \left[ \frac{k_{sp}}{k_{gas}} \right] \quad (4.24)$$

$$\frac{k_{sp}}{k_{gas}} = \frac{2}{P_t} \left( \frac{\left( B_t \left( \frac{k_{sol} + k_R}{k_{gas}} - 1 \right) \frac{k_{gas}}{k_{sol}} \right)}{P_t^2} \ln \left( \frac{k_{sol} + k_R}{k_{gas} \cdot B_t} \right) - \frac{B_t - 1}{P} - \frac{B_t + 1}{2} + \frac{B_t + 1}{2 B_t} \frac{k_R}{k_{gas}} \right) \quad (4.25)$$

Where  $\theta_b$  is the bed porosity,  $k_R$  is the contribution to conductivity by radiation,  $k_{gas}$  the thermal conductivity of the mixed gas,  $k_{sp}$  the conductivity across a bed of solid particles,  $B_t$  is shape factor, which was modified to account for non-spherical particles.<sup>104</sup>

$$B_t = 1.364 \left( \frac{1 - \theta_b}{\theta_b} \right)^{1.055} \quad (4.26)$$

$$P_t = 1 + \frac{k_R - B_t k_{gas}}{k_{sol}} \quad (4.27)$$

$$k_R = 4\sigma_{SB}F_e^*d_pT^3, F_e^* = \frac{\varepsilon_r}{2 - \varepsilon_r} \quad (4.28)$$

$\varepsilon_r$  is the particle emissivity,  $\sigma_{SB}$  is the Stefan-Boltzman constant, and  $F_e^*$  is an exchange factor. The used expression for  $F_e^*$  is a very simple form,<sup>105</sup> and likely a poor approximation as it does not relate to thermal conductivity or temperature variations in emissivity, however, the contribution from radiation is not significant in the bed below 1000°C, relative to the heat transport by conduction. The emissivity was estimated to 0.38, equivalent to measurements from literature.<sup>106,107</sup>

### Wall effect in packed beds

The effective thermal conductivity is a function of the porosity, which approaches unity near the wall, creating a *near-wall region*, where the flow is faster than the bulk flow in the bed.<sup>108</sup> According to calculations by Geb et al.,  $\frac{D_{tube}}{D_p} \geq 120$  is necessary to completely disregard wall-effects (An infinite packed bed was assumed by Schlünder).<sup>108</sup>

One approach, is described by Van Anterwerpen et al. (2012), for a pebble bed reactor.<sup>109</sup> However, it introduces a significant amount of parameters and assumes identical emissivity of wall and particles. Alternatively, the porosity can be introduced as a function of radial distance.<sup>105,110</sup>

A semi-empirical model proposed by Mueller was implemented, assuming randomly distributed, uniform spheres.<sup>110</sup>

$$\theta_b(r) = \theta_b + (1 - \theta_b)J_0\left(\alpha_\theta \frac{r}{d_p}\right) \exp\left(-\beta_\theta \frac{r}{d_p}\right) \quad (4.29)$$

Here,  $J_0$  is the zero order Bessel function, and  $\alpha_\varepsilon$  and  $\beta_\varepsilon$  are fitting factors defined by:

#### 4. CFD model implementation

---

$$\alpha_\varepsilon = 7.45 - \frac{11.25}{D_{tube}/d_p}, \text{ for } \frac{D}{d} \ll 13 \quad (4.30)$$

$$\beta_\varepsilon = 0.315 - \frac{0.725}{D_{tube}/d_p} \quad (4.31)$$

The radial porosity primarily influence the flow profile, but impact on the temperature profile was found negligible for small particles (Supplementary Figure S9.3.6).

### 4.2. Model verification

If CFD models were flawless, actual experimental work would be redundant. However, that is exceedingly rarely the case, considering the assumptions required by even the most elaborate models (Diffusion coefficients, homogenization, reaction kinetic models, etc.). With sufficient fitting parameters, any model can fit any given set of experimental data. A good model should represent as wide a range of experimental data with the least amount of fitting parameters possible, and ideally parameters that make physical sense.

For the resistance-heated model, three fitting parameters were found necessary to adequately fit the model to the experimental data. A fitting factor for the pre-exponential catalytic activity factor was introduced to account for potential deviations from the catalyst used by Xu & Froment in their kinetic model.<sup>83</sup> A second fitting factor was introduced to account for higher thermal conductivity of the granular insulation, likely related to non-optimal density relative to the data provided by the supplier (FreeFlow, Etex Industry). A third fitting factor was introduced to account for the layer thickness of the residual layer towards the outlet (Fig. 4.3), as it was modelled without mass transfer due to mesh constraints (Section 4.1).

The fitting factors were determined by a least square approach, comparing the model results to six experimental data sets, spanning the full range of flow and conversion. Equation 4.32 takes the measured conversion and all temperatures from mounted TCs into account (Fig. 2.1). A weight factor,  $W$ , is applied to the conversion to bring it within the same order of magnitude as the cumulative temperature error.

$$SSQ = \sum_j^M \left[ W \cdot (\bar{X}_{CH_4,j}^{exp} - X_{CH_4,j}^{Model})^2 + \sum_{i=1}^N (\bar{T}_{i,j}^{exp} - T_{i,j}^{Model})^2 \right] \quad (4.32)$$

Figure 4.8 show the cumulative error at different combination of the fitting factors, for the model comparison to six experimental datasets.

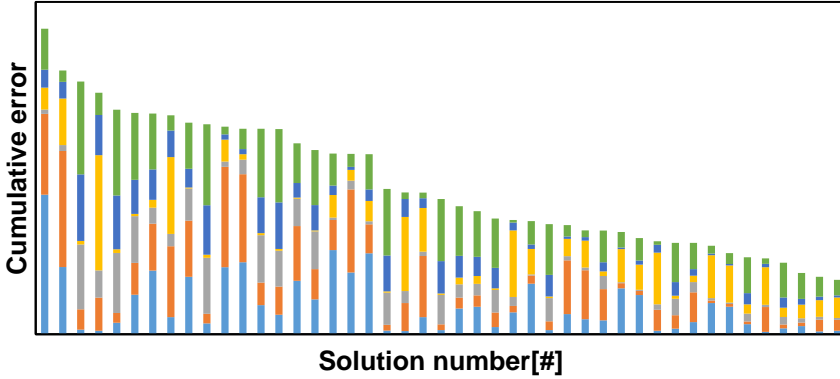


Figure 4.8: Cumulative least square fit Cumulative  $SSQ$  for the model compared to six different experimental data sets (The different colors in each bar). The data is sorted.

As evident from Figure 4.8, different combinations provide at optimum for different solutions. At the best fit, the standard temperature deviation across the sixteen thermocouples is less than  $10^{\circ}\text{C}$ , and methane conversion is predicted within  $\pm 2\%$ .

The insulation fitting factor, 1.7, was reproduced in a model system, without flow or reactions (Appendix 9.4). Removal of all thermocouples prevented measurement of the temperature profile, but did not change the conversion at equivalent conditions. The layer thickness of the residual layer towards the outlet achieved an optimum fit at  $1.5 \mu\text{m}$ , which is considered reasonable, compared to the observed thickness (Fig. 4.3), as it is modelled without mass transfer limitations.

The catalytic fitting factor was within an order of magnitude relative to the implemented kinetic model. The deviation is expected to be related to particle size, Nickel loading, catalyst support, or different heat supply.

A similar approach was used for the induction-heated model, introducing a fitting factor on the applied current instead of the thin layer. Fitting the current

## 4. CFD model implementation

---

could not account for the observed experimental data. The same fitting factor value for the insulation is used in the induction-heated model, but not other parameters are fitted. This is further elaborated in Chapter 5.

### 4.3. Characteristic timescales

The seven steps shown in Figure 4.9 characterize a typical reaction on a heterogeneous catalyst.<sup>34</sup> The steps to form the product is diffusion from bulk to catalyst, inter-particle diffusion, adsorption, reaction, and desorption. The product then has to diffuse out of the particle, and back into the bulk phase. Each step can be limiting, depending on the conditions of the reaction.

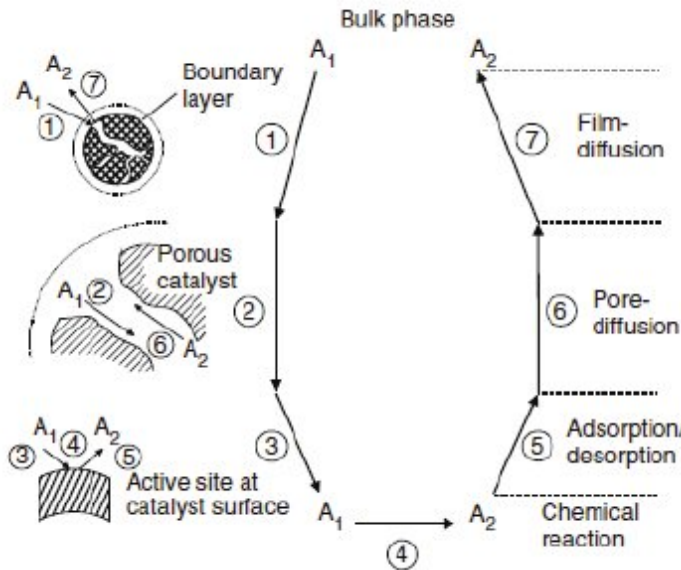


Figure 4.9: Heterogeneous catalytic cycle Steps in a chemical reaction. Figure from Chorkendorff & Niemantsverdriet.<sup>34</sup>

For reactor design, the performance limiting steps are typically bulk diffusion, internal diffusion, or reaction kinetics. For endothermic reactions, heat transfer is also a limiting parameter to take into account. For a Langmuir-Hinshelwood reaction mechanism adsorption, reaction, and desorption are lumped together in the kinetic model, which can include fitted absorption coefficients.

There is many different dimensionless numbers and models that can be used to assess limiting phenomena, such as the Thiele modulus for reaction rate to internal diffusion,<sup>85,111</sup> or Mears' criterion for limiting external mass transfer.<sup>111</sup>

Characteristic timescales enables comparative evaluation of the different phenomena.<sup>112,113</sup> For a conventional fired reformer, heat transport is limiting. The characteristic timescale for heat transport is an estimate for the time required for a thermal perturbation to equilibrate, and it can be expressed as:<sup>113</sup>

$$\tau_{thermal} = \frac{\delta_t^2}{\alpha_t}, \alpha_t = \frac{k_{eff}}{\rho C_p} \quad (4.33)$$

Here  $\delta_t$  [m] is the length which heat is transferred, and  $\alpha_t$  [m<sup>2</sup>/s] the thermal diffusivity. The characteristic length  $\delta_t$  could for instance be the reactor wall thickness, or the radius of a packed bed (The latter only if heat transfer is primarily by conduction).

Another phenomena of conventional SMR reformers is “eggshell” catalysts, where reactor performance scales with catalyst surface area, rather than volume.<sup>22</sup> This can occur when reaction rate is much faster than internal diffusion rate. The characteristic timescale for internal diffusion can be expressed as:<sup>113</sup>

$$\tau_{int} = \frac{\delta_{ID}^2}{D_{eff}} \quad (4.34)$$

Here  $\delta_{ID}$  is diffusion length scale, and  $D_{eff}$  the effective diffusion in the catalyst (Eq. 4.6).<sup>91</sup> The diffusion length for a spherical catalyst is the particle diameter, and for a coat, the thickness.<sup>113</sup>

Limiting external mass transport, bulk diffusion, can be expressed as:<sup>113</sup>

$$\tau_{ext} = \frac{\delta_{ED}^2}{2D_m Sh} \quad (4.35)$$

#### 4. CFD model implementation

---

Here  $\delta_{ED}$  is the characteristic length for external diffusion,  $D_m$  the diffusivity, and  $Sh$  the Sherwood number, expressing the ratio of convective to diffusive mass transport. For fully developed laminar flows, the Sherwood number is approximately equal to 4.364.<sup>85,114</sup> The transition from laminar to turbulent flow can be estimated by the Reynolds number  $Re$  (Ratio of inertial to viscous forces), indicating transition to turbulence for values exceeding 2100.<sup>85</sup>

Which of the adsorption, reaction, and desorption step is limiting can be estimated through *first principle* or *density functional theory* (DFT) calculations.<sup>34,115,116</sup> The characteristic reaction time for the reaction in Eq. 4.36, lumps the atomic scale steps together, in a simple approximation. The reaction time coefficient for methane can be expressed as:<sup>113</sup>

$$\tau_{re} = \frac{C_{CH_4}}{R_{CH_4}} \quad (4.36)$$

Here  $C_{CH_4}$  is the methane concentration [mol/m<sup>3</sup>], and  $R_{CH_4}$  the overall methane consumption rate [mol/m<sup>3</sup>/s]. For comparison to limiting mass transfer (internal and external) it is evaluated at the catalyst surface.

Process intensification is a term frequently used for improving reactor performance, and indicates that more product is produced per reactor volume. As the flowrate increases, insufficient residence time will eventually limit performance. The residence time is conventionally calculated as the flowrate at the inlet, divided by reactor volume. However, for a fully laminar flow, a parabolic velocity profile results in higher linear gas velocities in the center. The space-time can be expressed as:<sup>117</sup>

$$\tau_s = \frac{z_c}{u_{z_c}} \quad (4.37)$$

Where  $z_c$  is the axial position in the reactor, and  $u_{z_c}$  is the linear velocity, evaluated at  $z_c$ . It is typically desirable for the residence/space-time to exceed the limiting phenomena by at least an order of magnitude.<sup>111</sup>

## 5. Induction heating

Magnetic induction can heat ferromagnetic particles via three mechanisms: induced eddy currents, hysteresis losses, and magnetic resonance (Section 1.2). The prevalent mechanism is strongly dependent on the size of the particle and frequency of the oscillating magnetic field. Hysteresis heating of ferromagnetic catalytic particles enables a non-contact heat source, supplying energy directly to the catalytic sites, completely removing heat transfer limitations.

This chapter covers the experimental results of lab scale hysteresis heating of SMR (See Section 2.3), and the predictions by the implemented CFD model (Section 4.3). At the end of this chapter, considerations regarding applications and scalability are put in perspective, relative to current technology for SMR.

### 5.1. Induction-heated reforming: Experimental

To supply heat directly to the catalytic site, the catalyst must be ferromagnetic, catalytically active, and have a Curie temperature exceeding the reaction temperature. For the experimental work, a catalyst based on a cobalt-nickel spinel synthesized by Morten Vinum (Topsoe/KU) with a Curie temperature of 892°C was used.<sup>81</sup>

Temperatures exceeding 750°C, and 99% methane conversion was achieved using hysteresis heated SMR (Fig. 5.1).

## 5. Induction heating

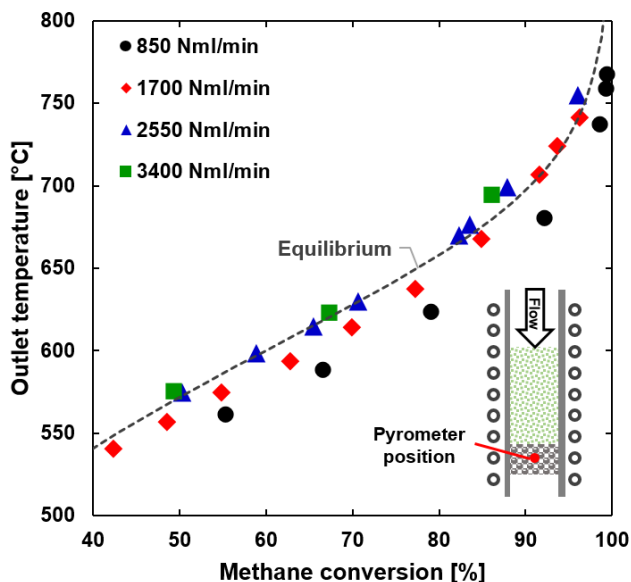


*Figure 5.1: Hysteresis heated reforming Measured outlet temperature (pyrometer) plotted against methane conversion. The dotted line is the equilibrium curve for steam reforming at ambient pressure calculated in the software HSC 6.1. Inlet composition;  $\text{CH}_4:\text{H}_2\text{O}:\text{H}_2$  (30/60/10). Experiments at ambient pressure, using a  $\text{Co}_{0.5}\text{Ni}_{0.5}/\text{Al}_2\text{O}_3$  sample synthesized by Morten Vinum.<sup>81</sup>*

The temperature was measured ca. 3 mm below the catalyst bed using an IR pyrometer to avoid an induced error by eddy currents. For a flowrate of 850-1700 Nml/min, the measured temperature is below the equilibrium temperature. This indicates either that the reaction is well below thermodynamic equilibrium, or that the temperature measurement does not accurately represent the peak outlet temperature of the catalyst. Operating 35°C below the thermodynamic equilibrium is estimated to be unlikely, and a more likely explanation is a temperature measurement error. A probable explanation could be heat loss between the catalyst and the pyrometer, as the deviation between the measured temperature and equilibrium decreases as the flow increases. A substantial radial heat loss is expected due to an insulation layer of just 5.4 mm between the 550-750°C catalyst and the 20°C coil. As the flowrate increases, the temperature approaches the equilibrium temperature, consistent with a decreasing relative loss.

Further work is required to improve the temperature measurements to better validate the CFD model, and to provide an accurate estimate of the reaction

equilibrium. If the current temperature measurements, against expectations, turns out to be correct, hysteresis heated catalysis has some exceptional potential for reactions susceptible to detrimental homogenous reactions.

## 5.2. Induction-heated reforming: Model predictions

The small dimensions and restrictions imposed by the magnetic field makes it difficult to obtain accurate measurements from within the catalytic bed. To elucidate the catalytic process and related phenomena, a CFD model was implemented (Section 4.2).

Figure 5.2 shows measured and modelled conversion and temperature as function of the applied magnetic field. The magnetic field for experimental data was calculated based on a calibration between the current supplied by the induction oven and the magnetic field within the center of the coil using a small pick-up coil. This correlation accounts for resistive losses in the transformer and coil, and deviation from an ideal solenoid (Supplementary Figure S9.3.7).

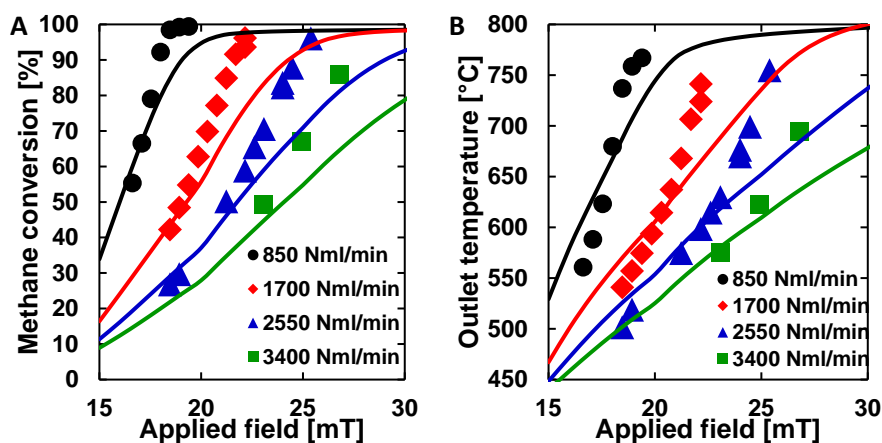


*Figure 5.2: Modelled hysteresis heated reforming A) Measured and modelled conversion and B) temperature for hysteresis heated SMR, as a function of the calculated peak magnetic field. Symbols are measured values, full lines are model predictions. The model predicts that significantly stronger magnetic fields are required to reach the measured level of conversion, and outlet temperatures. Experiments at ambient pressure,  $\text{CH}_4:\text{H}_2\text{O}:\text{H}_2$  (30/60/10), 196 kHz.*

The characteristic “S” shape of the conversion plotted against the magnetic field is apparent for both the measured and modelled data. As the magnetic field increases a larger hysteresis loop is accessible, increasing the heat

## 5. Induction heating

---

supplied to the reaction. While the trends displayed in the decreasing slope with increasing flowrate is reproduced by the model, the conversion is significantly underpredicted at high magnetic fields. For the temperature, the thermal losses between the catalyst and point of measurement may induce some error, especially at lower flow rates (Fig. 5.1).

A sharp cutoff in achievable temperature is visible in the model and weakly distinguishable in the measured data at 850 Nml/min (Fig. 5.2B) as the temperature reaches 770°C, consistent with the measured decay of the hysteresis area seen in the VSM data (Fig. 4.6).

Essentially, the experimental measurements indicate a significantly higher supply of heat at equivalent field than the model. The possible errors can be distributed into three categories: Model implementation and assumptions, Experimental error or uncertainty, and Model input (VSM data).

### **Errors in model implementation and assumptions**

The steeper slope of the experimental data in Figure 5.2 indicates higher conversion is achieved at a lower magnetic field than predicted by the model. Higher conversion for the endothermic reaction is equivalent to higher temperatures, as no deficit of catalytic activity was indicated in Figure 5.1. The temperature is balanced around the input (hysteresis) and output (endothermic reaction, heat losses). To increase the energy consumed by the reaction, either the input is larger than predicted or the heat losses are smaller. Looking at the latter, the heat loss depends on the thermal conductivity of the catalyst, quartz tube, and insulation. A sensitivity analysis of either, varying them individually does not significantly influence the model predictions, even when decreased by an order of magnitude.

The heat loss is correlated directly to the temperature difference across the insulation. The outgoing cooling water from the coil is continuously measured, and never exceeds 25°C (Which would cause the induction oven to trip). Increasing the cooling water temperature to 50°C in the model does not influence the model predictions either, and based on the excellent thermal conductivity of copper, temperature variations of that magnitude in the coil is unexpected.

The only source of heat is the magnetic hysteresis, implemented directly from the VSM measurements (Fig. 4.6). However, other mechanisms may contribute to the increase the supplied heat. One uncertainty is a higher inlet

temperature. Figure 5.3 shows the measured temperature near wall, at the top of the catalyst bed.

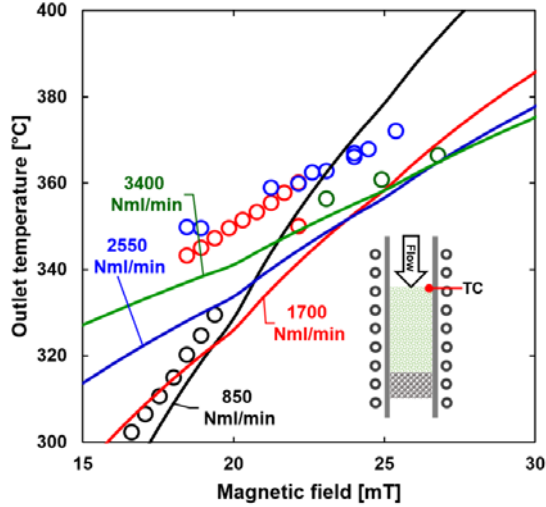


*Figure 5.3: Inlet temperature* Open circles are data measured by a 0.5 mm N-type thermocouple, full lines are model predictions. The gradients of the experimental data and the model are nearly identical, though a small difference is observed, in particular for a flowrate of 1700-2550 Nml/min. Ambient pressure, 196 kHz, CH<sub>4</sub>:H<sub>2</sub>O:H<sub>2</sub> (30/60/10).

Barring the small variations in the measured inlet temperature, a near linear increase is observed with increasing field. This increase may both be from eddy currents induced in the thermocouple, or increasing heat from the catalyst. The lower inlet temperature for a flowrate of 3400 Nml/min relative to 1700-2550 Nml/min is also predicted by the model, however, only at higher magnetic fields, equivalent to what was observed in Figure 5.2. The predicted inlet temperature deviates less 30°C, which alone is insufficient to account for the deviations between model and experimental data.

Alternatively, the assumption that all heat is supplied by hysteresis may be incorrect. As mentioned, induction can supply heat by three mechanisms. Effect generated by eddy currents in a wire can be estimated by:

$$P_{Eddy} = \frac{\pi^2 B^2 d^2 f^2}{k_s \sigma} \quad (5.1)$$

Here  $B$  is the magnetic field within the sample accounting for relative permeability,  $f$  is the frequency,  $k_s$  is a shape factor (12 for a wire), and  $\sigma$

## 5. Induction heating

the conductivity. Figure 5.4 shows the theoretical effect supplied by hysteresis relative to eddy currents for a cylindrical particle as a function of the diameter.

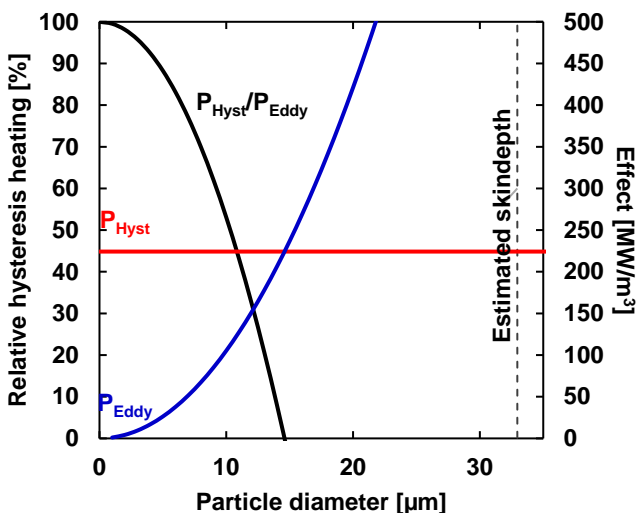


*Figure 5.4: Predicted contribution from induction heating mechanisms Comparison is calculated on the basis of cylindrical cobalt nanoparticles, parallel to the magnetic field. Conditions:  $B=20$  mT,  $f=196$  kHz,  $\sigma=1.7e.7$  S/m,  $\rho=7150$  kg/m<sup>3</sup>,  $\mu_r=70$ ,  $P_{Hyst}=0.16$  J/kg.*

Equation 5.1 is based on a cylindrical particle of pure cobalt and is expected to overpredict the contribution relative to a spherical particle. Yet, based on a simple equation for eddy currents, hysteresis is the prevalent mechanism up to 11  $\mu\text{m}$  particles. The average particle diameter of the catalytic sample is closer to 30 nm,<sup>81</sup> which based on Figure 5.4 should result in negligible contribution from eddy currents.

Another potential contribution could be magnetic resonance, but it is deemed unlikely at a frequency of 196 kHz. What may be influenced by frequency is the smaller particles of the catalyst. Superparamagnetism is dependent on particle volume, however, if the applied field oscillates faster than the Néel relaxation, the particles will exhibit hysteresis. The VSM sample is oscillated at 5 Hz, and the magnetic field significantly slower, and the several orders of magnitude faster induction heating for the experimental setup might achieve hysteresis heating smaller particles. A study of the specific absorption rate

(SAR) as a function of frequency could be used to elucidate this phenomena, but is yet to be done.

Another option based on particle size could be related to sintering occurring in the induction tests, where the particles are exposed to large partial pressure of steam at high temperatures. However, no discernable change in the hysteresis area was observed during the experiments. VSM and TEM measurements of the spent catalyst may provide significant insight into hysteresis related phenomena dependent on particle size. These measurements are unfortunately not yet available, but will be included in Paper 4 which is yet in preparation.

### **Experimental error and uncertainty**

There is always some uncertainty of experimental results. For the given setup, it is related to the current in the coil, temperature measurements, and the gas chromatograph. Starting with the latter, the GC was calibrated prior to the experiments, and found reasonably close to previous calibration data. While methane conversion exceeding 95% falls outside the calibrated area, the extrapolation is going through zero. In addition, equivalent values for methane content was obtained by both FID and TCD (Within 1%).

As shown in Figure 2.3 and 5.1, temperature measurements in an induction field can readily induce an error. While measurements of the IR pyrometer should be completely unaffected by the magnetic field, other parameters can influence the measurement. Especially the position of the pyrometer, as no heating below the catalyst results in steep decrease in temperature despite the insulation. Steep radial gradients are also present, however, visual confirmation of the pyrometer position before and after experiment placed it within 1 mm of the tube center, which alone is insufficient to explain the difference. The pyrometer was calibrated against alumina spheres identical to the experimental setup in a tube furnace (Supplementary Figures S9.3.2-3).

Some uncertainty is related to the induction oven, which supplies 1 to 10 ampere with a resolution of 0.1A, which is then transformed with a turn ratio of 23. To account for the resistive losses in the transformer and coil, and the deviation from an ideal solenoid, a calibration using a pick-up coil connected to an oscilloscope correlates the transformer current to the effective current in the coil (Supplementary Figure S9.3.7). It is however still uncertain how accurate the initial current supplied is, and any uncertainty is directly carried

## 5. Induction heating

---

into the corrected magnetic field. An attempt to measure the current with a current clamp did not yield quantitative results.

### **Model input (VSM measurements)**

A final source for the deviation between the experimental data and the model is the VSM input. One possible cause for error is the sample geometry. The area of uniform magnetic field between the pick-up coils for the VSM is small, and if the sample is not uniformly exposed, the hysteresis may be underpredicted. If the individual magnetic particles are not insulated, demagnetization may occur. However, if the latter is the case, magnetic shielding may occur as eddy currents are induced in the shell structure. It is assumed there is no relation between the individual particles, and subsequent neither eddy currents nor magnetic shielding.

Another probable source of error could be the different conditions. The VSM is measured in 1% H<sub>2</sub> in Argon, while in the experimental setup it is exposed to SMR conditions, which at the given composition should be thermodynamically reducing (Fig. 3.1). The VSM sample is measured in a small Boron-nitride cup, and while it is porous, it may inhibit full reduction of the sample, which given the small particle sizes could be a considerable reduction in magnetic material. A new VSM setup is in development to perform measurements at reaction conditions.

Yet another possibility is carbidization of the catalytic particles under reaction conditions, which for iron nanoparticles is reported to substantially increase the hysteresis area, but reduce the Curie temperature.<sup>77</sup> The measured temperature never exceed 800°C, though the equilibrium temperature based on conversion of the 850 Nml/min test approached 830°C.

As evident, several potential errors can explain the deviation between the data and the model. While no single model parameter can account for the deviation, cumulative error of many parameters may be responsible. Based on the resistance-heated model, it is plausible the error is correlated to the hysteresis heating. Either in the implementation into a finite element model, or as a consequence of the VSM measurement conditions.

### **5.3. Hysteresis heating reaction control**

While the implemented model for hysteresis heating does not quite fit the experimental data as described in the previous section, the trends predicted

by the model are similar to the experimental. Based on this, the modelled results presented in this section are not necessarily quantitative, but can give some insights into the phenomena of hysteresis heated reforming.

The most prominent difference relative to fired reforming is the supply of heat. In a fired reformer, heat is supplied from the combustion of fossil fuels, and is transferred to the catalyst by radiation, conduction, and convection. A catalyst heated by hysteresis will achieve the highest temperature at the susceptor – the catalytic site itself. In a reactor, this results in an inversed temperature profile, where the highest temperature occurs at the center.

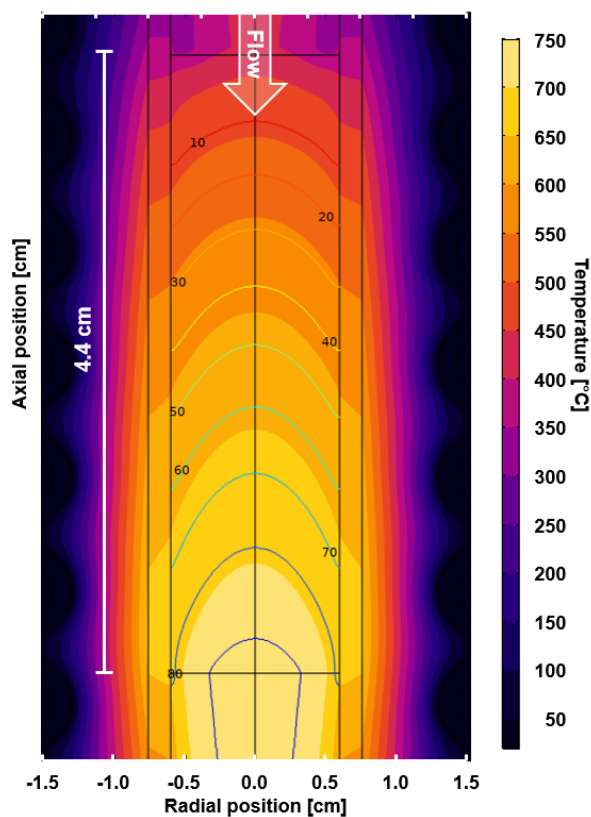


*Figure 5.4: Hysteresis-heated SMR Modelled temperature and methane conversion contours of hysteresis heated SMR. The highest temperature occurs at the center towards the outlet. The individual windings of the coil can be seen at the edge. Ambient pressure, 2550 Nml/min, ambient, 28 mT field,  $\text{CH}_4:\text{H}_2\text{O}:\text{H}_2$  (30/60/10). 85% methane conversion.*

## 5. Induction heating

Equivalent to the inversed temperature profile, methane conversion is highest at the center of the reactor. The thin insulation layer between the catalyst and coil results in a temperature difference exceeding  $700^{\circ}\text{C}$  across less than 1 cm. This inevitably results in a significant heat loss to the coil, contributing to the resistive losses. The coil is continually cooled, sustaining the steep thermal gradients. The overall energy efficiency is 10 to 20%, primarily depending on the flowrate, with the primary loss in copper coil.

The hysteresis area depends on the magnetic field and the temperature. For a bed height of 4.4 cm positioned in the center of the coil, the magnetic field deviates less than 1% across the sample. The temperature increases along the sample as the reaction proceeds, resulting in an uneven supply of heat (Fig. 5.5).

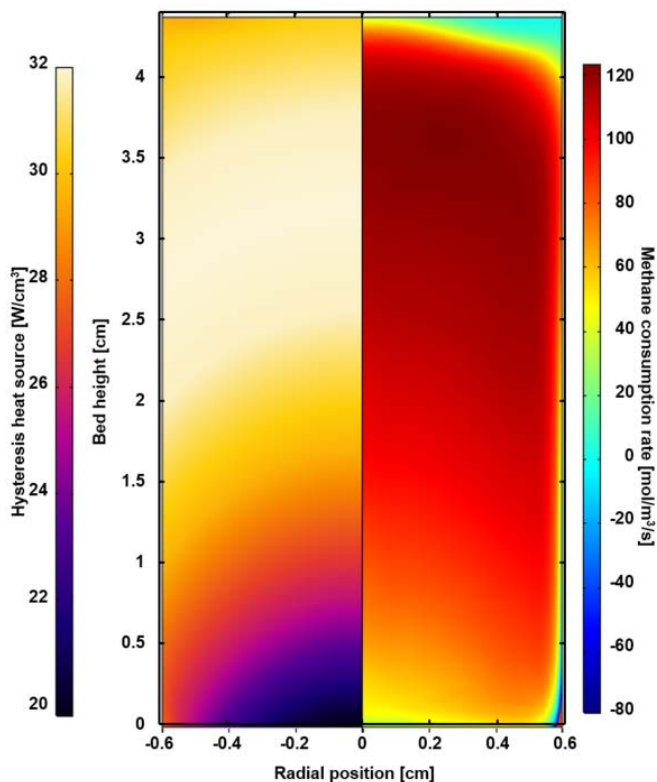


*Figure 5.5: Hysteresis heat source and reaction rate* Left: Hysteresis heat source peaking near the inlet where the temperature is lower (See Fig. 5.4). The heat source is lowest near the center toward the outlet where temperature and conversion peaks. Right: Methane consumption rate. Ambient pressure, 2550 Nml/min, 28 mT field,  $\text{CH}_4:\text{H}_2\text{O}:\text{H}_2$  (30/60/10).

Figure 5.5 highlights the challenge and potential of hysteresis-heated catalysis. The supply of heat peaks slightly below the top of the catalyst, where temperature is favorable (Fig. 4.6). The heatflux is smallest towards the outlet in the middle, where it bottoms at  $20 \text{ W/cm}^3$ . This minimum is due to the temperature dependence of the magnetic hysteresis, declining steeply as the temperature exceeds  $600^\circ\text{C}$  (Fig. 4.6). Towards the outlet, the temperature reaches  $750^\circ\text{C}$  where the hysteresis area is 60% of the peak value, corresponding to the variation in the heat flux.

The reaction rate is correlated to the heat flux, and similarly peaks just below the inlet (Fig. 5.5). Heat losses to the coil shapes the temperature profile, and results in reverse reaction near the wall at the outlet as the thermal losses exceed the hysteresis heating. The reaction rate decreases along the reactor as the increasing temperature results in a decreasing hysteresis area, sustaining a nearly constant approach to equilibrium for the lower half of the reactor.

While the heat flux is uneven, the variation is small compared to the gradients of fired industrial reformers. Increasing flowrate restricts the temperature, enabling heat flux exceeding  $40 \text{ W/cm}^3$  at  $3400 \text{ Nml/min}$  (90% conversion). For reference, the volume flux of industrial reformers is around  $3\text{-}5 \text{ W/cm}^3$  not including the furnace volume.<sup>23</sup> Heat flux exceeding  $65 \text{ W/cm}^3$  has been achieved in co-current fired microreactors.<sup>49</sup>

The temperature dependent hysteresis can be used to control reaction temperature, with practically no heat supplied as the reactor approach the Curie temperature (Fig. 5.6).

## 5. Induction heating

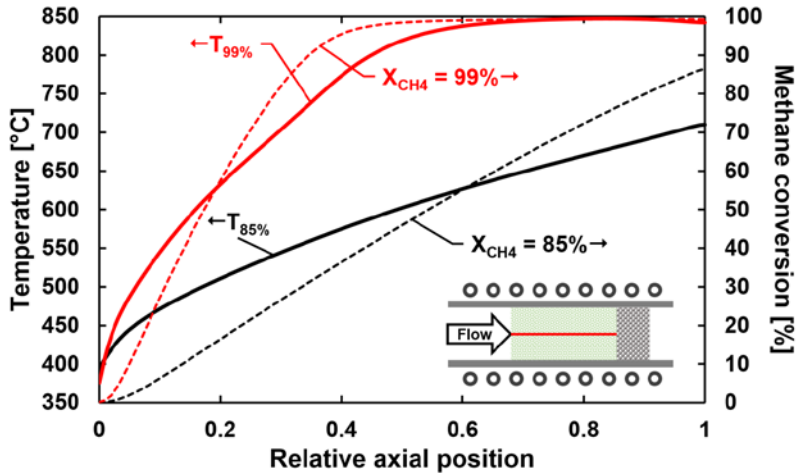
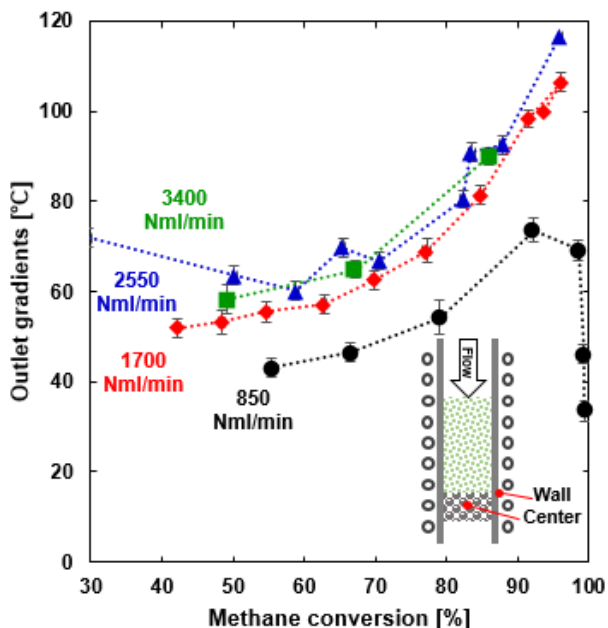


Figure 5.6: Curie temperature limitation Modelled axial temperature and conversion profile along the center displaying the curie temperature limitation. Both simulations at ambient pressure, 28 mT,  $\text{CH}_4:\text{H}_2\text{O}:\text{H}_2$  (30/60/10), 850 Nml/min and 2550 Nml/min.

Figure 5.6 shows the modelled temperature profile at a 28 mT magnetic field, for a flowrate of 850 and 2550 Nml/min. The latter reach 85% methane conversion, with a nearly linear temperature profile ending around 700°C. Decreasing the flow to 850 Nml/min, 99% methane conversion is achieved halfway through the reactor, where the temperature approach 850°C. At this temperature, the hysteresis area is practically zero (Fig. 4.7), and the temperature does not increase further. Towards the outlet it drops slightly due to increasing heat losses. Operating a reactor close to the Curie temperature decrease efficiency as it is effectively non-utilized reactor volume. This can be seen from the change in radial gradient evaluated at the outlet. Figure 5.7 shows the measured temperature difference between the catalyst center and the external wall temperature.



**Figure 5.7: Outlet gradients** Temperature difference between the hotter catalyst center and the external wall surface as a function of applied field. The gradient increase with temperature (ie. higher field). At high temperature, less heat will be generated at the center, relative to the wall, reducing gradients. The gradient is expected to be underpredicted, see explanation to Fig. 5.1. Experiments at ambient pressure, CH<sub>4</sub>:H<sub>2</sub>O:H<sub>2</sub> (30/60/10).

For higher flows, the measured radial gradient increase with applied magnetic field, following the temperature and conversion. For the flowrate of 850 Nml/min, the final data points corresponds to a conversion exceeding 98%, resulting in a declining gradient, because the higher temperature at the center results in a smaller effective hysteresis area due to the absence of endothermic reaction.

As heat is supplied directly to the catalytic nanoparticles, excellent thermal response can be achieved with hysteresis heating, providing enhanced reaction control.<sup>51</sup>

## 5. Induction heating

---

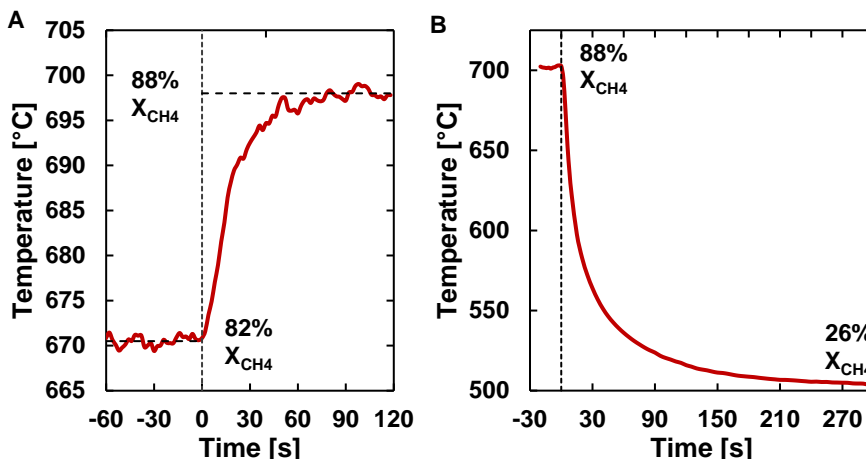


*Figure 5.8: Thermal response A) Temperature change when the coil current is increased. B) Temperature as current is reduced from 122A to 92A. The temperature initially drops quickly, as the endothermic reaction consumes heat. As the temperature decreases, reaction rate, and subsequent consumption of heat, drops. 3400 Nml/min, CH<sub>4</sub>:H<sub>2</sub>O:H<sub>2</sub> (30/60/10), ambient pressure.*

Figure 5.8A shows the measured outlet temperature for a change in applied magnetic field. A new steady state is reached in ca. 30 seconds, limited by the thermal mass of the system. Because the heat is applied directly to the catalytic site, the reaction is brought to equilibrium with the temperature. The small variations are related to fluctuations of the grid voltage.

Shutdown can be realized similarly fast, as seen in Figure 5.8B, where turning off the coil results in the temperature decreasing 200°C in ca. 2 minutes. The initial drop is facilitated by the endothermic reaction.

The thermal mass of the catalyst is orders of magnitude higher than the process gas, even at high pressures. Consequently, the higher the flow rate, the faster the reactor will reach operational temperature. The Curie temperature limitation can prevent overheating, but operating close to the limit decrease the efficiency.

### 5.4. Application of hysteresis heating

Low energy efficiency is the primary limitation for induction heating of SMR. The steep thermal gradient between the catalyst and the coil results in considerable heat losses, which is contributing to the heat that has to be

removed from the coil. If not removed, the strong temperature dependence of the conductivity for copper results in additional resistive losses, decreasing efficiency further. As the flow increases, the efficiency improves, as the heat loss through the insulation is nearly constant.

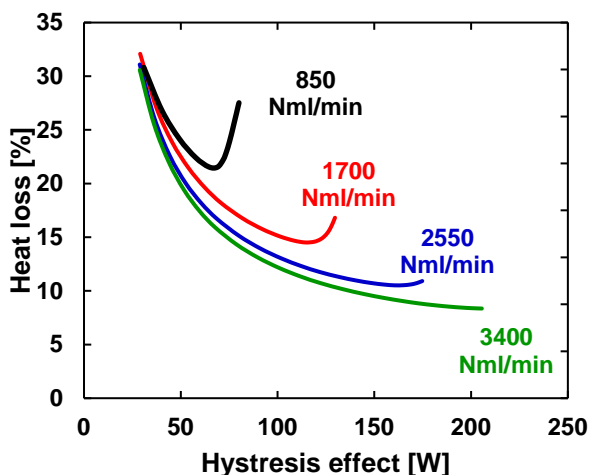


*Figure 5.9: Relative hysteresis heat loss Ratio of radial heat loss from the catalyst to the coil relative to the total effect supplied by hysteresis. Ambient pressure, CH<sub>4</sub>:H<sub>2</sub>O:H<sub>2</sub> (30/60/10).*

Increasing flowrate significantly reduce the relative heat loss. Figure 5.9 also shows the downside of operating close to the Curie temperature if it is higher than the equilibrium temperature. The efficiency improves as the conversion increases to the point where near full conversion is reached before the outlet. At this point, the reaction no longer consumes the supplied energy, causing the temperature to increase, consequently increasing heat losses. Increasing the flowrate further will equivalently improve the energy efficiency, however at the cost of increasing pressure drop.

Scaling the performance of the lab-scale setup based on the achieved 85% conversion at 3400 Nml/min, a reactor equivalent to an industrial capacity of 50.000 Nm<sup>3</sup> H<sub>2</sub>/h would require less than 2m<sup>3</sup> catalyst. The reactor volume can be reduced further by increasing the flow, but the increasing pressure drop will be detrimental unless larger catalyst particles are used. Increasing the scale of the hysteresis heated reaction can greatly improve the reactor efficiency as reactor volume scale steeper than losses in the coil.<sup>82</sup>

## 5. Induction heating

An obstacle for hysteresis heated steam methane reforming at industrial conditions is the temperature required to reach reasonable conversion at elevated pressure. The  $\text{Co}_{0.5}\text{Ni}_{0.5}$  spinel applied in this work has a Curie temperature of  $892^\circ\text{C}$ , but with a fast decaying hysteresis area above  $600^\circ\text{C}$ . At an outlet pressure of 30 bar, a temperature of  $750^\circ\text{C}$  (roughly the middle of the optimum and Curie temperature) only corresponds to 38% methane conversion at  $\text{S/C} = 1.8$ .

Increasing the cobalt/nickel ratio will yield a corresponding increase in the Curie temperature (Fig. 5.10).

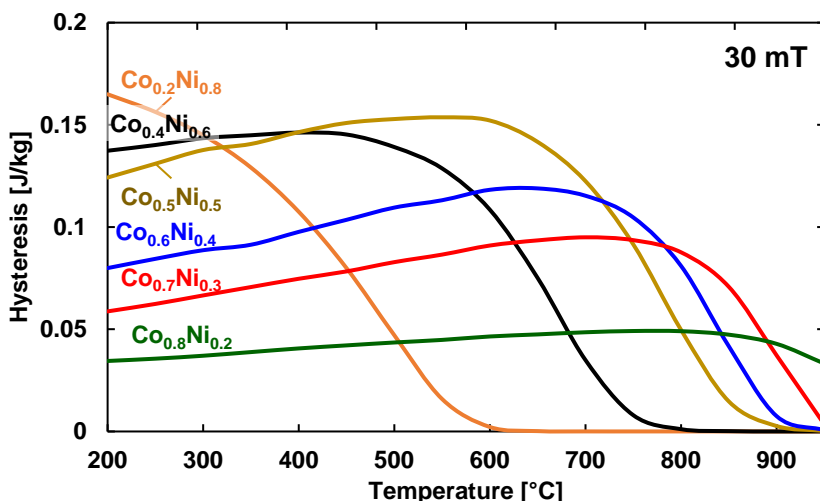


**Figure 5.10** Influence of Co/Ni ratio Hysteresis area for  $\text{Co}_x\text{Ni}_{1-x}$  catalysts at 30 mT. Increasing Co content increase Curie temperature, but reduce the hysteresis area. Catalysts synthesized by Morten Vinum (Topsoe/KU). VSM measurement by Mikkel F. Hansen (DTU). VSM analysis by Mads R. Almind (DTU).

As the cobalt content increases, the hysteresis area becomes less temperature dependent, indicating different temperature dependence on the sample coercivity. No steps are seen, indicating the Ni-Co alloy does not segregate. The highest hysteresis heating is observed for low cobalt content, which could indicate the higher coercivity of cobalt is limiting the accessible hysteresis area at moderate fields. The operational temperature range of a hysteresis heated reformer could be extended by utilizing high Ni/Co ratio particles near the inlet, and gradually transitioning towards high Co/Ni ratio towards the

outlet to achieve maximum hysteresis area as a function of the temperature profile.

While hysteresis heating can achieve full methane conversion for SMR at ambient pressure, the heat losses are detrimental to energy efficiency at small scale. Limiting Curie temperature prevents direct utilization at industrially relevant pressures for SMR. In perspective, the hysteresis heating based on the CoNi spinel is less appealing for large scale SMR due to the temperature requirements for reasonable conversion. A magnetic susceptor with a Curie temperature exceeding 1000°C, and ideally larger hysteresis area at moderate magnetic fields is required for hysteresis heating at industrial conditions.

That being said, delivery of heat directly to a catalytic site has an interesting potential for processes operating at lower temperatures than SMR. Delivering heat directly to the catalytic site may suppress some of the gas phase reactions that can be problematic with the steep thermal gradients of fired reformers.

Investigation into verification of temperature measurement and optimal layer structure for high temperature hysteresis heating is work in progress at the time of writing.

## 6. Resistance heating

There are many benefits available from an electrical supply of heat. Electrical heating is typically characterized by accurate thermal control, lower capital costs, and improved energy efficiency when compared to heat supplied by combustion.<sup>51</sup> Historically, direct conversion of fossil fuels has been the economically favorable solution in terms of operating costs and high achievable temperatures.<sup>7</sup> However, safe operation of combustion processes is associated with high capital costs, in part due to the extensive heat recovery required to reach high efficiency.<sup>22,33</sup>

This chapter explore the benefits of integrated resistance heating, and its application for industrial SMR. The results are based on experimental work on a laboratory-scale reformer (Chapter 2), and CFD modelling (Chapter 4). This chapter summarizes the primary results and conclusions of the work published (or to be) in Paper 1-3 (Appendix 9.1).

### 6.1. Experimental results

Precise thermal control is essential for the performance of endothermic reactions. With integrated electrical heating, the electric potential is uniformly converted to heat due to the resistivity of FeCrAl being practically independent of temperature.<sup>95</sup> Electrical heating is a *constant energy* heating mechanism. If heat is not continually removed, the temperature will rise until balanced by heat losses, opposed to heating by combustion or hysteresis, where the maximum temperature is restricted by the combustion- and Curie temperature, respectively. In the ideal SMR process, ca. 50-60% of the supplied energy goes into the reaction, while the rest is increasing the temperature of the process gas. This can be seen in the temperature profiles in Figure 6.1.

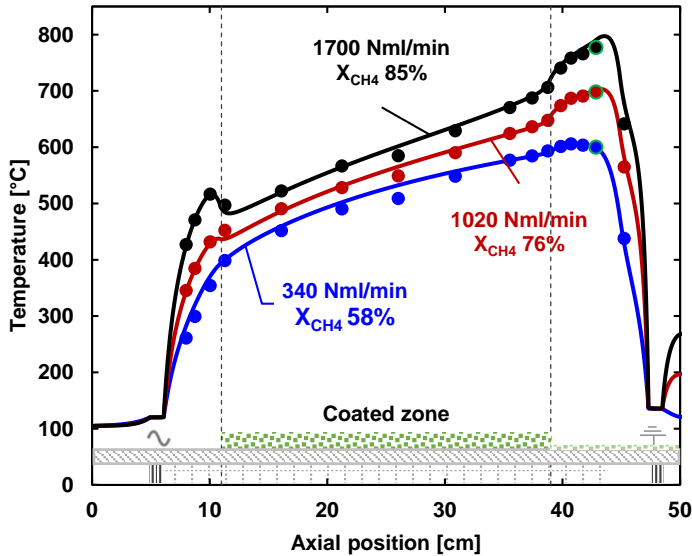


*Figure 6.1: Temperature profiles* Selected temperature profiles at different flows and conversions. Filled symbols represent measured values, solid lines the modelled profile. The last thermocouple in the residual catalytic region (peak temperature) is marked with a green border. Experiments performed at ambient pressure, 105 °C inlet temperature,  $\text{CH}_4:\text{H}_2\text{O}:\text{H}_2$  (30/60/10). The insert illustrates the different regions of the reactor, see Fig. 2.1.

The steep temperature gradient between the inlet copper socket and the coated zone (6-11 cm), shows how the supplied energy is heating the process gas. As the flowrate increase, a proportionally higher energy flux is required to obtain equivalent conversion, resulting in the gas being heated above the equilibrium temperature at higher flows (1700 Nml/min, 10 cm). The endothermicity of the SMR reaction is evident as the catalytic zone starts (11 cm), where the initial temperature slope changes drastically. For the pre-heated gas (1700 Nml/min), the temperature drops, as the endothermic reaction consumes more heat than locally supplied. Along the coated zone, the temperature profile is nearly linear, as the reaction constantly is kept near equilibrium by the available supply of heat. The second stretch of linear temperature profile (40-45 cm) is due to further endothermic reaction, but the steeper slope indicates it is kinetically limited. The kinetic limit is not unexpected as the residual layer is less than 5  $\mu\text{m}$  (Figure 4.3)

## 6. Resistance heating

---

For endothermic reactions, it can be beneficial from an operating perspective to express the approach to equilibrium (Eq. 4.8) as a temperature. For SMR (Reaction 1, Section 1), the approach to equilibrium temperature is calculated by subtracting the equilibrium temperature, calculated from the gas composition, from the actual temperature.

$$T_{app} = T_{exp} - T_{eq} \quad (6.1)$$

$$K(T_{eq}) = \frac{p_{CO}p_{H_2}^3}{p_{CH_4}p_{H_2O}} \quad (6.2)$$

Depending on the function used for the equilibrium constant, obtaining the equilibrium temperature can vary. The equilibrium temperature for SMR, based on a logarithmic fit of the equilibrium constant (Calculated in HSC 6.1), can be approximated as:

$$T_{eq} = -\frac{B}{\ln\left(\frac{p_{CO}p_{H_2}^3}{p_{CH_4}p_{H_2O}} \frac{1}{A}\right)} \quad (6.3)$$

$$A = 1.435e13[bar^2]$$

$$B = 2.703e4[K]$$

A process gas in equilibrium has an approach of zero degrees ( $\beta = 1$ ). A high approach temperature indicates more heat is supplied to the process gas, than can be consumed by the reaction, either due to mass transport or kinetic limitation. Figure 6.2 shows the approach temperature relative to the highest measured temperature (44.5 cm, Fig. 6.1), and the equilibrium temperature calculated from the GC measurements.

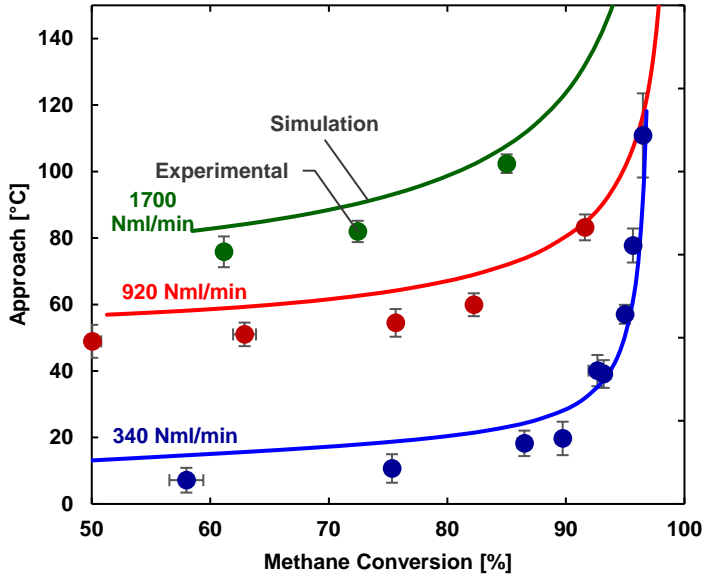


*Figure 6.2: Approach temperature for ambient reforming* Approach temperature calculated by subtracting the calculated equilibrium temperature from highest measured temperature ( $z = 44.5$ , Fig. 6.1). Symbols indicate experimental values, full lines are the model predictions. The linear part at low conversion indicate mass transfer limitation, while the exponential part indicate kinetic limitation. The vertical error bars indicate the standard deviation for the specific thermocouple.

At low conversion, the approach is nearly independent of conversion, but increases with flow, indicating external mass transfer limitation. As the conversion approaches unity, asymptotical behavior of the approach is observed, indicating a kinetic hindrance. The model slightly overpredicts the approach temperature at low conversion, but underpredicts as the conversion approaches unity. It is likely the activity towards the outlet is slightly too low in the model, and the deviation at high conversion is due to insufficient resolution of the gas chromatograph, as the methane fraction becomes increasingly small. Some deviation in the approximation of the equilibrium constant is also plausible.

## 6.2. Thermal gradients

Heat transport in a conventional fired reformer can be divided into three steps: Radiation from flame to reactor wall, conduction through reactor wall, and

## 6. Resistance heating

mixed conduction, convection, and radiation across the catalytic bed. The latter steps are limiting the catalyst performance, and gradients exceeding  $100^{\circ}\text{C}$  have been observed and predicted by modelling (Fig. 6.3A). The thermal gradients are a consequence of limiting thermal conductivity, and high heat fluxes. Modern reformers are highly optimized to provide the a high heat flux to every tubular reactor, while avoiding formation of hotspots.<sup>22</sup> Industrial tubular reformers typically contain more than 100 tubes, and operate at peak heat flux between  $60$  and  $150\text{ kW/m}^2$ .<sup>22–24,40,118</sup>

Integrated resistance heating removes the first step compared to conventional fired reforming, and as a consequence, the requirement of a large furnace. The thermal conductivity of the materials is comparable, but the shorter length scale, ca. three orders of magnitude, limits the thermal difference across the catalyst (Fig. 6.3B).

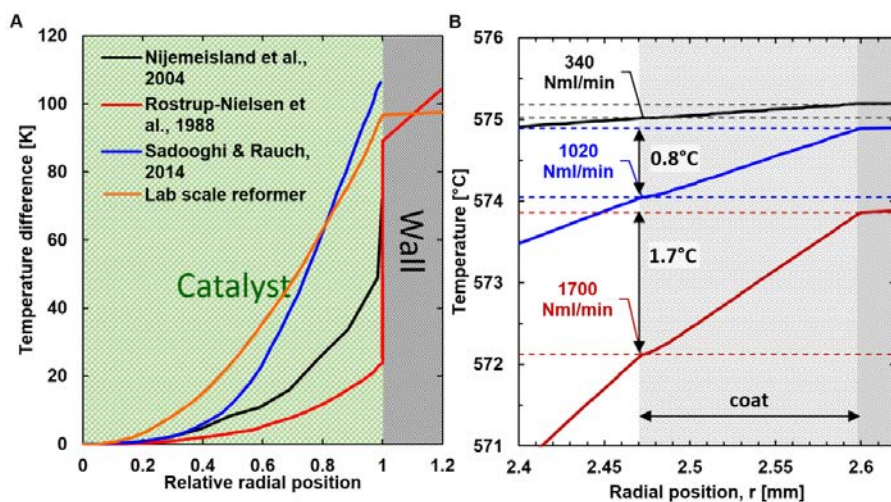


**Figure 6.3: Temperature profile across catalyst** A) Radial temperature profiles across packed bed catalyst for SMR reactors coat<sup>119–121</sup> (Lab scale model in Appendix 9.5). The temperature difference relative to the reactor center is used, as the absolute temperature depends on operating conditions. All predict a thermal difference exceeding  $100\text{K}$  between the wall and center of the catalyst. The data by Rostrup-Nielsen is based on experimental measurement<sup>120</sup>. B) Modelled temperature profiles across the catalytic washcoat. Simulation conditions:  $105^{\circ}\text{C}$  inlet, ambient pressure,  $\text{CH}_4:\text{H}_2\text{O}:\text{H}_2$  (30/60/10). Evaluated at 35, 27.5, and 22.5 cm for 340, 1020, and 1700 Nml/min respectively – See Fig. 6.1. Reproduced from<sup>97</sup>.

Depending on size and shape of the catalyst pellets, an insulating gas film can be formed at the internal reactor wall, due to the locally higher porosity

(Section 4.2).<sup>110,120</sup> Similar steep gradients are present in the resistance-heated reformer, but only in the gas phase, and correlated to the velocity flow profile. Compared to a reactor heated externally, integration of the heat source effectively remove internal temperature gradients across the reactor wall. A thermal gradient is formed across the catalytic washcoat, but displaying a temperature difference less than 2°C, at a flowrate of 1700 Nml/min and 85% methane conversion. In comparison to conventional fired reforming, reactor performance is not limited by thermal conductivity across the washcoated catalyst as the catalyst is nearly isothermal (at a given axial position). The temperature difference is directly correlated to the supplied heat flux (Supplementary Figure S9.3.8).

Because the resistivity of FeCrAl is nearly independent of temperature, the supply of heat is uniform in the reactor wall, consequently generating a near constant inward heatflux (Fig. 6.4).<sup>95</sup>

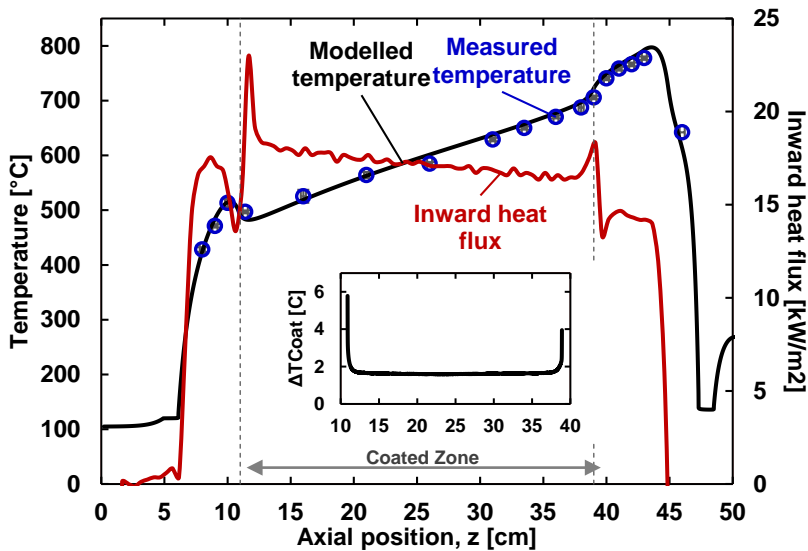


*Figure 6.4: Flux profile and thermal gradient Measured and modelled temperature profile with calculated inward heat flux profile. The insert shows the temperature difference across the reactor wall and catalytic washcoat. 1700 Nml/min, 85% Methane conversion, ambient pressure.*

The gentle slope of the inward heat flux in the coated zone is due to increasing heat loss through the insulation as the temperature increases (Fig. 6.4). Peaks in the heat flux at the ends of the coated zone is due edge effects of the

## 6. Resistance heating

---

catalytic washcoat, yielding locally higher reaction rates. The thermal difference across the catalytic washcoat is practically constant as external mass transport limits the reaction at the surface, balanced by the uniform supply of heat. The thermocouple at 26.2 cm was a shielded thermocouple, and the lower temperature may indicate it is not in direct contact with the reactor wall (Supplementary Figure S9.3.1).

The inherent uniform heat flux of resistive heating is a substantial advantage compared to fired heating, enabling enhanced reaction control. Uniform heating removes the risk of hotspots, and the adverse side effects they can cause, such as deposition of carbon and thermal stress. Better thermal control enables operating at higher temperatures than practical for a fired reformer, and closer to carbon deposition limits. This is further elaborated in Section 6.5.

### 6.3. Catalytic effectiveness factor

Operating at high efficiency is critical for industrial processes. To deliver sufficient inward heat flux, the combustion in a fired reactor must occur substantially higher temperatures than the reaction. Combustion of methane at ambient pressure reaches ca. 1400°C, which depending on reactor, results in a flue gas leaving the primary reformer around 1000°C.<sup>23</sup> As the flue gas is the single largest stream in an SMR plant, it limits energy efficiency of the primary reformer to ca. 50%, without extensive heat recovery.<sup>22,23,40</sup> In contrast integrated electrical heating can reach near full efficiency, as all generated heat is supplied to the process gas (barring small losses through insulation and external electrical resistance). It should be noted, when accounting for export of steam, that conventional SMR plants operate at more than 90% energy efficiency.<sup>22,29</sup>

Utilization of the catalyst can be expressed by the catalytic effectiveness factor,  $\eta_{cat}$ , which is the observed rate divided by the intrinsic, ie. without internal mass- and heat transfer limitations (equivalent to the Thiele Modulus). For a slab, it can be calculated by dividing the bulk rate, with the surface rate:

$$\eta_{cat} = \frac{\int_0^{\delta} R_{CH_4}(r) dr}{\delta_{coat} \cdot R_{CH_4}^{surface}} \cdot 100\% \quad (6.4)$$

Equation 6.4 calculates  $\eta_{cat}$  at a given axial position. For evaluation of the effectiveness factor for the entire reactor, the axial position is included in an additional integral.

At conventional industrial conditions,  $\eta_{cat}$  is less than 5%, resulting in reactor performance scaling with catalyst surface area rather than catalyst volume.<sup>22</sup> Higher surface area can be achieved by intricate shapes or smaller dimensions, the latter quickly increasing the pressure drop (Eq. 4.16). Large pressure drops are unfavorable due to the additional compression costs, limiting mechanical properties, and the additional fuel required to accommodate the thermodynamics. If  $\eta_{cat}$  is calculated based on average temperature of the process gas, it might be underpredicted for a packed bed, due to the steep thermal gradients (Fig. 6.3A), as the reaction kinetics are exponentially dependent on temperature.

Because there is practically no temperature difference across the catalytic washcoat, catalytic effectiveness factor depends on internal diffusion (Fig. 6.5).

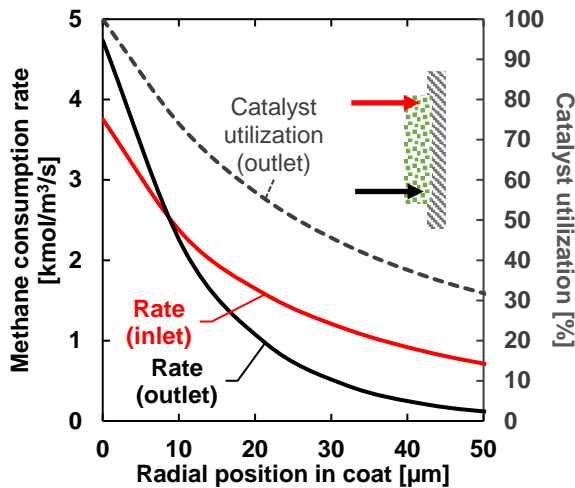


**Figure 6.5: Radial reaction rate** Reaction rate for methane consumption across the catalytic washcoat evaluated near top and bottom of the catalytic section (5 mm from either edge). Only the outermost 50 of 128  $\mu\text{m}$  of the coat is shown. Simulation at ambient pressure,  $\text{CH}_4:\text{H}_2\text{O}:\text{H}_2$  (30/60/10), 1700 Nml/min, and 85% methane conversion.

## 6. Resistance heating

Figure 6.5 shows the reaction rate evaluated across the catalytic washcoat. 90% of the reaction is carried out within 75  $\mu\text{m}$  of the coat at the inlet, and 20  $\mu\text{m}$  at the outlet. As the temperature increases, the exponentially dependent reaction rate converts more near the surface, decreasing catalyst utilization towards the outlet. By reducing washcoat thickness, the redundant catalyst is removed, directly increasing  $\eta_{cat}$  (Fig. 6.6).

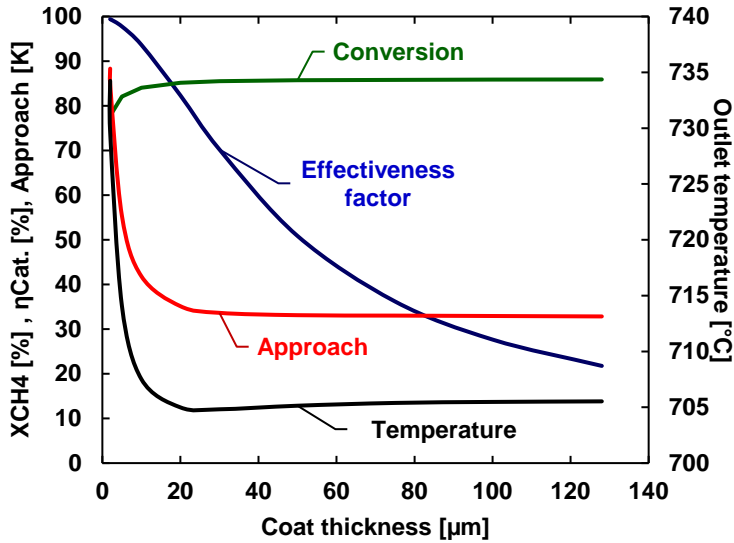
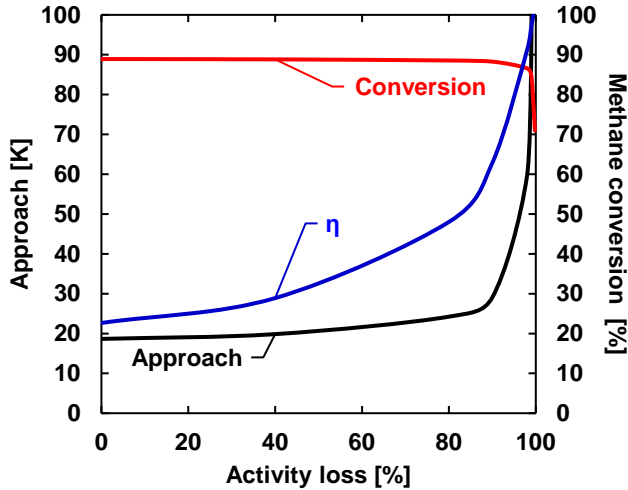


Figure 6.6: Influence of washcoat thickness Methane conversion, effectiveness factor, approach towards equilibrium and outlet temperature as a function of coat thickness. Simulations at 1700 Nml/min, ambient pressure,  $\text{CH}_4:\text{H}_2\text{O}:\text{H}_2$  (30/60/10).

Based on the implemented model, the coat thickness can be reduced to 30  $\mu\text{m}$  without influencing the reactor performance. Further reduction results in insufficient catalytic activity, initially near the inlet resulting in slightly higher temperatures required to reach equivalent conversion. Eventually, insufficient intrinsic activity is available, resulting in a steep increase in the approach to equilibrium. Because electrical heating is constant energy (Section 6.1), an initial deficiency in catalytic activity, will increase the temperature along the entire reactor (Supplementary Figure S9.3.9).

A disadvantage of operating with a high catalyst efficiency is the susceptibility to loss of activity by deactivation, such as sintering or

poisoning. Excess coat thickness can serve as a buffer in case of lost activity (Fig. 6.7).



*Figure 6.7: Catalyst deactivation* Approach to equilibrium temperature as a function of catalyst deactivation, modelled by reducing the pre-exponential activity factor. As the intrinsic activity drops, more of the coat is utilized, resulting in higher effectiveness factor. Eventually insufficient activity results in detrimental temperature increase and drop in conversion.

Assuming uniform deactivation of the catalyst (such as sintering), more than 80% of the catalyst surface area can be lost, without reduced methane conversion (Fig. 6.7). The required temperature (approach) slightly increases as internal diffusion starts to limit the reaction. With uniform deactivation of the catalyst, most of the reaction can no longer be carried out near the surface, resulting in an increasing catalyst effectiveness factor. Around 90% loss of initial activity, the temperature sharply increases, leading to an increased risk of carbon deposition, and loss of conversion, due to insufficient residual activity.

Operating with a very thick coat can provide good resistance to deactivation, but at a loss of reactor performance, as an equivalent increase in linear gas velocity is required if the metal structure is unchanged.

With a 30  $\mu\text{m}$  coat, a catalytic effectiveness factor of 75% is predicted, reducing the required amount of catalyst by nearly two orders of magnitude, relative to conventional fired plants. This decreases thermal limitations

## 6. Resistance heating

further, and makes less abundant catalysts with higher intrinsic activity and better carbon resistance, such as Ru or Rh an attractive approach.<sup>22,122</sup>

### 6.4. Transient response

Safe start-up procedure for conventional tubular reformers can take several days, to avoid formation of hotspots, catalyst deactivation, or mechanical stress from thermal expansion.<sup>22,123</sup> Uniform flow, and small (radial) thermal differences, enables fast thermal response of an electrically heated reformer. Figure 6.8 shows the measured temperature and methane fraction for instantaneous perturbations of applied voltage.

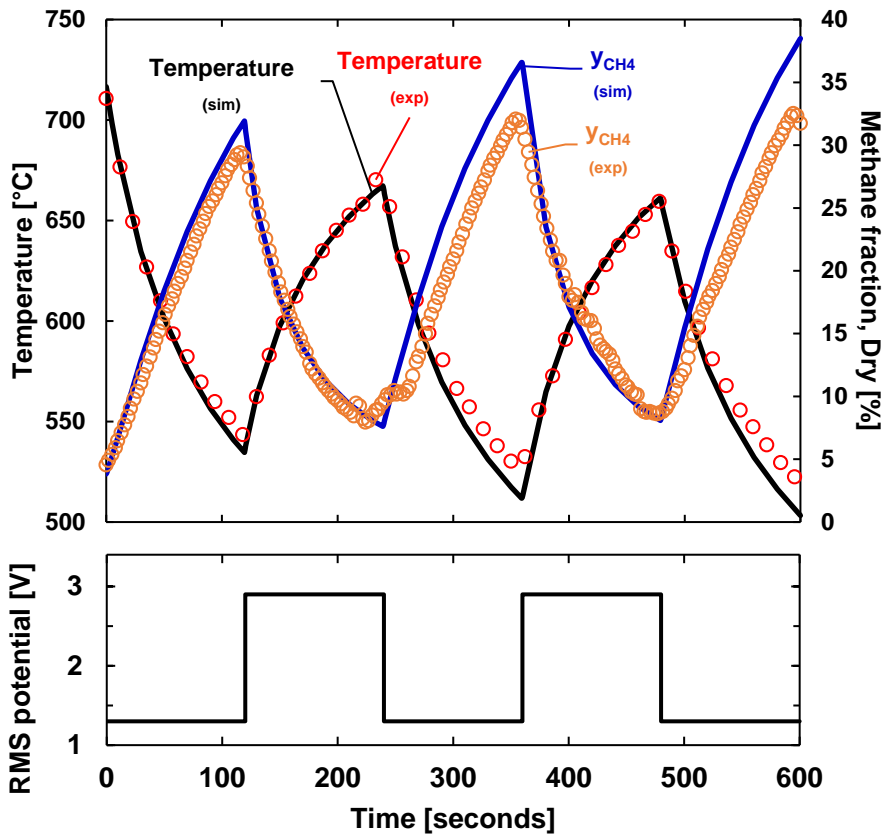


*Figure 6.8: Transient thermal response A) Measured outlet temperature ( $z=44.5$ ) and wet methane fraction compared to model predictions. Ambient pressure, 680 Nml/min, S/C 2, 10%  $H_2$  in feed, 20-85% methane conversion. The MS signal is correlated to GC calibrations of dry methane composition. The MS signal is shifted to account for delay in tubes. B) Applied potential (RMS).*

The peak temperature (0, 240, 480 seconds) decreases, indicating the reactor does not reach thermal equilibrium within 2 minutes, though this is mainly contributed to the insulation rather than the thermal mass of the reactor wall and process gas. The increasing deviation between measured and modelled methane fraction is correlated to the equivalent deviation in temperature. The temperature deviation is within 2°C at the high temperatures, and up to 23°C at low. The cause can be related to incorrect reaction kinetics (less active at low temperature), or incorrect material parameters, such as heat capacity, thermal conductivity, or emissivity.

Cooling of the reactor is to a large extent due to the endotherm reaction, consuming the latent heat of the reactor wall. Below 500°C, the reaction rate is insufficient ( $X_{\text{CH}_4} < 20\%$ ) to substantially influence the energy balance, and cooling will proceed by external and convection losses.

The reaction onset can be seen in Figure 6.9, where initial heating is independent of catalytic activity.

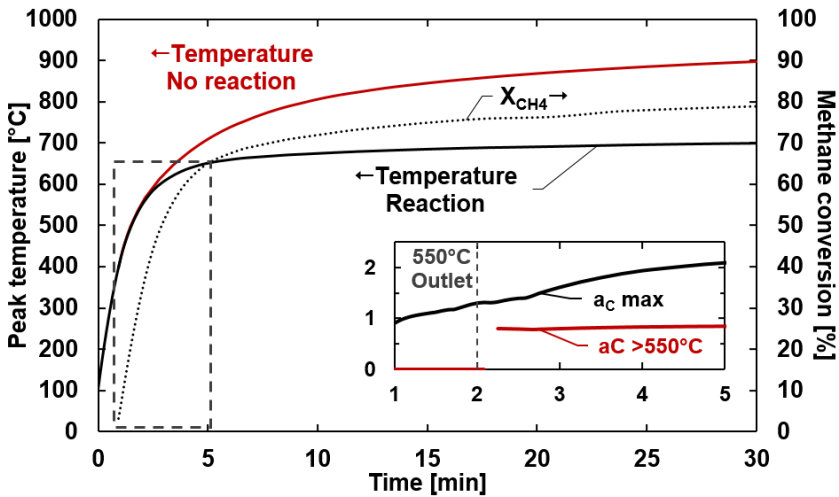


**Figure 6.9:** Transient response to cold start Modelled maximum temperature as a function of time, starting from 100°C at ambient pressure, directly applying operating potential equivalent to 85% methane conversion at 680 Nml/min, S/C 2. Red line indicates the temperature without catalytic activity. Insert shows peak carbon activity for the first 5 minutes. Carbon activity never exceeds unity in the catalytic region above 550°C, required for deposition of graphitic carbon.

## 6. Resistance heating

---

At fixed power, the catalytic reaction will reduce steady state temperature by ca. 100°C (at ambient conditions), compared to an inactive catalyst. Based on simulations, less than 7 minutes is required to reach within 95% of steady state temperature, but around 15 minutes for conversion. The characteristic timescale for thermal equilibrium across the insulation is ca. 3 hours. Characteristic timescales are elaborated in section 4.5.

The simulations indicate it is possible to heat the reactor within minutes, without increased risk of carbon deposition during heating. Scaled to industrial conditions, assuming ideal insulation, steady state for 90% methane conversion is predicted to be achievable within 3 minutes. Temporal response on a timescale in minutes provides the opportunity for reactor design aimed at flexible operation, utilizing the intermittent excess of renewable energy. This could either be exclusively operating during excess production, or by increasing flowrate (Fig. 6.2). Realization of an intermittent reactor requires every other unit operation required for SMR (Fig. 1.2) to be equally flexible.

Further work is required regarding catalytic and mechanical stability of the catalytic washcoat. Preliminary experimental work did not show quantifiable deactivation, despite exposure to atmospheric air (at room temperature, Supplementary Figure S9.3.10). The absence of observed catalytic deactivation may be related to the excess washcoat in the experiments, as described in section 6.3, or that overall kinetic activity remains high enough that mass transport remains limiting.

### **6.5. Scaling to industrial conditions**

Most reactions utilizing syngas (FT, MeOH, NH<sub>3</sub>) benefit from elevated pressure, though the thermodynamics of SMR is adversely impacted, it is economically favorable to minimize compression of the plant.

Typical conditions for conventional fired SMR is ca. 30 bar, increasing the temperature required to reach 75% conversion (at S/C 1.8) to 900°C, 200°C more than ambient pressure (Fig. 6.10).

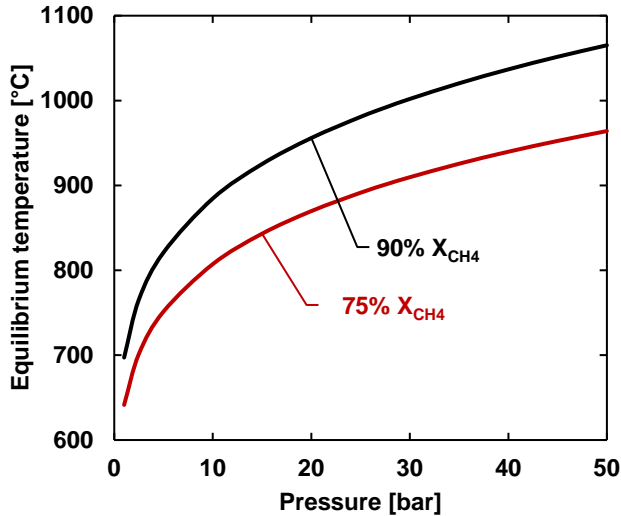


*Figure 6.10: SMR pressure dependence* Equilibrium temperature required to reach 75 and 90% methane conversion for SC 1.8 as a function of pressure. Calculations based on empirical equilibrium constants reported in literature (5). Figure reproduced from<sup>97</sup>.

Higher conversion require even higher temperature, which is typically limited by material properties for conventional fired reformers, where the tubular reactors support a 30 bar pressure difference at very high heat flux.

The steam content (S/C) is used to control carbon risk and product composition. High S/C yields a high H<sub>2</sub>/CO ratio, desirable for the production of hydrogen. For low temperature Fischer-Tropsch a H<sub>2</sub>/CO ratio of 2 is preferable, while the optimum for methanol is given at  $(\text{H}_2 - \text{CO}_2)/(\text{CO} + \text{CO}_2) = 2$ .<sup>22,31</sup>

Deposition of solid carbon typically proceeds through one of three reactions: thermal decomposition of methane, the Boudouard reaction, or reduction of CO:



## 6. Resistance heating

---

The carbon activity can be expressed based on the equilibrium constant. For Eq. 6.6 the equilibrium equation is defined in Eq. 6.9, and the carbon activity in 6.10:

$$K_{eq} = \frac{a_c p_{H_2}^2}{p_{CH_4}} \quad (6.9)$$

$$a_c = \frac{K_{eq} p_{CH_4}}{p_{H_2}^2} \quad (6.10)$$

Operating at high S/C ratio is less efficient, as heating of additional steam that does not participate in the reaction, increases the consumed energy. The catalytic reaction efficiency can be defined as:

$$\eta_{Reaction} = \frac{\Delta H_{out}^\circ}{\Delta H_{out}} \quad (6.5)$$

Where  $\Delta H_{out}^\circ$  is the enthalpy at standard conditions (1 atm, 25°C), and  $\Delta H_{out}$  is the enthalpy at the outlet temperature. This provides a measure of the energy supplied to drive the reaction, and energy supplied to heat the process gas. As the S/C ratio decreases, a smaller volume of excess gas is heated, however, higher temperatures are required to reach equivalent conversion. Figure 6.11 shows the reaction efficiency (Eq. 6.5) as a function of methane conversion and S/C ratio, and how it reduces the threshold for carbon deposition.

As S/C decreases, higher temperatures are required to reach equivalent conversion according to Le Chateliérs principle. At high conversion (>75%) there is no potential for carbon deposition if the approach temperature is below 50°. For decreasing S/C, the region where there is a risk for carbon deposition increases. Keeping the approach below 20° should prevent deposition of carbon, even at S/C = 1.

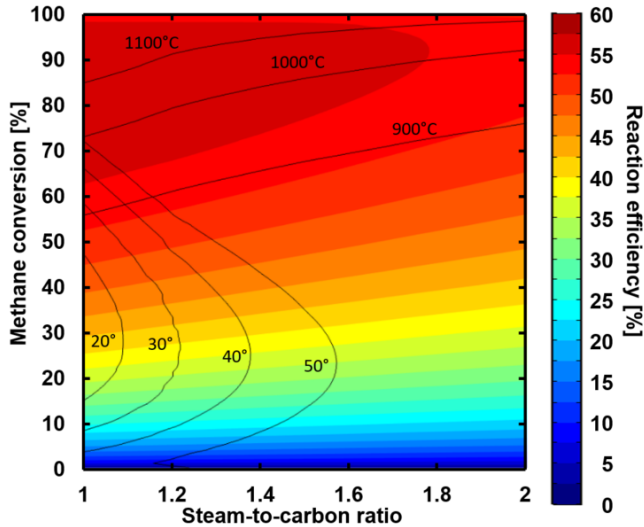


*Figure 6.11: Reaction efficiency and carbon deposition limits Thermodynamic reaction efficiency as a function of S/C and methane conversion calculated at 30 bar. Equilibrium temperature at 900-1100°C included. The regions for  $ac > 1$  as a function of the approach temperature is shown for 20-50° relative to graphitic carbon. The plot is based on calculations in HSC 6.1.*

If the process gas is far from equilibrium, eg. high approach temperature, the thermodynamic carbon potential increases. However, it is possible to operate with a thermodynamic potential exceeding unity, as long as the reaction kinetics for the SMR reaction is substantially faster than for carbon deposition. At temperatures below 600-650°C, the reaction rate for carbon deposition is generally negligible, which is crucial in case the gas is heated significantly above equilibrium, as is typically the case for industrial reformers, where the gas is pre-heated to reduce the volume of the primary reformer.<sup>22</sup>

The approach temperature for the resistance-heated reformer and how it correlates to the thermodynamic carbon potential is illustrated in Figure 6.12.

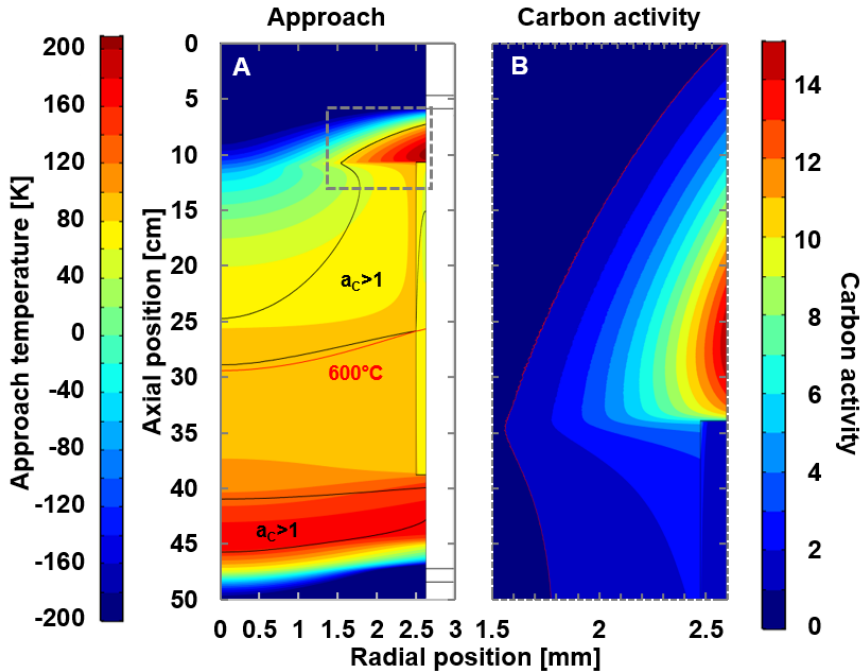


Figure 6.12: Temperature dependent carbon activity A) Modelled approach temperature for the resistance-heated reformer. The black lines indicate the domain where the thermodynamic carbon activity exceeds one, and the red line where the temperature exceeds 600°C. The dotted line highlights the region with the highest carbon activity. B) Magnification of the area with the highest carbon activity. Simulation at 1700 Nml/min, CH<sub>4</sub>, H<sub>2</sub>O, H<sub>2</sub> (30/60/10), ambient pressure, 85% methane conversion.

The process gas enters the reactor at a negative approach temperature due to the absence of CO. The gas is rapidly heated in the initial region without catalyst, leading to the process gas temperature significantly exceeding the equilibrium temperature. This initial heating could also be seen in the temperature profile in Figure 6.4. A second region of high approach occurs near the outlet, where the catalytic activity was insufficient. In both regions, the high approach leads to an increased risk for carbon activity, as predicted in Figure 6.11. Looking at the inlet region near the top of the coat (Fig. 6.12B), it can be seen how the carbon activity greatly exceeds unity above the catalyst, and how the proceeding reaction quickly suppress the carbon potential in the catalytic washcoat.

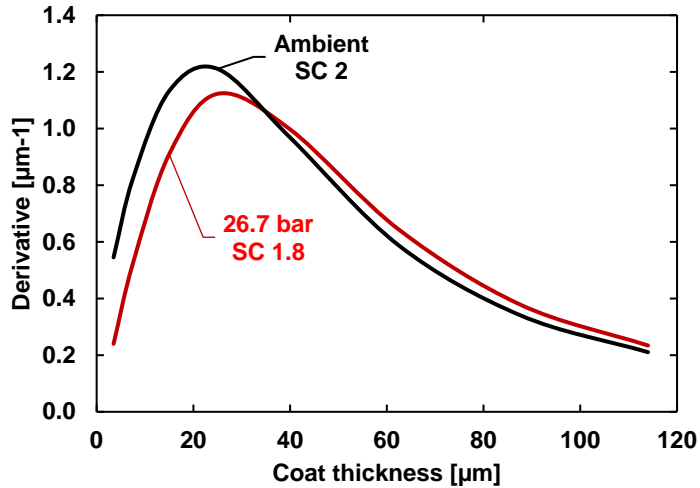
To have detrimental deposition of (graphitic) carbon, three conditions must be met: thermodynamic carbon activity exceeding one, sufficient temperature

to facilitate reaction ( $>600^{\circ}\text{C}$ ), and faster forward than reverse reaction.<sup>22,124</sup> With an  $S/C = 2$ , there is little risk of carbon formation, despite the carbon activity exceeding one, near the inlet of the lab scale resistance-heated reformer, due to insufficient temperature (Fig. 6.12A). A high carbon activity is also present near the outlet (inferred from the high approach temperature), however primarily in the gas phase, where homogenous formation of carbon is highly unlikely. Temperature and thermodynamics predict risk of carbon deposition on the residual coat near the outlet, however, no carbon was observed upon visual inspection of the reactor after experiments. It is possible formed carbon was removed during cooling of the reactor, as the approach temperature decreases at lower temperatures or flowrates.

Increasing flowrate results in higher heat flux and steeper thermal gradients, corresponding to increasing carbon deposition potential. The carbon deposition “hotspot” in Figure 6.12 (at the beginning of the coat, 11 cm), is due to pre-heating of the gas above its equilibrium temperature. A process gas with  $S/C > 1$  should never have a thermodynamic potential for carbon deposition if the approach temperature remains below  $20^{\circ}$ . Without pre-heating the gas, the initial “hotspot” can be circumvented entirely, removing the initial risk of carbon deposition, which may occur at industrial conditions due to the higher operating temperature (due to pressure).

### **Upscaling the ambient model**

Relevant material parameters of the solid materials are practically independent of pressure. Reaction kinetics are the most influenced, but implemented as a function of partial pressures. Bulk diffusion is inversely proportional to pressure, however, the same holds for linear velocity. Assuming the thermal molecular conductivity of the gas phase is independent of pressure and correct kinetic parameters, the model verified for ambient conditions can be extended to industrial conditions, where most results are comparable as seen in Figure 6.13.<sup>125</sup>



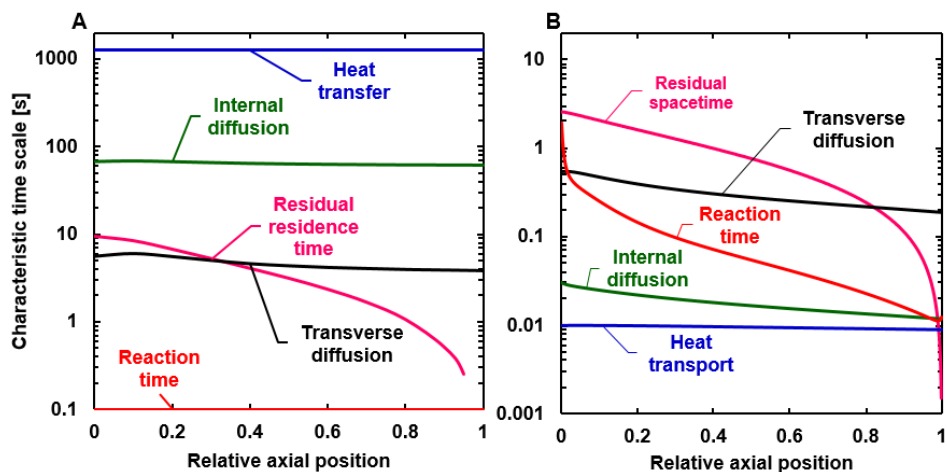
*Figure 6.13: Ideal coat thickness* Optimal effectiveness factor increase as a function of reduced coat thickness. Taken as the derivative of the effectiveness factor in Figure 6.6 relative to coat thickness

Figure 6.13 shows the optimal improvement of coat thickness at ambient and industrial conditions. The small deviation is primarily due to the diffusion being weakly dependent on temperature, increasing mass transfer rates with increasing temperatures. As the catalyst effectiveness reaches 100% near the inlet, the relative improvement decreases correspondingly.

Based on strong verification of the ambient model, extrapolation to industrial conditions is expected to provide reasonable estimates of the possibilities explored in the following sections.

### 6.6. Process intensification

Each step of a heterogeneous reaction cycle can be limiting for the performance of the overall reaction (Figure 4.9). For industrial endothermic processes, transport of heat is often the limiting phenomena. Characteristic timescale analysis allows comparison between the different reactions steps and phenomena, and can be used to assess the limiting order (Section 4.4). Figure 6.14 shows the different characteristic timescales evaluated across the catalysts for a conventional fired reformer and a simulation of the resistance-heated reformer at industrial conditions.



**Figure 6.14: Characteristic timescales.** A) Top-fired industrial reformer with a packed bed. 829°C outlet, 30 bar outlet,  $SC = 3.0$ , 3500 GHSV, 120 mm internal diameter, 71.2% methane conversion. Data for comparison based on<sup>23</sup>. B) Electric reformer at industrial conditions, 465°C inlet, 27.7 bar outlet,  $SC = 1.8$ , 6235h<sup>-1</sup> GHSV, 5.3 mm internal diameter, and 90% methane conversion. Figure reproduced from<sup>97</sup>.

As seen from Figure 6.14A, the characteristic timescale for heat transfer in conventional industrial reformers is more than an order of magnitude above the other phenomena, corresponding to the steep thermal gradients observed (Fig. 6.3A). The characteristic heat transfer is based on the average process gas temperature, and the model for thermal conductivity of a packed bed introduced in Section 4.2, accounting for turbulence. The next limiting phenomena is internal diffusion, which is approximated based on spherical pellets, 5.4 mm in diameter, assuming diffusion parameters are equivalent to those used in the induction-heated model (Section 4.2). A high characteristic timescale for internal diffusion further amplifies the low effectiveness factors typically observed at industrial conditions, and explains how observed catalytic activity scales with surface area rather than volume. The transverse diffusion does not include turbulence, and is likely predicted more limiting than in reality, however, the ratio between the residence time (assuming plugflow) and transverse diffusion, indicates limited radial mixing of the process gas. The low reaction time, estimated based on average process gas composition and the reaction kinetics introduced in Section 4, indicates a large surplus of available catalytic activity, and a reaction operated far from equilibrium.<sup>23,83</sup> There is a significant uncertainty coupled to the reaction

## 6. Resistance heating

---

time, as the steep radial temperature profiles in industrial reformers result in a large variation in reaction rate and concentration. Figure 6.14A is based on the radial average of temperature and concentration, and is likely underpredicted relative to the most reactive part near the internal wall.

The resistance-heated washcoat is in stark contrast to the conventional reformer, as heat transfer is the least limiting mechanism (Fig. 6.14B). Overall, the order of the limiting phenomena is practically inversed. This is primarily a consequence of the different catalyst configuration, changing the lengthscale for heat transfer by three orders of magnitude. The high timescale for transverse diffusion shows that external mass transfer is limiting for the majority of the reactor length, as predicted based on Figure 6.2. Shorter lengthscale for internal diffusion (coat thickness) alleviates limiting internal mass transfer. Near the inlet, the reaction time is limiting due to too low temperatures to achieve the sufficient catalytic activity to drive the reaction to equilibrium.

The characteristic timescale for transverse diffusion depends on the characteristic lengthscale and the diffusion rate. The bulk diffusion rate is dependent on pressure and temperature, however, economics and practicality limit the flexibility of those parameters. If turbulence could be achieved, at the expense of additional pressure drop, mass transfer would be less limiting. However, it is practically impossible to achieve turbulent flow in narrow pipes. Alternatively, the characteristic length scale for external diffusion (transverse) can be changed, by reducing the internal diameter of the tube (Fig. 6.15).

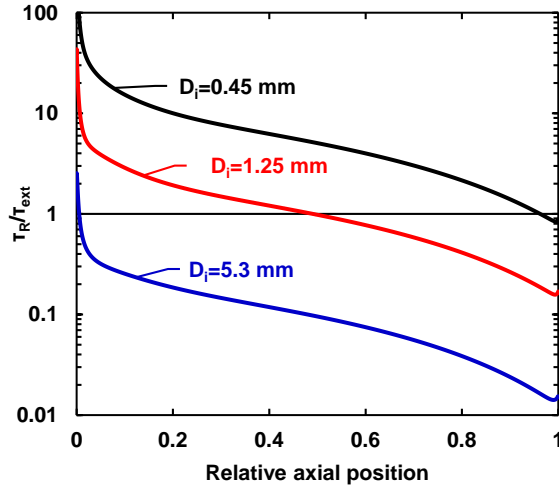


*Figure 6.15: Influence of reactor dimensions. Ratio of characteristic reaction time to bulk diffusion for 0.45, 1.25 and 5.3 mm internal diameter for  $L = 50$  cm. Outlet temperature of  $1015^{\circ}\text{C}$ ,  $27.7$  bar, SC 1.8, and  $290$  kJ/mol  $\text{CH}_4$ .*

By reducing the internal diameter, the diffusion path from bulk to washcoat becomes shorter, consequently reducing the transverse mass transfer limitation. Figure 6.15 shows the ratio of the reaction time to the transverse diffusion (Equivalent to the diffusive Damköhler number).<sup>111</sup> At values exceeding unity, reaction rate is limiting, and external diffusion when below. As apparent from Figure 6.15, at 5.3 mm internal diameter, transverse diffusion is limiting for the entire reactor. By reducing the internal diameter to 1.25 mm, the reactor is initially limited by reaction rate, but as the temperature increase along the reactor, the transverse diffusion is limiting towards the outlet. At an internal diameter of 0.45 mm, the reaction rate is limiting along the entire reactor, with bulk diffusion and reaction rate balanced at the outlet, equivalent to the findings of previous studies.<sup>126,127</sup> This yields on optimum for reactor performance, independent of reactor length (Fig. 6.16).

## 6. Resistance heating

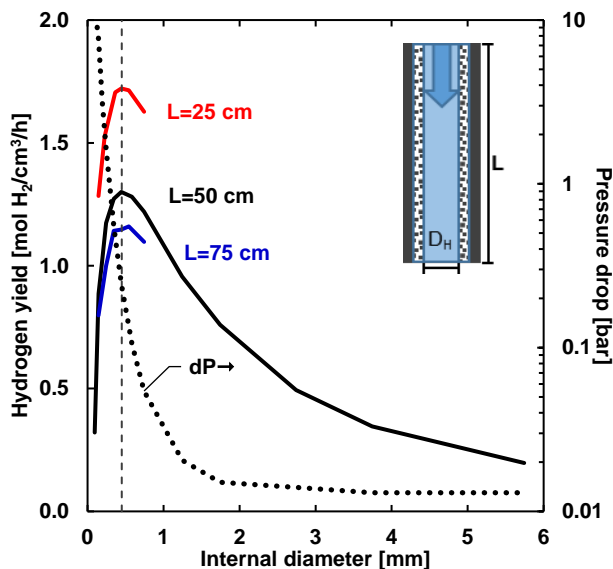


*Figure 6.16: Optimum reactor diameter* Modelled hydrogen yield as a function of internal diameter and reactor length. Outlet temperature of 1015°C, 27.7 bar, SC 1.8, and 290 kJ/mol  $CH_4$ .

An optimum is found where the reaction rate is equivalent to the bulk diffusion rate near the outlet, resulting in the reactor being limited by intrinsic activity. The optimal diameter is independent of reactor length because the boundary conditions specified in the model results in a nearly identical temperature profile. However, shorter reactors can provide a higher yield per volume, due to the smaller pressure drop, as it is proportional to reactor length.

As the internal diameter is reduced further than 0.45 mm, the performance declines, as the residence time becomes limiting due to high linear gas velocities, and large pressure drops, suppressing the reaction at the inlet.

Based on the simulations, an ideal 50 cm reactor with an internal diameter of 0.45 mm would yield 1.3 mol  $H_2/cm^3/h$ , calculated based on a 128  $\mu m$  coat, and including a 0.35 mm reactor wall. Assuming it could be manufactured reproducibly, and operated with similar uniform current density, a reactor equivalent of 100.000  $Nm^3 H_2/h$  would only be 3.6  $m^3$  (Not including wiring, insulation, power supply, etc.) For comparison, the furnace chamber for an

industrial, top-fired reformer producing 100.000 Nm<sup>3</sup> H<sub>2</sub>/h is ca. 3200 m<sup>3</sup>, yielding a difference of nearly three orders of magnitude in reactor volume.<sup>23</sup>

However, the optimal reactor from a performance perspective is practically unfeasible when considering preparation and operation requirements. A well-defined structure is required for uniform current density. In addition, application of coat and impregnation must be uniform. When scaling, consideration regarding electrical connections is critical, and these and external wiring must be able to support the high currents required to reach the necessary heat flux (Supplementary Figure S9.3.8).

Despite “optimal” conditions might not be achievable, a reduction of furnace volume exceeding two orders of magnitude is not unrealistic, and while the reactor is limited by external mass transfer, the additional control from resistance heating still enables operation beyond the constraints of conventional reformers, in terms of lower S/C ratios and higher outlet temperatures.

### **6.7. Industrial applications**

There are several benefits to resistance-heated reforming. The integration of the heat supply improves energy efficiency substantially, and removes the thermal gradients, limiting conventional fired reformers. The inherent uniform supply of heat provides improved reaction control, and consequently enables operation closer to thermodynamic constraints (carbon) and at temperatures exceeding what is practical in conventional tubular reactors. These effects combined intensifies the process, and enables industrial quantities in reactors two orders of magnitude smaller than fired reformers. In all, a very promising technology, if not now, then increasing economically competitive. This section aims at, briefly, proposing opportunities arising when implemented into industrial applications.

The most straightforward approach is replacing current fired reformers with electrically heated in industrial plants. The flowsheet of a typical fired plant was shown in Figure 1.2, outlining the flow of process gas, fuel, and heat recovery. Figure 6.17 shows how an SMR plant could look like based on an electrically heated primary reformer.

## 6. Resistance heating

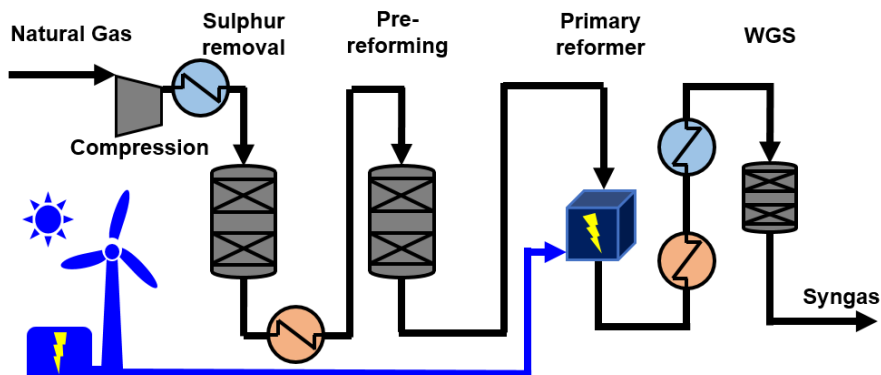


Figure 6.17: Electrified SMR plant Potential flowsheet for SMR based on an electrically heated primary reformer utilizing renewable electricity.

Most notably, the fuel (Natural gas/LPG) is replaced with renewable energy, removing the hottest and largest stream from the plant, as well as the exhaust. Without the flue gas, significantly less heat recovery is available/necessary. Pre-heating of the natural gas feed prior to Sulphur removal and pre-reforming can to some extent be recovered from the hot process gas before water-gas-shift. As reactor volume is no longer a constraint, and to avoid additional risk of carbon deposition, the gas from the pre-reformer is not pre-heated before reaching the primary reformer.

Unlike conventional fired reactors, the resistance-heated reformer does not benefit substantially from economy of scale, which can be an advantage, as it enables SMR plants at much smaller scale, than currently feasible based on fired reformers.

For hydrogen production, it is possible to reduce the  $\text{CO}_2$  emissions from  $9.7 \text{ kg}_{\text{CO}_2}/\text{kg}_{\text{H}_2}$  to  $6.4 \text{ kg}_{\text{CO}_2}/\text{kg}_{\text{H}_2}$ , by increasing methane conversion from 71 to 90%, and supplying heat from renewable electricity, assuming 95% separation efficiency for the resistance-heated process.<sup>23</sup> For reference, the thermodynamic minimum based on reaction stoichiometry is  $5.5 \text{ kg}_{\text{CO}_2}/\text{kg}_{\text{H}_2}$ .<sup>23</sup> If the non-converted methane and steam is recycled, the residual gas will consist of high purity  $\text{CO}_2$ , which may facilitate capture or sequestration to further decrease emissions.

As mentioned in the introduction, this work is not the first to suggest electrically heating for industrial SMR.<sup>54</sup> At the time (1994), it was of limited

economic viability due to the “abundance” of natural gas. However, with increasing climate concerns, and decreasing cost of electricity, electrically heated reforming becomes increasingly viable. Figure 6.18 provides a crude estimate of the operational costs relative to feed and fuel (including electricity), indicating a domain between conventional fired SMR and electrolysis, where production of hydrogen by electrically heated SMR is economically competitive. It should be stressed this is a greatly simplified estimation purely based on the cost of natural gas, electricity, and carbon tax, and consequently does not include capital investment, infrastructure, or additional unit operations.

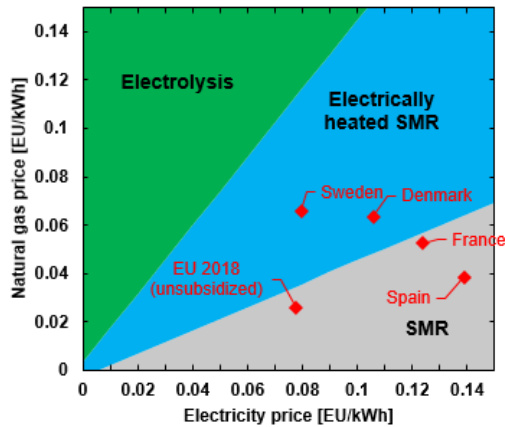


*Figure 6.18: Estimate of economic viability for hydrogen production* Estimated economic viability for electrically heated reforming. This estimate only takes cost of feed and estimated efficiencies into account, and no other unit operations required, nor capital investment. The overall efficiency for Electrolysis, Electrically heated SMR, and SMR is estimated to respectively; 0.75, 0.81, and 0.60 with respect to hydrogen production. Assuming 15 Euro/ton<sub>CO2</sub> carbon tax. Reference data based on medium sized industry.<sup>128–130</sup>

Assuming electrically heated SMR operates at 90% methane conversion, 95% separation efficiency, and 95% energy efficiency; it is close to being economically competitive to conventional SMR. The carbon tax only needs to increase from 15 Euro/ton<sub>CO2</sub> to 35 for electrically heated SMR to be competitive to SMR based on average European prices for natural gas and electricity (within the assumptions for Figure 6.18). The calculations behind Figure 6.18 assumes all methane is emitted as CO<sub>2</sub>, consequently, any carbon sequestration or capture will shift favorably towards SMR. The reference

## 6. Resistance heating

---

points are based on average electricity prices over a year, a point where the potential for intermittent applications become exceedingly interesting.

The primary shortcoming of current renewable energy sources is the discrepancy between production and consumption, both on a daily and long-term basis.<sup>14,131</sup> Conventional fired reformers can require more than a week to start-up to avoid hotspots or too fast thermal expansion, where preliminary experiments and simulations indicate the resistance-heated reformer can reach operating conditions within minutes (Section 6.4).

A reactor compatible with the fluctuations of renewable energy is desirable to fill a gap in current infrastructure, where a substantial part of the energy supplied to the grid originates from combustion based power plants to maintain balance. The electrically heated reformer can operate with large flexibility regarding load, as both process gas flowrate or power input can be adjusted (Fig. 6.2). However, this does not take into account the rest of the process (Sulphur removal, pre-reformer, WGS, separation, heat exchange).

Resistance-heated SMR is a strong platform for production of greener syngas, utilizing renewable resources. Coupled with secondary processes such as Fischer-Tropsch, Methanol, Ammonia, or DME synthesis, it may be a possible candidate for large-scale storage/conversion of excess renewable electricity as liquid fuels.<sup>132</sup> Highly compact reactors with fast thermal response may pave the way for new plant configurations, utilizing different pre-processing steps depending on feedstock, and different separation technologies depending on product applications.

While the resistance-heated reformer looks promising compared to conventional fired reformers and infrastructure development, there are many questions, especially regarding upscaling and operational stability, yet to be addressed. Further work is required to validate the resistance-heated reactor for practical applications.

## 7. Summary

Growing concerns for the global climate demands reconsideration of fossil-fueled processes. The development and implementation of renewable energy technologies in recent years has resulted in costs for renewable electricity comparable to electricity produced from fossil fuels. However, the intermittent nature of renewable energy and a lack of efficient large-scale storage creates a growing demand for technologies utilizing the excess renewable electricity. Production of synthesis gas by steam methane reforming is a relevant candidate, as the total production of syngas accounts for nearly 3% of global CO<sub>2</sub> emissions. For the strongly endothermic SMR process, a large fraction of the emissions stems from the combustion of fossil fuels, heating the process to the 900-950°C required by thermodynamics. Utilizing renewable energy to supply the necessary heat could reduce the CO<sub>2</sub> emissions of SMR by about a third, improve energy efficiency, and provide new possibilities for a technology today limited to large-scale facilities.

This work investigates the potential and limitations of electrically heated SMR based on two different approaches; induction heating via magnetic hysteresis of a ferromagnetic catalyst, and integrated resistance heating of washcoated catalytic structure. The focus of the project is on the implementation of CFD models based on experimental model systems and characterization, with the aim of elucidating process phenomena, and assess possibilities and limitations.

A catalyst heated by magnetic hysteresis must contain a ferromagnetic susceptor with a Curie temperature exceeding the desired reaction temperature. Cobalt is the only element with a sufficiently high Curie temperature, but displays poor activity for the SMR reaction. A magnetic susceptor based on cobalt protected by an alumina shell was developed, and for catalytic tests mixed with a high surface area support impregnated with nickel. However, unfavorable magnetic properties at current stage of development limited the energy efficiency.

Further experimental investigation of hysteresis heated SMR was carried out using a ferromagnetic catalyst based on a Cobalt-Nickel spinel, where the catalytic particles was heated directly. Methane conversion up to 99% was achieved at ambient pressure, with an average heat flux up to 32 W/cm<sup>3</sup>, ca.

## 7. Summary

---

an orders of magnitude higher than conventional fired reformers relative to the catalyst volume. The implemented CFD model for induction heating accurately predicted the experimental trends as a function of flow and conversion, but deviated from the specific values, indicating some mechanisms are not yet fully understood. The deviation is expected to originate from the characterization or implementation of magnetic properties. This was evident as more heat was supplied in the experimental setup than suggested possible by VSM characterization.

The primary obstacle at small scale is limited energy efficiency, due to resistive and thermal losses to the induction coil. Curie temperature can serve as a safety mechanism, preventing overheating of the reactor; however, it also constrains operation at industrially relevant pressures, where higher temperatures are required to reach reasonable conversion.

In contrast, direct resistance heating of a washcoated catalytic structure can exceed the temperatures feasible in conventional fired reformers, enabling higher degree of methane conversion. Integration of the heat source can resolve thermal limitations, and practically no temperature difference is predicted across the catalytic washcoat. This enables catalytic effectiveness factors exceeding conventional fired reformers by an order of magnitude, with further optimization achievable by reducing coat thickness. Electrical conductivity independent of temperature provides an inherent uniform supply of heat, reducing the risk of hotspots, and consequently enable operation at conditions closer to the thermodynamic boundaries for carbon deposition.

The high heat flux achievable for electrically heated SMR, inductive or integrated resistance, enables exceptionally compact reactors two orders of magnitude smaller than conventional fired reformers at equivalent capacity. Compact reactors heated by electricity are less susceptible to *economy of scale*, enabling a platform for SMR, relevant at different scales and configurations. Replacing a conventional fired reformer with an electrically heated in an industrial plant removes the largest and hottest waste stream (flue gas), and consequently alleviates heat recovery.

An additional benefit of the compact systems and uniform supply of heat is fast thermal response to perturbations, enabling startup time within minutes. This creates a possibility of intermittent operation, following the fluctuations

in production of renewable energy. If coupled with a secondary process this could potentially convert excess renewable energy into liquid fuels.

Further work is required before either of the investigated heating technologies are implemented at industrial scale. For hysteresis heating, several questions are posed regarding characterization and implementation of the heating mechanism, and specialized equipment may be necessary to elucidate the answers. The resistance-heated reformer relies on existing and tested elements, and the inherent high efficiency brings it closer to practical applications. Stability, especially if intended for intermittent operation is crucial, and further experimental work is required. Additionally, improved electrical connections are critical for efficient operation. With that in mind, electrically heated SMR is a promising platform for production of greener fuels and chemical in the transition towards a sustainable future.

## 8. Bibliography

1. International Energy Agency (IEA), *Key World Energy Statistics 2017*. (2017).
2. Met Office Hadley Centre observation datasheets. Global average temperature 1850-2018. (2018).  
<https://www.metoffice.gov.uk/hadobs/monitoring/index.html>
3. Dlugokencky, E. & Tans, P. Trends in Atmospheric Carbon Dioxide. Available at: [www.esrl.noaa.gov/gmd/ccgg/trends/](http://www.esrl.noaa.gov/gmd/ccgg/trends/). (Accessed: 13th June 2019)
4. Le Quéré et al., Global Carbon Budget 2018. *Earth Syst. Sci. Data* **10**, 2141–2194 (2018).
5. United Nations (UN). *Emissions Gap Report 2018*. (2018).
6. Climate Action Tracker. (2019).  
<https://climateactiontracker.org/data-portal/>. (Accessed: 13th June 2019)
7. Lazard. *Lazard's levelized cost of energy analysis - version 12.0*. (2018).
8. Service, R. F. Solar plus batteries is now cheaper than fossil power. *Science*. **365**, 108 (2019).
9. British Petroleum (BP). *BP Statistical Review of World Energy 2019*. *Journal of Policy Analysis and Management* (2019).
10. BloombergNEF. *'New Energy Outlook 2018'*. (2018).
11. International Renewable Energy Association (IRENA), *Renewable capacity statistics 2018*. (2018).
12. Rystad Energy. *Oil discoveries*. (2017).  
<https://www.rystadenergy.com/newsevents/news/press-releases/all-time-low-discovered-resources-2017>
13. Fthenakis, V. M. & Nikolakakis, T. Storage Options for Photovoltaics. in *Comprehensive Renewable Energy* **1**, 199–212 (Elsevier Ltd., 2012).
14. Johansson, B. Security aspects of future renewable energy systems e

- 
- A short overview. *Energy* **61**, 598–605 (2013).
15. Moran, E. F., Lopez, M. C., Moore, N., Müller, N. & Hyndman, D. W. Sustainable hydropower in the 21st century. *Proc. Natl. Acad. Sci. U. S. A.* **115**, 11891–11898 (2018).
  16. Waldman, J., Sharma, S., Afshari, S. & Fekete, B. Solar-power replacement as a solution for hydropower foregone in US dam removals. *Nat. Sustain.* (2019).
  17. Svendsen, S. H. Danmarks største havvindmøllepark placeres i nordsøen. *Horten* (2019).  
<https://www.horten.dk/Nyhedsliste/2019/Marts/Danmarks-stoerste-havvindmoellepark-placeres-i-Nordsoen>. (Accessed: 24th June 2019)
  18. Energistyrelsen, (Danmark). Eksisterende havvindmølleparker og aktuelle projekter. (2019).  
<https://ens.dk/ansvarsomraader/vindenergi/eksisterende-havvindmoelleparker-og-aktuelle-projekter>. (Accessed: 24th June 2019)
  19. International Energy Agency (IEA) & Organisation for Economic Co-operation and Development (OECD). *CO2 capture and storage. A key abatement option.* (2008).
  20. Barreto, L., Makihiro, A. & Riahi, K. The hydrogen economy in the 21st century: A sustainable development scenario. *Int. J. Hydrogen Energy* **28**, 267–284 (2003).
  21. Grand View Research. *Hydrogen Generation Market Size, Share & Trends Analysis Report By Application.* (2018).
  22. Rostrup-Nielsen, J. & Christiansen, L. J. *Concepts in Syngas Manufacture.* (Imperial College Press, 2011).
  23. Kumar, A., Baldea, M. & Edgar, T. F. A physics-based model for industrial steam-methane reformer optimization with non-uniform temperature field. *Comput. Chem. Eng.* **105**, 224–236 (2017).
  24. Latham, D. A., McAuley, K. B., Peppley, B. A. & Raybold, T. M. Mathematical modeling of an industrial steam-methane reformer for on-line deployment. *Fuel Process. Technol.* **92**, 1574–1586 (2011).
  25. International Energy Agency (IEA) & Organisation for Economic
-

## 8. References

---

- Co-operation and Development (OECD). Tracking Industrial Energy Efficiency and CO<sub>2</sub> Emissions. 83 (2007).
26. Spath, P. L. & Mann, M. K. *Life Cycle Assessment of Hydrogen Production via Natural Gas Steam Reforming*. (2001).
27. US Geological Survey (USGS). *Mineral Commodity Summary: Nitrogen*. US Geological Survey (2018).
28. Wismann, S. T. *et al.* Electrified methane reforming: A compact approach to greener industrial hydrogen production. *Science*. **364**, 756–759 (2019).
29. Twigg, M. V. & Ridler, D. E. Steam Reforming. in *Catalyst Handbook* (ed. Twigg, M. V.) 225–282 (1996).
30. Sehested, J. Four challenges for nickel steam-reforming catalysts. *Catal. Today* **111**, 103–110 (2006).
31. Aasberg-Petersen, K. *et al.* Natural gas to synthesis gas - Catalysts and catalytic processes. *J. Nat. Gas Sci. Eng.* **3**, 423–459 (2011).
32. Rostrup-Nielsen, J. R., Sehested, J. & Nørskov, J. K. Hydrogen and synthesis gas by steam- and CO<sub>2</sub> reforming. *Adv. Catal.* **47**, 65–139 (2002).
33. Bonaquist, D. Analysis of CO<sub>2</sub> Emissions, Reductions, and Capture for Large-Scale Hydrogen Production Plants. *A white paper* (2010).
34. Chorkendorff, I. & Niemantsverdriet, J. W. *Concepts of Modern Catalysis and Kinetics*. (Wiley, 2007).
35. Aasberg-Petersen, K. *et al.* Technologies for large-scale gas conversion. *Appl. Catal. A Gen.* **221**, 379–387 (2001).
36. Yu, Y. H. & Sosna, M. H. Modeling for Industrial Heat Exchanger Type Steam Reformer. *Korean J. Chem. Eng.* **18**, 127–132 (2001).
37. Wehinger, G. D. *et al.* Investigating dry reforming of methane with spatial reactor profiles and particle-resolved CFD simulations. *AIChE J.* **62**, 4436–4452 (2016).
38. Xu, J. & Froment, G. F. Methane steam reforming: II. Diffusional limitations and reactor simulation. *AIChE J.* **35**, 97–103 (1989).

- 
39. Behnam, M. & Dixon, A. G. 3D CFD simulations of local carbon formation in steam methane reforming catalyst particles. *Int. J. Chem. React. Eng.* **15**, 1–17 (2017).
  40. Darvishi, P. & Zareie-Kordshouli, F. A rigorous mathematical model for online prediction of tube skin temperature in an industrial top-fired steam methane reformer. *Chem. Eng. Res. Des.* **126**, 32–44 (2017).
  41. T-Raissi, A. & Block, D. L. Hydrogen: Automotive fuel of the future. *IEEE Power Energy Mag.* **2**, 40–45 (2004).
  42. Ricca, A., Palma, V., Martino, M. & Meloni, E. Innovative catalyst design for methane steam reforming intensification. *Fuel* **198**, 175–182 (2017).
  43. Baharudin, L. & Watson, M. J. Monolithic substrate support catalyst design considerations for steam methane reforming operation. *Rev. Chem. Eng.* **0**, 1–21 (2017).
  44. Prokopiev, S. I., Aristov, Y. I., Parmon, V. N. & Giordano, N. Intensification of hydrogen production via methane reforming and the optimization of H<sub>2</sub>:CO ratio in a catalytic reactor with a hydrogen-permeable membrane wall. *Int. J. Hydrogen Energy* **17**, 275–279 (1992).
  45. Yasuda, I. & Shirasaki, Y. Development and Demonstration of Membrane Reformer System for Highly-efficient Hydrogen Production from Natural Gas. *Mater. Sci. Forum* **543**, 1403–1408 (2007).
  46. Aasberg-Petersen, K., Nielsen, C. S. & Lægsgaard Jørgensen, S. Membrane reforming for hydrogen. *Catal. Today* **46**, 193–201 (1998).
  47. Buelens, L. C., Galvita, V. V, Poelman, H., Detavernier, C. & Marin, G. B. Super-dry reforming of methane intensifies CO<sub>2</sub> utilization via Le Chatelier ' s principle. *Science*. **354**, 449–452 (2016).
  48. Barelli, L., Bidini, G., Gallorini, F. & Servili, S. Hydrogen production through sorption-enhanced steam methane reforming and membrane technology: A review. *Energy* **33**, 554–570 (2008).
  49. Tonkovich, A. Y. *et al.* MicroChannel process technology for
-

## 8. References

---

- compact methane steam reforming. *Chem. Eng. Sci.* **59**, 4819–4824 (2004).
50. Tonkovich, A. L. Y. & Daymo, E. A. Microreaction Systems for Large-Scale Production. *Microchem. Eng. Pract.* 299–323 (2010).
51. Erickson, C. J. *Handbook of Electrical Heating for Industry*. (Institute of Electrical and Electronic Engineers, Inc., 1995).
52. Larhead, M., *Microwave methods in organic chemistry*. (Springer, 2006).
53. Nüchter, M., Ondruschka, B., Bonrath, W., Gum, A. & Jena, D.-. Microwave assisted synthesis – a critical technology overview. 128–141 (2004).
54. Alagy, J., Broutin, P., Busson, C. & Weill, J. Process for the thermal pyrolysis of hydrocarbons using an electric furnace. (1994). Patent number: US5321191A
55. Rieks, M., Bellinghausen, R., Kockmann, N. & Mleczko, L. Experimental study of methane dry reforming in an electrically heated reactor. *Int. J. Hydrogen Energy* **40**, 15940–15951 (2015).
56. Mleczko, L. *et al.* Axial flow reactor having heating planes and intermediate planes. (2013). Patent number: WO 2013/135660A1
57. Zhou, L., Guo, Y., Yagi, M., Sakurai, M. & Kameyama, H. Investigation of a novel porous anodic alumina plate for methane steam reforming : Hydrothermal stability , electrical heating possibility and reforming reactivity. *Int. J. Hydrogen Energy* **34**, 844–858 (2009).
58. Zhang, Q. *et al.* A 2D model for the cylinder methane steam reformer using Electrically Heated Alumite Catalyst. *16th World Hydrog. Energy Conf. 2006, WHEC 2006* **1**, (2006).
59. Lucía, O., Maussion, P., Dede, E. & Burdío, J. M. Induction heating technology and its applications: Past Developments, current Technology, and future challenges. *IEEE Trans. Ind. Electron.* **61**, 2509–2520 (2014).
60. Carrey, J., Mehdaoui, B. & Respaud, M. Simple models for dynamic

- 
- hysteresis loop calculations : Application to hyperthermia optimization. *J. Appl. Phys.* **109**, 083921 (2011).
61. Cullity, B. D. & Graham, C. D. Ch 4. Ferromagnetism. in *Introduction to Magnetic Materials, 2nd Edition* 115–149 (Wiley, 2009).
62. Cullity, B. D. & Graham, C. D. Chapter 11. Fine particles and thin films. *Introd. to Magn. Mater.* 359–408 (2009).
63. Cullity, B. D. & Graham, C. D. 09. Domains and the Magnetization Process. *Introd. to Magn. Mater. Second Ed.* **74**, 275–333 (2009).
64. O’Handley, R. C. *Modern Magnetic Materials - Principles and Applications*. (John Wiley & Sons, Inc., 2000).
65. Bean, C. P. & Livingston, J. D. Superparamagnetism. *J. Appl. Phys.* **30**, S120–S129 (1959).
66. Benz, M. Superparamagnetism : Theory and Applications. *Discussion of Two Papers on Magnetic Properties* 1–27 (2012).
67. Griffiths, D. J. *Electromagnetism for physicists*. (Pearson, 2015).
68. Dennis, C. L. & Ivkov, R. Physics of heat generation using magnetic nanoparticles for hyperthermia. *Int J Hyperth.* **29**, 715–729 (2013).
69. Inoue, O., Matsutani, N. & Kugimiya, K. Low Loss Mnzn-Ferrites: Frequency Dependence of Minimum Power Loss Temperature. *IEEE Trans. Magn.* **29**, 3532–3534 (1993).
70. Stoppels, D. Developments in soft magnetic power ferrites. *J. Magn. Mater.* **160**, 323–328 (1996).
71. Deissler, R. J., Martens, M. A., Wu, Y. & Brown, R. Brownian and Néel relaxation times in magnetic particle dynamics. *2013 Int. Work. Magn. Part. Imaging, IWMPi 2013* **1677**, 5522 (2013).
72. Pérez-Camacho, M. N., Abu-Dahrieh, J., Rooney, D. & Sun, K. Biogas reforming using renewable wind energy and induction heating. *Catal. Today* **242**, 129–138 (2015).
73. Fortin, J. P., Gazeau, F. & Wilhelm, C. Intracellular heating of living cells through Néel relaxation of magnetic nanoparticles. *Eur. Biophys. J.* **37**, 223–228 (2008).
-

## 8. References

---

74. Kirschning, A., Kupracz, L. & Hartwig, J. New Synthetic Opportunities in Miniaturized Flow Reactors with Inductive Heating. *Chem. Lett.* **41**, 562–570 (2012).
75. Ceylan, S., Klande, T., Vogt, C., Friese, C. & Kirschning, A. Chemical synthesis with inductively heated copper flow reactors. *Synlett* 2009–2013 (2010).
76. Ceylan, S., Coutable, L., Wegner, J. & Kirschning, A. Inductive heating with magnetic materials inside flow reactors. *Chem. - A Eur. J.* **17**, 1884–1893 (2011).
77. Bordet, A., Lacroix, L., Fazzini, P. & Carrey, J. Magnetically Induced Continuous CO<sub>2</sub> Hydrogenation Using Composite Iron Carbide Nanoparticles of Exceptionally High Heating Power. 1–6 (2016).
78. Varsano, F. *et al.* Dry reforming of methane powered by magnetic induction. *Int. J. Hydrogen Energy* (2019).
79. *CRC - Handbook of Chemistry and Physics.* (CRC Press, 2018).
80. Mortensen, P. M., Engbæk, J. S., Vendelbo, S. B., Hansen, M. F. & Østberg, M. Direct Hysteresis Heating of Catalytically Active Ni–Co Nanoparticles as Steam Reforming Catalyst. *Ind. Eng. Chem. Res.* *acs.iecr.7b02331* (2017).
81. Vinum, M. G. *et al.* Dual-function cobalt–nickel nanoparticles tailored for high-temperature induction-heated steam methane reforming. *Angew. Chemie - Int. Ed.* **57**, 10569–10573 (2018).
82. Almind, M. R. *et al.* Improving performance of induction-heated steam methane reforming. *Catal. Today* 1–8 (2019).
83. Xu, J. G. & Froment, G. F. Methane steam reforming, methanation and water-gas shift .1. Intrinsic Kinetics. *Aiche J.* **35**, 88–96 (1989).
84. Hou, K. & Hughes, R. The kinetics of methane steam reforming over a Ni/ $\alpha$ -Al<sub>2</sub>O catalyst. *Chem. Eng. J.* **82**, 311–328 (2001).
85. Bird, R. B., Stewart, W. E. & Lightfoot, E. N. *Transport Phenomena.* (Wiley, 2002).
86. Hansen, M. *Constitution of binary alloys.* (McGRAW-Hill Book

- 
- Company, 1958).
87. McAlister, A. J. The Al-Co (Aluminum-Cobalt) system. *Bull. Alloy Phase Diagrams* **10**, 646–650 (1989).
  88. Venezia, A. M. & Loxton, C. M. Low pressure oxidation of Ni<sub>3</sub>Al alloys at elevated temperatures as studied by x-ray photoelectron spectroscopy and Auger spectroscopy. *Surf. Sci.* **194**, 136–148 (1988).
  89. Hagel, W. C. The oxidation of iron, nickel and cobalt-base alloys containing aluminium. *Corrosion* **21**, 316–326 (1965).
  90. Langemark, N. Ø. Synthesis and characterisation of cobalt-alumina systems. *Master Thesis*, Technical University of Denmark, 2017.
  91. Nield, D. A. & Bejan, A. *Convection in porous media. Convection in Porous Media* (Springer, 2013). doi:10.1007/978-1-4614-5541-7
  92. Shen, L. & Chen, Z. Critical review of the impact of tortuosity on diffusion. *Chem. Eng. Sci.* **62**, 3748–3755 (2007).
  93. Cao, C., Zhang, N. & Cheng, Y. Numerical analysis on steam methane reforming in a plate microchannel reactor: Effect of washcoat properties. *Int. J. Hydrogen Energy* **41**, 18921–18941 (2016).
  94. Reid, R. C., Prausnitz, J. M. & Sherwood, T. K. *The properties of gases and liquids*. (McGRAW-Hill Book Company, 1977).
  95. MatWeb - Fecralloy. Available at: <http://www.matweb.com/search/datasheet.aspx?matguid=c2427c6297594858bedac2a4e5981d2f&ckck=1>. (Accessed: 12th September 2018)
  96. Gresho, P. M. & Sani, R. L. *Incompressible Flow and the Finite Element Method*. (Wiley, 2000).
  97. Wismann, S. T. *et al.* Electrified methane reforming: Understanding the dynamic interplay. *submitted* (2019). See Appendix 9.1.2
  98. Berkowitz, A. E., Schuele, W. J. & Flanders, P. J. Influence of crystallite size on the magnetic properties of acicular  $\gamma$ -Fe<sub>2</sub>O<sub>3</sub> particles. *J. Appl. Phys.* **39**, 1261–1263 (1968).
-

## 8. References

---

99. Wakao, N. Kato, K. Effective Thermal Conductivity of Packed Beds. *J. Chem. Eng. Japan* **2**, 24–33 (1969).
100. Wakao, N. & Kaguei, S. *Heat and Mass Transfer in Packed Beds - Topics in chemical engineering I*. (Gordon and Breach Science Publishers Ltd., 1982).
101. Schlünder, E. U. Transport Phenomena in Packed Bed Reactors. *Am. Chem. Soc.* 110–161 (1978).
102. Schlünder, E. U. Heat Transfer in Packed Beds. *Wärme - Und Stoffübertragung* **1**, 153–158 (1968).
103. Schlünder, E. U. Wärme- und Stoffübertragung zwischen durchströmten Schüttungen und darin eingebetteten Einzelkörpern. *Chemie Ing. Tech.* **38**, 967–979 (1966).
104. Hsu, C. T., Cheng, P. & Wong, K. W. Modified Zehner-Schlünder models for stagnant thermal conductivity of porous media. *Int. J. Heat Mass Transf.* **37**, 2751–2759 (1994).
105. Antwerpen, W. Van, Toit, C. G. & Rousseau, P. G. A review of correlations to model the packing structure and effective thermal conductivity in packed beds of mono-sized spherical particles. *Nucl. Eng. Des.* **240**, 1803–1818 (2010).
106. Živcová, Z. *et al.* Thermal conductivity of porous alumina ceramics prepared using starch as a pore-forming agent. *J. Eur. Ceram. Soc.* **29**, 347–353 (2009).
107. Sih, S. S. & Barlow, J. W. The Prediction of the Emissivity and Thermal Conductivity of Powder Beds. *Part. Sci. Technol.* **22**, 427–440 (2004).
108. Geb, D., Zhou, F. & Catton, I. Internal Heat Transfer Coefficient Determination in a Packed Bed From the Transient Response Due to Solid Phase Induction Heating. *J. Heat Transfer* **134**, 042604 (2012).
109. Van Antwerpen, W., Rousseau, P. G. & Du Toit, C. G. Multi-sphere Unit Cell model to calculate the effective thermal conductivity in packed pebble beds of mono-sized spheres. *Nucl. Eng. Des.* **247**, 183–201 (2012).
110. Mueller, G. E. Angular void fraction distributions in randomly

- 
- packed fixed beds of uniformly sized spheres in cylindrical containers. *Powder Technol.* **72**, 269–275 (1992).
111. Fogler, H. S. *Elements of Chemical Reaction Engineering*. (PHI, 2005).
  112. Ashraf, M. A., Sanz, O., Montes, M. & Specchia, S. Insights into the effect of catalyst loading on methane steam reforming and controlling regime for metallic catalytic monoliths. *Int. J. Hydrogen Energy* **43**, 11778–11792 (2018).
  113. Mbodji, M., Commenge, J. M. & Falk, L. Preliminary design and simulation of a microstructured reactor for production of synthesis gas by steam methane reforming. *Chem. Eng. Res. Des.* **92**, 1728–1739 (2014).
  114. Kays, W. M. & London, A. L. *Compact Heat Exchangers*. (McGraw-Hill, 1984).
  115. Cao, C., Zhang, N., Chen, X. & Cheng, Y. A comparative study of Rh and Ni coated microchannel reactor for steam methane reforming using CFD with detailed chemistry. *Chem. Eng. Sci.* **137**, 276–286 (2015).
  116. McGuire, N. E., Sullivan, N. P., Deutschmann, O., Zhu, H. & Kee, R. J. Dry reforming of methane in a stagnation-flow reactor using Rh supported on strontium-substituted hexaaluminate. *Appl. Catal. A Gen.* **394**, 257–265 (2011).
  117. Kockmann, N. *Transport phenomena in micro process engineering*. (Springer Berlin Heidelberg, 2008).
  118. Zamaniyan, A., Ebrahimi, H. & Mohammadzadeh, J. S. S. A unified model for top fired methane steam reformers using three-dimensional zonal analysis. *Chem. Eng. Process. Process Intensif.* **47**, 946–956 (2008).
  119. Nijemeisland, M., Dixon, A. G. & Stitt, E. H. Catalyst design by CFD for heat transfer and reaction in steam reforming. *Chem. Eng. Sci.* **59**, 5185–5191 (2004).
  120. Rostrup-Nielsen, J. R., Christiansen, L. J. & Bak Hansen, J. H. Activity of Steam Reforming Catalysts. *Appl. Catal.* **43**, 287–303 (1988).
-

## 8. References

---

121. Sadooghi, P. & Rauch, R. Experimental and modeling study of catalytic steam reforming of methane mixture with propylene in a packed bed reactor. *Int. J. Heat Mass Transf.* **78**, 515–521 (2014).
122. Jones, G. *et al.* First principles calculations and experimental insight into methane steam reforming over transition metal catalysts. *J. Catal.* **259**, 147–160 (2008).
123. Asia Industrial Gas Association (AIGA). *Safe Startup and Shutdown Practices for Steam Reformers Shutdown Practices*. (2013).
124. Mortensen, P. M. & Dybkjær, I. Industrial scale experience on steam reforming of CO<sub>2</sub>-rich gas. *Appl. Catal. A Gen.* **495**, 141–151 (2015).
125. Reid, R. C., Prausnitz, J. M. & Poling, B. E. *The Properties of Gases & Liquids*. (McGraw-Hill, 1987).
126. Zhai, X., Ding, S., Chang, Y., Jin, Y. & Cheng, Y. CFD simulation with detailed chemistry of steam reforming of methane for hydrogen production in an integrated micro-reactor. *Int. J. Hydrogen Energy* **35**, 5383–5392 (2010).
127. Mbodji, M. *et al.* Steam methane reforming reaction process intensification by using a millistructured reactor: Experimental setup and model validation for global kinetic reaction rate estimation. *Chem. Eng. J.* **207–208**, 871–884 (2012).
128. Energy EU, Energy Prices - January 2019. (2019) [https://www.energy.eu/electricity\\_natural-gas\\_prices\\_european\\_union/](https://www.energy.eu/electricity_natural-gas_prices_european_union/). (Accessed: 27th August 2019)
129. Eurostat. Gas prices by type of user. (2017). <https://ec.europa.eu/eurostat/databrowser/view/ten00118/default/table?lang=en>. (Accessed: 27th August 2019)
130. Eurostat. Electricity prices by type of user. (2017). <https://ec.europa.eu/eurostat/databrowser/view/ten00117/default/table?lang=en>. (Accessed: 27th August 2019)
131. Energinet. Vindmøller slog rekord i 2014. (2015). Available at: <http://energinet.dk/DA/El/Nyheder/Sider/Vindmoeller-slog-rekord-i-2014.aspx>. (Accessed: 4th June 2015)

- 
132. Mortensen, P. M., Grunwaldt, J. D., Jensen, P. A., Knudsen, K. G. & Jensen, A. D. A review of catalytic upgrading of bio-oil to engine fuels. *Appl. Catal. A Gen.* **407**, 1–19 (2011).
  133. Bhat, S. A. & Sadhukhan, J. Process Intensification Aspects for Steam Methane Reforming: An Overview. *AIChE J.* **55**, 408–422 (2009).
  134. Elnashaie, S. S. E. H. & Abashar, M. E. E. Steam reforming and methanation effectiveness factors using the dusty gas model under industrial conditions. *Chem. Eng. Process.* **32**, 177–189 (1993).
  135. Palma, V., Martino, M., Meloni, E. & Ricca, A. Novel structured catalysts configuration for intensification of steam reforming of methane. *Int. J. Hydrogen Energy* **42**, 1629–1638 (2017).
  136. Roh, H. S., Lee, D. K., Koo, K. Y., Jung, U. H. & Yoon, W. L. Natural gas steam reforming for hydrogen production over metal monolith catalyst with efficient heat-transfer. *Int. J. Hydrogen Energy* **35**, 1613–1619 (2010).
  137. Tronconi, E., Groppi, G., Boger, T. & Heibel, A. Monolithic catalysts with ‘high conductivity’ honeycomb supports for gas/solid exothermic reactions: Characterization of the heat-transfer properties. *Chem. Eng. Sci.* **59**, 4941–4949 (2004).
  138. Johnsen, K., Ryu, H. J., Grace, J. R. & Lim, C. J. Sorption-enhanced steam reforming of methane in a fluidized bed reactor with dolomite as CO<sub>2</sub>-acceptor. *Chem. Eng. Sci.* **61**, 1195–1202 (2006).
  139. Ma, R., Castro-Dominguez, B., Mardilovich, I. P., Dixon, A. G. & Ma, Y. H. Experimental and simulation studies of the production of renewable hydrogen through ethanol steam reforming in a large-scale catalytic membrane reactor. *Chem. Eng. J.* **303**, 302–313 (2016).
  140. Karim, A., Bravo, J., Gorm, D., Conant, T. & Datye, A. Comparison of wall-coated and packed-bed reactors for steam reforming of methanol. *Catal. Today* **110**, 86–91 (2005).
  141. Cavusoglu, G. *et al.* In situ characterization of catalysts and membranes in a microchannel under high-temperature water gas shift reaction conditions. *J. Phys. Conf. Ser.* **712**, (2016).
-

## 8. References

---

142. Lazard. *Lazard's Levelized Cost of Energy 10.0*, (2017).
143. International Energy Agency (IEA), *World Energy Outlook 2017*.
144. Govender, S. & Friedrich, H. Monoliths: A Review of the Basics, Preparation Methods and Their Relevance to Oxidation. *Catalysts* **7**, 62 (2017).
145. Rothenberg, G. Heterogeneous Catalysis. in *Catalysis: Concepts and Green Applications* 127–187 (Wiley-VCH Verlag GmbH & Co. KGaA, 2008).
146. Simonsen, S. B. *et al.* Direct observations of oxygen-induced platinum nanoparticle ripening studied by in situ TEM. *J. Am. Chem. Soc.* **132**, 7968–7975 (2010).
147. Vargaftik, N. B. *Tables on the thermophysical properties of liquids and gases*. (Hemisphere Publishing Group, 1975).
148. Chaplin, M. Water Models. (2017).  
[http://www1.lsbu.ac.uk/water/water\\_models.html](http://www1.lsbu.ac.uk/water/water_models.html). (Accessed: 13th July 2017)
149. Kingery, W. D., Francl, J., Coble, R. L. & Vasilos, T. Thermal Conductivity: X, Data for Several Pure Oxide Materials Corrected to Zero Porosity. *J. Am. Ceram. Soc.* **37**, 107–110 (1954).
150. Dixon, A. G. & Nijemeisland, M. CFD as a Design Tool for Fixed-Bed Reactors. *Ind. Eng. Chem. Res.* **40**, 5246–5254 (2001).
151. Applied Test Systems - Series 3110/3210. *Applied Test System - Heat Curves* (2017).  
<http://www.atspa.com/products/process-heating/lab-furnaces/1200-deg/series-3110-3210/>. (Accessed: 11th July 2017)
152. Dixon, A. G., Ertan Taskin, M., Nijemeisland, M. & Stitt, E. H. Wall-to-particle heat transfer in steam reformer tubes: CFD comparison of catalyst particles. *Chem. Eng. Sci.* **63**, 2219–2224 (2008).
153. Assael, M. J., Millat, J., Vesovic, V. & Wakeham, W. A. The Thermal Conductivity of Methane and Tetrafluoromethane in the Limit of Zero Density. *J. Phys. Chem. Ref* **19**, 1137–1147 (1990).

154. Millat, J. & Wakeham, W. A. The Thermal Conductivity of Nitrogen and Carbon Monoxide in the Limit of Zero Density. *Journal of Physical and Chemical Reference Data* **18**, 565–581 (1989).
155. Vesovic, V. & Wakeham, W. The transport properties of carbon dioxide. *Journal of Physical Chemical Reference Data* 763–808 (1990). doi:10.1063/1.555875
156. Blais, N. C. & Mann, J. B. Thermal Conductivity of Helium and Hydrogen at High Temperatures. *J. Chem. Phys.* **32**, 1459–1465 (1960).

## 9. Appendix

### 9.1 Appendix A: Appended papers

#### 9.1.1 Paper 1

**Electrified methane reforming: A compact approach to greener industrial hydrogen production**

Sebastian T. Wismann, Jakob S. Engbæk, Søren B. Vendelbo, Flemming B. Bendixen, Winnie L. Eriksen, Kim Aasberg-Petersen, Cathrine Frandsen, Ib Chorkendorff, Peter M. Mortensen

*Science*, **364**, 6442, pp. 756-759, **2019**.

DOI: 10.1126/science.aaw8775

*Cited as [28] in this thesis*

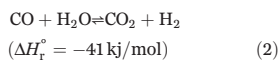
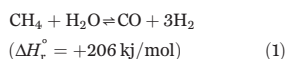
## INDUSTRIAL CATALYSIS

# Electrified methane reforming: A compact approach to greener industrial hydrogen production

Sebastian T. Wismann<sup>1</sup>, Jakob S. Engbæk<sup>2</sup>, Søren B. Vendelbo<sup>2</sup>, Flemming B. Bendixen<sup>3</sup>, Winnie L. Eriksen<sup>4</sup>, Kim Aasberg-Petersen<sup>4</sup>, Cathrine Frandsen<sup>1</sup>, Ib Chorkendorff<sup>1\*</sup>, Peter M. Mortensen<sup>4,\*</sup>

Electrification of conventionally fired chemical reactors has the potential to reduce CO<sub>2</sub> emissions and provide flexible and compact heat generation. Here, we describe a disruptive approach to a fundamental process by integrating an electrically heated catalytic structure directly into a steam-methane-reforming (SMR) reactor for hydrogen production. Intimate contact between the electric heat source and the reaction site drives the reaction close to thermal equilibrium, increases catalyst utilization, and limits unwanted byproduct formation. The integrated design with small characteristic length scales allows compact reactor designs, potentially 100 times smaller than current reformer platforms. Electrification of SMR offers a strong platform for new reactor design, scale, and implementation opportunities. Implemented on a global scale, this could correspond to a reduction of nearly 1% of all CO<sub>2</sub> emissions.

The synthesis of important chemicals such as hydrogen and ammonia has a substantial CO<sub>2</sub> footprint because the heating of the processes often relies on the combustion of hydrocarbons. One of the largest endothermic processes is the production of hydrogen by steam-methane reforming (SMR), which accounts for ~50% of the global hydrogen supply, where all hydrogen production is estimated to account for 3% of global CO<sub>2</sub> emissions (1, 2). In this strongly endothermic reaction, natural gas reacts with steam according to the following equations:



Where  $\Delta H_r^\circ$  is standard reaction enthalpy. Heat is typically supplied to the reaction by combustion of a mixture of natural gas and potential off-gases from the synthesis. In total, conventional SMR produces 6.6 to 9.3 metric tons of CO<sub>2</sub> per metric ton of H<sub>2</sub>, of which 17 to 41% is the direct product of hydrocarbon combustion (2, 3).

Today, a large-scale industrial SMR reformer consists of an array of more than 100 10- to 14-m-long tubular reactors in a large furnace, with gas burners positioned for an optimal distribution of heat among the reactor tubes (4–6). The com-

busion must occur considerably above the reaction temperature to generate the necessary inward heat flux, as illustrated by the temperature profile in Fig. 1A (5, 7). Because of limited thermal conductivity across the SMR catalyst and reactor walls, transporting the heat necessary to drive the reaction is a natural limitation (Fig. 1A), and typically less than 2% of the furnace volume contains catalyst (5, 8). Intrinsic catalytic activity is typically not a limiting factor for industrial reforming (9). Instead, the low thermal conductivity combined with a strongly endother-

mic reaction creates steep temperature gradients across the catalyst, leading to poor catalyst utilization and increasing the risk of detrimental carbon formation (10–12).

For decades, thermal conductivity of SMR has been the subject of research. Efforts include using catalysts with higher thermal conductivity (13), lowering the temperature of SMR by shifting the equilibrium (14–17), obtaining shorter characteristic length scales through  $\mu$ -reactors (18, 19), performing room-temperature reactions using plasma (20), or employing direct heating of magnetic catalysts by induction (21). Alternatively, electrical heating of an integrated catalytically coated heating element enables reactor temperatures exceeding what is feasible in conventional reactors (22), and allows substantially improved temporal response, pushing start-up times to within minutes (23). However, despite decades of research, no alternatives with lower CO<sub>2</sub> emissions have been implemented at the industrial scale.

This work describes a high-performing, fully electrically driven reformer based on direct resistive (ohmic) heating (Fig. 1B), which is scalable to industrial conditions and capacities. The intimate contact between the electric heat source and the catalyst enables energy to be supplied directly to the catalytic sites, removing thermal limitations and providing well-defined control of the reaction front. Electrification removes the fired section, substantially reducing reactor volume, CO<sub>2</sub> emissions, and waste-heat streams. This provides a disruptive advantage to existing industrial reformers, enabling the production of “greener” hydrogen for the large-scale synthesis of indispensable chemicals such as methanol, ammonia, and biofuels (24, 25).

For this work, we prepared a laboratory-scale reactor based on an FeCrAl-alloy tube, which was

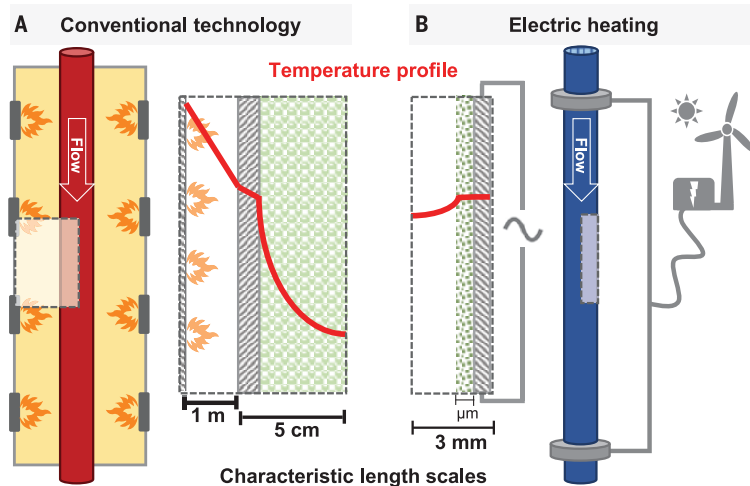


**Fig. 1. Heating principles.** (A) Conventional fired reactor. (B) Electric resistance-heated reactor. Characteristic radial length scales and temperature profiles are shown across the heat source, reactor wall (gray), and catalyst material (green). In (B), the heat source and reactor wall are one. Illustrations are not to scale.

<sup>1</sup>DTU Physics, Technical University of Denmark, 2800 Kongens Lyngby, Denmark. <sup>2</sup>Danish Technological Institute, 2630 Tåstrup, Denmark. <sup>3</sup>Sintex A/S, 9500 Hobro, Denmark. <sup>4</sup>Haldor Topsoe A/S, 2800 Kongens Lyngby, Denmark. \*Corresponding author. Email: ibchork@fysik.dtu.dk (I.C.); pmor@topsoe.com (P.M.M.)

chosen for its temperature-independent electrical resistance and coated with an  $\sim 130\text{-}\mu\text{m}$  nickel-impregnated washcoat on its interior (26). Copper sockets were mounted at opposite ends of the external surface of the reactor tube, and resistive heating was accomplished by applying an AC current along the tube (Fig. 2A). This allowed a direct heat supply to the catalytic washcoat (Fig. 2B). A section of the coat was removed at both ends of the reactor to obtain a quantified length of the catalyst (Fig. 2C) and to prevent reverse reaction toward the outlet. However, a thin residual layer of catalytically active coat ( $<5\text{ }\mu\text{m}$ ) was present at the lower section of the reactor (fig. S1) as a result of the impregnation method of the material. Temperature profiles were measured with multiple thermocouples spot welded to the tube (Fig. 2D). The entire reactor was encapsulated in high-temperature insulation material.

A feed mixture of  $\text{CH}_4$ ,  $\text{H}_2\text{O}$ , and  $\text{H}_2$  (30/60/10) was preheated to  $100^\circ\text{C}$  to prevent condensation before entering the reactor. The experiments were operated 50 mbar above ambient, as the reactor was not prepared for pressure-bearing application.

A computational fluid dynamics model (CFD), including calculation of electric currents, thermal energy, fluid dynamics, mass transport, and reaction kinetics, was implemented to further

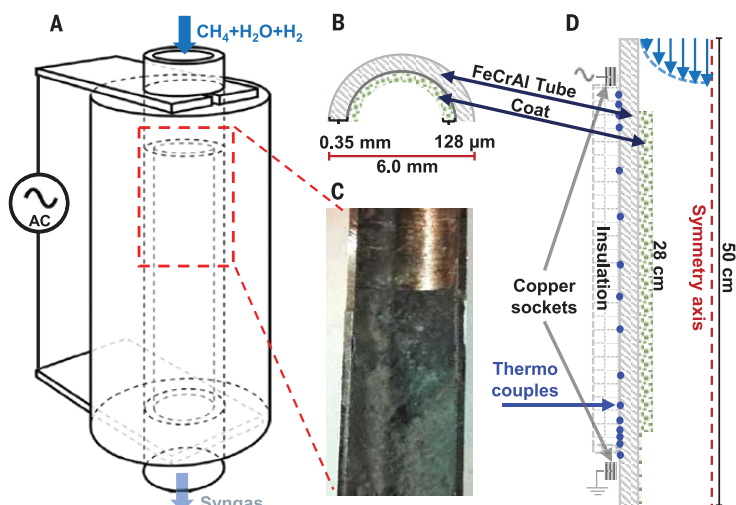


**Fig. 2. Laboratory-scale resistance-heated reactor.** (A) Resistance-heated reactor setup. The illustration is not to scale. (B) Cross-sectional illustration of the reactor in the coated region. (C) Axial cross-section of the reactor after experiments, showing the well-defined edge of the coat. (D) Axisymmetrical reactor cross-section, outlining the most relevant domains and thermocouple positions.

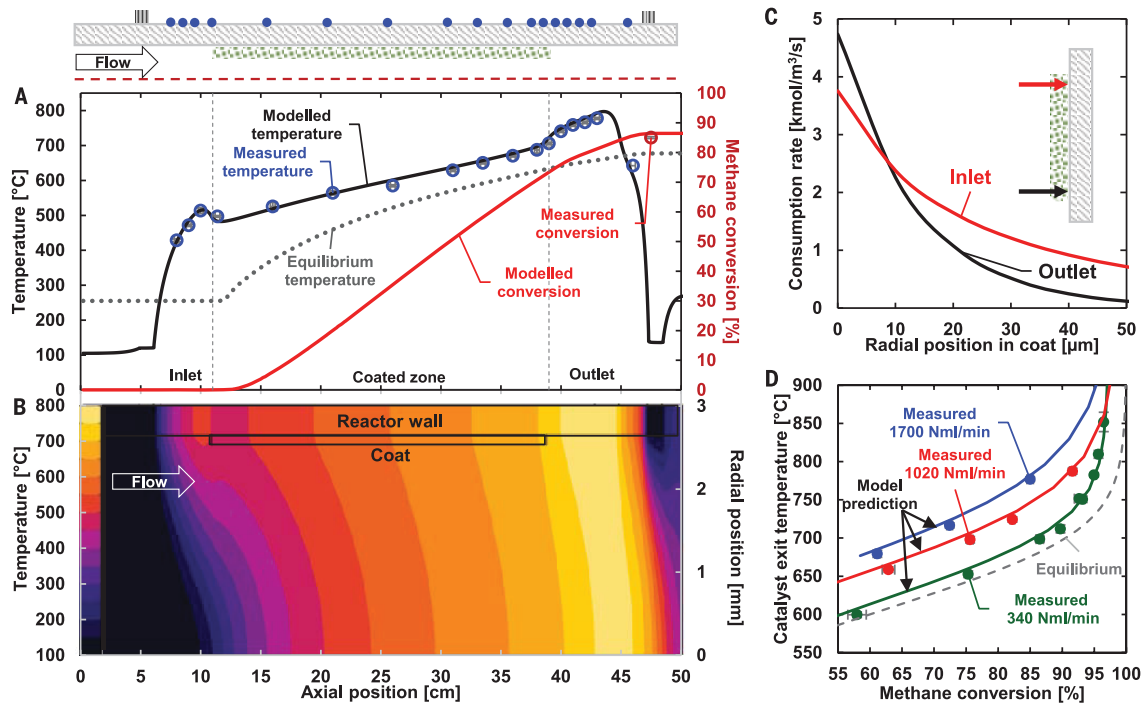


**Fig. 3. Experimental results and model predictions at ambient pressure.** (A) Axial temperature profile and methane conversion at 1.7 NL/min. The equilibrium temperature is the temperature at which a given gas composition is in thermodynamic equilibrium with respect to the SMR reaction (Eq. 1). (B) CFD-modeled thermal contours across the reactor. (C) Methane consumption rate for the innermost  $50\text{ }\mu\text{m}$  of the coat (out of  $128\text{ }\mu\text{m}$ ), evaluated near inlet and outlet; compare with (A). (D) Measured exit temperature against methane conversion for the resistance-heated reformer for different gas flows.

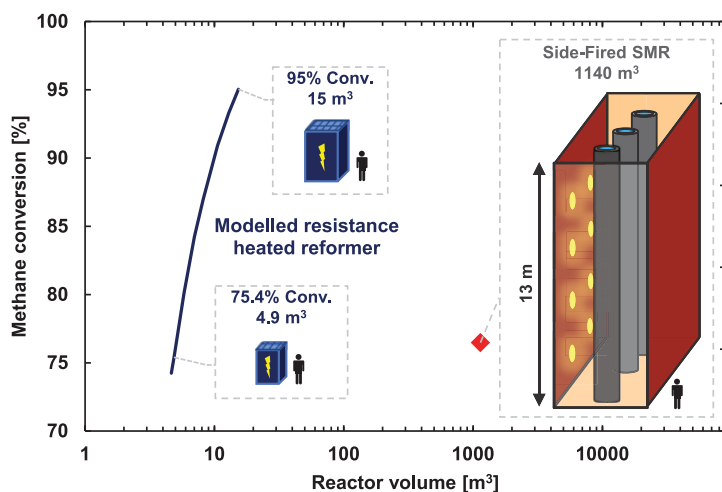


**Fig. 4. Scaling opportunities for industrial production.** Modeled methane conversion for a resistance-heated reformer scaled to a capacity of 2230 kmol  $\text{H}_2$ /hour compared with a side-fired SMR operating at 75.4% methane conversion. The comparison was done at industrial operating conditions ( $T_{\text{in}} = 466^\circ\text{C}$ ,  $T_{\text{out}} = 920^\circ\text{C}$ ,  $S/C = 1.8$ ,  $P_{\text{out}} = 26.7$  barg). The model is limited to a  $20^\circ\text{C}$  difference from the equilibrium temperature (26).

understand the experiments and to extrapolate results to industrially relevant conditions. The computational model accurately describes the measurable values, such as external temperature and methane conversion (figs. S2 to S4).

Figure 3 shows experimental and computational data. The reactor can be divided into three sections. The first section, at the inlet, yields a rapid increase in temperature between the copper socket and coated zone (Fig. 3A) as the entire heat supply is used for heating the process gas (Fig. 3B). In the second section, the coated zone, the temperature initially drops because the endothermic reaction consumes more heat than supplied for the process (Fig. 3A). Hereafter, the temperature profile is close to linear, with a substantially smaller slope than in the first zone, as the endothermic reaction consumes large amounts of heat. In the third section, the outlet (Fig. 3A), the temperature increases again more rapidly, reaching a maximum of  $800^\circ\text{C}$ , before dropping promptly to  $100^\circ\text{C}$ . Near the end of the reactor, the copper sockets exchange heat with ambient conditions, facilitating rapid cooling.

Owing to the uniform supply of heat to the process, the nearly constant heat flux (fig. S5) ensures that the gas mixture is kept close to equilibrium throughout the entire catalytic length (Fig. 3A), as opposed to what is observed for conventional reformers (6, 8). This results in better utilization of the reactor volume and limits detrimental side reactions such as carbon formation (figs. S6 and S7). Radial thermal gradients (Fig. 3B) primarily arise from the convection in the reactor. Temperature difference across the coat does not exceed  $2^\circ\text{C}$  along the linear section of the temperature profile. There is no discernible temperature gradient across the reactor wall,

a substantial benefit compared with a fired reformer, in which the temperature difference between the inner and outer wall of the tubular reactor can cause thermal stress, detrimental to mechanical strength and reactor lifetime (27).

Although internal diffusion limits the utilization of the catalyst, as the reaction quickly approaches equilibrium across the coat (Fig. 3C), the average catalyst utilization is 20% at the conditions shown in Fig. 3C, i.e., up to an order of magnitude higher than that reported for a heterogeneous catalyst for SMR (6, 28, 29). The most effective utilization of the catalyst is near the inlet, as lower temperature generates lower reaction rates (figs. S8 and S9). At the outlet, equilibrium is reached within the innermost  $50\ \mu\text{m}$  of coat, equivalent to 39% of the coat thickness. The improved catalyst utilization is primarily due to the absence of thermal gradient in the catalyst. Further optimization of the catalyst utilization is feasible; as shown in Fig. 3C, only  $40$  to  $50\ \mu\text{m}$  of a uniform coat is required for full conversion, increasing catalyst utilization up to 65%.

Because the flow is always completely laminar in the given process design [Reynolds number  $\ll 2100$  (30)], radial mass transport occurs solely by molecular diffusion to the surface of the catalyst, resulting in an external mass transport limitation (bulk to surface) that is correlated to the gas velocity (fig. S10). The external diffusion limit can be seen by the increased temperature required to reach equivalent conversion as the flow rate increases (Fig. 3D). Higher conversion may be achieved by increasing the reactor temperature, at the expense of increasing the temperature difference relative to equilibrium (Fig. 3D). As the process gas approaches full conversion, a vertical

asymptote is observed because of increasing kinetic hindrance of the reaction. The vertical asymptote occurs at lower conversion for higher flow rates, thus limiting the maximum conversion achievable without altering the geometry or operational conditions, such as the pressure or steam-to-carbon ratio. For reference, an industrial SMR rarely operates above 90% conversion of methane.

An important benefit of the resistance-heated design is the possibility for exceptionally compact reactors (23). If we use the model developed in this work for a single tube and extrapolate it to several parallel reformer tubes matching the capacity of an SMR, we find that a conventional  $1100\text{-m}^3$  side-fired reformer producing 2230 kmol  $\text{H}_2$ /hour can be replaced with an  $\sim 5\text{-m}^3$  resistance-heated reformer (Fig. 4). Operating at similar conditions, the resistance-heated reformer has no risk of carbon deposition (fig. S11). The substantial volume reduction obtained for the resistance-heated reformer is achievable because integration of the heat source makes the furnace obsolete, thus removing a substantial portion of the reactor volume. Further volume reduction is envisioned if the geometry or operation conditions are optimized; however, this was not pursued in this study. It should be noted that the comparison is based on the SMR furnace, and does not include essential equipment such as combustion air blowers and waste heat section [6]. For the resistance-heated reformer, wiring and power supply are equivalently omitted for this comparison.

The electrification, uniform heating, and potential for exceptionally compact reactors present a disruptive approach to resolving  $\text{CO}_2$  emission issues and current constraints regarding design, operation, and process integration for hydrogen production by SMR. In addition to reducing  $\text{CO}_2$  emissions, implementation of the resistance-heated reactor into existing plants could offer alternative operation conditions, reducing the steam-to-carbon ratio, or operate at increased methane conversion, typically limited by carbon deposition and temperatures (i.e., material constraints). High methane conversion coupled with an alternative purification technology could even provide a local source of  $\text{CO}_2$  for other processes. With less need for heat recovery, resistance-heated reforming is efficient and applicable at many different sizes, promoting delocalization designs by using the existing and well-developed infrastructure of natural gas and potentially also biogas. Low thermal mass can also lead to reformers optimized for intermittent operation, following the fluctuations in availability of excess renewable energy with possible startup times in seconds (23, 26). The operating costs for an electrified reformer are directly related to the cost of electricity, natural gas, and  $\text{CO}_2$  taxes. Preliminary estimates indicate that a resistance-heated reformer would be on par with current fired reformers in regions with a high production of renewable electricity.

This work illustrates the disruptive opportunities achievable by electrification of fundamental industrial processes. With the swiftly decreasing

cost of electricity from renewable sources, resistive heating is an environmental—and economically appealing—solution for providing the necessary heat for strongly endothermic industrial processes on the path toward a more sustainable society.

## REFERENCES AND NOTES

1. L. Barreto, A. Makihira, K. Riahi, *Int. J. Hydrogen Energy* **28**, 267–284 (2003).
2. International Energy Agency (IEA), *CO<sub>2</sub> Capture and Storage. A Key Abatement Option* (OECD, 2008).
3. P. L. Spath, M. K. Mann, Life Cycle Assessment of Hydrogen Production via Natural Gas Steam Reforming (National Renewable Energy Laboratory, 2001); <https://www1.eere.energy.gov/hydrogenandfuelcells/pdfs/27637.pdf>.
4. D. Bonaquist, A White Paper: Analysis of CO<sub>2</sub> Emissions, Reductions, and Capture for Large-Scale Hydrogen Production Plants (Praxair, 2010); <https://www.praxair.com/-/media/corporate/praxairus/documents/reports-papers-case-studies-and-presentations/our-company/sustainability/praxair-co2-emissions-reduction-capture-white-paper.pdf?la=en&rev=dc79ff3c7b4c4974a1328c7660164765>.
5. D. A. Latham, K. B. McAuley, B. A. Peppley, T. M. Raybold, *Fuel Process. Technol.* **92**, 1574–1586 (2011).
6. J. Rostrup-Nielsen, L. J. Christiansen, *Concepts in Syngas Manufacture* (Imperial College Press, 2011).
7. J. R. Rostrup-Nielsen, *Catal. Today* **145**, 72–75 (2009).
8. A. Kumar, M. Baldea, T. F. Edgar, *Comput. Chem. Eng.* **105**, 224–236 (2017).
9. I. Chorkendorff, J. W. Niemantsverdriet, *Concepts of Modern Catalysis and Kinetics* (Wiley, ed. 2, 2007).
10. G. D. Wehinger et al., *AIChE J.* **62**, 4436–4452 (2016).
11. M. Behnam, A. G. Dixon, *Int. J. Chem. React. Eng.* **15**, 1–17 (2017).
12. J. Sehested, *Catal. Today* **111**, 103–110 (2006).
13. Y. Hiramitsu, M. Demura, Y. Xu, M. Yoshida, T. Hirano, *Appl. Catal. A Gen.* **507**, 162–168 (2015).
14. K. Johnsen, H. J. Ryu, J. R. Grace, C. J. Lim, *Chem. Eng. Sci.* **61**, 1195–1202 (2006).
15. S. A. Wassie et al., *Int. J. Hydrogen Energy* **42**, 14367–14379 (2017).
16. L. C. Buelens, V. V. Galvita, H. Poelman, C. Detavernier, G. B. Marin, *Science* **354**, 449–452 (2016).
17. R. Ma, B. Castro-Dominguez, I. P. Mardilovich, A. G. Dixon, Y. H. Ma, *Chem. Eng. J.* **303**, 302–313 (2016).
18. A. Y. Tonkovich et al., *Chem. Eng. Sci.* **59**, 4819–4824 (2004).
19. A. Karim, J. Bravo, D. Gorm, T. Conant, A. Datye, *Catal. Today* **110**, 86–91 (2005).
20. L. Wang, Y. Yi, C. Wu, H. Guo, X. Tu, *Angew. Chem. Int. Ed. Engl.* **56**, 13679–13683 (2017).
21. M. G. Vinum et al., *Angew. Chem. Int. Ed. Engl.* **57**, 10569–10573 (2018).
22. M. Rieks, R. Bellinghausen, N. Kockmann, L. Mleczko, *Int. J. Hydrogen Energy* **40**, 15940–15951 (2015).
23. L. Zhou, Y. Guo, M. Yagi, M. Sakurai, H. Kameyama, *Int. J. Hydrogen Energy* **34**, 844–858 (2009).
24. A. L. Jongorius, P. C. A. Bruijninckx, B. M. Weckhuysen, *Green Chem.* **15**, 3049–3056 (2013).
25. M. Balakrishnan, E. R. Sacia, A. T. Bell, *ChemSusChem* **7**, 2796–2800 (2014).
26. Materials and methods are available as supplementary materials.
27. K. Aasberg-Petersen et al., *Appl. Catal. A Gen.* **221**, 379–387 (2001).
28. J. Xu, G. F. Froment, *AIChE J.* **35**, 97–103 (1989).
29. M. V. Twigg, D. E. Ridler, in *Catalyst Handbook*, M. V. Twigg, Ed. (Manson Publishing, ed. 2, 1996), pp. 225–282.
30. R. B. Bird, W. E. Stewart, E. N. Lightfoot, *Transport Phenomena* (Wiley, ed. 2, 2002).

## ACKNOWLEDGMENTS

**Funding:** This work was supported by Innovation Fund Denmark (IFD) under file no. 5160-00004B and research grant 9455 from Villum Fonden. **Author contributions:** All authors contributed substantially to this work. **Competing interests:** The authors declare no conflicts of interest. **Data and materials availability:** The catalyst can be made available under a material transfer agreement for Haldor Topsoe A/S. All other data are available in the main text or the supplementary materials.

## SUPPLEMENTARY MATERIALS

science.sciencemag.org/content/364/6442/756/suppl/DC1  
Materials and Methods  
Supplementary Text  
Figs. S1 to S12  
Table S1  
References (31–41)

1 February 2019; accepted 8 April 2019  
10.1126/science.aaw8775

9.1.2 Paper 2

**Electrified methane reforming: Understanding the dynamical interplay**

Sebastian T. Wismann, Jakob S. Engbæk, Søren B. Vendelbo, Winnie L. Eriksen, Cathrine Frandsen, Peter M. Mortensen, Ib Chorkendorff

Submitted to *Industrial Engineering & Chemistry Research*, August, 2019

*Cited as [97] in this thesis*

# Electrified methane reforming: Understanding the dynamic interplay

Sebastian T. Wismann<sup>1</sup>, Jakob S. Engbæk<sup>2</sup>, Søren B. Vendelbo<sup>2</sup>, Winnie L. Eriksen<sup>3</sup>, Cathrine Frandsen<sup>1</sup>, Peter M. Mortensen<sup>3\*</sup>, Ib Chorkendorff<sup>1\*</sup>.

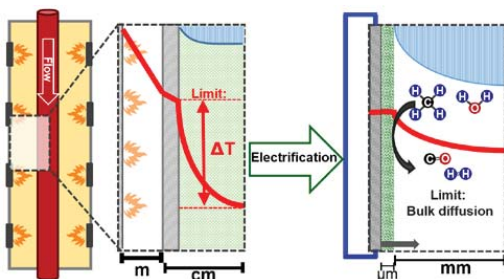
<sup>1</sup>Technological University of Denmark, 2800 Kgs. Lyngby, Denmark, <sup>2</sup>Danish Technological Institute, 2630 Tåstrup, Denmark, <sup>3</sup>Haldor Topsoe A/S, 2800 Kgs. Lyngby, Denmark.

**Corresponding authors:**\* [pmor@topsoe.com](mailto:pmor@topsoe.com) & [ibchork@fysik.dtu.dk](mailto:ibchork@fysik.dtu.dk)

**Keywords:** SMR, Electrification, Industrial catalysis, CFD, Process intensification

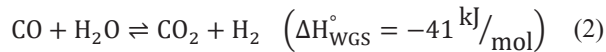
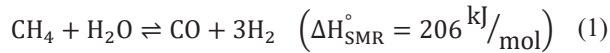
**Abstract:** Electrification of endothermic reactions has the potential to provide a compact and flexible reactor concept, and at the same time, substantially reduce CO<sub>2</sub> emissions relative to combustion-heated processes. Here, we show how electrification of steam methane reforming (SMR) using a wash-coated catalyst is able to solve the low thermal conductivity limitation of conventional-fired reformers. Integrated heating via electric resistance heating provides a uniform heat supply, enabling catalytic effectiveness factors an order of magnitude larger than conventional SMR plants at industrial comparable conditions. The effectiveness factor can be engineered to a certain degree by adapting the wash coat thickness. Overall, the approach diminishes the importance of having high catalytic efficiency. Instead, characteristic timescale analysis indicates that heat transfer is the least limiting mechanism for the electrified reformer, and substantial improvements of reactor capacity is achievable through optimization of reactor geometry. This is in direct contrast to the limitations of conventional-fired reforming.

## Graphical abstract:



## 1. Introduction

Constant supply of heat to catalytic sites is often limiting the efficiency of endothermic catalytic reactions.<sup>1</sup> One of the largest endothermic processes is the production of syngas by steam methane reforming (SMR), which supplies a range of chemical industries including synthesis of; ammonia, fuels, and methanol.<sup>2,3</sup> Reforming of natural gas and naphtha accounts for ca. 80% of the global hydrogen supply.<sup>3</sup> Collectively, global production of syngas by steam reforming accounts for nearly 3% of all CO<sub>2</sub> emissions.<sup>2,4</sup> In SMR, natural gas (methane) and steam is converted to carbon oxides and hydrogen through the overall endothermic reaction scheme in Reactions (1) and (2):



Typical syngas conversion processes such as ammonia, methanol, and Fischer-Tropsch are facilitated at high pressure, where process economy favors operating the SMR at high pressure to decrease compression cost in the plant design. However, the SMR reaction is adversely impacted by high pressure, consequently requiring high temperatures to drive the reaction due to Le Châteliers principle (Fig. S1). Typical economic and practical operation is limited to 30 bars and 900°C due to material constraints.<sup>5</sup> The reactors are typically fired from the outside. The high temperature requirement, limiting thermal conductivity, and endothermic reaction create steep temperature gradients inside the reactor and catalyst bed, increasing the risk of carbon deposition, and cause thermal stress detrimental to reactor lifetime.<sup>5-7</sup> The steep gradients in conventional fired reformers greatly limit catalytic efficiency, typically utilizing less than 10% of the available catalytic activity in conventional reactors.<sup>5,8,9</sup>

Previous research into reducing CO<sub>2</sub> emissions and resolving the low thermal conductivity for endothermic processes include; new materials with higher thermal conductivity,<sup>10-12</sup> reducing reaction temperature by shifting equilibrium,<sup>13-16</sup> reducing characteristic length scales for heat transfer,<sup>17-20</sup> or direct heating through induction.<sup>21-23</sup>

Integrated joule heating is a promising alternative, capable of operating with very quick start-up time, and practically no thermal gradients.<sup>24-26</sup> Combined with short characteristic length scales, this conveys the potential for exceptionally small and dynamic reactors, with a well-controlled reaction front.<sup>26</sup> With increasing implementation of renewable energy and concomitant decreasing energy costs,<sup>27,28</sup> electrification of chemical industry is a promising, efficient, and greener alternative to the conventional fired reformers of today.<sup>26</sup>

This work describes an experimental reformer, fully heated by integrated joule heating. A detailed and verified numerical model is used to extrapolate to industrially relevant conditions, to provide insight into the potential for operating beyond current conventional constraints, allowing improved

feed utilization and catalytic efficiency. On this basis, an optimal configuration is proposed based on characteristic timescale analysis.

## 2. Experimental setup

Experimental evidence for the computational model was provided by testing in a resistance heated reforming setup. A 50 cm long FeCrAl tube (Goodfellow, outer diameter 6 mm) was coated on the internal surface with a 130  $\mu\text{m}$  zirconia based coat.<sup>29</sup> Before calcination, 11 cm of the coat was removed from each end. The wash coat was impregnated with a nickel nitrate solution.<sup>30</sup> The wash-coated catalyst was reduced in 200  $\text{Ni H}_2/\text{h}$  for 4 hours, and passivated in 1%  $\text{O}_2$  in nitrogen at 25°C. Multiple 0.25 mm K-type thermocouples (Goodfellow) was spot-welded to the external surface in order to measure accurate temperature profiles during experiments (SR630 Thermocouple monitor with 10  $\text{M}\Omega$  Internal resistance). The reactor was heated by the joule effect, using AC current applied along the reactor through copper sockets (Fig. 1A). Input was adjusted with a vario transformer and a set of coils, transforming power supplied at ca. 220V. The contact resistance between the copper sockets and the reactor was minimized prior to experiments (*Keithley 2400 sourcemeter*). The applied potential was measured by an oscilloscope (*Agilent infiniiVision DSO-X 2014A*), and the current by a current probe (*Keysight 1146B*).

A feed mixture of  $\text{CH}_4$ ,  $\text{H}_2\text{O}$ , and  $\text{H}_2$  (30/60/10) was preheated to 105°C to avoid condensation. Steam was removed from the product by a drain trap (Armstrong 11LD). Dry gas composition was analyzed by gas chromatography (*Agilent 7890 GC System with TCD/FID*), with at least 4 consecutive measurements at each set of conditions. The outlet pressure was slightly above ambient (<50 mbar).

The methane conversion was evaluated by the mole fractions of carbon-containing species as normalized from the GC measurements:

$$X_{\text{CH}_4} = \frac{y_{\text{CO}} + y_{\text{CO}_2}}{y_{\text{CH}_4} + y_{\text{CO}} + y_{\text{CO}_2}} \cdot 100\% \quad (3)$$

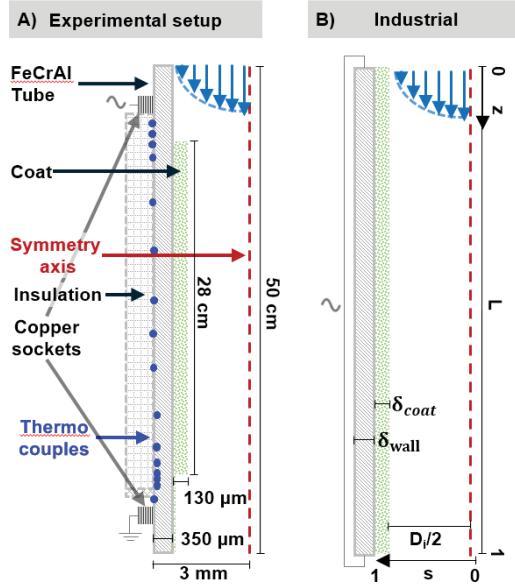


**Figure 1: Reactor geometry** A) Illustration of the axisymmetrical reactor geometry used for the CFD model. The indicated dimensions is for the experimental setup. The blue dots indicate positions of the spotwelded thermocouples on the reactor wall. B) Illustration of reduced channel geometry used in simulations at industrial conditions, with coat for the entire reactor length.  $\delta_{coat}$  is washcoat thickness,  $\delta_{wall}$  is wall thickness, and  $D_i$  the internal diameter – not including washcoat.  $L$  is reactor tube length.  $z$  and  $s$  denote, respectively, vertical and radial positions, normalized against reactor length and internal radius. Note that the center ( $s=0$ ) is defined on the symmetry axis. The illustrations are not to scale.

Based on reaction kinetics reported by Xu & Froment, the reaction rate was implemented as:<sup>31</sup>

$$R_1 = k_1 \frac{p_{CH_4} p_{H_2O}}{p_{H_2}^{2.5}} (1 - \beta) \quad (4)$$

Where  $k_1$  is a forward rate constant,  $p_i$  partial pressure of species  $i$ , and  $\beta$  is the ratio between the reaction quotient,  $Q_r$ , and the equilibrium constant,  $K_{eq,i}$ . The approach towards equilibrium for Reaction (1) is defined as:

$$\beta = \frac{Q_r}{K_{eq}} = \frac{p_{CO} \cdot p_{H_2}^3}{p_{CH_4} \cdot p_{H_2O} \cdot K_{eq,SMR}} \quad (5)$$

Where  $p_i$  are partial pressures, and  $K_{eq,SMR}$  is the equilibrium constant for Reaction 1.<sup>5</sup> At  $\beta$  equal unity, the reaction is at equilibrium, thus the sign and size of  $\beta$ , determines how far the reaction is

from equilibrium. The catalytic performance was estimated by the approach towards equilibrium,  $\beta$ .

### 3. Model implementation

A Computational Fluid Dynamics (CFD) model using standard equations for energy, fluid dynamics, mass transfer, and electric fields was implemented in Comsol 5.2a to obtain insight into parameters that could not be measured, and as a base to extrapolate towards industrially relevant conditions. The modelled domains of the ambient reactor setup are shown in Figure 1A. The implemented CFD model is fitted to three parameters; thermal conductivity of insulation, pre-exponential catalytic activity factor, and layer thickness of residual coat towards the outlet (Fig. S2). Fluid dynamics, mass transfer, and energy transport is implemented by standard equations,<sup>32</sup> and is described in the supplementary information. The CFD model was fitted using a least square approach, against six experimental data sets spanning different flows and conversion. All presented data is using the best fit, evaluated based on a weighted temperature profile and methane conversion, reproducing experimental data within an average error of  $\pm 2\%$ . Methane conversion is predicted within  $\pm 1.9\%$  (Fig. S3).

The model was extended to typical industrial conditions based on a side-fired SMR with a capacity of 50.000 Nm<sup>3</sup> H<sub>2</sub>/h. Ideal insulation, no electrical contact resistance, and gas properties behaving as ideal within moderate pressures are assumed for simulations at industrial conditions. The reduced geometry is shown in Fig. 1B.

It is stressed that these simulations assume an ideal coat, with homogeneous distribution of pores and catalytic activity.

### 4. Characteristic timescales

A typical heterogeneous catalytic reaction consists of five steps to form the product: bulk diffusion, internal diffusion, adsorption, reaction, and desorption.<sup>33</sup> Characteristic timescale analysis is introduced in order to detect the limiting phenomena between the space-time, and the timescales for external mass transfer, internal mass transfer, heat transfer, and reaction.<sup>34</sup>

The space-time is defined as:<sup>35</sup>

$$\tau_s = \frac{z_c}{u_{z_c}} \quad (6)$$

Where  $z_c$  is the axial position in the reactor, and  $u_{z_c}$  is the linear velocity, evaluated at  $z_c$ . When compared to average reaction time, it is evaluated at the entrance ( $z_c = 0$  cm). Because the flow at all points is laminar ( $Re < 2100$ ,<sup>32</sup>), space-time is used instead of average residence time. Space-time is evaluated by the velocity at the tube center, opposed to residence time calculated as the volume divided by flow.

The external mass transport time coefficient is defined as:<sup>36</sup>

$$\tau_{ext} = \frac{D_i^2}{2D_m Sh} \quad (7)$$

Here  $D_i$  is the internal diameter, not including catalytic washcoat.  $D_m$  is the averaged diffusion coefficient, and  $Sh$  the Sherwood number. The Sherwood number is a dimensionless number for mass transport defined as ratio of convective mass transfer rate to the diffusion rate. For fully developed laminar flows, the Sherwood number can be approximated to 4.364.<sup>32,37</sup> The flow is at all relevant points laminar and fully developed as  $L/D_i > 100$ ,<sup>37</sup> and the Reynolds number  $Re$  (Ratio of inertial to viscous forces) is less than 1200, well below the transition to turbulence at 2100.<sup>32</sup>

The internal mass transport time coefficient is defined as:<sup>36</sup>

$$\tau_{int} = \frac{\delta_{coat}^2}{D_{eff}} \quad (8)$$

Here  $\delta_{coat}$  is the coat thickness, and  $D_{eff}$  the effective diffusion in the coat.<sup>38</sup>

$$D_{eff} = \frac{\varepsilon}{\tau} \left( \frac{1}{D_K} + \frac{1}{D_m} \right)^{-1} \quad (9)$$

$$\tau = \varepsilon^{-1/2} \quad (10)$$

Here  $\varepsilon$  is coat porosity,  $\tau$  coat tortuosity calculated by the Bruggeman correlation,  $D_m$  the mixture-averaged bulk diffusion coefficient, and  $D_K$  the Knudsen diffusion, defined as:<sup>38</sup>

$$D_K = \frac{\alpha}{3} \sqrt{\frac{8RT}{\pi \bar{M}}} \quad (11)$$

Where  $\alpha$  is the average pore diameter,  $\bar{M}$  the average molecular weight of the gas species,  $R$  the gas constant, and  $T$  temperature. A simple correlation for tortuosity is implemented, as different approximations of tortuosity have very little influence for moderate porosities.<sup>39</sup>

The heat transfer time coefficient is defined as:<sup>32</sup>

$$\tau_{ht} = \frac{\delta^2}{\alpha} \quad (12)$$

Here  $\delta$  is the conduction length (wall coat thickness for the electrified reformer), and  $\alpha$  is thermal diffusivity, calculated by:

$$\alpha = \frac{k}{\rho C_p} \quad (13)$$

Where  $k$  is thermal conductivity,  $\rho$  is material density, and  $C_p$  is specific heat capacity. The coat is at all instances limiting compared to heat transfer across the reactor wall ( $\tau_{ht,wall} < \tau_{ht,coat}$ ) (Fig. S4).

The reaction time coefficient is defined as:<sup>36</sup>

$$\tau_{re} = \frac{C_{CH_4}}{R_{CH_4}} \quad (14)$$

Here  $C_{CH_4}$  is the methane concentration, and  $R_{CH_4}$  the overall methane consumption rate, both evaluated at the catalyst surface.

The catalyst effectiveness factor,  $\eta$ , is a measure of what fraction of the catalyst is utilized, by dividing the bulk rate with the ideal rate (no internal mass transport) evaluated at the surface:

$$\eta = \frac{\int_0^\delta R_{CH_4}(r) dr}{\delta_{coat} \cdot R_{CH_4}^{surface}} \cdot 100\% \quad (15)$$

The effectiveness in Equation (15) is calculated at a given axial position, across the coat. For evaluation of the effectiveness factor for the entire reactor, the axial position is included in an additional integral.

## 5. Results & Discussion

### 5.1. Experimental temperature profiles

To evaluate the performance of the electrified steam methane reforming lab reactor unit, it was operated at varying flow rates and input powers. Temperature profiles of the external reactor surface for different experimental conditions are shown in Figure 2. Between the copper socket and start of the catalytic coat (6-11 cm), the temperature quickly increases, as all supplied energy goes towards heating the process gas. The change in slope, followed by a linear temperature profile for the catalytic section (11-39 cm) is evidence of the endothermic reaction consuming the available heat. The following region (40-44 cm) with a second linear temperature profile indicates weak catalytic activity (Fig. S2), insufficient to keep the reaction at equilibrium, followed by rapid cooling, due to un-insulated heat exchange with the surroundings.

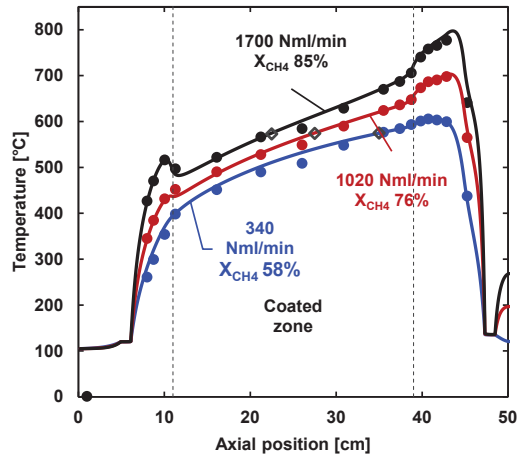


**Figure 2: Temperature profiles** Selected temperature profiles at different flows and conversions. Filled symbols represent measured values, solid lines the modelled profile. Open symbols indicate where the thermal gradient across the coat is evaluated in Figure 3. Experiments performed at ambient pressure, 105 °C inlet temperature, at a steam-to carbon ratio ( $S/C$ ) = 2, with 10% hydrogen in the feed.

The linear region of the temperature profile in the coated zone indicates the reaction is kept near equilibrium at the catalytic surface, with a near uniform heat flux (Fig. S5). Heat generation in the reactor wall is nearly constant, because the resistivity of FeCrAl (reactor wall) is practically independent of temperature. As a consequence, the gas is heated rapidly in the non-catalytic zone (6-11 cm). More energy is required as the flow and conversion increases, heating the gas above equilibrium in the non-catalytic zone, resulting in a drop in temperature at the beginning of the coated zone (Fig. 2). The additional latent energy of the pre-heated gas results in high reaction rates, quickly driving the reaction towards equilibrium, consuming more heat than supplied locally, causing the drop in temperature.

Low thermal conductivity typically results in steep thermal gradients in packed bed reactors, but with the uniform heat flux and catalytic wash-coat configuration, practically no thermal difference is observed across the catalytic coat, in stark contrast to the measured and modelled temperature profiles across packed bed catalysts for SMR (Fig. 3).

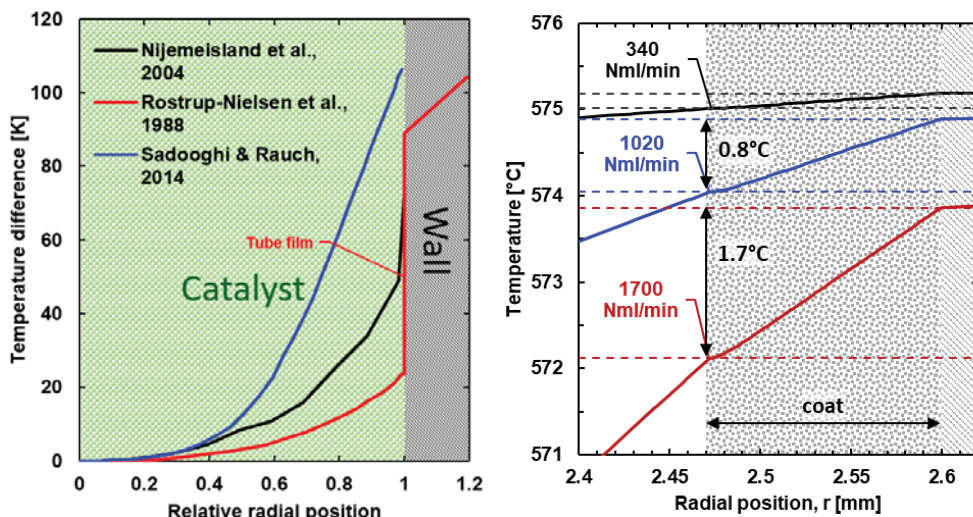


**Figure 3: Temperature profile across catalyst A) Radial temperature profiles across packed bed catalyst for SMR reactors coat.<sup>40–42</sup> The temperature difference relative to the reactor center is used, as the absolute temperature depends on operating conditions. All predict a thermal difference exceeding 100K between the wall and center of the catalyst. The data by Rostrup-Nielsen is based on experimental measurements.<sup>41</sup> B) Modelled temperature profiles across the catalytic washcoat. Simulation conditions: 105°C inlet, ambient pressure, S/C = 2, with 10% hydrogen in the feed. Evaluated at 35, 27.5, and 22.5 cm for 340, 1020, and 1700 Nml/min respectively – See Fig. 2.**

Thermal differences exceeding 100K between reactor wall and center is reported for packed bed reformers for SMR (Fig. 3A). The significant difference in limitation of the tube film layer, a zone between reactor wall and catalyst with a higher void,<sup>43</sup> is likely related to different catalyst size and shape, and operating conditions. As the flow rate and methane conversion increases, more power is required to drive the reaction, increasing the thermal difference across the catalytic coat, as the reaction concomitantly consumes more heat in the internal surface. However, the predicted temperature difference across the coat at the 85% methane conversion and 1700 Nml/min is less than 2°C (Fig. 3B). The temperature difference across the wall does not change significantly along the coated zone (Fig. S6). Moreover, there is no discernable gradient across the reactor wall (Fig. 3B,  $r > 2.6$  mm), a substantial benefit compared to conventional fired reformers, where thermal difference over the reactor wall is detrimental to reactor lifetime, and limiting catalyst utilization.<sup>5,44</sup>

Without thermal gradients, a substantial improvement of catalyst effectiveness can be achieved, exceeding 24% for the experimentally investigated configuration and conditions.<sup>26</sup>

## 5.2. Scaling to industrial conditions

A section without catalytic activity can be used for controlled pre-heating of the feed-gas, but serves no practical purpose in an industrial setting. By coating the entire reactor length (Fig. 1B), the process gas is kept close to equilibrium in the entire reactor. Based on the experimental work and model at ambient pressure, evidence of high accuracy of the model was verified.<sup>26</sup> Consequently, the CFD model is extrapolated to typical industrial conditions, based on a 50.000 Nm<sup>3</sup> H<sub>2</sub>/h side-fired SMR reformer. The most significant changes are the increased inlet temperature and outlet pressure. A temperature increase of 250°C is required to reach equivalent conversion as the outlet pressure is increased from ambient to 27.7 bar. Figure 4 shows the predicted temperature profile at industrial conditions, at 75% and 90% methane conversion.

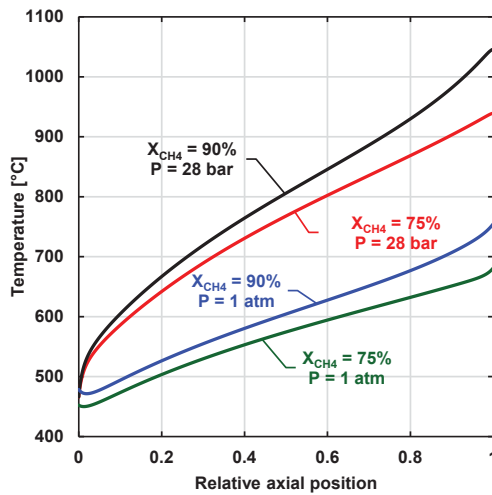


**Figure 4: Temperature profiles at ambient and industrial conditions** Modelled temperature profiles at ambient pressure and 28 bar for 75 and 90% methane conversion. Profiles are only along the coated zone (i.e., positions 11-39 cm in the experimental set up, cf. Fig. 2, and the entire tube length for the high-pressure profiles). Industrial conditions: 9900 GHSV, 27.7 bar, 465°C inlet, and S/C = 1.8. The inlet gas composition is in equilibrium. Ambient conditions: 9900 GHSV, 1 atm, 105 °C inlet, SC=2, with 10% hydrogen in feed gas. All simulations are for reactor tubes with length  $L = 50$  cm and inner diameter  $D_i$  of 5.3 mm

Similar to the experiments at ambient pressure, a steep increase in temperature is observed near the inlet, as high pressure results in low reaction rate at the inlet. A nearly linear temperature profile is observed along the majority of the reactor, as the reaction consumes available heat. Operating at a higher methane conversion, an increase in temperature is predicted towards the outlet, as the conversion near the catalyst surface approaches unity, kinetically limiting the reaction rate, thus

consuming less heat. Without altering geometry or operating conditions, this results in a practical upper limit of achievable conversion (Fig. S3).

### 5.3. Effectiveness factor

Low catalytic effectiveness factor in packed bed reactors for endothermic processes is typically due to insufficient thermal conductivity rather than lack of kinetic activity.<sup>5,44,45</sup> The average effectiveness factor for a conventional reformer is less than 3%.<sup>5</sup> As there is practically no thermal gradient across the washcoated catalyst of the electrified methane reformer (Figs. 3B and S6), a catalyst effectiveness factor near 25% was achieved at the experimental setup at ambient conditions,<sup>26</sup> up to an order of magnitude higher than typically achieved in conventional fired reactors.<sup>5</sup> No significant change to the effectiveness factor is expected at industrial conditions of similar geometry, as the current geometry is limited by mass transport, nearly independent of pressure, as both linear gas velocity and bulk diffusion is inversely proportional to pressure.<sup>32</sup> As the catalyst effectiveness factor is evaluated as the ratio of the rate at the surface to the bulk rate, and the rate rapidly declines across the catalytic layer (Fig. S7), it is possible to increase the effectiveness factor, by decreasing the washcoat layer thickness (Fig. 5).

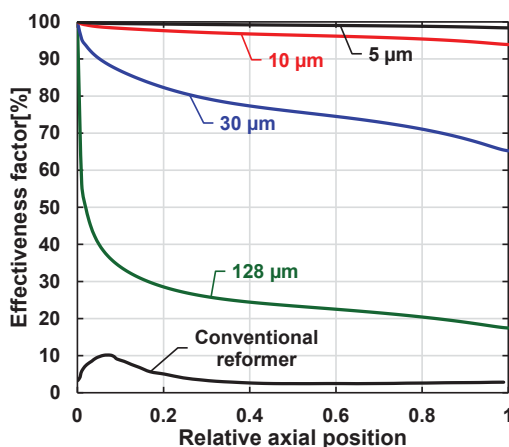


**Figure 5: Catalyst effectiveness factor** Axial effectiveness profiles for decreasing coat thickness. Conventional top-fired reformer adapted from <sup>5</sup>. Simulations at 27.7 bar, SC=1.8, 1 NL/h, 465 °C inlet, and ca. 90% methane conversion.

The peak in effectiveness factor near the inlet for the conventional reformer (Fig. 5) is a result of preheating the gas to around 650°C, driving the reaction from the latent heat. In the model for the electrified reformer, the gas is not preheated, yielding relative low reaction rates near the inlet (Fig. S8), allowing the gas to equilibrate across the coat, resulting in a local effectiveness factor near

unity. As the temperature increases along the reactor (Fig. 4), the reaction rate at the surface follows, where the overall bulk rate is limited by diffusion (Fig. S8), observed in the declining effectiveness factor along the reactor. Towards the outlet of the reactor, the effectiveness factor declines faster, as the methane conversion at the coat surface approaches unity due to very fast kinetics at the highly elevated temperatures (Fig. S9).

In steady state, a surplus amount of catalyst has little to no impact on conversion, as illustrated by Figure 6. However, continuous removal of the catalyst eventually leads to insufficient catalytic material to facilitate the reaction, resulting in an increasing outlet temperature and a risk of detrimental side reactions, as seen as the asymptotic behaviors at 0-10  $\mu\text{m}$  coat thickness in Figure 6. The increase in average effectiveness factor (Fig. 6) yields an optimum around 30  $\mu\text{m}$  of coat to guarantee sufficient catalytic activity (Fig. S10). This corresponds well with predictions by Mbodji *et al.* for a microstructured SMR reactor at short residence time.<sup>36</sup> Further reduction leaves insufficient catalytic activity, as seen from the sharp increase in approach towards equilibrium,  $\beta$ , and outlet temperature.

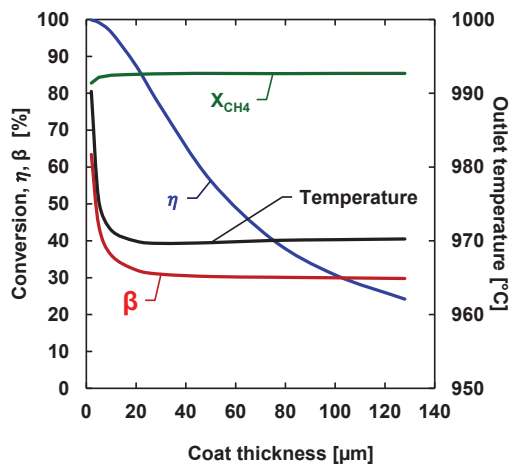


**Figure 6: Influence of washcoat thickness** Methane conversion, effectiveness factor, approach towards equilibrium ( $\beta$ ) and outlet temperature as a function of coat thickness. Simulations at 1  $\text{NL/h}$ , constant energy input, 27.7 bar,  $S/C = 1.8$ , 465°C,  $L = 50$  cm, fixed 5.3 mm internal reactor diameter, including washcoat.

From a practical perspective, very thin coats are more susceptible to loss of activity, from poisoning or loss of surface area due to sintering.<sup>46</sup> Ideal coat layer thickness will therefore be a compromise between safety margins and optimal use of catalyst raw materials. Thicker coats will induce larger thermal gradients, increase linear gas velocity, and does not yield improved performance for a mass transfer limited reaction. While very thin coats (<20  $\mu\text{m}$ ) provide very

high catalytic effectiveness factors, the approach to equilibrium increases substantially, indicating a kinetic limit for the reaction.

Assuming stable operation at 30  $\mu\text{m}$  of coat, the catalyst volume can be reduced by nearly two orders of magnitude relative to a conventional reformer, resulting in an average effectiveness factor around 75%.

#### 5.4. Characteristic timescales

The limiting phenomena can be estimated through analysis of the characteristic timescales for the system (Eq. 6-14). The characteristic timescales for the electrified reformer are compared to a typical fired reformer in Figure 7.

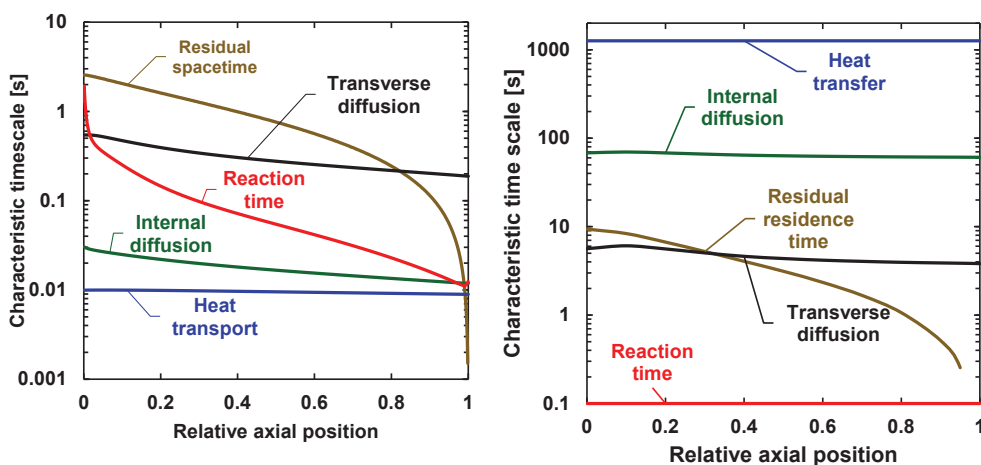


**Figure 7: Characteristic timescales** Axial characteristic timescales. A - Left) Electric reformer at industrial conditions, 465°C inlet, 27.7 bar outlet,  $S/C = 1.8$ , 6235 $h^{-1}$  GHSV, 5.3 mm internal diameter, and 90% methane conversion. B - Right) Top-fired industrial reformer with a packed bed. 829°C outlet, 30 bar outlet,  $S/C = 3.0$ , 3500 GHSV, 120 mm internal diameter, 71.2% methane conversion. Data for comparison based on<sup>47</sup>.

Figure 7A shows that reaction kinetics is limiting the first part of the electrified reformer, as this has the highest characteristic timescale up to a relative axial position of ca. 0.05. However, transverse diffusion rapidly surpasses the reaction rate, representing the limiting phenomena for the majority of the reactor. In practice, this means that the transport, e.g. diffusion, of the molecules from the center of the flow channel to the catalyst surface is the slowest mechanism of the system. Notably, heat transport is the least limiting mechanism as shown by the lowest line in Figure 7A.

For comparison, the heat transfer is by far the limiting phenomena for a conventional fired reformer, as shown in Fig. 7B, with characteristic timescale orders of magnitude above the rest.

The exceptionally high characteristic timescale for heat transport is primarily a result of low thermal conductivity and long diffusion length. As mentioned, it is an approximation of how fast a thermal perturbation is equilibrated across the domain. This is reflected in the steep thermal gradients observed in conventional reformers, which can exceed 100°C across the catalytic bed.<sup>45</sup> Moreover, the residual residence time in the fired reformer is below the transverse diffusion, indicating radial mixing of the gas is slow (Fig. 7B). It should however be noted the transverse diffusion in Fig. 7B does not take turbulence into account, which may lower it. The internal diffusion in Figure 7B is based on a 5.4 mm pellet,<sup>47</sup> and supports previous observations, that performance of fired packed-bed reformers scales with catalyst surface area rather than volume.<sup>5</sup> The reaction time in Figure 7B is calculated based on average process gas composition.<sup>47</sup> Scaled differently (Fig. S11), the reaction time displays a trend similar to the effectiveness factor (Fig. 5), indicating a substantial surplus of available catalytic activity, and that the average gas composition is far from equilibrium, based on the kinetic model by Xu & Froment.<sup>31</sup> A reaction close to equilibrium will have a high characteristic timescale, as the approach towards equilibrium is near unity, suppressing the reaction rate (Equation 4).

### **5.5. Influence of diffusion length scale**

Transverse diffusion represents the main limiting phenomena for the electrified reformer (as illustrated by Figure 7A). This is primarily dependent on the characteristic length scale for mass transport, which for flow in pipes is the internal diameter. As there is negligible flow in the wash-coat, it is not included in the internal diameter for calculating characteristic bulk diffusion. Figure 8A shows reactor performance for different reactor length and internal diameter, operating at an average outlet temperature of 1015°C, assuming a fixed coat (130 μm) and wall thickness (350 μm), and a constant ratio between supplied energy and methane flow. As the internal diameter is the characteristic bulk diffusion length scale, decreasing it reduce the mass transfer limitation alleviating concentration gradients across the reactor (Fig. S9).

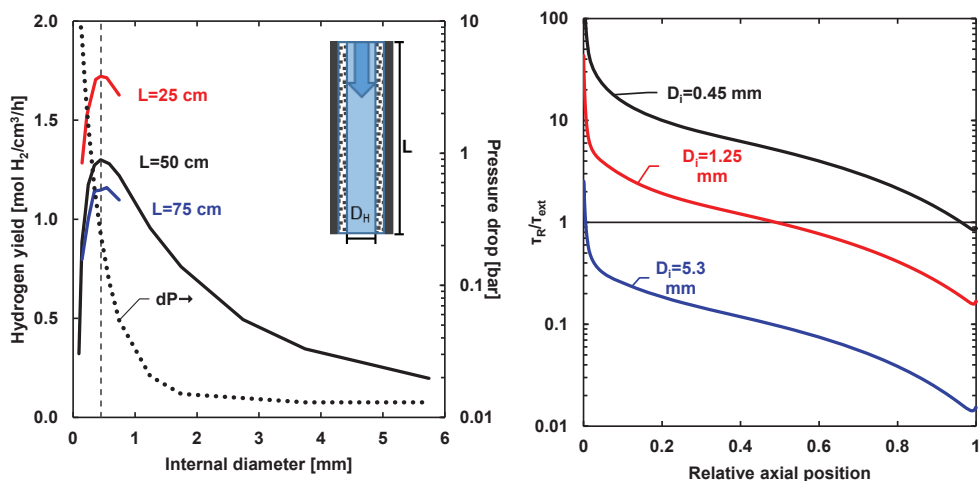


**Figure 8: Influence of reactor dimensions** A - Left) Modelled hydrogen yield as a function of internal diameter and reactor length. B - Right) Ratio of characteristic reaction time to bulk diffusion for 0.45, 1.25 and 5.3 mm internal diameter for  $L = 50$  cm. Outlet temperature of  $1015^{\circ}\text{C}$ ,  $27.7$  bar, S/C 1.8, and  $290$  kJ/mol  $\text{CH}_4$

A significant increase in reactor capacity is predicted by reducing the internal diameter, but with an increasing pressure drop (Fig. 8A). For comparison, a typical fired reformer operates at ca.  $0.1$  mol  $\text{H}_2/\text{cm}^3_{\text{cat}}/\text{h}$  relative to the catalyst volume.<sup>47</sup> An optimal diameter of  $0.45$  mm is predicted at the given conditions, independent of reactor length within the given range, in agreement with previous results for micro-reactor studies.<sup>48,49</sup> The optimum is encountered where reaction time and mass transfer are balanced towards the outlet, as seen in Figure 8B. Further reduction in diameter results in a steep drop, as the space-time becomes smaller than the characteristic reaction time (Fig. S12). This is in part due to the increasing pressure drop, increasing the required temperature to facilitate the reaction (Fig. S1). Shorter reactors incur a lower pressure drop and can operate at higher flow rates per reactor volume (Figs. 8 and S13). For reactors shorter than  $20$  cm, insufficient contact time results in decreasing methane conversion, and increasing risk of adverse side-effects (Fig. S13). With increasing feed flow an equivalent increase in heat flux is required to drive the reaction, resulting in a higher temperature difference across the catalytic coat (Fig. S14). It should be emphasized that the predicted temperature gradients across the coat, for reactors longer than  $20$  cm, are less than  $5^{\circ}\text{C}$  (Fig. S15).

For an internal diameter of  $5.3$  mm, performance for practically the entire reactor length is limited by mass transport as  $\tau_R/\tau_{ext} < 1$  (Fig. 8B), as also predicted in Figure 7A. At a diameter of  $0.45$  mm, performance of nearly the entire reactor is limited by reaction kinetics rather than mass

transport resulting in a higher performance due to the facile kinetics, as seen in Figure 8. The pressure drop is strongly dependent on the internal diameter, and scales linearly with reactor length and flowrate.<sup>32</sup> Doubling reactor length and flow will require equivalent average heat flux to reach equivalent conversion, but with the pressure drop increasing fourfold. It should be noted that the pressure drop is based on fully laminar flow in smooth tubes. The Reynolds number never exceeds 1200, well below the transition to turbulence at 2100.<sup>32</sup> For practical operation, the uneven surface of the wash-coat may yield a larger pressure drop – however, still at a fraction of what is observed in typical conventional reformers.<sup>5,47</sup>

Assuming steady state, ideal coat, and Knudsen diffusion, internal diffusion will at no point be limiting, but thermal conductivity may result in small gradients unless coat thickness is reduced (Fig. S14).

While 0.45 mm diameter and 20 cm length are predicted favorable dimensions in terms of reactor performance, this does not account for practical limitations to coating procedures, electrical connections, or the cross-section area, relevant for the voltage required to supply the electrified reformer. The determination of which geometry complies with practicality regarding upscaling, construction, and operation, requires further work within more defined conditions, regarding intended scale, operating conditions, and electrical connection.

## 6. Conclusions

This study shows how the kinetic, mass- and heat transport interplay mechanism are radically changed in electrified steam methane reforming compared to current industrial standards. Hence, the electrified reformer to a large extent eliminates the constraints imposed by the current industrial standards. Utilization of wash-coated catalyst and integrated joule heating provides an effectiveness factor, which is markedly higher than industrial steam methane reforming, and which in principle can be engineered to any desired level. Characteristic timescale analysis reveals that heat transfer is the least limiting mechanism, the performance instead governed by diffusion. Optimal performance based on fluid dynamic simulations favors channels below 0.5 mm in diameter, and high linear gas velocities, towards alleviating mass transfer limitations. Electrified steam methane reforming is a promising alternative to the current industrial fired reformers, as it is a more elegant solution resolving thermal limitations, while at the same time offering improved utilization of hydrocarbon feed and reduced CO<sub>2</sub> emissions.

**Associated content:** Implementation of the CFD model and additional figures are included in the supporting information.

Supporting information

Supporting Figures: Fig. S1-S16

**Author contribution:** All authors contributed substantially to this work.

**Funding:** This work was supported by Innovation Fund Denmark (IFD) under file no. 5160-00004B and research grant 9455 from Villum Fonden.

**Competing interests:** The authors declare no conflicts of interest.

**Data and materials availability:** The catalyst can be made available under a material transfer agreement for Haldor Topsoe A/S. All other data are available in the main text or the supplementary materials.

**Abbreviations:**

CFD: Computational Fluid Dynamics

GHSV: Gas hourly space velocity

S/C: Steam-to-Carbon ratio CFD: Computational Fluid Dynamics

SEM: Scanning Electron Microscopy

SMR: Steam Methane Reforming

**References:**

- (1) Bhat, S. A.; Sadhukhan, J. Process Intensification Aspects for Steam Methane Reforming: An Overview. *AIChE J.* **2009**, *55* (2), 408–422. <https://doi.org/10.1002/aic.11687>.
- (2) International Energy Agency (IEA). Tracking Industrial Energy Efficiency and CO<sub>2</sub> Emissions. **2007**, 83. [https://doi.org/10.1007/978-3-642-29446-4\\_14](https://doi.org/10.1007/978-3-642-29446-4_14).
- (3) Grand View Research. *Hydrogen Generation Market Size, Share & Trends Analysis Report By Application*; 2018.
- (4) Le Quéré, C., Moriarty, R., Andrew, R.M., Peters, G.P., Ciais, P., Friedlingstein, P., Jones, S.D., Sitch, S., Tans, P., Arneeth, A., Boden, T.A., Bopp, L., Bozec, Y., Canadell, J.G., Chini, L.P., Chevallier, F., Cosca, C.E., Harris, I., Hoppema, M., Hough, N. Global Carbon Budget 2018. *Earth Syst. Sci. Data* **2018**, *10*, 2141–2194. <https://doi.org/10.5194/essd-7-349-2015>.
- (5) Rostrup-Nielsen, J.; Christiansen, L. J. *Concepts in Syngas Manufacture*; Hutchings, G. J., Ed.; Imperial College Press, 2011.
- (6) Sehested, J. Four Challenges for Nickel Steam-Reforming Catalysts. *Catal. Today* **2006**, *111* (1–2), 103–110. <https://doi.org/10.1016/j.cattod.2005.10.002>.
- (7) Behnam, M.; Dixon, A. G. 3D CFD Simulations of Local Carbon Formation in Steam Methane Reforming Catalyst Particles. *Int. J. Chem. React. Eng.* **2017**, *15* (6), 1–17. <https://doi.org/10.1515/ijcre-2017-0067>.

- 
- (8) Xu, J.; Froment, G. F. Methane Steam Reforming: II. Diffusional Limitations and Reactor Simulation. *AIChE J.* **1989**, *35* (1), 97–103. <https://doi.org/10.1002/aic.690350110>.
- (9) Elnashaie, S. S. E. H.; Abashar, M. E. E. Steam Reforming and Methanation Effectiveness Factors Using the Dusty Gas Model under Industrial Conditions. *Chem. Eng. Process.* **1993**, *32* (3), 177–189. [https://doi.org/10.1016/0255-2701\(93\)80014-8](https://doi.org/10.1016/0255-2701(93)80014-8).
- (10) Palma, V.; Martino, M.; Meloni, E.; Ricca, A. Novel Structured Catalysts Configuration for Intensification of Steam Reforming of Methane. *Int. J. Hydrogen Energy* **2017**, *42* (3), 1629–1638. <https://doi.org/10.1016/j.ijhydene.2016.06.162>.
- (11) Roh, H. S.; Lee, D. K.; Koo, K. Y.; Jung, U. H.; Yoon, W. L. Natural Gas Steam Reforming for Hydrogen Production over Metal Monolith Catalyst with Efficient Heat-Transfer. *Int. J. Hydrogen Energy* **2010**, *35* (4), 1613–1619. <https://doi.org/10.1016/j.ijhydene.2009.12.051>.
- (12) Tronconi, E.; Groppi, G.; Boger, T.; Heibel, A. Monolithic Catalysts with “high Conductivity” Honeycomb Supports for Gas/Solid Exothermic Reactions: Characterization of the Heat-Transfer Properties. *Chem. Eng. Sci.* **2004**, *59* (22–23), 4941–4949. <https://doi.org/10.1016/j.ces.2004.07.018>.
- (13) Johnsen, K.; Ryu, H. J.; Grace, J. R.; Lim, C. J. Sorption-Enhanced Steam Reforming of Methane in a Fluidized Bed Reactor with Dolomite as CO<sub>2</sub>-Acceptor. *Chem. Eng. Sci.* **2006**, *61* (4), 1195–1202. <https://doi.org/10.1016/j.ces.2005.08.022>.
- (14) Buelens, L. C.; Galvita, V. V.; Poelman, H.; Detavernier, C.; Marin, G. B. Super-Dry Reforming of Methane Intensifies CO<sub>2</sub> Utilization via Le Chatelier’s Principle. *Science* (80-. ). **2016**, *354* (6311), 449–452. <https://doi.org/10.1126/science.aah7161>.
- (15) Ma, R.; Castro-Dominguez, B.; Mardilovich, I. P.; Dixon, A. G.; Ma, Y. H. Experimental and Simulation Studies of the Production of Renewable Hydrogen through Ethanol Steam Reforming in a Large-Scale Catalytic Membrane Reactor. *Chem. Eng. J.* **2016**, *303*, 302–313. <https://doi.org/10.1016/j.cej.2016.06.021>.
- (16) Aasberg-Petersen, K.; Nielsen, C. S.; Lægsgaard Jørgensen, S. Membrane Reforming for Hydrogen. *Catal. Today* **1998**, *46* (2–3), 193–201. [https://doi.org/10.1016/S0920-5861\(98\)00341-1](https://doi.org/10.1016/S0920-5861(98)00341-1).
- (17) Tonkovich, A. Y.; Perry, S.; Wang, Y.; Qiu, D.; Laplante, T.; Rogers, W. A. MicroChannel Process Technology for Compact Methane Steam Reforming. *Chem. Eng. Sci.* **2004**, *59* (22–23), 4819–4824. <https://doi.org/10.1016/j.ces.2004.07.098>.
- (18) Karim, A.; Bravo, J.; Gorm, D.; Conant, T.; Datye, A. Comparison of Wall-Coated and
-

- Packed-Bed Reactors for Steam Reforming of Methanol. *Catal. Today* **2005**, *110*, 86–91. <https://doi.org/10.1016/j.cattod.2005.09.010>.
- (19) Tonkovich, A. L. Y.; Daymo, E. A. Microreaction Systems for Large-Scale Production. *Microchem. Eng. Pract.* **2010**, 299–323. <https://doi.org/10.1002/9780470431870.ch13>.
- (20) Cavusoglu, G.; Dallmann, F.; Lichtenberg, H.; Goldbach, A.; Dittmeyer, R.; Grunwaldt, J. D. In Situ Characterization of Catalysts and Membranes in a Microchannel under High-Temperature Water Gas Shift Reaction Conditions. *J. Phys. Conf. Ser.* **2016**, *712* (1). <https://doi.org/10.1088/1742-6596/712/1/012054>.
- (21) Vinum, M. G.; Almind, M. R.; Engbæk, J. S.; Vendelbo, S. B.; Hansen, M. F.; Frandsen, C.; Bendix, J.; Mortensen, P. M. Dual-Function Cobalt–Nickel Nanoparticles Tailored for High-Temperature Induction-Heated Steam Methane Reforming. *Angew. Chemie - Int. Ed.* **2018**, *57* (33), 10569–10573. <https://doi.org/10.1002/anie.201804832>.
- (22) Almind, M. R.; Vendelbo, S. B.; Hansen, M. F.; Vinum, M. G.; Frandsen, C.; Mortensen, P. M.; Engbæk, J. S. Improving Performance of Induction-Heated Steam Methane Reforming. *Catal. Today* **2019**, No. September 2018, 1–8. <https://doi.org/10.1016/j.cattod.2019.05.005>.
- (23) Mortensen, P. M.; Engbæk, J. S.; Vendelbo, S. B.; Hansen, M. F.; Østberg, M. Direct Hysteresis Heating of Catalytically Active Ni–Co Nanoparticles as Steam Reforming Catalyst. *Ind. Eng. Chem. Res.* **2017**, *acs.iecr.7b02331*. <https://doi.org/10.1021/acs.iecr.7b02331>.
- (24) Zhang, Q.; Iqbal, A.; Sakurai, M.; Kitajima, T.; Takahashi, H.; Nakaya, M.; Ootani, T.; Kameyama, H. A 2D Model for the Cylinder Methane Steam Reformer Using Electrically Heated Alumite Catalyst. *16th World Hydrog. Energy Conf. 2006, WHEC 2006* **2006**, *1* (June).
- (25) Rieks, M.; Bellinghausen, R.; Kockmann, N.; Mleczko, L. Experimental Study of Methane Dry Reforming in an Electrically Heated Reactor. *Int. J. Hydrogen Energy* **2015**, *40* (46), 15940–15951. <https://doi.org/10.1016/j.ijhydene.2015.09.113>.
- (26) Wismann, S. T.; Engbæk, J. S.; Vendelbo, S. B.; Bendixen, F. B.; Eriksen, W. L.; Aasberg-petersen, K.; Frandsen, C.; Chorkendorff, I.; Mortensen, P. M. Electrified Methane Reforming: A Compact Approach to Greener Industrial Hydrogen Production. *Science (80-. )*. **2019**, *364* (6442), 756–759. <https://doi.org/10.1126/science.aaw8775>.
- (27) Lazard. *Lazard's Levelized Cost of Energy*; **2017**.
- (28) International Energy Agency (IEA), *World Energy Outlook 2017*, **2017**
-

- 
- (29) Govender, S.; Friedrich, H. Monoliths: A Review of the Basics, Preparation Methods and Their Relevance to Oxidation. *Catalysts* **2017**, *7* (12), 62. <https://doi.org/10.3390/catal7020062>.
- (30) Rothenberg, G. Heterogeneous Catalysis. In *Catalysis: Concepts and Green Applications*; Wiley-VCH Verlag GmbH & Co. KGaA: Weinheim, Germany, 2008; pp 127–187.
- (31) Xu, J. G.; Froment, G. F. Methane Steam Reforming, Methanation and Water-Gas Shift .1. Intrinsic Kinetics. *Aiche J.* **1989**, *35* (1), 88–96. <https://doi.org/10.1002/aic.690350109>.
- (32) Bird, R. B.; Stewart, W. E.; Lightfoot, E. N. *Transport Phenomena*, 2nd ed.; Anderson, W., Ed.; Wiley, 2002.
- (33) Chorkendorff, I.; Niemantsverdriet, J. W. *Concepts of Modern Catalysis and Kinetics*, 2nd Revisi.; Wiley, 2007.
- (34) Ashraf, M. A.; Sanz, O.; Montes, M.; Specchia, S. Insights into the Effect of Catalyst Loading on Methane Steam Reforming and Controlling Regime for Metallic Catalytic Monoliths. *Int. J. Hydrogen Energy* **2018**, *43* (26), 11778–11792. <https://doi.org/10.1016/j.ijhydene.2018.04.126>.
- (35) Kockmann, N. *Transport Phenomena in Micro Process Engineering*; Springer Berlin Heidelberg, 2008. <https://doi.org/10.1007/978-3-540-74618-8>.
- (36) Mbodji, M.; Commenge, J. M.; Falk, L. Preliminary Design and Simulation of a Microstructured Reactor for Production of Synthesis Gas by Steam Methane Reforming. *Chem. Eng. Res. Des.* **2014**, *92* (9), 1728–1739. <https://doi.org/10.1016/j.cherd.2013.11.022>.
- (37) Kays, W. M.; London, A. L. *Compact Heat Exchangers*, 3rd ed.; McGraw-Hill, 1984.
- (38) Nield, D. A.; Bejan, A. *Convection in Porous Media*; Springer, 2013. <https://doi.org/10.1007/978-1-4614-5541-7>.
- (39) Shen, L.; Chen, Z. Critical Review of the Impact of Tortuosity on Diffusion. *Chem. Eng. Sci.* **2007**, *62* (14), 3748–3755. <https://doi.org/10.1016/j.ces.2007.03.041>.
- (40) Nijemeisland, M.; Dixon, A. G.; Stitt, E. H. Catalyst Design by CFD for Heat Transfer and Reaction in Steam Reforming. *Chem. Eng. Sci.* **2004**, *59* (22–23), 5185–5191. <https://doi.org/10.1016/j.ces.2004.07.088>.
- (41) Rostrup-Nielsen, J. R.; Christiansen, L. J.; Bak Hansen, J. H. Activity of Steam Reforming Catalysts. *Appl. Catal.* **1988**, *43*, 287–303.
-

- (42) Sadooghi, P.; Rauch, R. Experimental and Modeling Study of Catalytic Steam Reforming of Methane Mixture with Propylene in a Packed Bed Reactor. *Int. J. Heat Mass Transf.* **2014**, *78* (2014), 515–521. <https://doi.org/10.1016/j.ijheatmasstransfer.2014.06.084>.
- (43) Geb, D.; Zhou, F.; Catton, I. Internal Heat Transfer Coefficient Determination in a Packed Bed From the Transient Response Due to Solid Phase Induction Heating. *J. Heat Transfer* **2012**, *134* (4), 042604. <https://doi.org/10.1115/1.4005098>.
- (44) Aasberg-Petersen, K.; Bak Hansen, J. H.; Christensen, T. S.; Dybkjaer, I.; Christensen, P. S.; Stub Nielsen, C.; Winter Madsen, S. E. L.; Rostrup-Nielsen, J. R. Technologies for Large-Scale Gas Conversion. *Appl. Catal. A Gen.* **2001**, *221* (1–2), 379–387. [https://doi.org/10.1016/S0926-860X\(01\)00811-0](https://doi.org/10.1016/S0926-860X(01)00811-0).
- (45) Wehinger, G. D.; Kraume, M.; Berg, V.; Korup, O.; Mette, K.; Schlögl, R.; Behrens, M.; Horn, R. Investigating Dry Reforming of Methane with Spatial Reactor Profiles and Particle-Resolved CFD Simulations. *AIChE J.* **2016**, *62* (12), 4436–4452. <https://doi.org/10.1002/aic>.
- (46) Simonsen, S. B.; Sehested, J.; Helveg, S.; Chorkendorff, I.; Dahl, S.; Skoglundh, M. Direct Observations of Oxygen-Induced Platinum Nanoparticle Ripening Studied by in Situ TEM. *J. Am. Chem. Soc.* **2010**, *132* (23), 7968–7975. <https://doi.org/10.1021/ja910094r>.
- (47) Kumar, A.; Baldea, M.; Edgar, T. F. A Physics-Based Model for Industrial Steam-Methane Reformer Optimization with Non-Uniform Temperature Field. *Comput. Chem. Eng.* **2017**, *105*, 224–236. <https://doi.org/10.1016/j.compchemeng.2017.01.002>.
- (48) Zhai, X.; Ding, S.; Chang, Y.; Jin, Y.; Cheng, Y. CFD Simulation with Detailed Chemistry of Steam Reforming of Methane for Hydrogen Production in an Integrated Micro-Reactor. *Int. J. Hydrogen Energy* **2010**, *35* (11), 5383–5392. <https://doi.org/10.1016/j.ijhydene.2010.03.034>.
- (49) Mbodji, M.; Commenge, J. M.; Falk, L.; Di Marco, D.; Rossignol, F.; Prost, L.; Valentin, S.; Joly, R.; Del-Gallo, P. Steam Methane Reforming Reaction Process Intensification by Using a Millistructured Reactor: Experimental Setup and Model Validation for Global Kinetic Reaction Rate Estimation. *Chem. Eng. J.* **2012**, *207–208*, 871–884. <https://doi.org/10.1016/j.cej.2012.07.117>.

## Supporting information

### **Implementation of CFD model**

The CFD model was implemented in the commercial software Comsol, version 5.2a using a 2D-axisymmetric geometry (Fig. 1). The model is solved with fully coupled equations for momentum, mass transfer, energy, and electric currents. A mapped mesh was used for the catalytic coat, with triangular for the fluid domain. A minimum axial resolution of 0.1 mm was used, with a finer radial resolution depending on geometry, with at least 20 points across both flow and porous domain. Higher mesh resolution did not influence the solutions. The following sections describe the implementation of the equations, and is in part reproduced from previous work <sup>1</sup>.

#### I. Fluid momentum equations

Fluid momentum was implemented by the Brinkman equation,<sup>2</sup> which reduces to the standard Navier-Stokes for non-porous domains:

$$\frac{\rho}{\theta_p} (\mathbf{u} \cdot \nabla) \frac{\mathbf{u}}{\theta_p} = -\nabla p + \nabla \cdot \left[ \frac{1}{\theta_p} \left\{ \mu_{mix} \nabla \mathbf{u} - \frac{2}{3} \mu_{mix} (\nabla \cdot \mathbf{u}) \mathbf{I} \right\} \right] - \left( \frac{\mu_{mix}}{\kappa} \right) \mathbf{u} \quad (\text{S1})$$

Here,  $\rho$  is the density [kg/m<sup>3</sup>],  $\theta_p$  is the washcoat porosity,  $\mathbf{u}$  is the velocity field vector [m/s],  $p$  is pressure [bar],  $\kappa$  is permeability [m<sup>2</sup>],  $\mathbf{I}$  is an identity matrix, and  $\mu$  is mixed viscosity [kg/m/s], calculated by:<sup>3</sup>

$$\mu_{mix} = \sum_{i=1}^N \frac{x_i \mu_i}{\sum_j x_j \Phi_{ij}} \quad (\text{S2})$$

Here,  $x_i$  is molar fraction of species  $i$ ,  $\mu_i$  viscosity, and  $\Phi_{ij}$  is a dimensionless quantity defined as:<sup>3</sup>

$$\Phi_{ij} = \frac{1}{\sqrt{8}} \left( 1 + \frac{M_i}{M_j} \right)^{-1/2} \left[ 1 + \left( \frac{\mu_i}{\mu_j} \right)^{1/2} \left( \frac{M_j}{M_i} \right)^{1/4} \right]^2 \quad (\text{S3})$$

Here  $M_i$  is molecular weight, and  $\mu_i$  is dynamic viscosity.  $i$  and  $j$  represent the gas species, as detailed in the mass transfer section below.

The inlet boundary condition for fluid momentum is specified as a mass flow, with a fully developed laminar profile. The flow is at all points laminar (Reynolds number < 2100) relevant for the evaluation of the Sherwood number used in the characteristic timescale for transverse diffusion.<sup>3,4</sup> The outlet condition is specified by pressure (1 atm or 26.7 barg).

Temperature-dependent density calculated assuming the gas behaving as ideal.<sup>5</sup> Temperature-dependent viscosity is implemented by Chapman-Enskog kinetic gas theory,<sup>3</sup> except for steam where data from literature were fitted to a 1<sup>st</sup> order polynomial (Supplementary Figure S16).<sup>6</sup>

## II. Mass transport

Mass transport was implemented as:

$$\rho(\nabla \cdot \mathbf{u})\omega_i = -\nabla \cdot \mathbf{j}_i + R_i \quad (S4)$$

Here,  $\omega_i$  is the mass fraction of species  $i$ ,  $\mathbf{j}_i$  mass flux vector [kg/m<sup>2</sup>], and  $R_i$  a rate expression for consumption or production [kg/m<sup>3</sup>/s]. The mass flux is defined as:

$$\mathbf{j}_i = -\rho D_{eff} \frac{\nabla x_i}{x_i} \quad (S5)$$

Here,  $D_{eff}$  is an effective, mixture-averaged diffusion coefficient [m<sup>2</sup>/s], accounting for tortuosity by the Bruggeman correlation,<sup>7</sup> which for porous domains is calculated as:

$$D_{eff} = \frac{\theta_p}{\tau} \left( \frac{1}{\bar{D}_m} + \frac{1}{D_{i,K}} \right)^{-1}, \tau = (\theta_p)^{-3/2} \quad (S6)$$

Here,  $\bar{D}_m$  is the averaged molecular diffusion, and  $D_{i,K}$  – the Knudsen diffusion:<sup>8</sup>

$$D_K = \frac{d_{pore}}{3} \sqrt{\frac{8RT}{\pi M_w}} \quad (S7)$$

For non-porous domains, a mixture-averaged model was used:

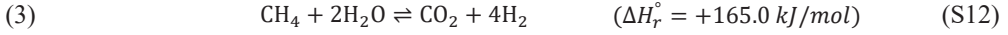
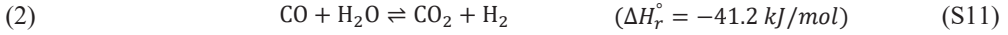
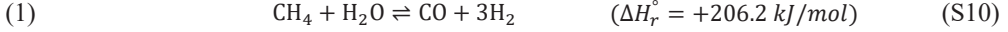
$$D_i^m = \frac{1 - \omega_i}{\sum_{k \neq i}^N \frac{x_k}{D_{ik}}} \quad (S8)$$

Here,  $D_{ik}$  is a binary diffusion coefficient, calculated by the Chapman-Enskog kinetic gas theory:<sup>3</sup>

$$D_{ik} = \frac{3}{16} \sqrt{\frac{2(RT)^3}{\pi} \left( \frac{1}{M_i} + \frac{1}{M_k} \right) \frac{1}{\tilde{N} p \sigma_{ik}^2 \Omega_{D,ik}}} \quad (S9)$$

Here,  $\tilde{N}$  is the Avogadro number [1/mol],  $p$  is the absolute pressure [Pa],  $\sigma_{ik}$  is the Lennard-Jones parameter derived from viscosity [ $\text{\AA}$ ],<sup>9</sup> and  $\Omega_{D,ik}$  is the collision integral.<sup>3</sup>

The rate expression was based on the kinetic model derived by Xu & Froment,<sup>10</sup> calculated for the following reactions:



The rate expressions for the equations are given as:

$$r_1 = \frac{k_1}{p_{\text{H}_2}^{2.5}} \left( p_{\text{CH}_4} p_{\text{H}_2\text{O}} - \frac{p_{\text{H}_2}^3 p_{\text{CO}}}{K_1} \right) / \text{DEN}^2 \quad (\text{S13})$$

$$r_2 = \frac{k_2}{p_{\text{H}_2}} \left( p_{\text{CO}} p_{\text{H}_2\text{O}} - \frac{p_{\text{H}_2} p_{\text{CO}_2}}{K_2} \right) / \text{DEN}^2 \quad (\text{S14})$$

$$r_3 = \frac{k_3}{p_{\text{H}_2}^{3.5}} \left( p_{\text{CH}_4} p_{\text{H}_2\text{O}}^2 - \frac{p_{\text{H}_2}^4 p_{\text{CO}_2}}{K_3} \right) / \text{DEN}^2 \quad (\text{S15})$$

$$\text{DEN} = 1 + K_{\text{CO}} p_{\text{CO}} + K_{\text{H}_2} p_{\text{H}_2} + K_{\text{CH}_4} p_{\text{CH}_4} + K_{\text{H}_2\text{O}} p_{\text{H}_2\text{O}} / p_{\text{H}_2} \quad (\text{S16})$$

The reaction rates are implemented in the porous coat as:

$$R_1 = k_{as} \frac{k_1 p_{\text{CH}_4} p_{\text{H}_2\text{O}} \rho_{coat} (1 - \beta)}{p_{\text{H}_2}^{2.5} \text{DEN}^2}, \quad \beta = \frac{p_{\text{H}_2}^3 p_{\text{CO}}}{K_1 p_{\text{CH}_4} p_{\text{H}_2\text{O}}} \quad (\text{S17})$$

Here,  $k_1$  is an Arrhenius type expression [ $\text{kmol} \cdot \text{bar}^{1/2} / \text{kg}_{cat} / \text{h}$ ],  $K_1$  an equilibrium constant [ $\text{bar}^2$ ],<sup>11</sup>  $\rho_{coat}$  the coat density [ $\text{kg}/\text{m}^3$ ], and  $K_\alpha$  in equation S16, the various adsorption coefficients.<sup>10</sup>  $k_{as}$  is a fitting parameter, reflecting change in support/particle size/loading relative to the catalyst employed by Xu & Froment.<sup>10</sup> As the overall reaction is strongly endothermic, they contribute as a heat sink in the model, which is calculated by:

$$Q_r = R_i \Delta H_{r,i}. \quad (\text{S18})$$

A thin layer with catalytic activity but without mass transport limitation,  $\delta_m$  was implemented at the internal surface beneath the coat to account for the presence of residual nickel from impregnation (Fig. S2). This layer was too thin to accurate mesh for modelling of transport limitations, and the thickness of the layer,  $\delta_m$ , is used as a fitting variable instead.

The composition of the feed gas was specified in molar fractions at the inlet of the reactor (Fig. 1).

### III. Energy transport

Energy, specifically temperature, was implemented according to:

$$\rho C_p \mathbf{u} \cdot \nabla T = k_{eff} \nabla^2 T + Q_h + Q_r + Q_{rad} \quad (S19)$$

Here,  $C_p$  is the heat capacity [J/kg/K],  $k_{eff}$  the effective thermal conductivity [W/m/K],  $Q_h$  the heat source from electric currents [W/m<sup>3</sup>], and  $Q_r$  the heat sink for the endothermic reactions [W/m<sup>3</sup>]. The effective thermal conductivity for the porous coat was implemented as parallel:

$$k_{eff} = \theta_p k_{solid} + (1 - \theta_p) k_{mix} \quad (S20)$$

Here,  $k_{solid}$  is the thermal conductivity of the solid phase (e.g., zirconia or FeCrAlloy), with  $k_{mix}$  being the mixed thermal conductivity for the gas phase, calculated equivalent to the mixed viscosity:<sup>3</sup>

$$k_{mix} = \frac{\sum_{i=1}^N x_i k_i}{\sum_j x_j \Phi_{ij}} \quad (S21)$$

Thermal conductivity of the insulation was implemented as temperature dependent, according to the manufacturers data (FreeFlow), but with a fitting parameter to account for non-ideal density, assuming uniform density. External heat losses were included both as a constant heat flux coefficient, and by radiation,  $Q_{rad}$ , assuming temperature independent emissivity, and constant ambient temperature. Including radiation on internal boundaries did not influence the results. Fixed temperature was specified at the inlet for all simulations at 105°C or 466°C, and on the vertical external surface of the copper sockets for ambient simulations (Fig. 1).

### IV. Electric currents

The electric currents are implemented according to Ohm's law:

$$\mathbf{J} = \sigma \mathbf{E} \quad (S22)$$

Here,  $\mathbf{J}$  is the current density flux [A/m<sup>2</sup>], and  $\mathbf{E}$  the electric field vector [V/m]. The measured root mean square (RMS) potential is set as a boundary on one of the copper socket, with the other assigned as ground. The contact resistance measured between the copper sockets and the FeCrAlloy tube was implemented equivalent to heat transfer coefficients:

$$\mathbf{n} \cdot \mathbf{J}_i = h_c (V_i - V_j) \quad (S23)$$

Here,  $\mathbf{n}$  is the normal vector on the contact resistance surface,  $\mathbf{J}_i$  is the current density vector [A/m<sup>2</sup>],  $(V_i - V_j)$  the potential difference across the surface [V], and  $h_c$  a resistance factor [S/m<sup>2</sup>]. The heat generation was calculated as:

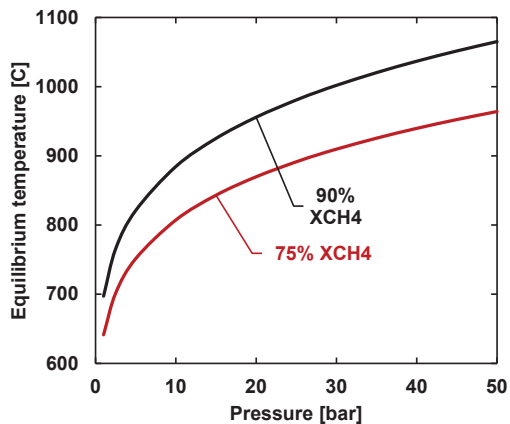
$$Q_h = \mathbf{E} \cdot \mathbf{J} \left[ \frac{W}{m^3} \right] \quad (S24)$$

For temperature dependence of the FeCrAlloy, the linearized resistivity approximation is used, based on data from the manufacturer (Goodfellow).

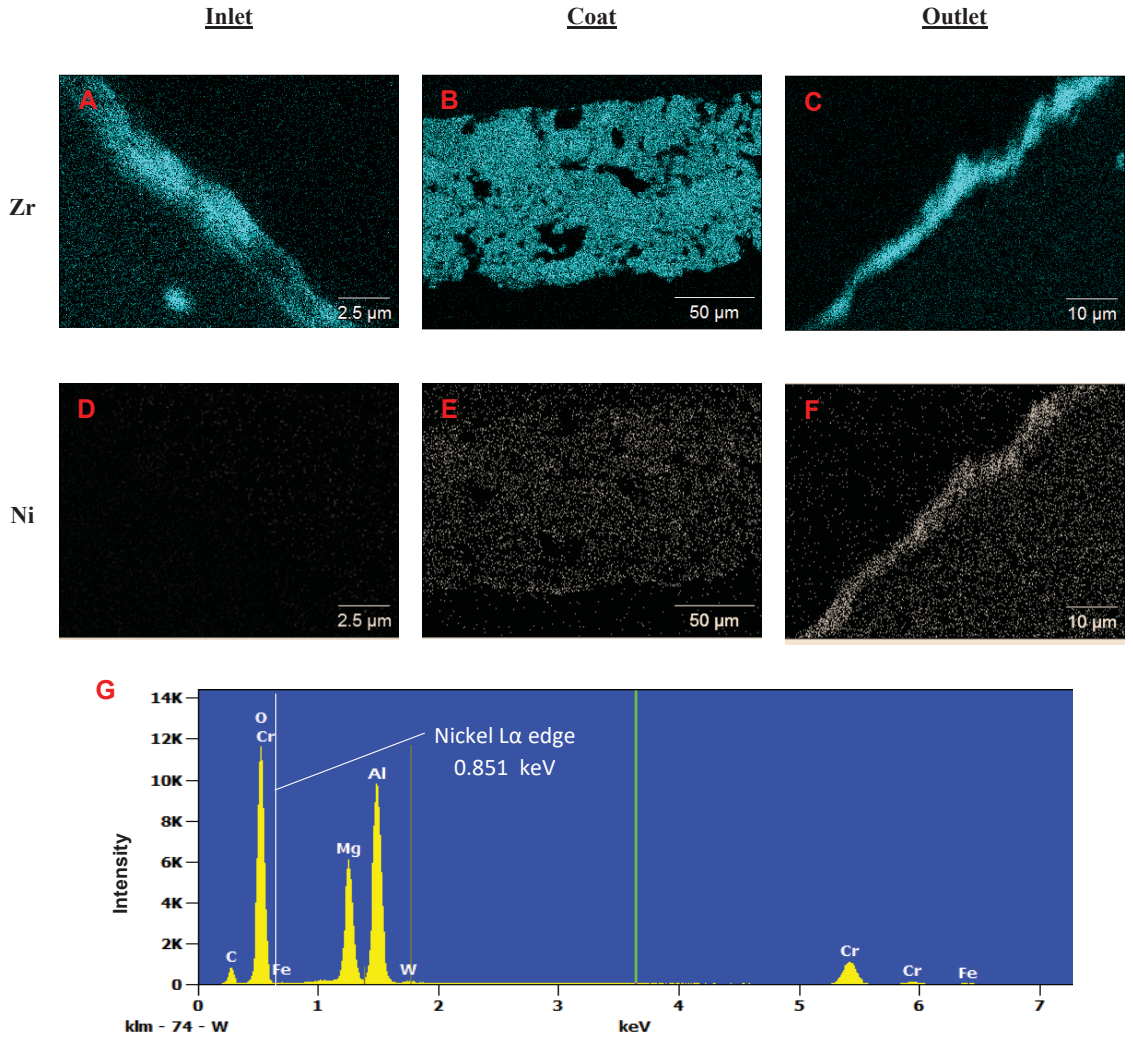
$$\sigma = \frac{1}{\rho_{ref}(1 + \alpha(T - T_{ref}))} \quad (S25)$$

Here,  $\sigma$  [ $\Omega \cdot m$ ] is the electrical conductivity,  $\rho_{ref}$  [ $S/m$ ] is the reference resistivity, and  $\alpha$  [ $1/K$ ] is the temperature coefficient of resistivity.

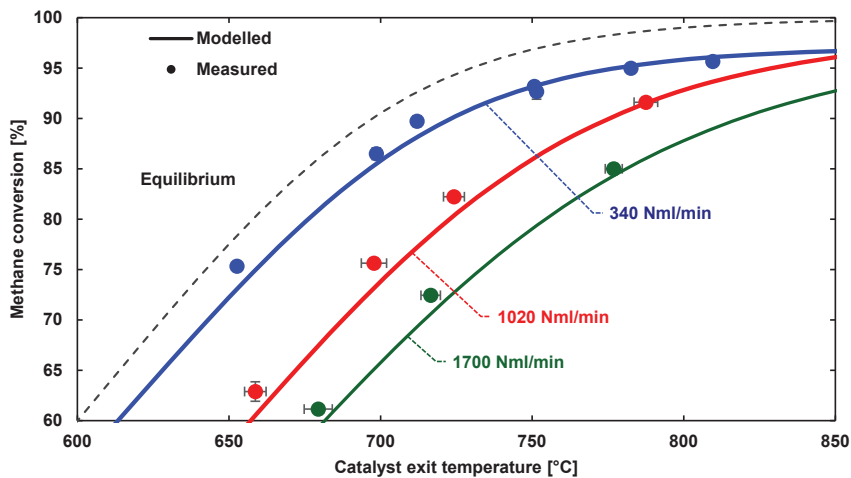
**Supplementary figures**



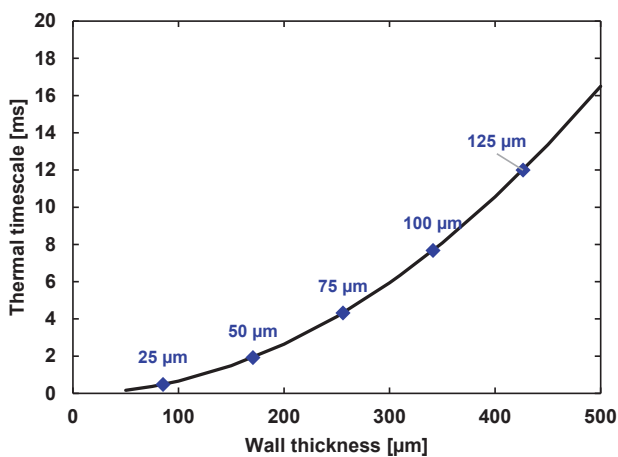
*Supplementary Figure S1: Equilibrium temperature required to reach 75 and 90% methane conversion for S/C 1.8 as a function of pressure. Calculations based on empirical equilibrium constants reported in literature (5).*



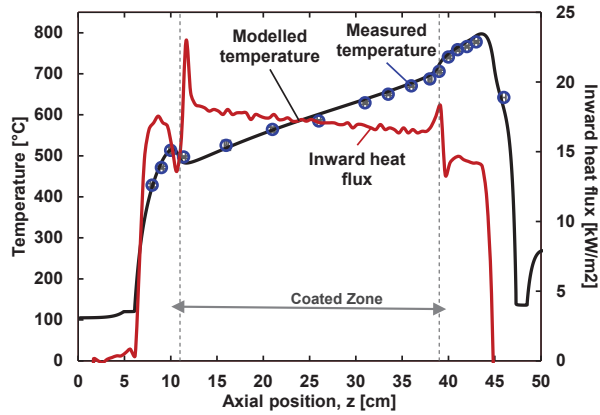
Supplementary Figure S2: A-F) SEM EDX elemental maps of zirconia and nickel signals sampled on a cross-section taken from inlet, coat, and outlet. As seen from A & C, there is a thin layer of residual zirconia coat present, but from D-F, that nickel is only present in the coat and residual coat towards the outlet. G) SEM EDX point scan at residual coat at inlet with no detection of nickel. Figure reproduced from <sup>1</sup>



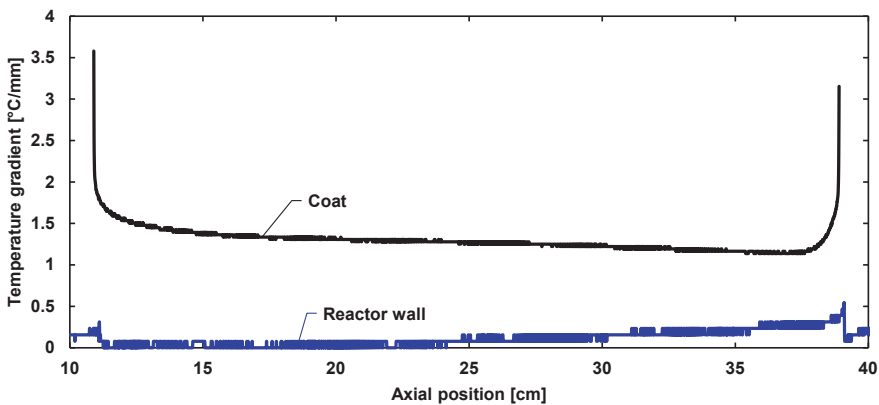
Supplementary Figure S3: Calculated approach and modelled temperature at  $z = 44.5$  cm for different flow and conversion. The over prediction in temperature could indicate the reaction running slightly backwards relative to the measured point. The average error for temperature and conversion is  $\pm 9.5^\circ\text{C}$  and  $\pm 1.75\%$ , respectively.



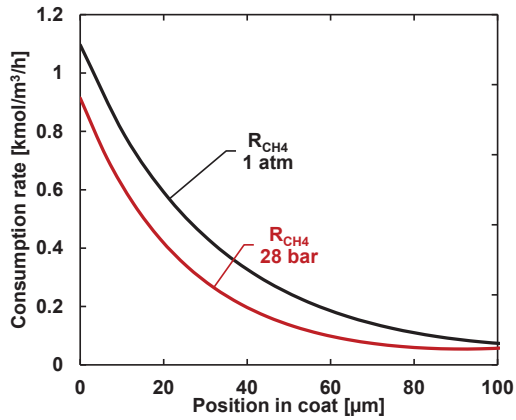
Supplementary Figure S4: Characteristic thermal timescale for the reactor wall with corresponding coat thickness for equivalent limit. The reactor wall of the experimental setup is  $350\ \mu\text{m}$ . Thermal timescale for wall is across the entire wall, with external fluctuation. Assuming uniform electric heating, characteristic timescale for the wall should be divided by 4.



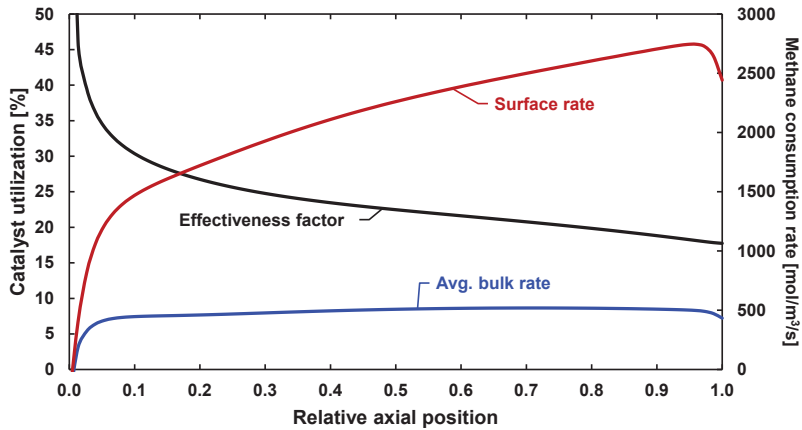
Supplementary Figure S5: Measured and modelled axial temperature profile, and calculated inward heat flux. Temperature profile reproduced from [Article 1 ref]. 1700 Nml/min, S/C 2, 50 mbarg, 85% methane conversion. Along the coated zone, there is a near constant heat flux, as the endothermic reaction consumes the available energy. The slow decline is due to increasing losses through the external insulation, related to the higher temperatures towards the outlet.



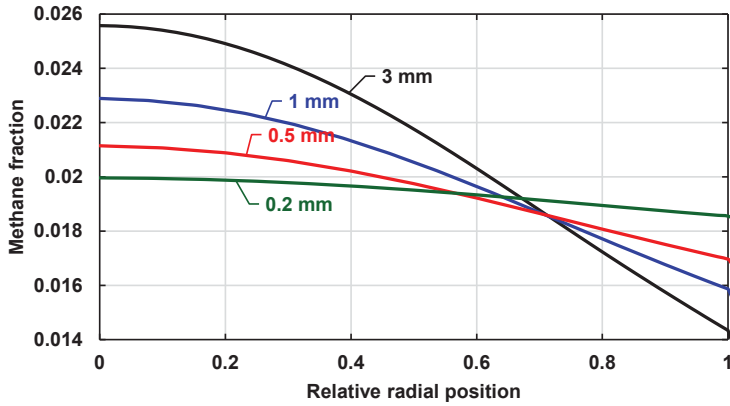
Supplementary Figure S6: Modelled temperature difference across wall and coat evaluated along the z-axis. 1700 Nml/min, ambient pressure, S/C 2, 85% methane conversion. The peaks at the end of the coat is related to the increased exposed surface area, correlated to a higher heat consumption from the endothermic SMR reaction.



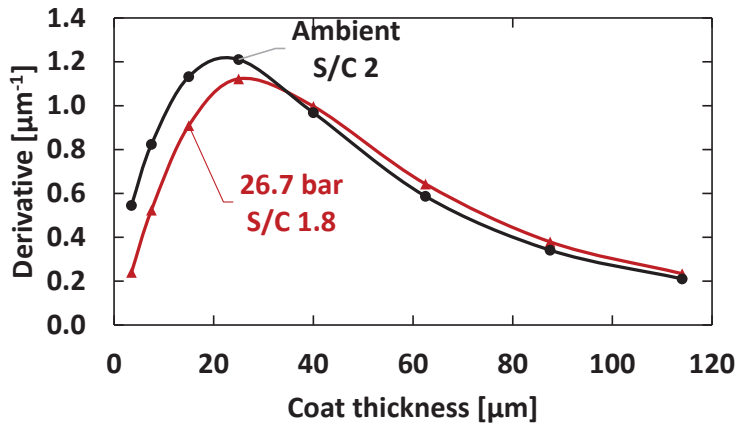
Supplementary Figure S7: Radial reaction rate evaluated at  $z = 25$  cm, at ambient and industrial conditions (See Table 1). Both at  $L/DH = 105$ .



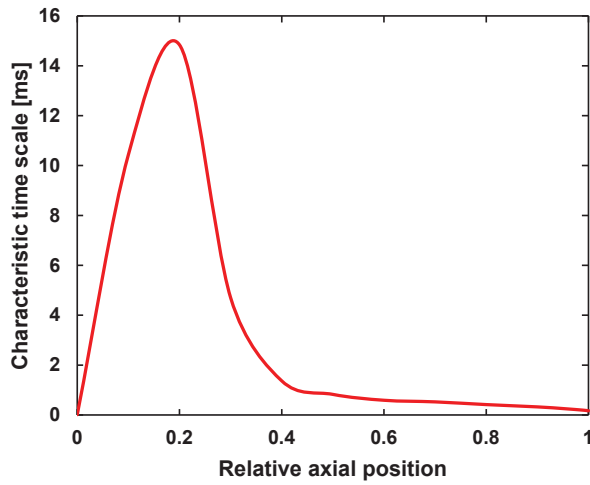
Supplementary Figure S8: Axial methane consumption rate evaluated at the surface and averaged across the bulk. The effectiveness factor is the ratio between bulk and surface rate.



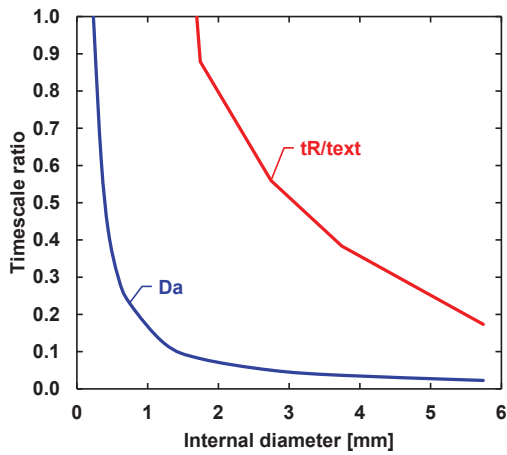
Supplementary Figure S9: Methane fraction profile evaluated at outlet for different reactor diameters. The relative radial position is evaluated between the reactor center and the surface of the coat.



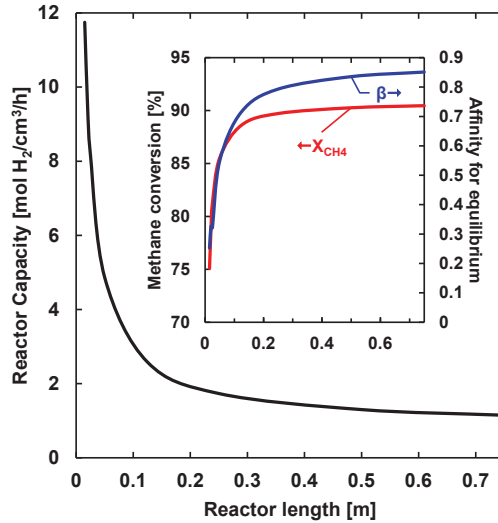
Supplementary Figure S10: Optimal effectiveness factor increase as a function of reduced coat thickness. Taken as the derivative of the effectiveness factor in Figure 5 relative to coat thickness



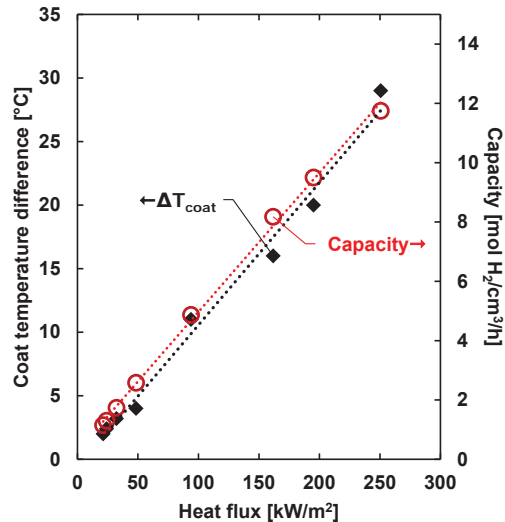
Supplementary Figure S11: Reaction time for a typical industrial reformer. Based on data from <sup>12</sup>.



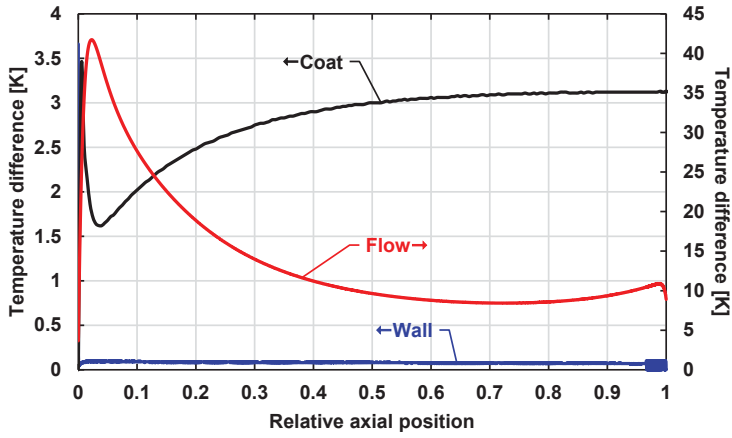
Supplementary Figure S12: Characteristic timescale for increasing diameter. Evaluated at 1015°C outlet and 90% methane conversion.



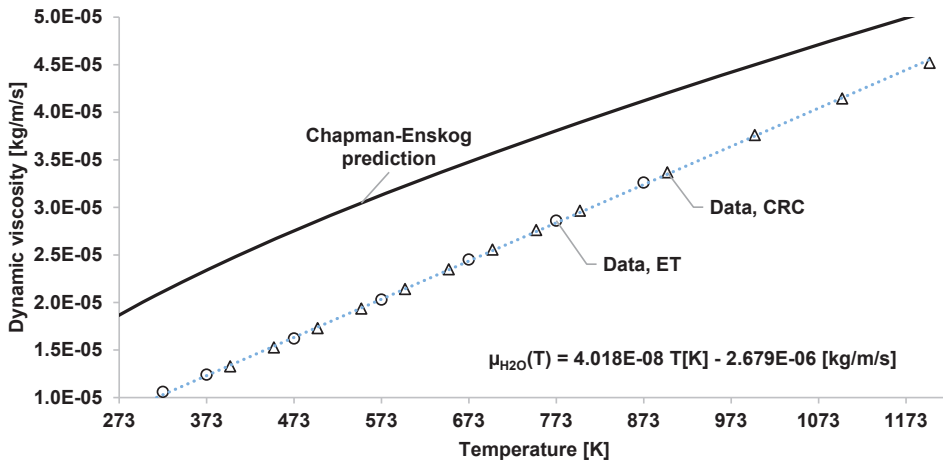
Supplementary Figure S13: Hydrogen yield as a function of reactor length, showing improved yield at shorter reactor lengths. As the reactor length decrease, a drop in methane conversion and approach to equilibrium is observed, indicating a decrease in reaction efficiency. 1015°C outlet temperature, 27.7 bar outlet, S/C 1.8, 466°C inlet temperature, 290 kJ/mol CH<sub>4</sub> energy supply.



Supplementary Figure S14: Thermal difference across the coat and reactor capacity as a function of heat flux. A linear correlation between heat flux and capacity is seen, based on results of SI, Fig16. As the heat flux increase, so does the temperature difference across the coat. 1015°C outlet temperature, 27.7 bar outlet, S/C 1.8, 466°C inlet temperature, 290 kJ/mol CH<sub>4</sub> energy supply.



Supplementary Figure S15: Temperature difference across coat, wall, and flow at industrial conditions, 90% methane conversion. 0.45 mm internal diameter.



Supplementary Figure S16: Chapman-Enskog predicted viscosity, compared against literature values. <sup>6, 13</sup>

- (1) Wismann, S. T.; Engbæk, J. S.; Vendelbo, S. B.; Bendixen, F. B.; Eriksen, W. L.; Aasberg-petersen, K.; Frandsen, C.; Chorkendorff, I.; Mortensen, P. M. Electrified Methane Reforming: A Compact Approach to Greener Industrial Hydrogen Production. *Science* (80-. ). **2019**, *364* (6442), 756–759. <https://doi.org/10.1126/science.aaw8775>.
- (2) Nield, D. A.; Bejan, A. *Convection in Porous Media*; Springer, 2013. <https://doi.org/10.1007/978-1-4614-5541-7>.
- (3) Bird, R. B.; Stewart, W. E.; Lightfoot, E. N. *Transport Phenomena*, 2nd ed.; Anderson, W., Ed.; Wiley, 2002.
- (4) Mbodji, M.; Commenge, J. M.; Falk, L. Preliminary Design and Simulation of a Microstructured Reactor for Production of Synthesis Gas by Steam Methane Reforming. *Chem. Eng. Res. Des.* **2014**, *92* (9), 1728–1739. <https://doi.org/10.1016/j.cherd.2013.11.022>.
- (5) Reid, R. C.; Prausnitz, J. M.; Sherwood, T. K. *The Properties of Gases and Liquids*; McGRAW-Hill Book Company, 1977.
- (6) *CRC - Handbook of Chemistry and Physics*, 99th ed.; Rumble, J. R., Ed.; CRC Press, 2018.
- (7) Shen, L.; Chen, Z. Critical Review of the Impact of Tortuosity on Diffusion. *Chem. Eng. Sci.* **2007**, *62* (14), 3748–3755. <https://doi.org/10.1016/j.ces.2007.03.041>.
- (8) Cao, C.; Zhang, N.; Cheng, Y. Numerical Analysis on Steam Methane Reforming in a Plate Microchannel Reactor: Effect of Washcoat Properties. *Int. J. Hydrogen Energy* **2016**, *41* (42), 18921–18941. <https://doi.org/10.1016/j.ijhydene.2016.09.034>.
- (9) Reid, R. C.; Prausnitz, J. M.; Poling, B. E. *The Properties of Gases & Liquids*, 4th ed.; McGraw-Hill: New York, 1987.
- (10) Xu, J. G.; Froment, G. F. Methane Steam Reforming, Methanation and Water-Gas Shift .1. Intrinsic Kinetics. *Aiche J.* **1989**, *35* (1), 88–96. <https://doi.org/10.1002/aic.690350109>.
- (11) Rostrup-Nielsen, J.; Christiansen, L. J. *Concepts in Syngas Manufacture*; Hutchings, G. J., Ed.; Imperial College Press, 2011.
- (12) Kumar, A.; Baldea, M.; Edgar, T. F. A Physics-Based Model for Industrial Steam-Methane Reformer Optimization with Non-Uniform Temperature Field. *Comput. Chem. Eng.* **2017**, *105*, 224–236. <https://doi.org/10.1016/j.compchemeng.2017.01.002>.
- (13) Engineering Toolbox. Gases - Dynamic Viscosities [http://www.engineeringtoolbox.com/gases-absolute-dynamic-viscosity-d\\_1888.html](http://www.engineeringtoolbox.com/gases-absolute-dynamic-viscosity-d_1888.html) (accessed Jun 6, 2019).

9.1.3 Paper 3

**Electrified methane reforming: Transient thermal response and carbon activity assessment**

Wismann et al. *in preparation*

**Abstract**

Increasing implementation of renewable energy requires an infrastructure compatible with the intermittent production of green electricity. Electrical heating of the strongly endothermic reforming processes can reduce CO<sub>2</sub> emissions and substantially intensify the reactors. Herein we show through CFD modelling of a lab scale reactor, the phenomena related to fast thermal response. The experimental reactor could reach 75% methane conversion from an idle state within 2 minutes, limited by the thermal mass, thus scalable to industrial conditions. It is shown how reaction control obtained from integration of the heat source can suppress carbon formation, and enable steam to carbon ratios down to one. Optimizing inlet conditions can completely alleviate the risk of carbon deposition.

## 9.2 Appendix B: Estimation of simulation data

### 9.2.1 Estimation of Binary Diffusion coefficients

Binary diffusion coefficients are determined based on the Chapman-Enskog kinetic gas theory, which for an ideal gas is defined as:<sup>85</sup>

$$\mathcal{D}_{AB} = \frac{3}{16} \sqrt{\frac{2(RT)^3}{\pi} \left( \frac{1}{M_A} + \frac{1}{M_B} \right)} \frac{1}{\tilde{N} P \sigma_{AB}^2 \Omega_{\mathcal{D}_{AB}}} \left[ \frac{m^2}{s} \right] \quad (9.1)$$

Where  $M_i$  is the molecular weight [kg/mol],  $\tilde{N}$  is Avogadro's number [ $\text{mol}^{-1}$ ],  $P$  is pressure [Pa],  $\sigma_{AB}^2$  is the Lennard-Jones parameter for the mixture, given by:

$$\sigma_{AB} = \frac{1}{2} (\sigma_A + \sigma_B) \quad (9.2)$$

And  $\Omega_{\mathcal{D}_{AB}}$  is the collision integral, which can be approximated as:

$$\Omega_{\mathcal{D}_{AB}} = \frac{1.06036}{T^{*0.15610}} + \frac{0.19300}{\exp(0.47635T^*)} + \frac{1.03587}{\exp(1.52996T^*)} + \frac{1.76474}{\exp(3.89411T^*)} \quad (9.3)$$

With:

$$T^* = \frac{k_B T}{\varepsilon_{AB}} \quad (9.4)$$

Where  $k_B$  is the boltman constant  $1.38066 \cdot 10^{-23} \left[ \frac{J}{K} \right]$ , and  $\varepsilon_{AB}$  is a Lennard-Jones parameter for the mixture, calculated as:

$$\varepsilon_{AB} = \sqrt{\varepsilon_A \varepsilon_B} \quad (9.5)$$

The relevant parameters to for calculating binary diffusivities, are given in Table .

## 9.2 Appendix B: Estimation of simulation data

Table 9.1: Parameters for calculating binary diffusivity

	CH4	H2O	CO	H2	CO2	REF.
$M_w$ [g/mol]	16.042	18.016	28.011	2.016	44.011	<sup>147</sup>
$\sigma_{LJ}$ [Å]	3.78	3.165	3.59	2.915	3.996	<sup>85,148</sup>
$\epsilon_{LJ}/k_B$ [K]	154	78.2	110	38	190	<sup>85,148</sup>

The binary diffusion coefficients were calculated as a function of temperature, and fitted to a single term power law expression of the form  $\mathcal{D}_{AB} = c \cdot T^b$ , yielding exponents in the range of 1.663-1.717. The expression coefficients are listed in Table 9.2:

Table 9.2: Binary diffusion coefficient expressions at 1 bar, and temperature in Kelvin,  $\mathcal{D}_{AB} = c \cdot T^b$

GAS COMPOSITION	$c \times 10^{-10}$ $\left[ \frac{m^2}{s \cdot K^b} \right]$	$b$
CH4-H2O	19.990	1.684
CH4-CO	14.578	1.694
CH4-H2	55.654	1.667
CH4-CO2	9.919	1.717
H2O-CO	20.310	1.675
H2O-H2	74.702	1.659
H2O-CO2	14.387	1.690
CO-H2	61.048	1.663
CO-CO2	9.872	1.702
H2-CO2	48.191	1.671

The diffusion coefficients are in the range of  $\sim 10^{-4} - 10^{-5}$  [m<sup>2</sup>/s], corresponding to expected values from literature<sup>22,38,85</sup>.

Self-diffusion coefficients are not used in the implemented *mixture-average* model.

### 9.2.2 Estimation of viscosity

Dynamic viscosities are calculated based on gas kinetic theory<sup>85</sup>:

$$\mu = \frac{5}{16} \frac{\sqrt{\pi m k_B T}}{\pi \sigma^2 \Omega_\mu} \left[ \frac{kg}{m \cdot s} \right] \quad (9.6)$$

Where  $m$  is molecular mass [kg],  $k_B$  is the boltzman constant [J/K],  $\sigma$  is a Lennard Jones parameter [m], and  $\Omega_\mu$  is the collision integral for viscosity, approximated by:

$$\Omega_\mu = \frac{1.16145}{T^{*0.14874}} + \frac{0.52487}{\exp(0.77329T^*)} + \frac{2.6178}{\exp(2.43787T^*)} \quad (9.7)$$

Where

$$T^* = \frac{k_B T}{\varepsilon_{LJ}} \quad (9.8)$$

Values for  $\varepsilon_{LJ}$  are listed in Table 9.1Table . The calculated viscosities are shown in Figure 9.1, including experimental values found in the literature.

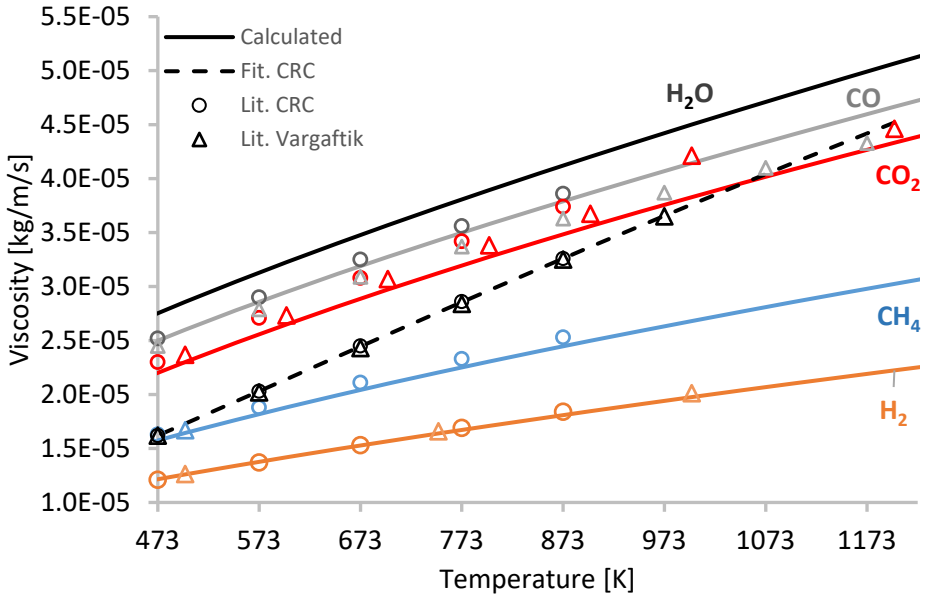


Figure 9.1: Comparison of calculated viscosities and literature values. References: CRC <sup>79</sup>, Vargaftik <sup>147</sup>

As apparent from Figure , the predicted viscosity of steam deviates significantly from values reported in literature, but is plausible due to not accounting for polarity. For steam, a function fitted to the viscosity reported in literature is used instead of the calculated values.

The mixed viscosity is calculated by Chapman-Enskog theory<sup>85</sup>, given by:

$$\mu_{mix} = \sum_{i=1}^N \frac{x_i \mu_i}{\sum_j x_j \Phi_{ij}} \quad (9.9)$$

Where  $x_i$  is the molar fraction of species  $i$ , with viscosity  $\mu_i$  [kg/m/s], and  $\Phi_{ij}$  is a dimensionless quantity defined as:

$$\Phi_{ij} = \frac{1}{\sqrt{8}} \left( 1 + \frac{M_i}{M_j} \right)^{-1/2} \left[ 1 + \left( \frac{\mu_i}{\mu_j} \right)^{1/2} \left( \frac{M_j}{M_i} \right)^{1/4} \right]^2 \quad (9.10)$$

The calculated mixed viscosity at 200 and 950°C based on equilibrium composition changes from 1.63e-5 to 4.15e-5 [kg/m/s], which is very close to the viscosity of steam. The viscosity of steam was fitted to a 1<sup>st</sup> order polynomial:

$$\mu_{H_2O} = 4.018 \cdot 10^{-8} T - 2.679 \cdot 10^{-6} \left[ \frac{kg}{m \cdot s} \right] \quad (9.11)$$

With the temperature in Kelvin. This expression was fitted between 200-1000°C for data at 1 bar. Viscosity changes negligibly with pressure (below 20 atm).<sup>147</sup>

### 9.2.3 Estimation of mixed thermal conductivity

Expressions for the thermal conductivity of the pure gases are based on polynomial fits based on literature data, and are illustrated in **Error! Reference source not found.**

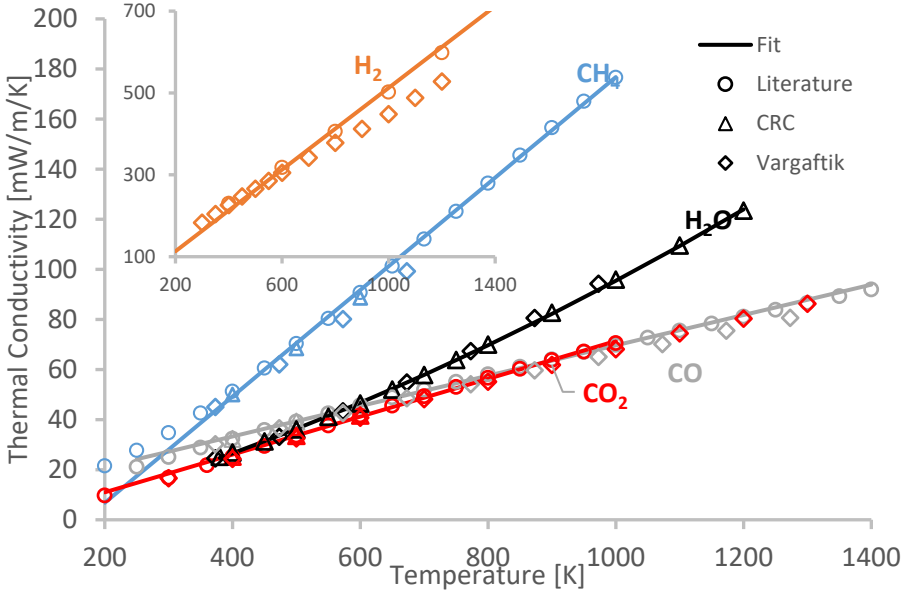


Figure 9.2: Thermal conductivity of pure gases, compared to literature values. Fits of CH<sub>4</sub>, H<sub>2</sub>O, CO, H<sub>2</sub> and CO<sub>2</sub> are based, respectively on: <sup>79,153,154,155,156</sup>

The mixed thermal conductivity is implemented according to Chapman-Enskog theory equivalent to the mixed viscosity.<sup>85</sup>

$$k_{mix} = \sum_{i=1}^N \frac{x_i k_i}{\sum_j x_j \Phi_{ij}} \quad (9.12)$$

It was found that a simple volumetric average yielded 16% higher mixed thermal conductivity, compared equation 9.12, and the full correlation was implemented.

The conductivity of the solid, porous phase was based on a correlation by Zivcova et al.,<sup>106</sup> and the density of a non-porous MgAl<sub>2</sub>O<sub>4</sub> spinel reported by Kingery et al.,<sup>149</sup> The expression for porous conductivity is given as:

$$k_{sol} = \exp\left(-\frac{1.5\varepsilon}{1-\varepsilon}\right) k_{non-porous} \quad (9.13)$$

Where the non-porous conductivity was fitted to a 2<sup>nd</sup> order polynomial, illustrated in Figure 9.3:

## 9.2 Appendix B: Estimation of simulation data

---

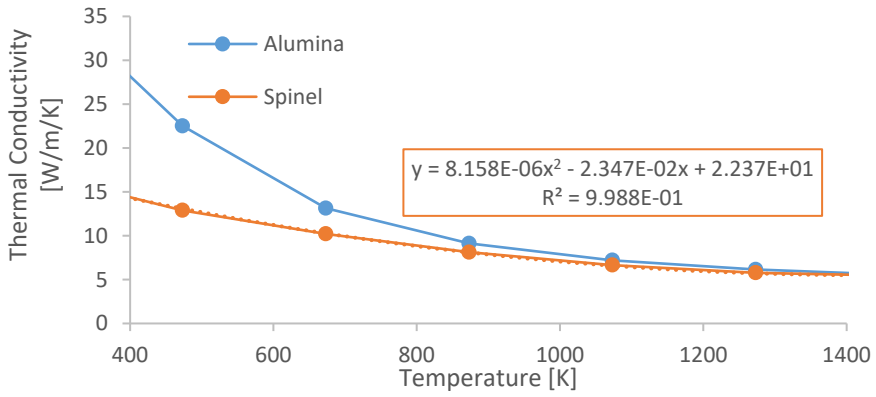
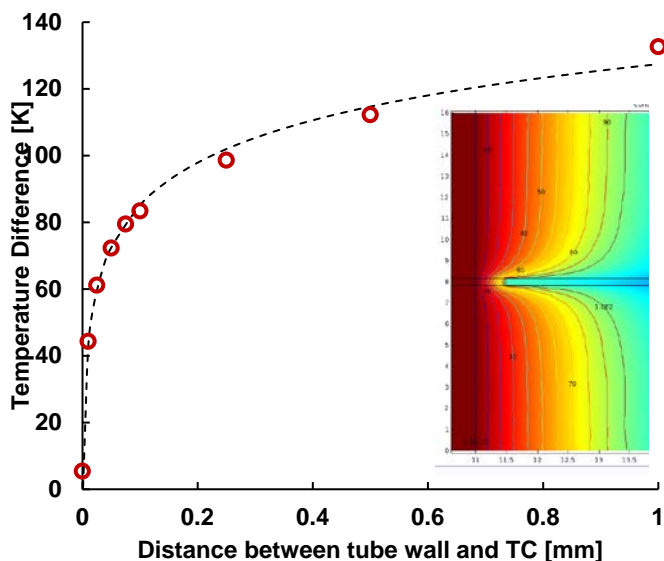
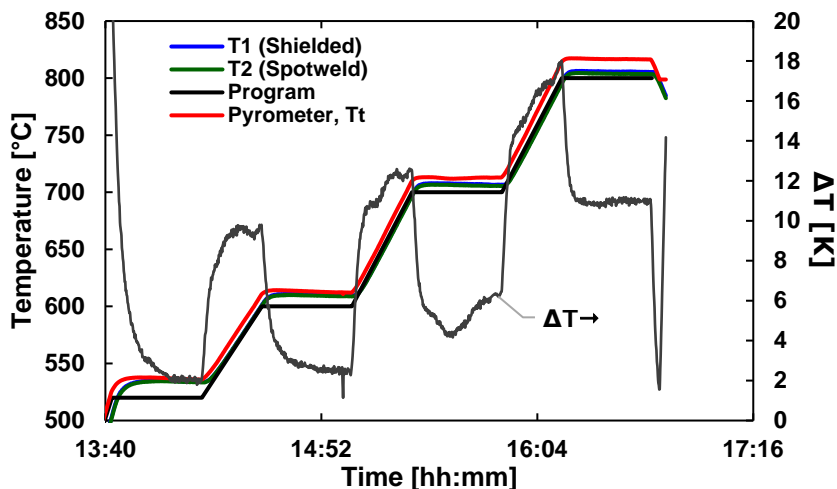


Figure 9.3: Thermal conductivity of selected non-porous ceramics. Based on <sup>149</sup>

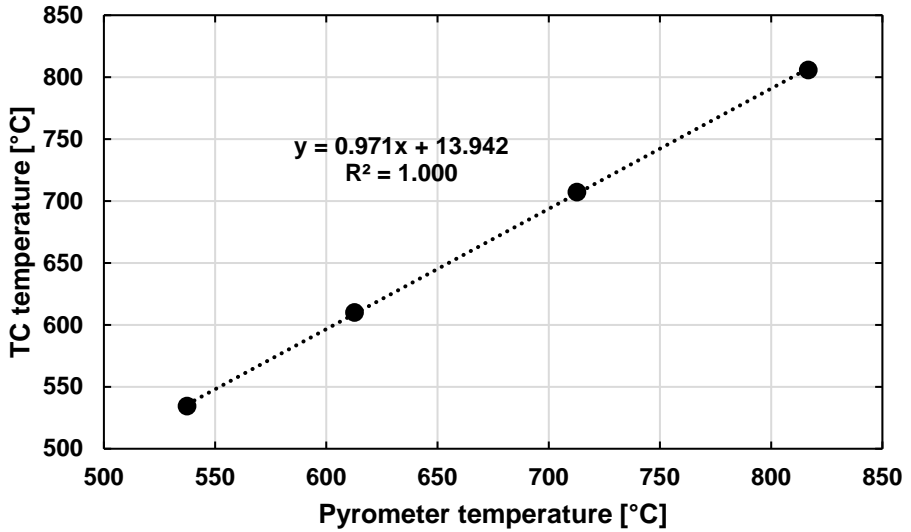
## 9.3 Appendix C: Supplementary figures



*Supplementary Figure S9.3.1: TC measurement error* Difference between actual wall temperature and temperature measured by a 1 mm K-type TC as a function of distance between wall and TC. Insert shows temperature gradient in the insulation around the thermocouple.



*Supplementary Figure S9.3.2: Pyrometer calibration* Temperature program and temperature measured by a shielded K-type TC, a spotwelded K-Type TC, and an IR pyrometer in a bed of 3 mm alumina spheres. The deviation between the two K-type TCs are at all points below 2°C. The difference between the shielded K-Type TC and the pyrometer (assuming emissivity = 1) is included in the plot, and increases with temperature.



*Supplementary Figure S9.3.3: Pyrometer correction* The “true” temperature measured by a K-type TC plotted against the temperature measured by the IR pyrometer assuming perfect black body radiation of alumina spheres (emissivity equal to unity). Each data point is an average based on the steady state temperature in Supplementary Figure S9.3.4.

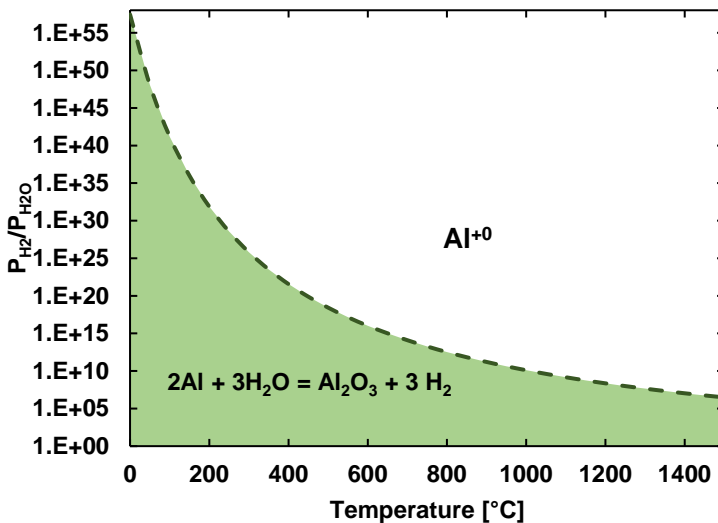
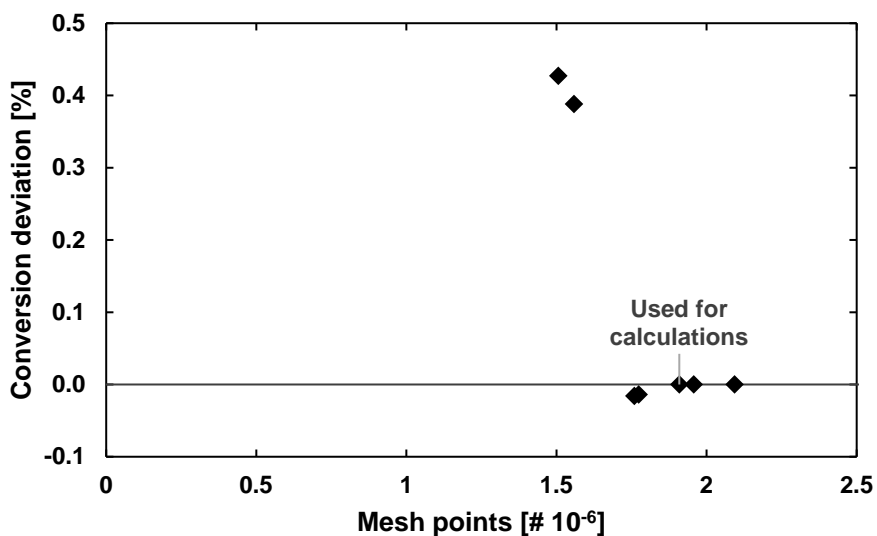
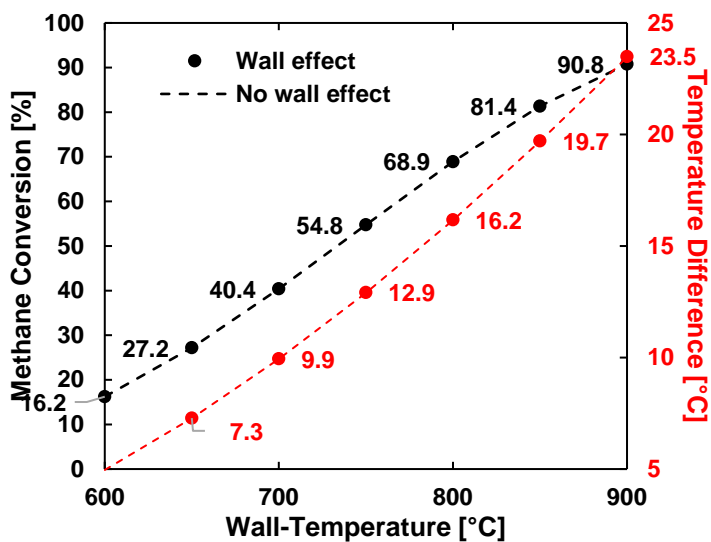


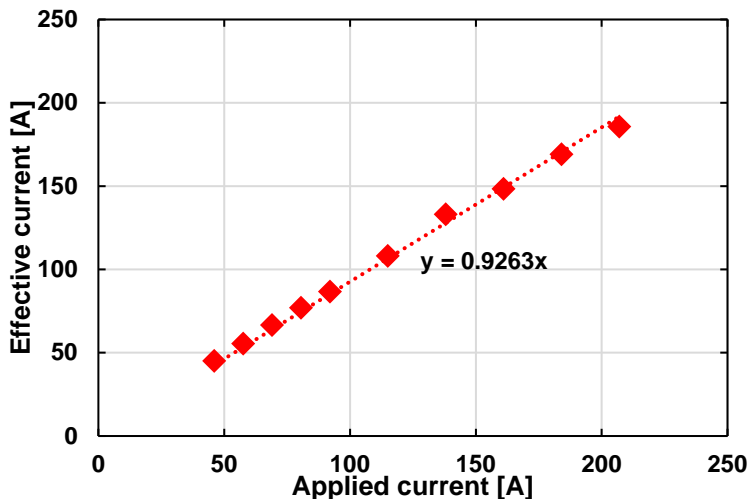
*Figure S9.3.4: Thermodynamic potential for reduction of Alumina* Thermodynamically required  $H_2/H_2O$  ratio to reduce alumina as a function of temperature. Calculations performed in HSC 6.1.



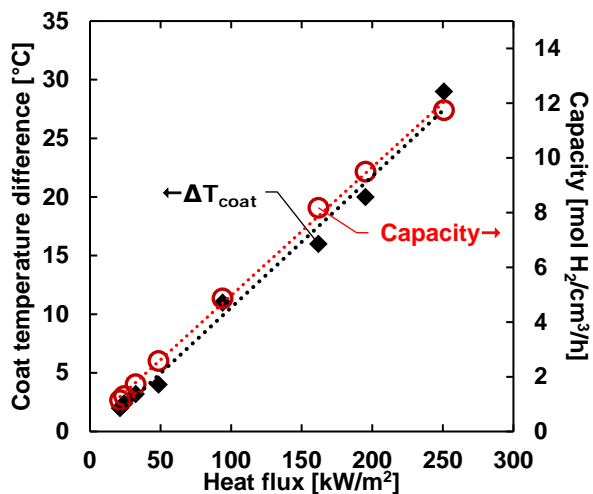
*Supplementary Figure S9.3.5: Mesh refinement analysis* Deviation from stable conversion with increasing number of elements in a mesh sensitivity analysis. Conversion is relative to the final point with the highest mesh resolution. Reproduced from<sup>28</sup>



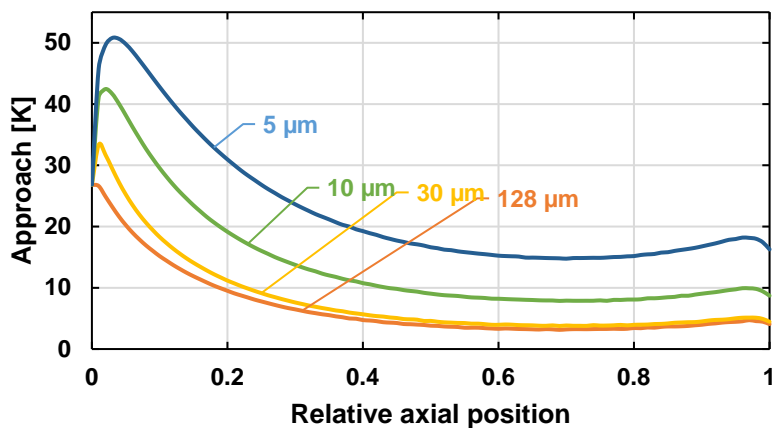
*Supplementary Figure S9.3.6: Addition of wall effect for small particles* Implementation of the wall effect proposed described in Section 4. For the small particles used in experiments, no distinguishable effect is predicted.



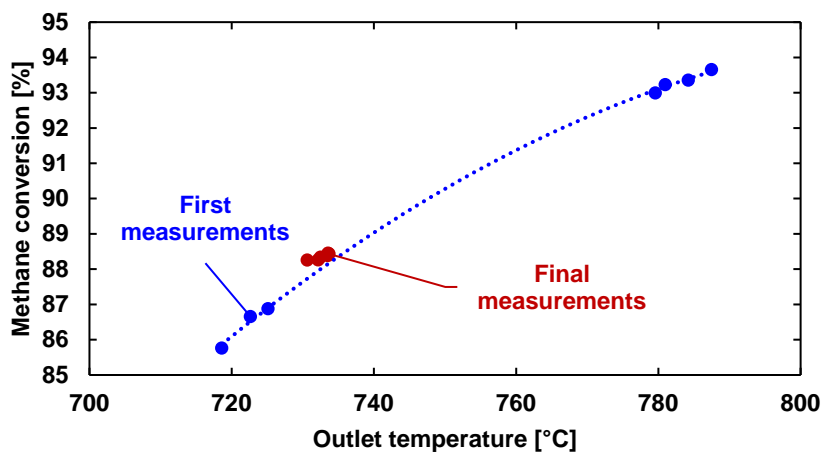
*Supplementary Figure S9.3.7: Effective coil current Calibration between current applied by the induction oven, and the effective current in the coil, correlated by pick-up coil measurements. Measurements performed by DTI.*



*Supplementary Figure S9.3.8: Heat flux dependence Thermal difference across the coat and reactor capacity as a function of heat flux. A linear correlation between heat flux and capacity is seen, based on results of SI. Fig16. As the heat flux increase, so does the temperature difference across the coat. 1015°C outlet temperature, 27.7 bar outlet, SC 1.8, 466°C inlet temperature, 290 kJ/mol CH<sub>4</sub> energy supply. Reproduced from Article 2.*



*Supplementary Figure S9.3.9: Axial approach for varying coat thickness Approach to equilibrium temperature at the internal coat surface along the coated section of the reactor. Simulation at 1700 Nml/min, ambient pressure, S/C 2, with 10% H<sub>2</sub> in feed, ca. 85% methane conversion.*



*Supplementary Figure S9.3.10: Catalyst deactivation Methane conversion plotted against measured exit temperature for the first measurement on the newly prepared system, and final measurements before disassembly for post-analysis. No discernible loss in activity was observed. Measurements were performed at 680 Nml/min, with 50 mbarg, and a gas composition of CH<sub>4</sub>, H<sub>2</sub>O, and H<sub>2</sub> (30/60/10).*

### 9.4 Appendix D: Thermocouple model system

Based on initial experimental measurements precise placement of spotwelded thermocouples is crucial to minimize the induced error (Fig. 2.1). In addition, it was found that a fitting factor for the thermal conductivity of the insulation was required to reproduce the experimental temperature profile (Section 4.3). To estimate the error and reproducibility of spotwelded thermocouples, a simpler model system was used (Fig. 9.4.2).

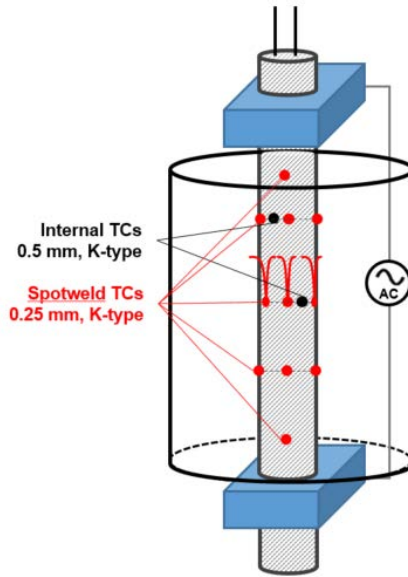
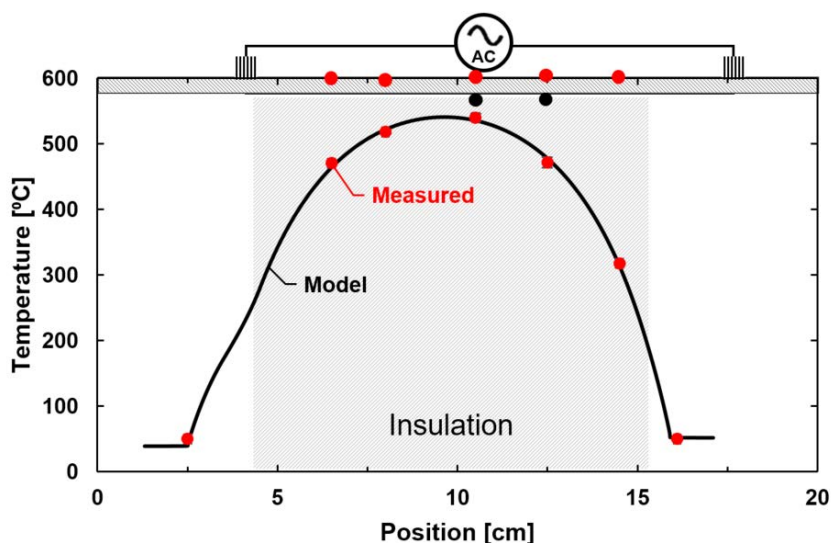


*Figure 9.4.1: TC model system 20 cm FeCrAl tube with 14 spotwelded 0.25 mm K-type TCs, 12 of which are placed in groups of four at equivalent axial position. Two 0.5 mm, shielded, K-type TCs were placed inside, at same axial position as two of the spotwelded groups. The shielded K-type was separated with a glassfiber sleeve, which also prevented any flow in the tube. The tube was insulated with 4 cm FreeFlow (Etex Industries). The tube was heated by AC potential applied across the copper sockets.*

As the temperature profile of the resistance heated reformer (Fig. 6.1) is strongly dependent on the endotherm reaction and axial convection, the model system is without flow and reaction kinetics to isolate thermal phenomena. The measured and modelled temperature profile is shown in Figure 9.4.2.



*Supplementary Figure S9.4.2: Thermocouple error* Temperature for the different positions. The cumulative standard error deviation is  $\pm 8.5^{\circ}\text{C}$ , but less than  $2.5^{\circ}\text{C}$  for the individual TCs when evaluated over 6 minutes at steady state, including the internal shielded TCs. The parabolic shape of the temperature profile is consistent with constant energy heating.

The cumulative standard error deviation is  $8.5^{\circ}\text{C}$ , with  $2.5^{\circ}\text{C}$  error for the individual thermocouples when averaged over 6 minutes. The model system only contains one fitting parameter, thermal conductivity of the insulation. It was found that the insulation conducted heat 1.55 times better than reported by the manufacture. Some of the error likely relates to non-optimal density, as the ideal insulation was reported at  $220\text{ kg/m}^3$ , where the measured density of the insulation in the model system was  $263\text{ kg/m}^3$ . In the model system, it was possible to “tap” the insulation, likely providing a better packing compared to the resistively heated system for the catalytic experiments, where the insulation was found to conduct 1.7 times better. Density variations or higher humidity than the reported test are expected to be the cause for deviation between calculated and reported values, and judged to be within reason.

## 9.5 Appendix E: Conventional SMR lab scale reactor model

This appendix is an unpublished document on the implementation of a CFD model for a lab scale setup used for SMR experiments. This work is the framework of the later models, and was concluded in July, 2017. Figure and page numbers updated.

### Model documentation – Conventional SMR lab scale reactor

Report on lab scale reactor ACU-117 at Topsoe for SMR experiments. The goal of the experiments was to create a dataset for which to implement a model to test the applicability of Comsol 5.2a as CFD software for further model development. The objective of this report is to document the model development.

### Nomenclature

$r_{i,obs}$	$\left[\frac{mol}{kg \cdot s}\right]$	Observed rate for species $i$	$k_1, k_3$	$\left[\frac{mol}{kg \cdot s}\right]$	Pre-exponential rate expression factor, Reaction 1 & 3
$\rho_{bed}$	$\left[\frac{kg}{m^3}\right]$	Skeletal porosity	$k_2$	$\left[\frac{mol}{kg \cdot s \cdot Pa}\right]$	Pre-exponential rate expression factor, Reaction 2
$\Delta H_r$	$\left[\frac{J}{mol}\right]$	Reaction enthalpy	$D_T$	$[m]$	Tube diameter
$D_p$	$[m]$	Particle diameter	$n$		Reaction order
$k_c$	$\left[\frac{m}{s}\right]$	Mass transfer coefficient	$C_{i,bulk}$	$\left[\frac{mol}{m^3}\right]$	Bulk concentration of species $i$
$\rho_{solid}$	$\left[\frac{kg}{m^3}\right]$	Density of non-porous support	$D_{eff}$	$\left[\frac{m^2}{s}\right]$	Effective diffusion coefficient
$C_{i,surf}$	$\left[\frac{mol}{m^3}\right]$	Surface concentration of species $i$	$C_M$		Mears Criterion
$C_{WP}$		Weizs-Prater Criterion	$\rho_g$	$\left[\frac{kg}{m^3}\right]$	Gas density
$\varepsilon$		Bed porosity	$\varepsilon_r$		Emissivity
$\mathbf{u}$	$\left[\frac{m}{s}\right]$	Velocity (Vector)	$P$	$[Pa]$	Absolute pressure

## 9.5 Appendix E: Conventional lab scale reactor model

$\mu$	$\left[\frac{kg}{m \cdot s}\right]$	Dynamic viscosity	$R_i$	$\left[\frac{mol}{m^3 \cdot s}\right]$	Rate of formation/consumption
$x_i$		Molar fraction of species $i$	$\omega_i$		Weight fraction of species $i$
$M_i$	$\left[\frac{g}{mol}\right]$	Molecular weight of species $i$	$R_c$	$\left[\frac{J}{mol \cdot K}\right]$	Gas constant
$T$	$[K]$	Temperature	$q$	$\left[\frac{W}{m^2}\right]$	Heat flux density
$j_i$	$\left[\frac{mol}{m^2 \cdot s}\right]$	Mass flux	$D_{AB}$	$\left[\frac{m^2}{s}\right]$	Binary diffusion coefficient
$k_i$	$\left[\frac{W}{m \cdot K}\right]$	Thermal conductivity of species $i$	$\Phi_{ij}$		Chapman-Enskog factor
$k_{solid}$	$\left[\frac{W}{m \cdot K}\right]$	Thermal conductivity of support material	$\kappa$	$[m^2]$	Permeability
$\hat{C}_p$	$\left[\frac{J}{kgK}\right]$	Mass based specific heat capacity	$\varphi$		Contact area fraction in porous bed
$k_D$	$\left[\frac{W}{m \cdot K}\right]$	Smoluchowski conductivity	$k_{rad}$	$\left[\frac{W}{m \cdot K}\right]$	Thermal conductivity from radiation
$h_r$	$\left[\frac{W}{m^2 \cdot K}\right]$	Heat transfer coefficient	$p_i$	$[Pa]$	Partial pressure of species $i$
$K_2$		Equilibrium constant for reaction 2	$K_1, K_3$	$[Pa^2]$	Equilibrium constant for reaction 1 & 3
$K_{H_2}$	$\left[\frac{1}{Pa}\right]$	Adsorption coefficient for H <sub>2</sub>	$K_{CO}$	$\left[\frac{1}{Pa}\right]$	Adsorption coefficient for CO
$K_{CH_4}$	$\left[\frac{1}{Pa}\right]$	Adsorption coefficient for CH <sub>4</sub>	$K_{H_2O}$		Adsorption coefficient for H <sub>2</sub> O
$\beta$		Reverse reaction term	$k_{as}$		Activity fitting factor

## **Contents**

<b>Nomenclature</b> .....	166
<b>Introduction</b> .....	168
<b>Geometry &amp; Domains</b> .....	168
Operation parameters .....	169
<b>Model equations</b> .....	171
<b>Simulations</b> .....	172
Parameter Influence .....	172
Results – Validation Experiment .....	173
<b>Summary</b> .....	176
<b>References</b> .....	177

## **Introduction**

---

Computational Fluid Dynamics (CFD) is a strong tool for construction of increasingly realistic models <sup>150</sup>, to predict performance, and elucidate variables and phenomena, impossible to measure. The aim of this model is a reasonable representation of a conventional Methane Steam Reforming (MSR) lab scale reactor. The results from this model can be used to tune a number of key parameters, to be used in models extended to magnetic heating, where parameters such as temperature is exceedingly difficult to measure with conventional equipment. Model implementation is done in COMSOL 5.2a.

## **Geometry & Domains**

---

The geometry is based on R117 at Haldor Topsoe, which is intended for initial validation experiments of the model. Figure 1 is a schematic of the reactor. It should be noted that the scaling is distorted to better visualize different domains.

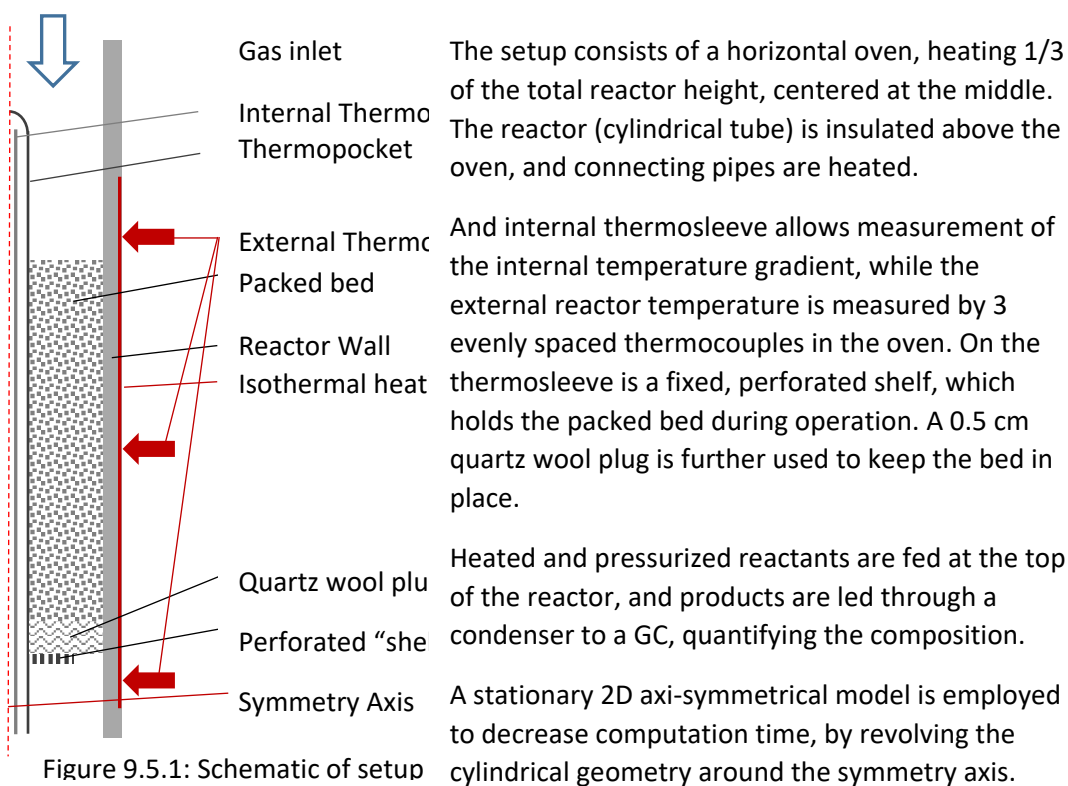


Figure 9.5.1: Schematic of setup

The model can be separated into 3 types of domain: Fluid, Solid, and Porous. The reactor wall, the shelf, and the thermopocket are treated as solid domains, where the packed bed, and quartz plug are porous. The remaining domains are treated as free fluid flow.

### Operation parameters

Initial conditions are necessary if any calculations are to be carried out. Flow, inlet temperature, oven temperature, pressure, and feed composition have to be specified to resolve the conversion. A flow of 5000 GHSV was chosen as initial value, resulting in a Reynolds number around 50, well within the laminar flow regime. The feed is preheated to 200°C to keep the water as steam. For the oven temperature an isothermal temperature is defined on the

external reactor wall, leaving the internal temperature gradient to be solved by the model. The isothermal domain is a reasonable approximation based on the oven manual.<sup>151</sup> An S/C ratio of 2.8 is employed, with 3% hydrogen in the feed. Trace amounts of CO & CO<sub>2</sub> included to help resolve initial kinetic step. The absolute pressure is set to 2 bar, to prevent backflow. An overview of initial conditions can be found in Table 1:

Table 9.5.1: Initial parameters

PARAMETER		PARAMETER	
T_INLET	200 [°C]	Flow	5000 GHSV
T_EXT	700-950 [°C]	S/C	2.8
PRESSURE (ABS)	2 [Bar]	Methane fraction, $x_{CH_4}$	0.25
PARTICLE DIAMETER, $D_p$	300 [µm]	Porosity, $\epsilon$ (Bulk)	0.35
BED DENSITY	1790 [kg/m <sup>3</sup> ]	Emissivity, $\epsilon_r$	0.8

Mear's criterion can be used to predict if the external diffusivity is limited<sup>85</sup>:

$$C_M = \frac{-r_{a,obs} \cdot \rho_{bed} \cdot R_{par} \cdot n}{k_c C_{A,bulk}} \Rightarrow C_{M,CH_4} \sim 0.0158 < 0.15$$

A rough approximation indicates that the reactor is not limited by external diffusion (at least at the top). As the conversion of methane proceeds, the bulk concentration drops significantly, increasing the value. The equivalent for inter-particle diffusion limitation is the Weizs-Prater criterion:

$$C_{WP} = -\frac{r_{obs} \rho_c R_{par}^2}{D_{eff} C_{A,surf}} \ll 1 \text{ for no internal diffusion limitation}$$

Assuming there is no external transport limitation, the bulk and surface concentrations are the same, and including Knudsen diffusion in the effective diffusion term, gives:

$$C_{WP,CH_4} \sim 3.07 > 1$$

As expected from literature, the Weisz-Prater criterion indicates that only little of the catalyst volume is active, which can be observed when the activity scales with external particle surface area. This typically results in a very low effectiveness factor.<sup>22,119,152</sup>

## **Model equations**

---

To model a heterogeneous, catalytic reaction in gas phase, 4 sets of domain equations are required: Momentum, Mass transfer, Energy, and Reaction kinetics. Momentum governs the fluid dynamics, such as velocity, density, and is influenced by eg. viscosity. Mass transfer is important to determine concentration gradients in the system, and is influenced by the velocity field and diffusion coefficients. The energy transport includes the temperature, which is crucial as almost every variable (viscosity, conductivity, equilibrium constants, etc.) is temperature dependent. All of these interact with the reaction kinetics, which for SMR introduce a layer of complexity, as the generated hydrogen has significantly different thermophysical properties compared to the other constituents.

A revised description of the CFD equations for the model are included in Section 4.2, without the magnetic field and hysteresis heating. A measured temperature profile on the external surface was used as boundary condition.

## Simulations

### Parameter Influence

A sensitivity study of selected model parameters was performed to investigate how it influences the temperature profile along the reactor center.

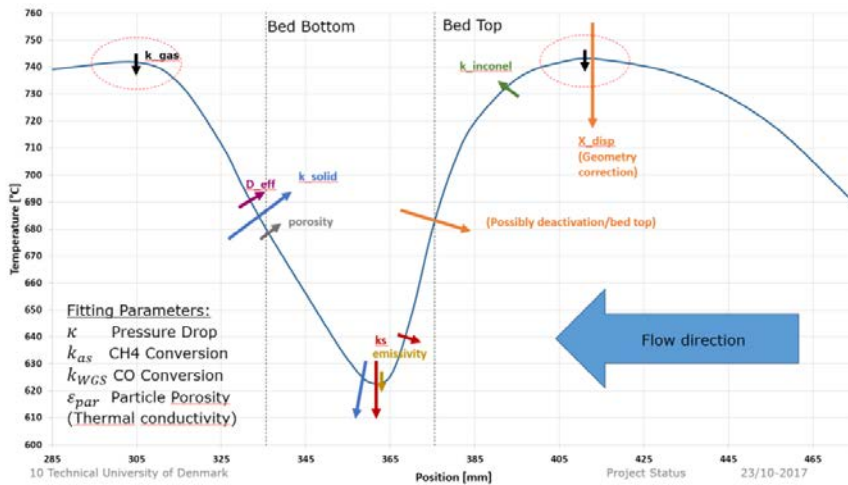


*Figure 9.5.2 Axial temperature profile and parameter influence* Modelled axial temperature profile with arrows indicating the change in the profile by increasing the different model parameters. The arrows are approximately to scale relative to the influence on the model for a change of an order of magnitude.  $k_{gas}$  is the thermal conductivity of the mixed gas phase,  $k_{inconel}$  is the reactor wall conductivity,  $D_{eff}$  is the effective porous diffusivity,  $k_{solid}$  is the conductivity of the catalyst,  $k_s$  is the activity fitting factor.  $x_{disp}$  is a geometry fitting factor, and directly influence the position, but not the shape of the endothermic drop.

Thermal conductivity of the catalyst had the most pronounced effect on the shape of the temperature profile, as evident from the figure above. The second most prominent effect is by adjusting reactor activity, for this model equivalent to an effectiveness factor.

## Results – Validation Experiment

### Temperature

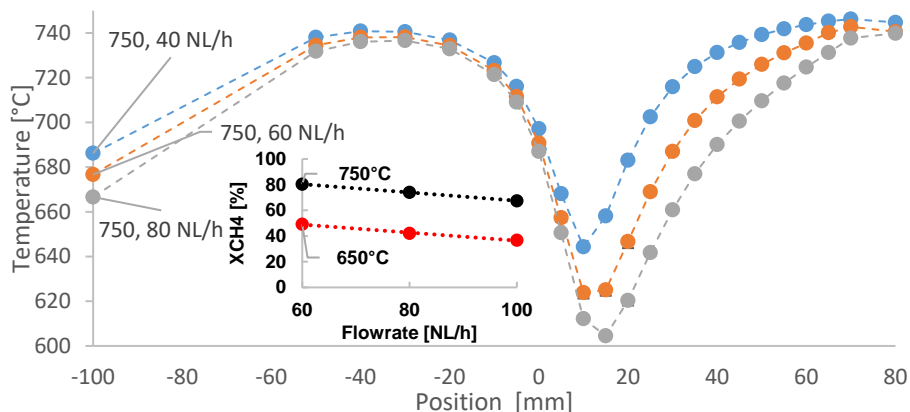


**Figure 9.5.3: Internal temperature profile** Temperature profile as a function of flow at 750°C,  $S/C = 2$ . Insert shows the methane conversion as a function of flowrate.

As the flowrate increases, a steeper temperature drop is observed along with the minimum shifting further towards the top of the bed. The inlet temperature (80 mm) is nearly the same temperature for all flowrates, but the additional cooling of high flows yield slightly lower outlet temperatures (-100 mm). Figure 9.5.4 shows the modelled temperature profile against the measured temperature profile for 60 NI/h at 750°C.

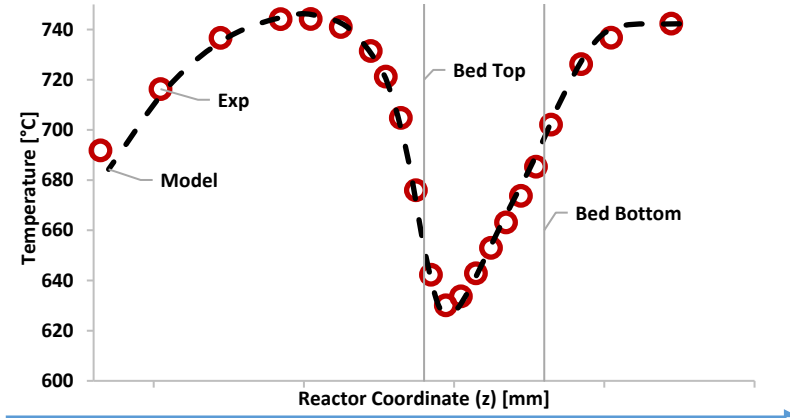
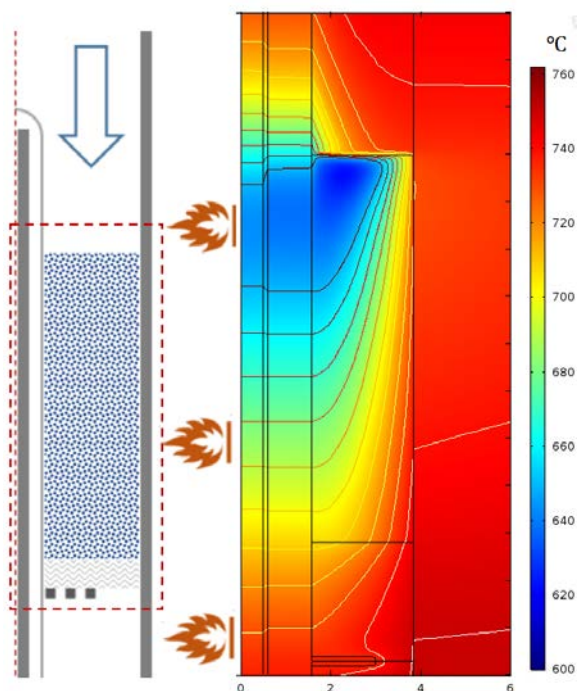


Figure 9.5.4: Modelled and measured temperature profile. At 750°C, 60 NI/h, S/C = 2.

The model is fitted to four parameters; SMR activity, WGS activity, permeability, and thermal conductivity of the catalyst. The permeability only relates to the pressure drop, as the low pressure drops of the experimental setup (<300 mbar) has negligible influence on the reaction kinetics. A heat map illustrating the “coldspot” is shown in Figure 9.5.5



*Figure 9.5.5 Thermal contours* Heat map of the reactor cross section corresponding to Figure 9.5.3. The coldest part of the reactor is near the inlet, just below the top of the catalyst. The external wall is nearly isothermal, deviating less than 15°C along the catalytic bed.

As the process gas is preheated to 750°C before reaching the catalyst, the latent energy drives the reaction, and rapidly cools upon contact. Heat is supplied from the external furnace through the reactor wall, where the temperature difference along the catalytic bed is less than 15°C. The bed exhibits fully developed plug flow, and the thermal contours are a result of the available heat. A radial temperature difference exceeding 100°C is observed across the bed near the top.

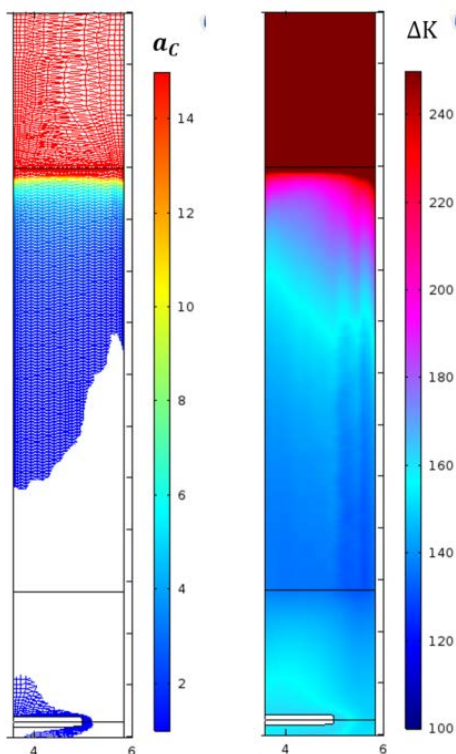


*Figure 9.5.6: Carbon activity and approach to equilibrium* The carbon activity relative to deposition of graphitic carbon for thermal decomposition of methane exceeds unity, at temperatures sufficient for the detrimental reaction. The removed section is for  $a_c < 1$ . This is also reflected in the approach to equilibrium, exceeding 100K for most of the catalytic bed.

The pre-heating of the gas results in high carbon activity for deposition of graphitic carbon near the inlet. An approach to equilibrium exceeding 100K indicates insufficient kinetic activity to bring the reaction to equilibrium. This is in large part due to the excessive pre-heating and short catalyst bed, where an equilibrium is never reached.

## Summary

The model was found to adequately reproduce experimental measurements, in terms of conversion, pressure drop, and temperature profile, using an external temperature profile as model input. An overall effectiveness factor around 10% was found to fit the experimental data best, but an additional

factor for the WGS reaction was required to reproduce outlet composition. The temperature drop correlated to flowrate and methane conversion, where high flowrates results in lower conversion and up to 115°C difference along the reactor.

## References

---

The references are included in the Complete list in Section 8.

*Authors note: This document makes a lot more sense if you start at the other end*